UNSW SYDNEY

Evolution of climate anomalies and variability of Southern Ocean water masses on interannual to centennial time scales

Author:
Santoso, Agus

Publication Date:
2005

DOI:
https://doi.org/10.26190/unsworks/17768

License:
https://creativecommons.org/licenses/by-nc-nd/3.0/au/
Link to license to see what you are allowed to do with this resource.

Downloaded from http://hdl.handle.net/1959.4/33355 in https://unsworks.unsw.edu.au on 2024-04-24

School of Mathematics

The University of New South Wales

Evolution of climate anomalies and variability of Southern Ocean water masses on interannual to centennial time scales

by

Agus Santoso, BSc (Hons.) UNSW

A thesis submitted in accordance with the requirements of The University of New South Wales for the degree of Doctor of Philosophy

Australia

December 2005

Certificate of originality

I hereby declare that this submission is my own work and to the best of my knowledge it contains no materials previously published or written by another person, nor material which to a substantial extent has been accepted for the award of any other degree or diploma at UNSW or any other educational institution, except where due acknowledgement is made in the thesis. Any contribution made to the research by others, with whom I have worked at UNSW or elsewhere, is explicitly acknowledged in the thesis. I also declare that the intellectual content of this thesis is the product of my own work, except to the extent that assistance from others in the project's design and conception or in style, presentation and linguistic expression is acknowledged.

Agus Santoso

Acknowledgements

I express my deepest appreciation to my supervisor Matthew England who has been a constant source of encouragements and support throughout my candidature. I have been fortunate to have an excellent supervisor with a vast knowledge in oceanography and climatology, who always tries his best despite his busy schedule, to put time aside for his students. I thank him for his time and effort to read drafts of this thesis. His level of patience and understanding will always be my source of inspirations.

The CSIRO Aspendale staff and HPSCCC personnel are gratefully acknowledged for providing model output and access to their computing network, particularly I acknowledge Barry Hunt who instigated the 10,000 year run of the CSIRO Mark 2 model. I am especially indebted to Tony Hirst for his support on this thesis project and for the valuable help with the arrangements for the data preparation, access, and download, and for constructive discussions. I gratefully acknowledge Siobhan O'Farrell for providing the model tracer data for deeper analysis of the water mass ventilation. The effort of Mark Collier and Tracey Elliott in preparing the large model data in a format convenient for analyses is sincerely acknowledged.

I am grateful to Peter Oke and Elena Goloubeva for their help in the early phase of the project. Discussions with John You, Ryo Furue, Chris Reason, and Steve Rintoul are all gratefully acknowledged. I also thank David Jackett for making the equation of state routines available, and Jo Jacka for providing the observed sea ice data. The UNSW School of Mathematics IT support is also acknowledged, as well as Alex Sen Gupta for providing access to his disk storage. It was indeed an enjoyable experience to work with Matthew England and Caroline Ummenhofer in the study of the southwest Western Australian rainfall variability, which resulted in the England, Ummenhofer, and Santoso (2006) paper published in the *Journal of*

Climate. The oceanography lab and the mathematics department I work at have been filled with friendly and helpful people like Chris Aiken, Mark Baird, Willem Sijp, Chris Zhuang, Russell Morison, Helen Armstrong and many others who have made my stay there enjoyable.

The journey of the thesis project has been very meaningful with many good friendships made along the way. I thank all my friends and teachers in UNIBUDS for their support and encouragements toward my studies during my terms of service to the society. I thank Evelyn Ong for her whole being and to help archive my collection of research papers. Also to Eveline Dejardin for her guidance and support since my arrival in Australia 12 years ago. This thesis is dedicated to my parents and family back home who have shown me unconditional love, motivation, and full support in every step I take. They have worked hard throughout their lives for my well being and my success toward the completion of this thesis.

Supporting publications

Santoso, A., and M. H. England, 2004: Antarctic Intermediate Water circulation and variability in a coupled climate model. *J. Phys. Oceanogr.*, **34**, 2160-2179.

Santoso, A., M. H. England, and A. C. Hirst, 2006: Circumpolar Deep Water circulation and variability in a coupled climate model. *J. Phys. Oceanogr.*, (in press).

England, M. H., C. C. Ummenhofer, and A. Santoso, 2006: Interannual rainfall extremes over southwest Western Australia linked to Indian Ocean climate variability. *J. Climate*, **19**, 1948-1969.

Santoso, A., and M. H. England, 2006: Antarctic Bottom Water circulation and variability in a coupled climate model. *J. Phys. Oceanogr.*, (to be submitted).

Santoso, A., and M. H. England, 2006: Evolution of Indian Ocean heat content anomalies towards southwest Western Australian rainfall extremes. *J. Climate*, (in preparation).

Abstract

In this study the natural variability of Southern Ocean water masses on interannual to centennial time scales is investigated using a long-term integration of the Commonwealth Scientific and Industrial Research Organisation (CSIRO) coupled climate model. We focus our attention on analysing the variability of Antarctic Intermediate Water (AAIW), Circumpolar Deep Water (CDW), and Antarctic Bottom Water (AABW). We present an analysis of the dominant modes of temperature and salinity ($T - S$) variability within these water masses. Climate signals are detected and analysed as they get transmitted into the interior from the water mass formation regions. Eastward propagating wavenumber-1, -2, and -3 signals are identified using a complex empirical orthogonal function (CEOF) analysis along the core of the AAIW layer. Variability in air-sea heat fluxes and ice meltwater rates are shown by heat and salt budget analyses to control variability of Antarctic Surface Water where density surfaces associated with AAIW outcrop. The dominant mode in the CDW layer is found to exhibit an interbasin-scale of variability originating from the North Atlantic, and propagating southward into the Southern Ocean. Salinity dipole anomalies appear to propagate around the Atlantic meridional overturning circulation with the strengthening and weakening of North Atlantic Deep Water formation. In the AABW layer, $T - S$ anomalies are shown to originate from the southwestern Weddell Sea, driven by salinity variations and convective overturning in the region.

It is also demonstrated that the model exhibits spatial patterns of $T-S$ variability for the most part consistent with limited observational record in the Southern Hemisphere. However, some observations of decadal $T - S$ changes are found to be beyond that seen in the model in its unperturbed state. We further assess sea surface temperature (SST) variability modes in the Indian Ocean on interannual time scales

in the CSIRO model and in reanalysis data. The emergence of a meridional SST dipole during years of southwest Western Australian rainfall extremes is shown to be connected to a large-scale mode of Indian Ocean climate variability. The evolution of the dipole is controlled by variations in atmospheric circulation driving anomalous latent heat fluxes with wind-driven ocean transport moderating the impact of evaporation and setting the conditions favourable for the next generation phase of an opposite dipole.

Contents

Certificate of originality **i**

Acknowledgements **ii**

Supporting publications **iv**

Abstract **v**

Preface **1**

Figure captions 7

Figures 8

Part I: Antarctic Intermediate Water circulation and variability in a coupled climate model **12**

Abstract 13

1. Introduction 14

2. The coupled model and methodology 19

a. The coupled model 19

b. Diagnosis of AAIW variability 20

c. Mechanisms forcing AAIW variability 22

3. Model AAIW: mean properties and circulation 24

a. Potential temperature and salinity 24

b. Circulation 26

4. Model AAIW: interannual to centennial variability 28

a. $\theta - S$ properties 28

b. Comparison with observations 30

c. Propagation of $\theta - S$ anomalies 30

d. Complex EOF analysis 31

5. Mechanisms of variability 37

6. Discussion and Conclusions 43

Table captions 48

Figure captions 49

Tables 53

Figures 55

Part II: Circumpolar Deep Water circulation and variability in a coupled climate model 71

Abstract 72

1. Introduction 73

2. Methodology 76

a. The coupled model 76

b. Deep water structure: isopycnal layer definitions 76

c. Spatio-temporal variability analyses 79

3. Model CDW: mean properties and circulation 80

a. Upper layer 80

b. Lower layer 81

c. Summary 82

4. CDW variability patterns 82

a. $\theta - S$ properties 82

b. Comparison with observations: decadal changes 84

c. Modes of variability: EOF analyses 86

5. Variability mechanisms 88

a. First mode 88

b. Second mode 94

c. Third mode 96

6. Summary and Conclusions 97

Appendix 100

Table captions 107

Figure captions 109

Tables 115

Figures 118

Part III: Antarctic Bottom Water circulation and variability in a coupled climate model 143

Abstract 144

1. Introduction 146

2. The coupled model 150

3. AABW definition, properties, and circulation 153

a. AABW definition 153

b. AABW spreading and distributions of properties 158

c. Summary 159

4. Structure and propagation of $\theta - S$ anomalies 160

5. Variability mechanisms 164

a. Connection with overturning variability 164

b. The role of air-sea and ice-sea fluxes 169

c. Link to Southern Ocean climate modes 172

6. Summary 173

Table captions 178

Figure captions 179

Tables 185

Figures 187

Part IV: Indian Ocean variability and links to regional rainfall 214

Abstract 215

1. Introduction 217

2. Data and data analysis 222

3. Indian Ocean climatology 225

a. Annual-mean state: comparison of model and observations 225

b. Indian Ocean monsoon: atmospheric conditions 226

c. Indian Ocean monsoon: ocean surface circulation 227

4. Indian Ocean climate variability 229

a. Modes of SST variability: EOF analysis 229

b. Anomalous conditions related to extreme events 234

c. Remote forcings on the Indian Ocean SST variability 238

5. SWWA rainfall extremes linked to Indian Ocean variability 242

a. SWWA rainfall variability and extreme events 242

b. Surface anomalies during SWWA rainfall extremes 243

c. Seasonal evolution of climate anomalies 246

d. Evolution of heat flux anomalies 249

6. Summary 254

Table captions 259

Figure captions 261

Tables 267

Figures 269

Concluding Remarks 299

References 301

List of Acronyms 325

Preface

The focus of this study is on the Southern Ocean which plays a key role in the global climate system. The Antarctic sector of the Southern Ocean is a region of major oceanic heat loss driving the global thermohaline circulation, with the resulting cold waters and deep overturn driving enhanced oxygen uptake and high absorption of CO_2 and other atmospheric gases, particularly via the intermediate waters (Sabine et al. 2004). The lack of meridional boundaries makes the Southern Ocean the only oceanic region to allow a complete circumpolar flow, connecting the three major ocean basins; the Atlantic, Indian, and Pacific Oceans. In the Southern Ocean, interactions of the world's most voluminous water masses take place (Fig. 1). The Antarctic Intermediate Water (AAIW) characterised by low salinity, extends from the surface of the subpolar regions to about 1000-m depth near the Equator. Found above AAIW in the subpolar region is the more saline Subantarctic Mode Water (SAMW) characterised by deep wintertime mixed layers. Below AAIW, the voluminous Circumpolar Deep Water (CDW) upwells in the Southern Ocean and is derived from a combination of North Atlantic Deep Water (NADW), old recirculated waters from the Pacific, mixing with the northward flowing AAIW above, and mixing from Antarctic Bottom Water (AABW) below.

Situated in a regime of the world's strongest zonal wind stress, the Southern Ocean is characterised by a massive oceanic transport via the Antarctic Circumpolar Current (ACC), marked by steep meridional density gradients which are set by the westerly winds and thermohaline forcings. The existence of sea ice around Antarctica further makes the Southern Ocean a unique yet complex region for climate variability studies. The southern flank of the ACC coincides with the northern-most extent of sea ice, thereby influencing sea-ice dynamics, melting, and forming in the region where constant density (isopycnal) surfaces associated with the Southern Ocean

water masses outcrop (Fig. 1). Variations in atmospheric and sea-ice processes alter heat and freshwater fluxes into the ocean, giving rise to anomalous sea surface temperature (SST) and salinity (SSS). These climate anomalies in the form of SST and SSS anomalies are then transmitted into the interior along isopycnal surfaces where the anomalies are most effortlessly mixed and transported to other parts of the world over long time scales. The Southern Ocean is thus a window connecting climate variability at the air-sea and ice-sea interface to the deep global ocean. Hence, an improved knowledge of the structure and mechanisms of temperature and salinity variability in the Southern Ocean interior will assist the understanding, interpretation, and prediction of global climate variability.

Detection of climate change signals in the ocean interior has received significant attention in recent decades. This comes about due to the concern over the rise of global temperature with increasing emission of anthropogenic CO_2 into the atmosphere. Uncertainties remain whether the temperature and salinity changes within deep water masses are signals of anthropogenic climate change or part of a low frequency natural variability. It is thus of fundamental importance to gain an insight into the characteristics and mechanisms of the natural variability in the ocean. However, the paucity of historical data limits our knowledge of the natural variability structure of these deep water masses; they are characterised by slow ventilation rates of the order of decades to hundreds of years. High quality observational data sets such as those obtained during the period of the World Ocean Circulation Experiment (WOCE), coupled with sparse data sets pre 1980, are insufficient to characterise the variability over such time scales. Climate models integrated over millennia serve as a promising tool for this purpose. Even using modern supercomputing facilities, such long integration times are only possible in coarse-resolution non-eddy resolving models.

Numerical models of the physical system have evolved from an early stage in the 1960s, such as that developed by Bryan (1969), into a sophisticated form as of today. Yet, to date, there are still virtually no models that can accurately simulate the earth's climate. This is due in part to our current lack of complete understanding of the underlying physical processes, especially at the mesoscale. Nevertheless, comprehensive analyses of the natural variability of water masses within climate models provides a viable means of tackling this issue. Apart frrom a better understanding of the natural variability, the analyses are also necessary to advance our understanding of the current state of climate models and to guide future model validation and improvements.

The aim of the present study is to document the spatial and temporal natural variability of the Southern Ocean water masses in a climate model, with a focus on the interannual to centennial time scales. Dominant modes and mechanisms of temperature-salinity variability within the AAIW, CDW, and AABW are identified and investigated. Such a study requires the use of a fully coupled climate model which simulates interactions between components of the climate system, exhibiting a realistic representation of the key climate phenomena as observed in the physical world. It is also a fundamental requirement that the model must at least simulate (1) a realistic structure/distribution of water mass properties and pathways, (2) a reasonable distribution of temporal variability and (3) minimal long-term drift, even in the mid-depth oceans.

We have employed the Commonwealth Scientific and Industrial Research Organisation Mark 2 climate model (CSIRO Mk2) which consists of atmospheric, oceanic, sea-ice, and biospheric submodels coupled together to simulate the present-day climate. The model was run for 10,000 years with a constant atmospheric CO_2 level. The model is coarse with horizontal resolution of approximately 5.6° longitude by

3.2° latitude and 9 sigma-levels in the amospheric component and 21 z-levels for the ocean submodel. Specifications of the model are outlined in section 2 of Part I−IV of the thesis and further details can be found in Gordon and O'Farrell (1997) and Hirst et al. (2000). The CSIRO Mk2 has been a widely used and well documented climate model. Its capability in simulating realistic climate variability, such as the El Niño-Southern Oscillation (ENSO) and the Antarctic Circumpolar Wave (ACW), has been well established (e.g., Cai et al. 1999; Walland et al. 2000; Hunt 2001; Cai and Watterson 2002; Vimont et al. 2002; Hunt and Elliott 2003). The water mass ventilation in the Northern Hemisphere oceans is well simulated as documented in O'Farrell (2002). The CSIRO Mk2 also performs well in the Coupled Model Intercomparison Project (CMIP; Covey et al. 2000) and the Ocean Carbon Model Intercomparison Project (OCMIP; Dutay et al. 2002).

We analyse the 1000-year model output towards the end of the 10,000-year integration by which time the model exhibits very minor drift. This is depicted in Fig. 2 showing the annual mean of global averaged temperature south of 20°S at the top model level (Fig. 2a) and at the deepest model level (Fig. 2b). The model also exhibits considerably rich temporal variability at the surface and in the interior, as compared to that in the extended integrations of the GFDL model as used by Manabe and Stouffer (1996) which exhibits significantly large climate drift (Fig. 2c, d).

In terms of temporal variability, the CSIRO Mk2 model is superior to the IPCC version of the CSIRO Mk3 model, which is a successor to CSIRO Mk2 with a finer horizontal and vertical resolution (Fig. 2e, f). The 500-year output of the CSIRO Mk3 model was only made available towards the end phase of our study. This version of the model was also used for the IPCC Fourth Assessment report and includes undesirable features such as the unrealistically high ACC transport through

the Drake Passage (Fig. 3a) with a mean of 306 Sv as compared to 100 Sv in the CSIRO Mk2 (Fig. 3b) and the observed of about 130 Sv (e.g., Sloyan and Rintoul 2001). The Mk3 version has since then been undergoing upgrades, and its ability to simulate natural variability without flux corrections will likely make it useful for future variability analyses.

The CSIRO Mk2 model simulates water mass structure and distributions closest to the observed as compared to many other models, including the Manabe and Stouffer version of the GFDL model (used by Rintoul and England 2002) and the IPCC version of CSIRO Mk3. This is shown in Fig. 4 which displays the global zonally averaged salinity in the models (Fig. 4a-c) and the Levitus climatology (Fig. 4d). It may be noted that the interior density and salinity in the models deviate from the observed values which is a long-standing problem in ocean models. However, given the reasonable distribution of water mass properties matching the observed structure, the spatial patterns of variability in the CSIRO Mk2 likely represent those of the real system reasonably well. Furthermore, as shown in this thesis, the water-mass circulation and property distribution in the Southern Ocean are carefully assessed and shown to match the observed with a good level of accuracy. This justifies its use in the analysis of the Southern Ocean water masses and their natural variability.

In summary, the goal of the study is to document the spatio-temporal patterns of temperature and salinity variability within the Southern Ocean water masses on interannual to centennial time scales using the CSIRO Mk2 climate model. We aim to identify the dominant modes of variability and to investigate the mechanisms giving rise to the variability within AAIW, CDW, and AABW. These are covered in Part I (see also Santoso and England 2004), Part II (Santoso, England, and Hirst 2006), and Part III (Santoso and England 2006) of the thesis, respectively. One

of the findings of this study is that the variability in the properties of these water masses are dominated by climate anomalies created at the water-mass formation region. Thus, knowledge of the characteristics and mechanisms of these variability modes can improve detection of climate change signals in the ocean interior and aids in future prediction of climate variability. References to observational studies of decadal changes are made wherever possible for comparison with the model variability. In the last part of the thesis (Part IV; an expansion of the study by England, Ummenhofer, and Santoso 2006), we investigate the Indian Ocean variability in the CSIRO Mk2 model and observations. We demonstrate its influence on regional rainfall variability, particularly in the southwest Western Australian region. Its link to regional rainfall and the possible influence from the Southern Ocean highlights the role of the ocean in regional climate variability.

This thesis is essentially a compilation of four research papers assigned into separate parts (Part I–IV). Consequently, the format for each part is chosen to follow that of a submitted manuscript with each part consisting of an abstract and independent set of figures and tables. The numbering of figures, tables, and equations is independent for each part. Cross reference between parts is done by referring to the figure/equation/table number of the specified part (e.g., Fig. 10 of Part II, etc.). On the other hand, the references for the entire dissertation are listed in the reference section on page 290. Editorial and scientific conventions used by the *Journal of Physical Oceanography* are adopted throughout the thesis.

Figure captions

Figure 1: Schematic illustration of the Southern Ocean water masses showing isopycnal surfaces and meridional flow direction.

Figure 2: Time series of averaged ocean temperature south of 20°S for the top model level (left column) and the deepest model level (right column) in the CSIRO Mk2 (top row), the GFDL model (middle row), and the CSIRO Mk3 (bottom row).

Figure 3: ACC transport through the Drake Passage in (a) the CSIRO Mk3 and (b) the CSIRO Mk2 models.

Figure 4: Global zonally averaged salinity in (a) the CSIRO Mk2, (b) the GFDL model of Manabe and Stouffer (1996), (c) the CSIRO Mk3, and (d) the Levitus climatology. The dashed contours mark potential density surfaces referenced to the surface. The solid contours mark potential density surfaces referenced to 2000 db.

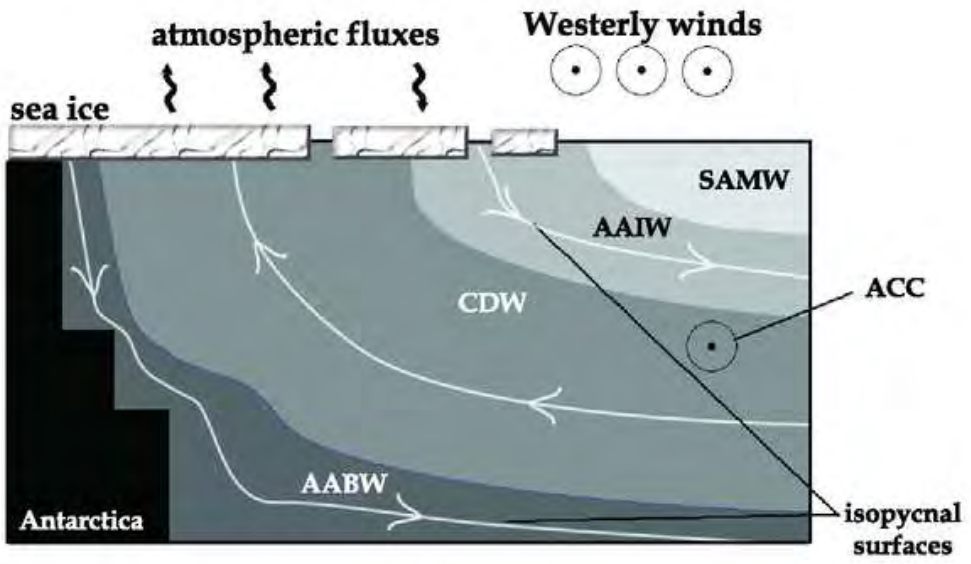

Figure 1: Schematic illustration of the Southern Ocean water masses showing isopycnal surfaces and meridional flow direction.

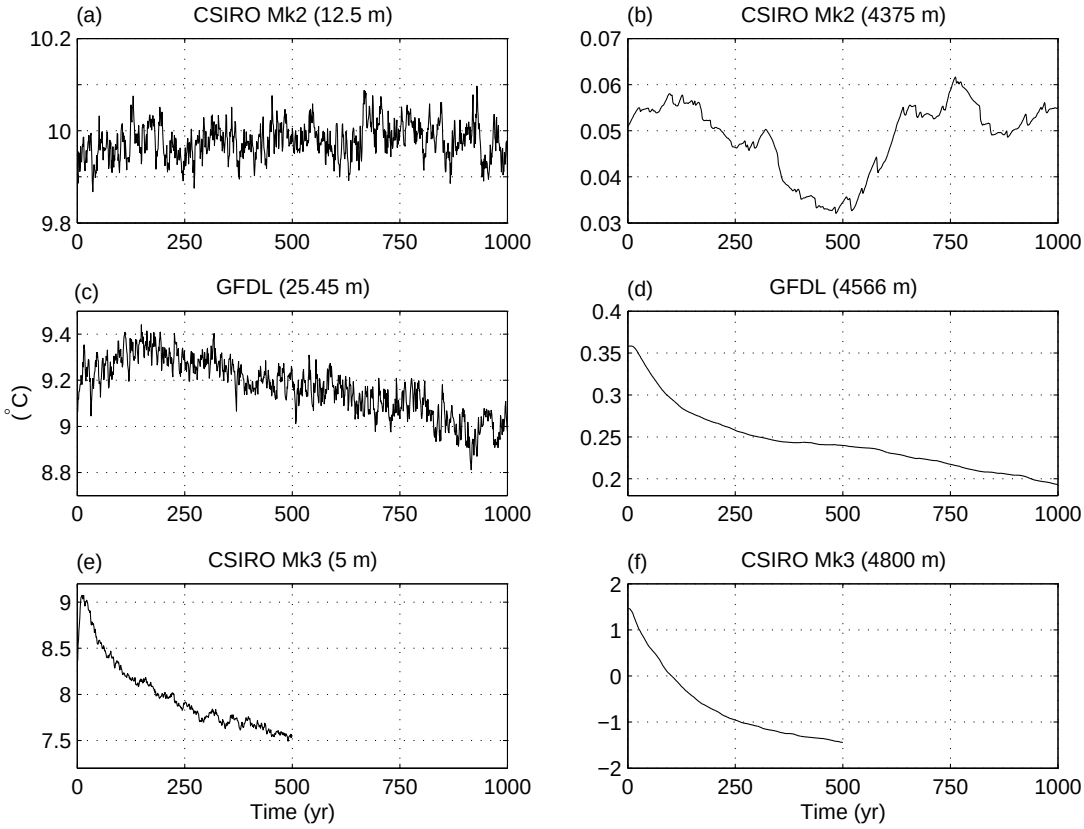

Figure 2: Time series of averaged ocean temperature south of 20°S for the top model level (left column) and the deepest model level (right column) in the CSIRO Mk2 (top row), the GFDL model (middle row), and the CSIRO Mk3 (bottom row).

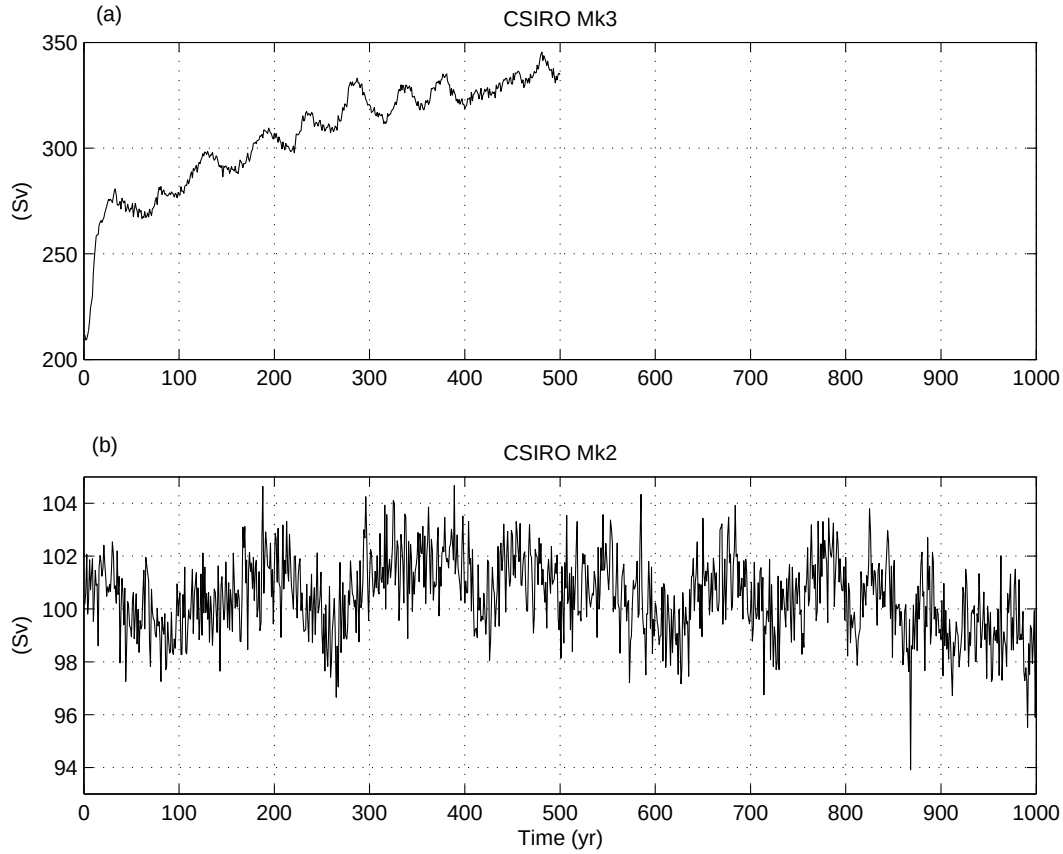

Figure 3: ACC transport through the Drake Passage in (a) the CSIRO Mk3 and (b) the CSIRO Mk2 models.

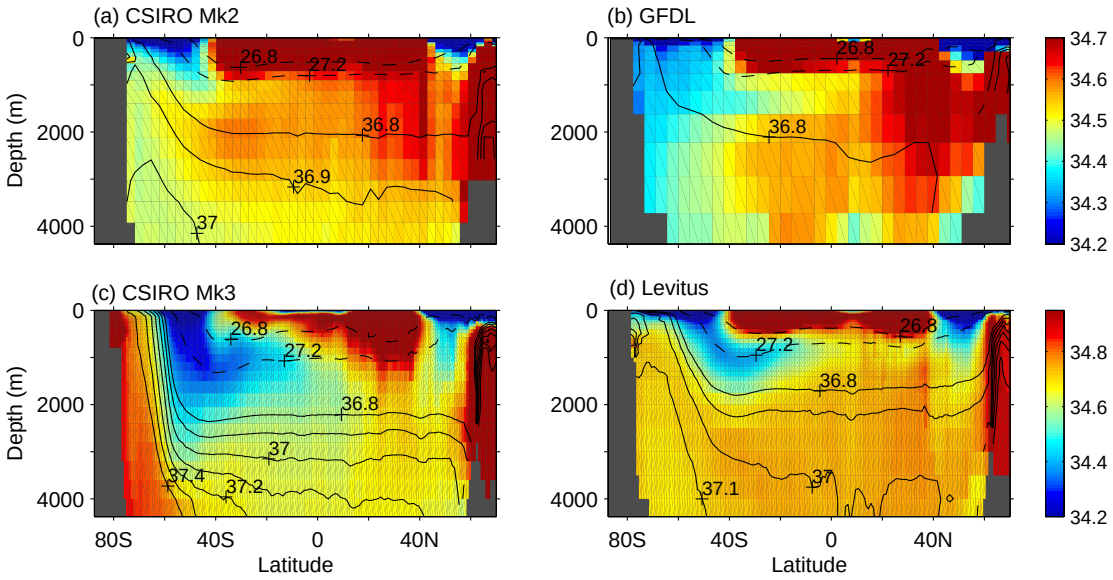

Figure 4: Global zonally averaged salinity in (a) the CSIRO Mk2, (b) the GFDL model of Manabe and Stouffer (1996), (c) the CSIRO Mk3, and (d) the Levitus climatology. The dashed contours mark potential density surfaces referenced to the surface. The solid contours mark potential density surfaces referenced to 2000 db.

Part I: Antarctic Intermediate Water circulation and variability in a coupled climate model

Abstract

The variability of Antarctic Intermediate Water (AAIW) in a long-term natural integration of a coupled climate model is examined. The mean state of the climate model includes a realistic representation of AAIW, which appears centered on the σ_θ = 27.2 kg m^{-3} density surface (hereafter $\sigma_{27.2}$) both in observations and the model. An assessment of ventilation rates on the $\sigma_{27.2}$ surface suggests this particular climate model forms AAIW in a mostly circumpolar fashion, with a significant contribution from Antarctic Surface Water. This motivates us to assess oceanic variability along this core AAIW isopycnal surface. Complex empirical orthogonal function analyses decompose the variability into 3 dominant modes showing circumpolar patterns of zonal wavenumber-1, 2 and 3 on the $\sigma_{27.2}$ density surface. The modes contain eastward propagating signals at interannual to centennial timescales. Mechanisms forcing this variability are investigated using heat and salt budget analyses at the wintertime outcrop of the $\sigma_{27.2}$ surface. Such an approach ignores the mechanism of AAIW variability sourced by Subantarctic Mode Water variations, which has been examined previously and is, for the most part, beyond the present study. Variability in meltwater rates and atmospheric heat and freshwater fluxes are found to dominate the intermediate water variability at the outcrop region. In contrast, northward Ekman transport of heat and salt plays a significant but localised role in AAIW temperature-salinity variability. There is also an important contribution from the Antarctic Circumpolar Current to the variability at the outcrop region via zonal transport of heat and salt. Whilst the magnitude of AAIW natural variability can be large near the outcrop of the salinity minimum layer, recent observations of cooling and freshening at depth are suggested to be beyond that of the unperturbed system.

1. Introduction

An increasing number of studies on Antarctic Intermediate Water (AAIW) formation and variability (e.g., Piola and Georgi 1982; England 1992; England et al. 1993; Johnson and Orsi 1997; Wong et al. 1999; Arbic and Owens 2001; Sørensen et al. 2001; Saenko et al. 2003) reflects the importance of this water mass in balancing the global-scale oceanic heat and salt transport. Understanding and quantifying natural variability of AAIW is crucial to an understanding of longer-term climate change. In particular, the detection and attribution of climate change at intermediate layers of the Southern Ocean depends on a knowledge of the magnitude and dynamics of AAIW variability. The goal of this study is to quantify and explain interannual to centennial scale variability of AAIW using a coupled climate model.

AAIW is found in all sectors of the Southern Hemisphere oceans to the north of the Antarctic Polar Front (APF). AAIW temperature-salinity properties and circulation have already been documented in many studies based on observational data (e.g., Deacon 1933; Georgi 1979; Piola and Georgi 1982). Depending on the location in the ocean, AAIW has generally been characterised as a salinity minimum water mass extending from the Antarctic Polar Front Zone (APFZ) with a typical salinity of 34.2-34.4 psu and temperature of 3°-5°C (e.g., Georgi 1979; Piola and Georgi 1982). AAIW spreads northward to intermediate depths of approximately 800-1000 m at 40°S and is found as far north as 30°N in the North Atlantic (e.g., Pickard and Emery 1991; Talley 1996). As it flows northward from the source region, its salinity increases as it mixes with more saline water from above and below. The density surfaces associated with the core of AAIW fall in the range 1027.2-1027.3 kg m^{-3} (e.g., Molinelli 1981; Piola and Georgi 1982) and shoal south of the APF (refer to Molinelli 1981, his Fig. 11).

The formation process of AAIW has long been an area of research resulting in a

variety of mechanisms still under debate. As first described by Wüst (1935), AAIW is identified in the Southern Ocean by a salinity minimum layer that descends near the APFZ. Sverdrup et al. (1942) proposed that AAIW is formed by circumpolar subduction or along-isopycnal transport along the APFZ, supported by the circumpolar presence of AAIW. In contrast, McCartney (1977) suggested that AAIW is primarily a by-product of Subantarctic Mode Water (SAMW), formed in a deep convective mixed layer in the southeast Pacific Ocean off southern Chile, feeding into the Pacific Ocean and via the Drake Passage to the southwest Atlantic. Molinelli (1981), on the other hand, suggested that isopycnal processes, both mixing and geostrophic flow, dominate AAIW formation along the APFZ, with Antarctic Surface Water (AASW) mixing with waters at depth in the Subantarctic Zone. In addition, Molinelli (1981) found significant input of AASW along the σ_θ =27.2-27.3 kg m^{-1} isopycnal layer in the southeast Pacific and near Kerguelen Island (80°E). Other studies based on observational data support one or a combination of McCartney's (1977) and Molinelli's (1981) suggestions on AAIW formation in the southeast Pacific and southwest Atlantic (e.g., Georgi 1979; Piola and Georgi 1982; Piola and Gordon 1989; Talley 1996). A recent study by Sloyan and Rintoul (2001) found that cross-frontal exchange of AASW to SAMW together with deep winter mixing, dominate the renewal of AAIW via diapycnal exchange. This is in contrast to the along-isopycnal process proposed by Molinelli (1981). In short, mechanisms of AAIW renewal are still under vigorous debate.

Model simulations of AAIW have improved with the evolution of prognostic z-coordinate ocean general circulation models. England (1992) was the first to capture a salinity minimum in the Southern Ocean in a coarse resolution model, although his AAIW was too saline and lacked the northward penetration observed. This could be attributed to the unphysical treatment of horizontal mixing in these

earlier ocean models. Some improvement was realised upon the inclusion of the Redi (1982) mixing scheme for along-isopycnal diffusion (England 1993), with the AAIW formation mechanism largely consistent with McCartney's (1977) view (England et al. 1993). Further improvement in AAIW representation can be achieved upon the inclusion of the Gent and McWilliams (1990) parameterisation (GM) for adiabatic transport of tracers by eddies (e.g., Hirst and McDougall 1996; Large et al. 1997; Duffy and Caldeira 1997; Duffy et al. 1999; Sørensen et al. 2001), although not all such models attain realistic AAIW temperature-salinity. In GM models it appears that AASW plays a more significant role in AAIW formation along the APFZ, including the model used in this study, as a result of reduced midlatitude to subpolar convection in the Southern Ocean (e.g., Sørensen et al. 2001).

The model sensitivity of AAIW to choice of surface forcing has also been studied (e.g., England 1993; Hirst and McDougall 1996; Duffy et al. 1999). However, only recently has the effect of freshwater forcing due to Antarctic sea ice been shown to be important (Duffy et al. 2001; Saenko and Weaver 2001). Using a coupled ocean-ice model, Saenko and Weaver (2001) showed that high latitude westerlies at the Antarctic sea-ice margin induce northward Ekman transport of sea ice where it melts and feeds freshwater in the regions where AAIW isopycnal surfaces outcrop. Furthermore, using the same model Saenko et al. (2003) found non-uniform subduction of AAIW and a localised northward flux of freshwater in the southeast Pacific. This is in contrast to the 2-D circumpolar view of AAIW formation found by Sørensen et al. (2001), though the Sørensen et al. (2001) study ignores sea-ice effects in an uncoupled configuration.

Spatial variations in the $T - S$ properties of AAIW are detected in different locations of the Southern Ocean. For example, a study conducted by Piola and Georgi (1982) based on observational data documents the circumpolar properties of

AAIW in the latitude band 40°S-45°S. They found different varieties of AAIW in each of the three ocean basins. The Indian Ocean AAIW is warmer and saltier than in the South Atlantic while AAIW salinity decreases abruptly east of 160°W where the South Pacific variety of AAIW is found. Furthermore, Piola and Georgi (1982) found that large changes in the properties of AAIW occur in the transition regions between the three ocean basins.

Due to sparsity of observational data, only a few studies of temporal changes in AAIW have been carried out. Bindoff and Church (1992) found a significant cooling of approximately 0.05-0.2°C and freshening of 0.01-0.04 psu (estimated from their Fig. 3) along density surfaces within 600-1000 m depth in the Tasman Sea at 43°S and 28°S on the basis of measurements made 22 years apart. Wong et al. (1999) found a basin wide freshening (zonally averaged decrease of 0.021 psu) along density surfaces of AAIW based on a 20-yr difference measured in the Pacific Ocean along 17°S. Based on the same measurements, Wong et al. (2001) found that the freshening and cooling along the density surfaces were also accompanied by freshening and cooling along isobars. They found that the $T - S$ decrease extends southward to the Subantarctic Front along 150°W. Johnson and Orsi (1997) found mean cooling and freshening between 1968/69 and 1990 of approximately 0.1°C and 0.03 psu (estimated from their Fig. 5) along isopycnals associated with AAIW in the Pacific along 170°W from 48°S to 20°S. Based on the methodology of Bindoff and McDougall (1994), Johnson and Orsi (1997) propose that the change is a result of surface freshening at high latitudes where isopycnals associated with AAIW outcrop before the water ventilates the base of the subtropical thermocline. Decadal changes in the Indian Ocean across 32°S between 1962-87 have been documented by Wong et al. (1999) and Bindoff and McDougall (2000) with average cooling and freshening of 0.33°C and 0.06 psu along a neutral surface equivalent to the AAIW 1027.3 kg m^{-3}

potential density surface. Arbic and Owens (2001) document an average warming of about 0.5°C century^{-1} and a salinity increase of 0.1 psu century^{-1} along isobars near 1000-db at 32°S and 24°S in the southwestern Atlantic (see their Figs. 3 and 4). They attributed the warming along the isobars, where AAIW is found, to be mostly due to water-mass changes along isopycnal surfaces. Thus, variability in the ocean interior along isopycnals, where true water mass properties are defined, is attributable to variability at the region of water mass formation (e.g., Bindoff and Church 1992; Bindoff and McDougall 1994; Wong et al. 2001). Banks et al. (2000) compare the observed decadal changes, particularly for the Indian Ocean 32°S section, with the natural variability in a coupled climate model. They found weaker cooling and freshening than observed along intermediate water isopycnals in the 32°S section. Based on the weaker changes in the model, they suggest that the observed decadal changes in Bindoff and McDougall (2000) are likely to be a signal of anthropogenic climate change.

Whilst the above studies have furthered our knowledge of natural and forced variations in AAIW at several isolated locations, there has been relatively little attention given to the mechanisms controlling water-mass variability at intermediate depths. This is due in part to the sparsity and short period of observational data in the Southern Ocean. The goals of the present study are (1) to document the spatial and temporal variability of AAIW along isopycnal surfaces in a multi-century integration of a coupled atmosphere-ocean-ice model, (2) to evaluate the mechanisms controlling this variability by conducting heat/salt budget analyses at the late-winter outcrop locations of the isopycnal surfaces, and (3) to examine the patterns of propagation of these anomalies along isopycnals in space and time. We will address these three goals in sections 4 and 5. Firstly, though, the coupled model and methods of analysis are described in section 2, and a brief description of the model simulated

AAIW is provided in section 3. Finally, we summarise the study in section 6.

2. The coupled model and methodology

a. The coupled model

The model used in this study is the Commonwealth Scientific and Industrial Research Organisation (CSIRO) 10,000-yr natural pre-industrial CO_2 coupled ocean-atmosphere-ice-land surface model. This is an updated version of the 1000-yr coupled model employing the GM scheme as described in Hirst et al. (2000). The atmospheric model is discretised on nine levels in a sigma-coordinate system. The model has full diurnal and annual cycles, gravity wave drag, a mass flux scheme for convection, semi-Lagrangian water vapour transport, and a relative humidity-based cloud parameterisation (for details see Gordon and O'Farrell 1997; Hirst et al. 2000). The ocean model is based on the Bryan-Cox code (Cox 1984) employing GM and zero horizontal diffusivity. It has a resolution of approximately 5.6° in longitude and 3.2° in latitude, with 21 vertical levels of irregular grid box thickness. The ocean model resolution is typical of that used in previous studies of AAIW properties and dynamics (e.g., England et al. 1993; Sørensen et al. 2001). The atmospheric model is spectral with horizontal resolution limited by a rhomboidal truncation at wavenumber-21. A full description of the sea-ice model can be found in O'Farrell (1998). Advection and divergence of sea ice can result from both wind stress and motion by ocean currents. Constant annual but seasonally varying flux adjustment (heat, freshwater, and wind stress) is applied in the coupling between the ocean and atmosphere (and sea ice) submodels to reduce drift.

We analyse 1000 yr of model data from the latter stages of the 10,000-yr run. It may be noted that the model exhibits minimal drift at this latter stage of the run. Variables analysed include ocean potential temperature (denoted as θ hereafter),

salinity (S), horizontal ocean velocities (u,v), as well as air-sea flux properties such as surface wind stress (τ^x, τ^y), and air-sea heat (Q) and equivalent salt (H) fluxes. Only data south of 20°S are considered in our analyses since the focus of this study is on the water masses of the Southern Ocean.

b. Diagnosis of AAIW variability

We divide this study into two parts. The first part is to document the variability of AAIW in the model. To this end, we analyse $\theta - S$ properties on the potential density surface $\rho_\theta = 1027.2$ kg m^{-3} (referred as $\sigma_{27.2}$ hereafter). This density surface is chosen as it approximately coincides with both the model and observed intermediate water salinity minimum reaching depths of 700-1000 m to the north of 40°S (as can be seen in Fig. 1; discussed further in section 3). This potential density surface outcrops in winter near the maximum sea-ice margin in the model (Fig. 2a), as well as in the real ocean (Fig. 2b). In Figure 2, discussed further in section 5, the observed $\theta - S$ data is based on Levitus (1994) climatology and the sea-ice extent data is based on the monthly US NAVY/NOAA Joint Ice Center and passive microwave Defense Meteorological Satellite Program (DMSP) extending from January 1973 to September 1998.

It is of some interest to diagnose the relative ventilation rate along the chosen $\sigma_{27.2}$ AAIW density surface, in part to resolve where we should analyse model variability of this water mass. Figure 3 shows the $\sigma_{27.2}$ distribution of a passive tracer after 50 yr of release in the coupled climate model. The passive tracer is set to a value of 100% at the surface in the Southern Hemisphere for all time steps (and zero in the Northern Hemisphere surface layer; further details can be found in O'Farrell 2002). The passive tracer suggests an approximately zonally-uniform distribution of AAIW ventilation over multi-decadal time scales. The highest concentration of

tracer occurs at the layer outcrop near 60°S, decreasing northward into the ocean interior along $\sigma_{27.2}$. The circumpolar penetration of passive tracer into the interior suggests Antarctic Surface Water (AASW) is the major source of AAIW formation in the model, both by direct subduction and indirectly via cross-front mixing at the APFZ. Recycled mode water also contributes, with a slightly enhanced ventilation detected in the southeast Pacific Ocean, the Tasman Sea, and the southeast Indian Ocean. Thus, the model's AAIW formation process seems to be primarily following the circumpolar mechanism of Sverdrup et al. (1942), with some additional localised spiking from SAMW. This agrees with the study by Sørensen et al. (2001) in which mid-latitude convection is reduced upon GM inclusion (see also Hirst and McDougall 1996; Duffy et al. 1999) thereby reducing the amount of diapycnal mixing in the region off the coast of Chile, in contrast to models without isopycnal and/or GM mixing (e.g., England 1992; England 1993). In analysing AAIW variability in the present paper we will focus our attention on ventilation along the $\sigma_{27.2}$ surface, while acknowledging that lighter density water, in particular SAMW, also contributes to ventilation in the model's intermediate layers. For studies of SAMW variability in observations and models the reader is referred to Rintoul and England (2002) and Bryden et al. (2003).

Since AAIW formation tends to occur in late winter when surface waters are at their most dense, and mixed layers at their deepest, we use late-winter data for our analyses. For this purpose, we define 'late winter' as the mean of September and October properties. The late-winter ocean variables (θ, S, u and v) are mapped onto the $\sigma_{27.2}$ surface by means of spatial linear interpolation and averaging. A high-pass filter on the frequency-domain is applied to the ocean data on the isopycnal to remove variabilities with period longer than 200 yr. A cosine-taper is used to smooth the edge of the filter to reduce the effect of ringing or Gibb's phenomenon

in the time domain (Emery and Thomson 1998). Complex empirical orthogonal function (CEOF) analysis in the time domain is used in this study to decompose the $\theta - S$ variability into orthogonal modes, and to capture propagating signals as the domain of interest lies within the influence of the eastward flowing Antarctic Circumpolar Current (ACC). The CEOF analysis has been used widely in climate studies (e.g., Mizoguchi et al. 1999; Putman et al. 2000); for a description of the CEOF technique the reader is referred to Barnett (1983) and Horel (1984). The power spectral density of each orthogonal mode's principal component time series is estimated using the Thomson multitaper method described in Percival and Walden (1993) and Mann and Lees (1996). Red noise processes represent noise with low-frequency fluctuations resulting from the integration of white noise forcing via slow ocean processes. The background spectrum of a first order autoregressive (AR-1) red noise process is estimated and fitted onto the total spectrum (using the robust method described in Mann and Lees 1996) to provide a basis for identifying significant AAIW variability beyond that of a red-noise signal at the 95% confidence level.

c. Mechanisms forcing AAIW variability

The second part of our study is to explain the model $\theta - S$ variability in AAIW by examining water-mass variability at the $\sigma_{27.2}$ outcrop. This approach assumes that a substantial fraction of AAIW is sourced from AASW (either via direct subduction or cross-frontal mixing at the APFZ). This seems to be the case in the present model, as ventilation on the $\sigma_{27.2}$ surface is genuinely circumpolar; with only weak evidence of enhanced formation rates in mode water formation regions (see Fig. 3). We perform heat and salt budget analyses as in Rintoul and England (2002) using the following equations in which all of the surface variables have been interpolated

onto the late-winter $\sigma_{27.2}$ outcrop:

$$\frac{\partial\theta}{\partial t} = \frac{Q_{net}}{\rho_0 C_p h} - \mathbf{u}\cdot\nabla\theta - w\frac{\partial\theta}{\partial z} + \theta'_{mix} \quad (1)$$

$$\frac{\partial S}{\partial t} = \frac{H_{net}}{h} - \mathbf{u}\cdot\nabla S - w\frac{\partial S}{\partial z} + S'_{mix} \quad (2)$$

where θ and S are the surface layer temperature and salinity located at model grid 12.5-m depth, Q_{net} and H_{net} are the air-sea heat and equivalent salt fluxes, ρ_0 is density which equals 1027.2 kg m^{-3}, C_p the specific heat capacity of sea water (taken as 3986 J kg^{-1} K^{-1}), h is surface layer thickness (25 m), $\mathbf{u} = (u, v)$ is horizontal velocity, w vertical velocity, and θ'_{mix}, S'_{mix} are the heat and salt budget terms due to mixing (vertical, isopycnal, convective and GM). Note that the units of the heat and salt budget terms in Eqs. 1 and 2 are in °C s^{-1} and psu s^{-1}, respectively.

The seasonal and year-to-year displacements of the $\sigma_{27.2}$ outcrop position are illustrated in Fig. 4a. The isopycnal outcrop moves to a new geographical position in response to atmospheric forcings and ocean dynamics. For example, following surface warming/freshening (cooling/salination) due to seasonal and year-to-year variations, the late-winter isopycnal outcrop would be displaced southward (northward). Hence to obtain heat/salt budget closure on the late-winter $\sigma_{27.2}$ outcrop in each model year, the heat and salt content terms, $\partial\theta/\partial t$ and $\partial S/\partial t$, are calculated by subtracting late-summer $\theta - S$ (defined as the average over March and April) from late-winter $\theta - S$ on the annually fixed but zonally-varying position of the late-winter $\sigma_{27.2}$ outcrop (∂t then $\approx$ 6 months). All variables on the right hand side of Eqs. 1 and 2 are defined as the mean (winter) values averaged over April to September. The conventional season definition of the variables is shown in Fig. 4b. The budget equations then explain transformations in $\theta - S$ properties from late summer to late winter as a function of winter air-sea fluxes and ocean dynamical processes at the late-winter outcrop position for each year. It may be noted that the component of horizontal advection of heat and salt due to wind-driven Ekman

transport can be calculated as $\mathbf{u_e} \cdot \nabla\theta$, $\mathbf{u_e} \cdot \nabla S$, where $\mathbf{u_e} = (\tau^y/\rho f h, -\tau^x/\rho f h)$ with f the Coriolis parameter.

The surface heat and salt flux terms can be further decomposed into their respective components:

$$Q_{net} = Q_{solar} - (Q_{evp} + Q_{sh} + Q_{lw}) - Q_{oi} \quad (3)$$

$$H_{net} = E - P + H_{ice} \quad (4)$$

where Q_{solar} is the incoming solar radiation; Q_{evp}, Q_{sh}, and Q_{lw} are the sea-to-air heat flux terms namely evaporative, sensible heat and long wave radiation, respectively; Q_{oi} is the ocean-to-ice sensible heat flux; E and P are effective salt fluxes due to evaporation and precipitation, and H_{ice} is the equivalent salt flux due to sea-ice melting and formation. The role of sea ice is anticipated to be important in controlling the variability on $\sigma_{27.2}$ as the isopycnal breaks the surface near the Antarctic sea-ice margin in the model and in observations (as seen in Figs. 2a, 2b). Note that the outcrop can exist at more than one meridional location at certain longitudes (Figs. 2a, 2b) in which only the northern-most part contributes to AAIW. In such instances the heat/salt budget analyses are conducted only on the northern-most part of the $\sigma_{27.2}$ outcrop.

3. Model AAIW: mean properties and circulation

a. Potential temperature and salinity

The structure of AAIW simulated by the model can be seen in Fig. 1 (left column), which shows the zonally averaged meridional section of late-winter salinity in each ocean basin. The corresponding observed salinity reproduced from the Levitus climatology is displayed in the right column of Fig. 1 for comparison. The $\sigma_{27.2}$ contour shown, indicating the isopycnal used for analysis in this study, marks

the approximate core of AAIW, both in the model and observed, which extends down from the surface outcrop region at 60°S to intermediate depths of 700-1000 m. Overall AAIW representation is very good in the CSIRO climate model, though the northward extent of the simulated salinity minimum is weaker than the observed particularly in the Indian Ocean. The weak salinity minimum in the Indian Ocean appears to be due to unrealistically deep penetration of SAMW at 40°-50°S, marked by a relatively deep mixed layer there in the model salinity field (Fig. 1, Indian Ocean panels). Weak northward penetration of AAIW has been a common problem in coarse-resolution ocean models, though improvement is realised here using zero horizontal diffusion and GM mixing. Overall the representation of AAIW shown in Fig. 1 is as good as can be expected in a climate model of coarse resolution.

The late-winter $\theta - S$ distribution along $\sigma_{27.2}$ in the model and observed is presented in Figs. 5a and 5b, respectively. Values of $\theta - S$ discussed here are those found on the $\sigma_{27.2}$ surface, unless otherwise specified. In both model and observations, relatively cold and fresh water of 1.0-2.0°C and 33.90-34.10 psu is found near the outcrop region. Temperature and salinity increase northward with depth as AASW mixes with adjacent waters during its subduction into the interior. The coldest and freshest AAIW variety on $\sigma_{27.2}$ is found in the Atlantic sector with salinity fresher than 34.4 as far north as 43°S. The model Atlantic basin-wide averaged $\theta - S$ at 43°S is 4.5°C and 34.32 psu at $\approx$ 600-m depth, in reasonable agreement with the corresponding observed values of 3.9°C and 34.26 psu. The Indian sector AAIW is the warmest and saltiest variety; for example the basin-wide averaged $\theta - S$ values at 43°S are 5.6°C and 34.51 psu at 800-m depth. Further to the north at 30°S, the Indian Ocean AAIW has typical $\theta > 6.0$°C and $S > 34.60$ psu, which is warmer and saltier than observed due to excessive overturn of SAMW (see Fig. 1). The depth of the $\sigma_{27.2}$ surface in this region is also generally about 100-m

shallower than observed (Fig. 1), overlying the model's S minimum. In contrast, the core of AAIW in the Pacific coincides well with the $\sigma_{27.2}$ surface. There, model $\theta - S$ values are in fairly good agreement with the observed, albeit a little warmer and saltier due to a weaker northward penetration of AAIW in the model. In particular, the low salinity tongue in the southeast Pacific is not sufficiently reproduced in the model. This is likely due to insufficient mixing in the model as well as the reduced convection in the region due to the inclusion of GM parameterisation which in turn tends to underestimate midlatitude convective mixing (see also Sørensen et al. 2001). Thus, contribution from the cold and fresh SAMW to AAIW formation also seems to be underestimated in the model. Nonetheless, the Atlantic AAIW is slightly cooler and fresher than its counterpart in the Pacific. Abrupt changes in $\theta - S$ properties at transition regions between ocean basins are seen in both the model and observations. Despite the generally warmer and saltier nature of model AAIW on $\sigma_{27.2}$, its qualitative spatial variation is consistent with the observations of Georgi (1979), Piola and Georgi (1982), and Levitus (1994).

b. Circulation

The simulated mean circulation along $\sigma_{27.2}$ to the north of the Polar Front (PF) is shown in Fig. 6. Note that along the isopycnal layer, depth increases northward from approximately 200 m along the northern flank of the PF to 1000 m depth to the north of 40°S. The magnitude of current velocities decreases with the northward increase of depth. The strongest current with zonal velocity of approximately 5 cm s^{-1} occurs within the influence of the ACC south of 40°S, transporting the water mass along $\sigma_{27.2}$ eastward in a circumpolar manner. In the south Pacific, two branches of intermediate water transport exist in the southeastern region. The northern branch channels the intermediate water northward by the eastern boundary

current as part of the subtropical South Pacific gyre (as in England et al. 1993). The southern branch transports the intermediate water eastward by the ACC through the Drake Passage turning northward as it flows into the South Atlantic. There, part of the intermediate water is deflected to the north joining the subtropical South Atlantic gyre. Northern and southern branches are visible at about 40°W, 25°S along the western boundary current, as documented by the observations of Schmid et al. (2000). Gordon et al. (1992) found a significant interocean exchange of thermocline and intermediate water between the South Indian and South Atlantic Oceans within the Benguela Current via geostrophic and eddy transports of the Agulhas Current system. However, our model does not resolve this westward transport of saline water from the evaporative Indian Ocean. The GM parameterisation of eddy-induced advection is also insufficient to match the eddy transport in the real ocean (Treguier et al. 2003) which likely results in the horizontal $\theta - S$ gradients that are too strong there. The model does capture a southwestward flow as part of the subtropical gyre at about 35°S just to the south-east of Africa (Fig. 6), though no Indian to Atlantic leakage occurs via westward advection. A final feature of AAIW circulation worth noting in Fig. 6 is the northward flow in the Tasman Sea along $\sigma_{27.2}$. This pathway is similar to that proposed by Sokolov and Rintoul (2000) and Rintoul and Sokolov (2001), though in the model transport persists much further to the north. Sokolov and Rintoul (2000) showed that the AAIW actually turns southward and westward into the Indian Ocean. This flow is not resolved by the model. The northward penetration of AAIW in the Tasman Sea is achieved by eddy transport (Sokolov and Rintoul 2000).

4. Model AAIW: interannual to centennial variability

a. $\theta - S$ properties

We now turn our attention to the magnitude and structure of $\theta - S$ variability simulated in the coupled climate model. Temperature-salinity scatter plots presented in Fig. 7 show the spread of $\theta - S$ properties over 1000 yr both on $\sigma_{27.2}$ (marked with crosses) and at constant depths (marked with dots) at chosen locations in the Southern Ocean (see Fig. 6 for geographic positions). Locations are selected to give representation of (i) AASW in each ocean sector (left column of Fig. 7), (ii) AAIW at about 500-m depth downstream of these AASW locations (middle column of Fig. 7), and (iii) AAIW variability at about 900-m depth in regions of relatively rapid renewal (right column of Fig. 7). Variability at fixed grid points (i.e., at constant z-levels) are presented for comparison with variability along isopycnals to provide a more complete picture of the scale of variability in both z- and $\sigma_{27.2}$ space (see also e.g., Bindoff and McDougall 2000; Arbic and Owens 2001). The $\theta - S$ variability on fixed z-levels is obtained by tracking changes along the salinity minimum level closest to $\sigma_{27.2}$ without interpolation between model grid points. Therefore, by implication of the model's coarse resolution, some of the $\theta - S$ scatter plots shown have slightly higher or lower mean density than 27.2 kg m^{-3}.

The $\theta - S$ diagrams in Fig. 7 demonstrate how the properties of the simulated water mass along $\sigma_{27.2}$ vary in space and time. The range of AASW $\theta - S$ variability on the $\sigma_{27.2}$ outcrop at the locations shown (left column of Fig. 7) is up to 5°C and 0.5 psu. The Pacific sector exhibits the largest AASW $\theta - S$ variability, this range then progressively decreases eastward into the Atlantic and Indian Oceans. The AASW variability at fixed locations is smaller than along the $\sigma_{27.2}$ isopycnal, which

suggests variations in the latter are mainly due to interannual meridional displacement of the outcrop position. This is supported by a strong positive correlation ($\approx$ 0.9 correlation coefficient) between along-isopycnal $\theta - S$ variations and meridional displacement of the late-winter outcrop around Antarctica. The positive correlation implies that the outcrop generally moves southward (northward) with decreasing (increasing) surface $\theta - S$ along the isopycnal, in response to variations in surface forcing and/or Ekman transport.

While the surface outcrop displaces meridionally, the isopycnal surface at depth can move upward and downward in response to interior dynamics (Fig. 4). At 545-m depth, $\theta - S$ variability is much smaller than the variability at the surface, with an along-isopycnal range of 0.2-0.7°C and 0.03-0.10 psu (comparable to the magnitude of variability along isobars). The variability is largest south of Australia and decreases into the Drake Passage and the South Atlantic. The comparable magnitude of variability along the $\sigma_{27.2}$ isopycnal with that on fixed z-levels suggests that the variability of AAIW at this depth can be explained largely by changes along the isopycnal, which is most likely to be driven by changes in surface properties at the isopycnal outcrop (Bindoff and McDougall 1994). Down to 900-m depth, $\theta - S$ variability decreases further, with an along-isopycnal range of order 0.1°C and 0.01-0.02 psu. This is now smaller than the fixed z-level range of order 0.2-0.5°C and 0.01-0.03 psu. The larger variability on isobars is most easily explained by variability in the circulation of the subtropical gyres, which forces 'heaving' of the isopycnal surfaces (see Bindoff and McDougall 1994), superimposed on the changes along the isopycnal itself.

b. Comparison with observations

It is worth commenting that the size of decadal changes along $\sigma_{27.2}$ in the model is generally weaker than the observations documented earlier in section 1. Changes over 22-25 yr in the model at the observed regions show maximum basin-scale cooling and freshening of the order 0.05°C and 0.010 psu. More specifically, the strongest 20-yr freshening and cooling over the model's 1000-yr record along $\sigma_{27.2}$ in the Indian Ocean (32°S; 0.05°C, 0.007 psu), southwest Pacific (0.07°C, 0.009 psu along 170°W), and the southwest Atlantic (32°S; 0.07°C, 0.011 psu) are weaker than observed (e.g., Bindoff and McDougall 2000; Johnson and Orsi 1997; for values see section 1). In the Tasman Sea, the maximum model cooling and freshening (0.08°C, 0.014 psu) are comparable to changes documented by Bindoff and Church (1992). The weaker changes in our model as compared to the observed support the argument that an anthropogenic climate change signal is detectable in the observations, as also suggested by Banks et al. (2000). However, we note that the weaker model variability may also be due to the climate model heat and freshwater flux adjustment terms, which tend to damp $\theta - S$ variability at the sea surface.

c. Propagation of $\theta - S$ anomalies

The variability of $\theta - S$ properties shown in Fig. 7 propagates eastward with the ACC as well as northward at certain longitudes (refer also to Fig. 6). In this subsection we analyse how $\theta - S$ anomalies propagate along the $\sigma_{27.2}$ isopycnal surface in the model. We define the local $\theta - S$ anomalies as the deviation of the late-winter $\theta - S$ values from their long-term 1000-yr (late-winter) means. Figure 8 shows a typical 40-yr record of $\sigma_{27.2}$ AAIW salinity anomalies in 4-yr increments (by density conservation we need not show θ). It can be seen from the time series that this region is characterised by eastward propagating signals of anomaly with

magnitude of the order of 0.02-0.04 psu (matching θ anomalies of 0.2-0.4°C, Fig. not shown). The eastward propagating signals can bifurcate into northward flow; for example, if blocked by eastern continental boundaries. One such case is seen in the South Pacific during years 304-308 when a strong negative anomaly (freshening and cooling) centered at approximately 120°W splits to flow northward along the coast of Chile as well as continuing through the Drake Passage into the Atlantic (year 312). Note that the magnitude of anomalies decreases with northward flow due to the mixing of water masses. Another example of an apparent propagation of anomaly can be seen during years 320-336 originating south of New Zealand. In year 320, a significant warm salty anomaly sits southwest of New Zealand, just upstream from a notable cold fresh signal. During the next sixteen years this dipole signature can be seen propagating eastwards and then northwards in the South Pacific subtropical gyre. Note that northward propagating anomalies can also be seen in the Tasman Sea along the east coast of Australia, as well as in the Indian (years 336-348) and Atlantic sectors (years 324-332).

d. Complex EOF analysis

To summarise the structure of $\theta - S$ anomaly propagation along the $\sigma_{27.2}$ isopycnal, and how this evolves in space and time, we now employ complex empirical orthogonal function (CEOF) analyses. To avoid biasing the CEOFs to the surface layer variability where meridional displacement of the isopycnal occurs, we analyse the $\sigma_{27.2}$ isopycnal from below the base of the winter mixed layer. The shallowest depth in the CEOF analysis is at about 200 m. The pattern of each successive CEOF mode of temperature turns out to be virtually identical to that of salinity, with the corresponding principal component time series highly positively correlated at zero lag. Thus, we refer only to the CEOF modes of salinity in our discussion. This

similarity of pattern in the θ and S modes is because a change in temperature along the AAIW isopycnal must be accompanied by a corresponding change in salinity, so that density remains unaltered by variability in $\theta - S$.

Because most of the AAIW $\theta - S$ variance is contained to the south, it is expected that the decomposition of the first few CEOF modes will mainly resolve the eastward propagation of anomalies within this region. Figure 9a presents the first 3 dominant orthogonal modes of salinity anomaly, explaining 53% of the total salinity variance on $\sigma_{27.2}$. It may be noted that according to the North's rule of thumb, modal degeneracy only starts to occur beyond the sixth eigenmode. Each mode is presented at a phase interval of 90°, showing a clear eastward propagation of anomalies. This eastward propagation is also implied by the spatial phase maps showing increasing phase eastward within the circumpolar region and northward into the ocean interior (Fig. 9b). The eastward propagation of anomalies is due to the dominant influence of the ACC. Other studies also document eastward propagating anomalies of ocean surface variables in observations (e.g., White and Peterson 1996) and in model simulations (e.g., Bonekamp et al. 1999; Cai et al. 1999). The magnitude of the CEOF modes decreases northward with increasing depth, in part due to background mixing in the model which tends to damp interior $\theta - S$ variability.

The first CEOF mode shows an eastward propagating wavenumber-1 pattern (Fig. 9a), accounting for 24% of the total variance. Temporal characteristics of the first mode are presented in Fig. 10 (left column) showing the real part of the first principal component (PC1) time series, its power spectral density, and the temporal phase function. The dashed curve superimposed on the power spectrum indicates the 95% confidence limit of the estimated background noise. This first CEOF mode is dominated by signals with decadal to interdecadal periods. The variance is weighted increasingly towards the low frequency fluctuations up to an

equivalent of a 62.5-yr period. The estimated 95% confidence level of the background noise suggests that the periods longer than 20 yr are not different from red noise, which can be interpreted as an integrated white noise forcing transmitted from the outcrop region via ocean mixing and processes. The ≈ 9-yr and 20-yr cycles, however, are significantly above the background noise and are most likely to be related to $\theta - S$ variability transmitted from the surface. A correlation analysis between the real and imaginary part of PC1 suggests an approximate 2-3 yr interval for each 90° phase. This suggests it takes about 8-12 yr for the wavenumber-1 signal to encircle the globe, matching the approximate advective time-scale of the ACC at the surface. However, this phase speed estimation is not accurate as it is biased towards the higher frequency components of the time series. The temporal phase of PC1 shown in Fig. 10 (lower left panel) suggests a large variation in the period of the first mode ranging from decadal to interdecadal timescales, with irregularity in phase speed. This estimation using the temporal phase function takes into account the slowly propagating components and results in a slower average phase speed; of the order of 0.03 m s^{-1} (matching current velocities at depth ≈ 400 m along $\sigma_{27.2}$).

The second CEOF mode shows a propagating wavenumber-2 pattern. This mode accounts for 16% of the total salinity variance on $\sigma_{27.2}$. The power spectral density for the second mode (Fig. 10, middle column) shows a dominant peak at 9-yr period, which for a wavenumber-2 pattern means the anomaly will take approximately 18 yr to encircle the globe. This phase speed matches the propagation rate of the ACC at the base of the winter mixed layer (≈ 200 m). As we have presented previously, the typical zonal current velocity at about 200-m depth along the isopycnal is about 5 cm s^{-1}, which implies about 16 yr to complete one circumpolar cycle at 50°S. However, there is also a significant signal at 20-yr period above the 95% confidence limit of estimated background noise (Fig. 10, middle panel). Variability at longer

periods is also noted, though not significantly distinct from red noise processes. The wavenumber-2 pattern suggests this mode is related to Antarctic Circumpolar Wave (ACW)-like signals transmitted along the intermediate water isopycnal layer. Bonekamp et al. (1999) show from their hindcast run that ACW-like signals are detectable in the deeper ocean with similar frequency and patterns as the surface signals, but with phase shifts and a reduced amplitude. The standing period of the interior signal is about twice that of the surface ACW signal found by White and Peterson (1996), which propagates eastward at average speeds of 6-8 cm s^{-1} to take 8-10 yr for each phase to travel around the globe. It should be noted that the speed of the ACC in the model is smaller than the observed ACC which is of the order of 5−10 cm s^{-1} at 900-m depth (Davis 2005). Thus, we would expect a higher frequency variability in the real ocean than that found in the model.

The third CEOF mode on $\sigma_{27.2}$ shows a propagating wavenumber-3 pattern and explains 13% of the total variance. Variability related to the third mode is distributed over interannual to centennial timescales (Fig. 10, right column). There are significant spectral peaks at about 20-yr period and at ≈ 6-7 yr periods (i.e., the peaks appearing above the 95% confidence limit of background noise). The longer timescale periodicity of order 50-150 yr is not significantly distinct from a red noise process, and is likely to be associated with northward mixing along isopycnals (particularly in the Indian basin, Fig. 9). For example, it takes about 80 yr for a $\theta - S$ anomaly to be mixed a distance of 20° latitude using a scale mixing distance of $\Delta y \approx (2\kappa t)^{1/2}$, where $\kappa = 1 \times 10^7$ cm^2 s^{-1} is the model isopycnal diffusivity and t is time. The shorter period energy of the wavenumber-3 CEOF (PC3) is likely associated with the model equivalent of the ACW. For example, Cai et al. (1999) found a predominant quasi-stationary wavenumber-3 pattern with standing oscillation of 4-5 yr using 60 yr of SST and SSS data in the earlier version of CSIRO

climate model. They filtered all variability outside the timescale of 1-10 yr. This wavenumber-3 pattern would thus take 12-16 yr to encircle the Antarctic continent. Cai et al. (1999) relate this mode to the ACW marked by the advection of SST anomalies by the surface ACC. The dominant shorter periodicity of the third mode that we find here (6-7 yr) is slightly longer than that of the Cai et al. (1999) ACW. This difference is likely due to the different mixing schemes used in the two models; in particular our model employs GM whereas Cai et al. (1999) do not, and GM tends to decelerate the ACC.

The results of the CEOF analyses can be summarised in a frequency-wavenumber spectrum of signals along the southern-most boundary of the CEOF domain (shown in Fig. 11). The spectrum decomposes the variance in terms of wavenumber and frequency and partitions the total variance into contributions from eastward and westward travelling signals (refer to Storch and Zwiers 1999). As we can see from Fig. 11, the energy of the spectrum is dominated by eastward travelling waves and is notably high between 20-60 cpy^{-1} with a wavenumber-1 spatial pattern. Decreasing variance is explained with increasing frequency implying the dominance of low-frequency processes along this region. Wavenumber-5 patterns are the highest wavenumber to appear in the analysis, though these explain only a very small amount of the total variance. Eastward propagating wavenumber-4 and 5 appear in the 5^{th} and 7^{th} CEOF modes (not shown), accounting for 6% and 3% of the total variance respectively. It is worth mentioning that the fourth and sixth CEOF modes (also not shown) are non-propagating modes. The fourth mode, accounting for 9% of total variance shows a standing-wave fluctuation with a more-or-less uniform circumpolar (wavenumber-0) pattern. This mode is not significantly different (at 95% confidence level) from a red noise AR-1 process, suggesting integrated white noise via oceanic mixing. CEOF6 (4% of total variance) shows a standing wave fluctua-

tion at multidecadal-centennial timescales, concentrated at the tip of South Africa (see Fig. 8, years 316-336). This region is characterised by relatively large standard deviations of $\theta - S$ (Fig. not shown), a result of the sharp front between the warm salty Agulhas Current and the cold fresh South Atlantic Current. $\theta - S$ variability in this region is influenced by fluctuations in the strength of these currents.

To further assess the propagation characteristics of interior anomalies, a Hovmöller diagram is shown in Fig. 12 of the salinity anomaly on $\sigma_{27.2}$ in the Pacific across approximately 180°-80°W at three different latitudes. This figure shows that the period and spatial pattern of the anomaly vary with increasing depth. Thus, the speed of the propagating anomaly is affected by the decreasing speed of the ACC with depth, in contrast to the studies by Bonekamp et al. (1999) and Cai et al. (1999). This mismatch results because our analyses are based on interannual to centennial timescales, while only periods less than 10 yr are taken into account by Bonekamp et al. (1999) and Cai et al. (1999). Ocean mixing, a more gradual process than advection, results in a shift in spectral energy towards low frequencies (red spectrum). In our case, variability is gradually dominated by low frequencies of multidecadal to centennial timescales with increasing depth as advection effects decrease, allowing mixing to play a greater role. Indeed, the spectral energy of interannual and interdecadal timescale processes (due to surface forcing and sub-surface advection) become relatively small at the deeper reaches of AAIW (Fig. not shown). Since phase speed is a function of frequency, the phase speed of the anomaly is thus seen to increase with depth as shown in Fig. 12. Note also the phase shifts and reduction in the anomaly amplitudes with depth. In addition, the north-westward lag shown in the spatial CEOF patterns in Fig. 9a is also due to the time taken for the anomaly to be transmitted from the surface into the interior.

5. Mechanisms of variability

Under a *circumpolar* view of AAIW formation (e.g., Sverdrup et al. 1942; Sørensen et al. 2001), the surface forcing and/or ocean dynamics at the AAIW outcrop region play a crucial role in controlling intermediate water variability at depth. Even under a *non-circumpolar* formation view (e.g., McCartney 1977; England et. al. 1993), with mode waters subducted and/or convected at preferential locations, variability in the surface outcrop region still controls variability in the interior via cross-front processes at the APFZ. To investigate mechanisms of AAIW variability, we therefore perform heat and salt budget analyses in terms of $\theta - S$ changes on the late-winter $\sigma_{27.2}$ outcrop, as described in section 2. This analysis is thus focussed on the variability of Antarctic Surface Water, rather than other AAIW ingredients, such as SAMW (which is studied by Rintoul and England 2002). Note that significant year-to-year variations in the location of the late-winter outcrop occur, with mild (severe) winters resulting in poleward (equatorward) excursions of the $\sigma_{27.2}$ outcrop. Also, at particular locations where the Antarctic coast extends further to the north (e.g., the Antarctic Peninsula and off East Antarctica between 50°E-100°E), the $\sigma_{27.2}$ layer does not necessarily outcrop throughout the full 1000 yr of model simulation. This will occur during years of mild winter conditions. In such instances no heat budget calculations are made during the years of no winter outcrop.

To summarise the magnitude of variability of each process, the zonally averaged standard deviation of the heat budget terms is given in Table 1. An attempt is made to calculate all the terms in Eq. 1, except for θ'_{mix}, as mixing in the model tends to damp anomalies rather than create them (see also Rintoul and England 2002). The net surface heat flux term has the highest standard deviation in comparison to the other budget terms. This suggests that the anomalies created by surface

heat fluxes dominate the variability of AAIW sourced at the $\sigma_{27.2}$ outcrop. The heat storage rate term ($\partial\theta/\partial t$) is much smaller than the net heat flux term (Q_{net}), confirming that mixing plays an important role in damping anomalies in the model. Northward Ekman transport also contributes significantly to the variability. Vertical Ekman advection (Ekman pumping), on the other hand, makes little contribution to the variability at this layer. Zonal advection has a relatively small magnitude of variability on the zonal mean, but as we shall see below, plays an important role in some locations. This suggests that the ACC contributes, to some extent, to the variability at the outcrop layer. Table 1 also provides the breakdown of surface heat flux components of Eq. 3. Variability of the ocean-to-ice sensible flux Q_{oi} is small compared to the variability of the air-sea heat fluxes, so wintertime θ variability is likely controlled by atmospheric (not ice) heat fluxes at the $\sigma_{27.2}$ outcrop. The air-sea heat flux components have comparable magnitudes of variability at the $\sigma_{27.2}$ outcrop, with the sensible heat flux (Q_{sh}) and the solar heat flux (Q_{solar}) the larger of the four terms.

A similar table for salinity flux terms is shown for the $\sigma_{27.2}$ outcrop region in Table 2. The net surface freshwater flux has the largest variability in comparison to the other salt budget terms. This suggests that surface freshwater fluxes have a major influence on the variability of AASW in the model. Among the surface freshwater flux terms, variability in the ice-ocean flux contributes most to the variability of AASW, as suggested by the highest standard deviation of that term (Table 2). This suggests that sea ice plays a major role in salinity variability at the outcrop region of the $\sigma_{27.2}$ isopycnal surface. This is not surprising given the close proximity of the outcrop location to the maximum sea-ice extent in both the model and observations (Fig. 2). The result is also consistent with the coupled model analyses of Saenko and Weaver (2001), who found mean AAIW S properties to be set, in part, by sea-ice

processes. The meridional Ekman advection term is also significantly high in the model, implying that it too plays an important role in controlling the variability of S at the outcrop region. The zonal advection also plays an important role, with the fraction of salt storage rate variability higher than that in the heat budget. This is probably because zonal salinity gradients persist for longer in the ocean than zonal temperature gradients, as air-sea salt fluxes do not act to damp S anomalies in the same way air-sea heat fluxes damp θ anomalies.

To further understand the mechanisms controlling $\theta - S$ variability along the AAIW layer outcrop, we have calculated term correlation coefficients at each longitude over the first 100 yr of the model data. Significant positive correlation at zero-lag between net winter surface heat flux and $\partial\theta/\partial t$ is found over much of the outcropping layer (Fig. 13a). The positive correlation implies increasing sea-to-air heat loss in winter corresponds with a higher temperature difference between late winter and late summer. That is, air-sea heat fluxes control the winter sea surface temperature variability. Significant positive correlation is also found at similar longitudes between the effective net surface salt flux and $\partial S/\partial t$ (Fig. 13b). This implies air-sea and/or ice-sea freshwater fluxes are controlling wintertime S variability at these locations.

In contrast to the surface flux correlations, northward Ekman transport of heat and salt shows only limited locations of significant correlation with the $\partial\theta/\partial t$, $\partial S/\partial t$ terms (Fig. 13c, 13d). For example, a significant correlation with heat storage rate holds in the South Pacific around 160°W and in the southeastern Atlantic near $40° - 60°$W. Both of these locations coincide with regions where the $\sigma_{27.2}$ outcrop is found further away from the Antarctic coast (refer to Fig. 2). In other regions, where the outcrop layer is closer to the coast, northward Ekman transport tends to be small in magnitude and gives little contribution to the variability in AASW

heat content. Instead, atmospheric heat fluxes play the dominant role. Salinity variability due to northward Ekman transport is only significant in the Southeast Pacific (near $80° - 100°$W) and in isolated locations of the South Atlantic and South Indian Oceans (Fig. 13d).

Analysis of correlations between $\partial\theta/\partial t$, $\partial S/\partial t$ and zonal advection at the $\sigma_{27.2}$ outcrop is shown in Figs. 13e and 13f. This reveals some locations where eastward propagation of anomalies is significantly in phase with $\theta - S$ trends. There is a tendency for this correlation to be high wherever surface flux and northward Ekman advection correlations are low, particularly for salinity (e.g., between 100°E and 160°E). In these regions, ACC variability and/or variations in $\partial\theta/\partial x$ and $\partial S/\partial x$ play an important role in controlling surface water mass variability along $\sigma_{27.2}$. Finally, it may be noted that near 100°E neither surface fluxes nor ocean advection are in phase with variability in $\theta - S$. This suggests variability in mixing, most likely convective overturning, is controlling surface water mass variability in this region.

Because a variety of water types and densities contribute to AAIW, it is of some interest to assess variability mechanisms in other density classes. Most notably SAMW is known to contribute to AAIW ventilation (McCartney 1977), and whilst its variability has been studied elsewhere (Rintoul and England 2002), we briefly discuss here the mechanisms controlling $\theta - S$ anomalies along the outcrop of this lighter water mass ($\sigma_\theta \approx$26.9 kg m^{-3}). Meridional Ekman heat and salt transports play a more significant role in driving $\theta - S$ variability along the $\sigma_\theta = 26.9$ kg m^{-3} outcrop (refer to Tables 1 and 2). In particular, the northward Ekman transport now contributes almost as much variability as the surface flux terms. In addition, there are more regions of significant correlation between ocean advection and $\theta - S$ variations (Fig. not shown). Rintoul and England (2002) argue that SAMW variability is controlled by Ekman advection in both observations and a coupled

model. However, we also find some SAMW regions in the CSIRO climate model where air-sea heat fluxes drive variability in $\partial\theta/\partial t$, notably in the South Pacific. In contrast to $\sigma_{27.2}$, though, ice-ocean coupling clearly plays no role at SAMW formation regions. In summary, in moving to lighter density classes than $\sigma_{27.2}$, Ekman advection plays a greater role in generating surface $\theta - S$ variability, whilst air-sea fluxes play a lesser role (and ice processes become negligible). For the rest of this paper we continue our focus on the $\sigma_{27.2}$ surface, namely, the AASW contribution to AAIW variability.

As noted previously, the mean position of the $\sigma_{27.2}$ outcrop layer exists at or just north of the absolute maximum sea-ice extent. That is, sea-ice frequency and concentration are generally low during the model 1000-yr simulation at $\sigma_{27.2}$ (refer to Figs. 14a, 14b). This suggests the $\sigma_{27.2}$ outcrop is normally exposed to the atmosphere, which means atmospheric heat and freshwater fluxes can have a significant influence on the layer. Since the climate model includes sea-ice dynamics which allow the transport of sea ice by wind and ocean currents, the transport of ice also represents a transport of heat and salt (O'Farrell 1998). When ice is transported northward by the wind (or currents) at these latitudes, it melts and feeds in cold and fresh water to the intermediate water outcrop region, from where it will be mixed along isopycnals to intermediate depths. Fig. 14c shows that the mean position of the outcrop lies within the region of negative ice-to-ocean salt flux, indicating meltwater input north of the sea-ice margin. Further analysis shows that anomalies in this meltwater rate are controlled, in part, by variations in the Ekman transport of ice to the north. Fig. 15a shows the correlation between zonal winds versus ice-to-ocean fluxes over 100 yr of the model simulation. The band of negative correlations near 60°S corresponds to stronger westerly winds driving stronger meltwater rates. Thus, over much of the outcrop region, anomalous zonal wind can result in variations

in ice-sea freshwater fluxes, which affect variability of S along $\sigma_{27.2}$. This mechanism occurs on interannual to interdecadal time scales of up to ≈ 25 yr. This is illustrated in Fig. 16a showing the coherence spectrum of the meltwater flux versus the zonal wind stress circumpolarly averaged along the northern-most winter sea-ice extent (i.e., in the region of negative ice-ocean salt flux where $\sigma_{27.2}$ outcrops; see Fig. 14c). It is apparent in Fig. 16a that the coherence drops off at periods beyond 26 cpy^{-1}. The spectral structures of the zonal wind stress and meltwater flux are presented in Fig. 16c, d, showing various peaks. It may be noted that the two zonally averaged variables are correlated significantly with a 0.52 correlation coefficient. Interestingly, the cross spectrum shows the decadal peaks captured by CEOF1 and CEOF2 (see Fig. 10), namely the 20.4 cpy^{-1} and 8.8 cpy^{-1} periodicities. This provides evidence on the link between the dominant modes of $\theta - S$ variability along the core of AAIW and the wind-driven meltwater mechanism described above.

The dotted lines in Fig. 14c show the northern and southern-most outcrop locations over the 1000 yr model run, implying that the $\sigma_{27.2}$ outcrop can lie within ice-free, ice-melting, and ice-forming regions (though it is not often in the latter). This geographic variability itself contributes to variability in surface heat and salt fluxes along the outcrop layer as these fluxes depend strongly on latitude. In addition, the mean outcrop layer is sometimes located over regions where sea-ice concentration variability is high; for example, in the southeast Pacific (Fig. 14d). This region corresponds to an area where $\theta - S$ variations are strongly controlled by anomalies in air-sea and ice-sea fluxes (Figs. 13a, 13b).

Finally, it is worth noting an important negative feedback mechanism that tends to stabilise the location of the $\sigma_{27.2}$ outcrop, whilst also creating density-compensated $\theta - S$ anomalies in AASW. We have seen already that an increased zonal wind field induces sea ice melting (Fig. 15a). This melt-back of ice means the surface water is

more greatly exposed to increased latent and sensible heat fluxes (Fig. 15b). The meltwater reduction in surface salinity contributes to lighter AASW, which means a southward displacement of the outcrop layer (Fig. 15c). However, because of increased evaporative and sensible heat loss due to exposure of the ocean to cold air and wind, temperature decreases, leading to denser AASW (which is thus followed by a tendency for the outcrop layer to return northward, Fig. 15d)[1]. This mechanism allows sea ice variability to play a direct role in AASW $\theta - S$ variations by partly controlling thermohaline properties at the outcrop location.

6. Discussion and Conclusions

The natural variability of AAIW $\theta - S$ properties and mechanisms is analysed using a coarse resolution climate model along the 1027.2 kg m^{-3} isopycnal surface ($\sigma_{27.2}$). This isopycnal surface coincides well with both the model and observed intermediate water salinity minimum (Fig. 1). The distribution of a passive tracer on the $\sigma_{27.2}$ surface suggests a mostly circumpolar formation of AAIW in the model with a substantial contribution from AASW (Fig. 3), as also seen in some other coarse-resolution models employing GM (e.g., Sørensen et al. 2001). Under this approach and based on the tendency of water properties to be mixed along isopycnals (e.g., Molinelli 1981), our study has focused on the AAIW variability sourced from AASW without taking into account the contribution from SAMW (a lighter density class of AAIW).

The CSIRO climate model performs well in simulating mean AAIW $\theta - S$ properties and circulation resembling the observed. This is most likely due to a more realistic mixing parameterisation and an improved representation of sea-ice processes

[1] A net southward displacement of the isopycnal outcrop generally occurs with freshening despite cooling. This suggests that S has a larger effect on buoyancy than θ at the outcrop region.

incorporated in the model as shown in other studies (e.g., Sørensen et al. 2001; Duffy et al. 2001; Saenko and Weaver 2001). The variability of $\theta - S$ properties on the $\sigma_{27.2}$ isopycnal surface is documented at various timescales showing anomalies propagating eastward within the ACC with decreasing magnitude as they subduct northward into the interior (see Fig. 8). The CEOF analyses decompose the variability into 3 dominant modes showing mainly eastward propagating signals advected by the ACC (Fig. 9). The first mode shows a wavenumber-1 pattern consisting of signals at interannual to multidecadal timescales. Since the analysis is done on an isopycnal surface, isopycnal mixing most likely contributes to the low frequency propagation (on centennial timescales). The high frequency signals consist of subducted surface $\theta - S$ anomalies due mainly to variability in atmospheric heat fluxes and meltwater rates. The wavenumber-1 mode may also be in some way related to the Antarctic Dipole (ADP). Yuan and Martinson (2001) found the ADP to be a quasi-stationary wave existing as the dominant interannual variance structure in the sea-ice edge and surface air temperature fields in observations. The exact relation between the first AAIW mode in our study and the model's ADP requires further analysis, so is only speculative at this stage. The wavenumber-2 pattern of the second AAIW mode resembles the observed ACW, though showing a longer period than that described by White and Peterson (1996). A wavenumber-3 pattern is apparent in the third AAIW mode found in our CEOF analyses. This mode is analogous to that described by Cai et al. (1999), who employ a similar coupled model. The period of the wavenumber-3 AAIW mode in this study is mostly in the range 7-20 yr (see Fig. 10). The first three CEOFs of AAIW $\theta - S$ account for a total variability of about 53%. Higher CEOF modes (not shown), each accounting for a small fraction of total AAIW variability ($< 9\%$), exhibit eastward propagating zonal wavenumber-4 and 5, and non-propagating patterns.

A CEOF analysis on the SST field in the model's Southern Ocean between 33°-62°S (not shown), is found to exhibit a zonal wavenumber-2 pattern with 8.9 and 20-yr periods as well as a wavenumber-3 pattern with a dominant peak at 6.8-yr period. These patterns are similar to those found in AAIW CEOF modes 2 and 3, respectively. In addition, we also found variability in the sea-ice extent at 6.8 and 19.6-yr periods (Fig. not shown). This provides evidence of coherence between the spatial-temporal characteristics of variability at the surface and that in the interior at interannual to interdecadal timescales. It is worth mentioning that the dipole pattern that appears in the South Pacific could be sourced from the localised SST dipole pattern shown in Fig. 18 (Part IV) as also seen in the observed (Fig. 20, Part IV). Together with the detection of ACW-like signals transmitted along the $\sigma_{27.2}$ surface from AASW into the interior, this suggests the role of AAIW in spreading climate signals to other parts of the globe.

It is worth mentioning that since the core layer of AAIW in the model is predominantly fed by the AASW, climate anomalies at the $\sigma_{27.2}$ outcrop region are found to dominate the variability along this isopycnal layer. However, in the real ocean where more of AAIW is formed in the southeast Pacific, we could anticipate an additional mode of variability sourced in the region. Nonetheless, it is still reasonable to argue that anomalies in AASW dominate AAIW variability since the isopycnal surface corresponding to its core outcrops at high latitudes of the Southern Ocean where strong westerlies are likely to play a dominant role in generating variability. Due to model limitations in simulating the real system, we could also expect some discrepancies in terms of the frequency and amplitude of the variability modes. For example, a higher speed of the observed ACC would generate higher frequency anomalies than those found here. In terms of comparison to recent observational studies of $\theta - S$ changes in AAIW, we found that the most extreme model cooling and freshening

over 22-25 yr on the $\sigma_{27.2}$ surface is generally weaker than the observed (Bindoff and Church 1992; Johnson and Orsi 1997; Bindoff and McDougall 2000). This is likely due to the flux adjustment employed which tends to damp the variability in the model, although the presence of a longer-term anthropogenic climate change signal in the observations may also account for the discrepancy.

The heat and salt budget analyses at the $\sigma_{27.2}$ outcrop region suggest salinity variability of AASW, (a major source of the model's AAIW), to be mainly due to sea-ice variability near the sea-ice margin (via meltwater). This is possible as the $\sigma_{27.2}$ isopycnal surface outcrops near the maximum sea-ice margin during winter in both the model and in the real ocean (Fig. 2). The temperature variability, on the other hand, is controlled mainly by air-sea heat fluxes. We have found evidence that northward Ekman transport and zonal advection also play a significant but localised role in contributing to the variability. In the model Southern Ocean at $30° - 60°$S, changes in the late-winter sea surface temperature are generally accompanied by changes in sea surface salinity in a way that mostly conserves density (Fig. 26, Part III; see also Rintoul and England 2002, their Fig. 6). Yet we find ice-ocean freshwater fluxes to control S, and air-sea heat fluxes to control θ. One possible way to achieve this would be for variations in the subpolar winds to control variations in the rate of sea-ice melting due to northward Ekman transport (Fig. 15a) which then controls the variation of evaporative and sensible heat loss (Fig. 15b). This mechanism is shown to occur on interannual to interdecadal time scales (Fig. 16). Under this scenario, an increased wind field drives ocean cooling and freshening via (respectively) air-sea and ice-ocean fluxes. Any variability in wind-stress would also affect the strength of the ACC and thus affect variability at the outcrop region via zonal advection. Meridional Ekman advection would also be altered by the wind stress variations in such a way as to change θ and S in phase (this also dominates

SAMW variability in Rintoul and England 2002). Thus, we expect wind stress variations to play a major role in AASW $\theta - S$ variability via any of these four mechanisms.

Finally, we noted that heat and salt budget analyses on a lighter density class (σ_θ =26.9 kg m^{-3}, see Tables 1 and 2), corresponding to SAMW, suggest a greater role for meridional Ekman advection in generating surface $\theta - S$ variability (consistent with Rintoul and England 2002). Air-sea heat fluxes play a lesser role and ice-ocean fluxes become negligible because the $\sigma_\theta = 26.9$ kg m^{-3} isopycnal outcrops substantially north of the sea-ice margin. However, as noted previously, SAMW appears to be a secondary contributor to AAIW renewal in this particular climate model, with subducted AASW playing the more dominant role.

Regardless of the AAIW formation mechanism, we find the water-mass properties along the core intermediate water layer to be largely controlled by variability in air-sea and freshwater fluxes, and sea-ice meltwater rates (with ocean advection playing a smaller role). Variations in these air-sea and ice-sea fluxes can introduce anomalies along the AAIW layer on time scales from years to decades.

Table captions

Table 1: Standard deviation of surface heat budget terms over 1000 years zonally averaged over the late-winter $\sigma_{27.2}$ outcrop position. The $\partial\theta/\partial t$ term is obtained by subtracting late-summer temperature from late-winter temperature. All other terms are the average over April to September. The zonal Ekman advection term is significantly smaller than the total zonal advection term and hence is not presented. The standard deviation of heat flux components is provided. Values for the $\sigma_{26.9}$ outcrop are displayed for comparison.

Table 2: Standard deviation of surface salinity budget terms at the $\sigma_{27.2}$ and $\sigma_{26.9}$ outcrops. The terms are calculated as for those in Table 1. The zonal Ekman advection term is significantly smaller than the total zonal advection term and hence is not presented. For consistency of units, evaporation and precipitation have been converted to equivalent salt fluxes (psu s^{-1}).

Figure captions

Figure 1: Cross-section of the zonally averaged late-winter salinity fields in the Pacific, Atlantic, and Indian sectors in the model (left column) and Levitus (right column). The thick line indicates the mean position of the σ_θ = 27.2 kg m^{-3} isopycnal. Note that the same colour scale is used for comparing the model and observed salinity for each ocean sector.

Figure 2: Mean position of the late-winter σ_θ = 27.2 kg m^{-3} outcrop (solid contour) and the maximum late-winter sea-ice extent (dashed contour) in (a) the model and (b) observations. The maximum late-winter sea-ice extent is the northern-most latitude of late-winter ice coverage (a) in the model over the full 1000-yr simulation and (b) observed during 1973-1998. The colour shading shows mean late-winter surface salinity values. The observed late-winter outcrop position is calculated using Levitus (1994). For both model and observed, late-winter $\theta - S$ values are derived from a mean over September and October. The observed sea ice data are from the US NAVY/NOAA Joint Ice Center and passive microwave DMSP observations from 1973-1998.

Figure 3: Dye tracer concentration field (as a percentage) on σ_θ=27.2 kg m^{-3} ($\sigma_{27.2}$) after 50 years of tracer release in the coupled climate model. Grey shaded areas are poleward of the $\sigma_{27.2}$ outcrop.

Figure 4: (a) Schematic diagram illustrating processes in the high latitudes of the Southern Ocean which influence the location of the σ_θ=27.2 kg m^{-3} surface ($\sigma_{27.2}$). Note the seasonal and year-to-year displacement of the isopycnal. (b) Conventional season definitions used in the heat and salt budget analyses.

Figure 5: Late-winter potential temperature (shown as contours) and salinity on $\sigma_{27.2}$ in (a) the model and (b) the observed Levitus (1994) climatology. The

dashed contour marks the mean location of the $\sigma_{27.2}$ surface outcrop during late winter.

Figure 6: Mean circulation on the $\sigma_{27.2}$ density surface shown by late-winter velocity vectors averaged over 1000 years. Velocity fields are shown only at depths below 200 m. Depth contours are shown in colours. Mean position of the late-winter $\sigma_{27.2}$ outcrop is shown by the black contour. Coloured dots indicate locations of $\theta - S$ scatter plots in Fig. 7.

Figure 7: 1000-yr $\theta - S$ scatter plots at specified ocean grid boxes (shown in Fig. 6) having density closest to $\sigma_\theta = 27.2$ kg m^{-3} (marked with dots) and along the isopycnal (marked with crosses), at the surface (left column), 545 m (middle column), and at 905 m (right column). Note that at the surface the scatter plot along the $\sigma_{27.2}$ isopycnal varies with latitude, and in the interior varies with depth.

Figure 8: Late-winter salinity anomaly along $\sigma_{27.2}$ from year 304 to year 348 in a 4-yr interval. Grey shaded areas denote regions south of the CEOF domain (base of the $\sigma_{27.2}$ mixed layer).

Figure 9: (a) The first three complex EOF modes of salinity shown at 90° phase intervals along $\sigma_{27.2}$. The three modes account for a total of 53% of the net S variance on $\sigma_{27.2}$. The first (CEOF1), second (CEOF2) and third (CEOF3) modes account for 24%, 16%, and 13% respectively. An equivalent CEOF analysis of θ on $\sigma_{27.2}$ shows similar modal structure, so is not shown here. (b) Spatial phase angle of CEOF1-3 indicating the direction of phase propagation of each mode from 0° to 360°. Apparent phase discontinuities occur because the phase is defined only between 0° to 360°.

Figure 10: Top row: Principal component timeseries of CEOF1-3 is displayed

from year 300-500. Middle row: Power spectral density (PSD) of the principal component timeseries with an estimated AR-1 background spectrum at 95% confidence level (dashed curve). Bottom row: Temporal phases obtained from CEOF1-3 displayed from year 300 to 500. The temporal phase angles in the lower panels are defined between 0° to 360°.

Figure 11: Frequency-wavenumber spectrum of salinity anomaly along the southernmost boundary of the CEOF domain on $\sigma_{27.2}$. The analysis decomposes spatial-temporal signals and shows mostly eastward propagating components (positive frequencies).

Figure 12: Hovmöller diagram of salinity anomaly on $\sigma_{27.2}$ in the South Pacific between 180°-80°W at 52.5°S, 46.2°S, and 43°S. Note that the depth of the isopycnal increases northward with average depths of 554 m, 884 m, and 963 m for each of the latitudes.

Figure 13: Correlation coefficients of heat and salt storage rate ($\partial\theta/\partial t$, $\partial S/\partial t$) versus winter (a) net air-sea heat flux (Q_{net}), (b) net air-sea equivalent salt flux (H_{net}), northward Ekman heat (c) and salt (d) transports, and zonal heat (e) and salt (f) advection at the $\sigma_{27.2}$ outcrop latitudes. Note that the calculation is based on the first 100 years of the model simulation, and is typical of the full 1000-yr run. Correlation is significant above the dashed line which indicates a 95% significance level and is highlighted for clarity. Note that the advection terms require negative correlations to account for variability in the wintertime AAIW $\theta - S$ properties (refer also to Eqs. 1 and 2). Thus, for convenience, the correlation axes in panels (c)-(f) have been inverted so that the longitudes of significant correlation correspond to those regions above the dashed line.

Figure 14: April to September average of ice extent over 1000 years showing (a)

frequency of ice coverage, (b) mean ice concentration as a ratio of grid box area, (c) mean winter ice-ocean salt flux (H_{ice}), and (d) the standard deviation of the ice concentration. The mean location of the late-winter $\sigma_{27.2}$ outcrop is indicated by the solid line where the layer exists for the whole 1000 years and by a dashed line otherwise. Dotted lines in (c) and (d) denote maximum and minimum displacement of $\sigma_{27.2}$ outcrop ever attained over the 1000-yr model run (the southern-most extent excludes those years of no outcrop). North of 60°S in (c), sea-ice concentration is generally less than 60% and is marked by negative H_{ice} (freshwater input). Southward excursions of the $\sigma_{27.2}$ outcrop (i.e., low density AASW) generally coincide with years of limited Antarctic sea ice.

Figure 15: Correlation maps for (a) winter zonal wind stress (τ^x) versus winter ice-ocean salt flux (H_{ice}), (b) winter H_{ice} versus winter surface heat flux (Q, which is dominated by outgoing heat fluxes), and (c) late-winter surface salinity and (d) late-winter surface temperature versus $\sigma_{27.2}$ outcrop displacement. Correlation coefficients are calculated using 100 years of model simulation. The values are displayed when they are above the 95% significance level (refer to colorbar). The contour indicates the mean location of the late-winter $\sigma_{27.2}$ outcrop.

Figure 16: Figure 16: (a) Coherence spectrum, (b) cross spectrum, and the power spectral density of (c) zonal wind stress and (d) meltwater flux zonally averaged along the northern-most winter sea-ice extent near the mean location of the late-winter $\sigma_{27.2}$ outcrop where there is a mean input of ice-to-ocean freshwater (see Fig. 14c). The dashed horizontal line in (a) represents the 95% significance level.

Table 1. Standard deviation of surface heat budget terms over 1000 years zonally-averaged over the late-winter $\sigma_{27.2}$ outcrop position. The $\partial\theta/\partial t$ term is obtained by subtracting late-summer temperature from late-winter temperature. All other terms are the average over April to September. The zonal Ekman advection term is significantly smaller than the total zonal advection term and hence is not presented. The standard deviation of heat flux components is provided. Values for the $\sigma_{26.9}$ outcrop are displayed for comparison.

Budget term	$\sigma_{27.2}$ ($\times 10^{-7}$°C s^{-1})	$\sigma_{26.9}$ ($\times 10^{-7}$°C s^{-1})
$\partial\theta/\partial t$	0.28	0.20
Zonal advection ($u\partial\theta/\partial x$)	0.15	0.16
Meridional advection ($v\partial\theta/\partial y$)	0.45	0.58
Meridional Ekman advection ($v_e\partial\theta/\partial y$)	0.44	0.57
Vertical advection ($w\partial\theta/\partial z$)	4.6×10^{-3}	4.8×10^{-3}
Net surface heat flux (Q_{net})	1.18	0.89
Air to ocean solar radiation (Q_{solar})	0.66	0.33
Ocean to air long wave radiation (Q_{lw})	0.40	0.25
Ocean to air sensible heat flux (Q_{sh})	0.87	0.42
Ocean to air evaporative heat flux (Q_{evp})	0.48	0.59
Ocean to ice sensible heat flux (Q_{oi})	0.13	1.2×10^{-5}

Table 2. Standard deviation of surface salinity budget terms at the $\sigma_{27.2}$ and $\sigma_{26.9}$ outcrops. The terms are calculated as for those in Table 1. The zonal Ekman advection term is significantly smaller than the total zonal advection term and hence is not presented. For consistency of units, evaporation and precipitation have been converted to equivalent salt fluxes (psu s^{-1}).

Budget term	$\sigma_{27.2}$ ($\times 10^{-8}$ psu s^{-1})	$\sigma_{26.9}$ ($\times 10^{-8}$ psu s^{-1})
$\partial S/\partial t$	0.35	0.32
Zonal advection ($u\partial S/\partial x$)	0.29	0.38
Meridional advection ($v\partial S/\partial y$)	0.39	0.67
Meridional Ekman advection ($v_e\partial S/\partial y$)	0.36	0.66
Vertical advection ($w\partial S/\partial z$)	4.9×10^{-3}	3.8×10^{-3}
Net surface salt flux (H_{net})	0.85	0.77
Evaporative salt flux (E)	0.27	0.33
Precipitative salt flux (P)	0.24	0.27
Ice to ocean salt flux (H_{ice})	1.66	4.0×10^{-3}

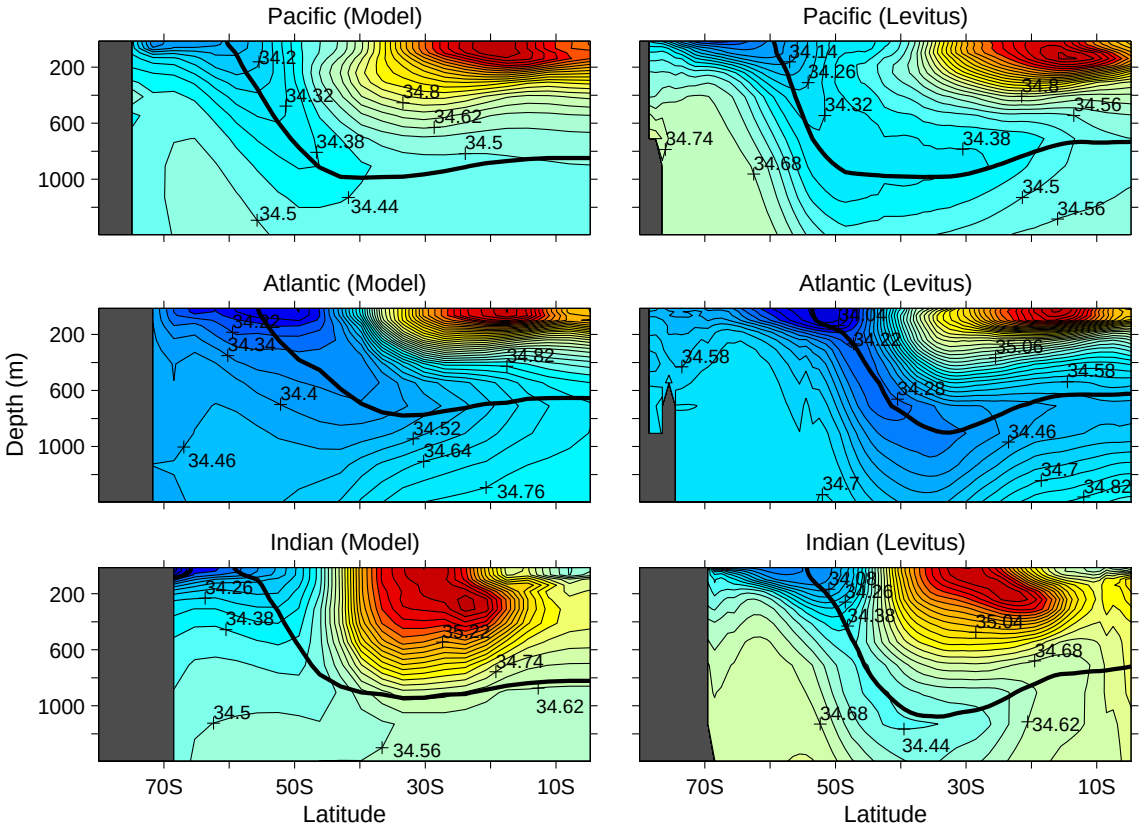

Figure 1: Cross-section of the zonally averaged late-winter salinity fields in the Pacific, Atlantic, and Indian sectors in the model (left column) and Levitus (right column). The thick line indicates the mean position of the $\sigma_\theta = 27.2$ kg m^{-3} isopycnal. Note that the same colour scale is used for comparing the model and observed salinity for each ocean sector.

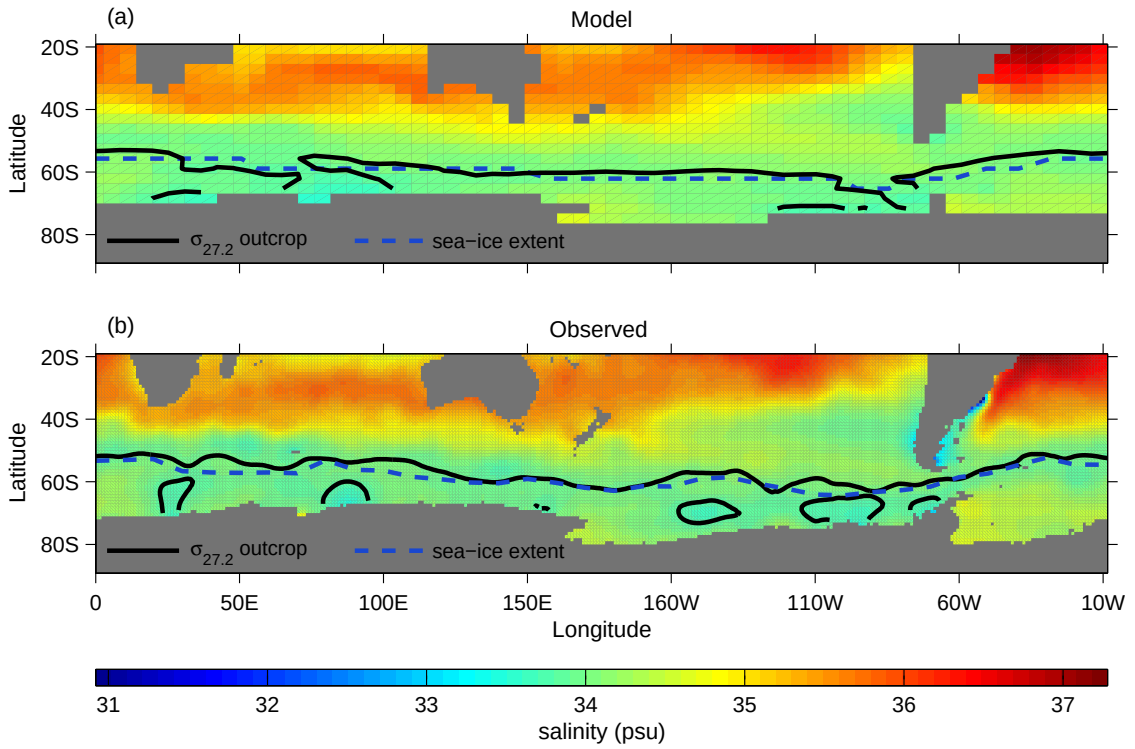

Figure 2: Mean position of the late-winter $\sigma_\theta = 27.2$ kg m^{-3} outcrop (solid contour) and the maximum late-winter sea-ice extent (dashed contour) in (a) the model and (b) observations. The maximum late-winter sea-ice extent is the northern-most latitude of late-winter ice coverage (a) in the model over the full 1000-yr simulation and (b) observed during 1973-1998. The colour shading shows mean late-winter surface salinity values. The observed late-winter outcrop position is calculated using Levitus (1994). For both model and observed, late-winter $\theta - S$ values are derived from a mean over September and October. The observed sea ice data are from the US NAVY/NOAA Joint Ice Center and passive microwave DMSP observations from 1973-1998.

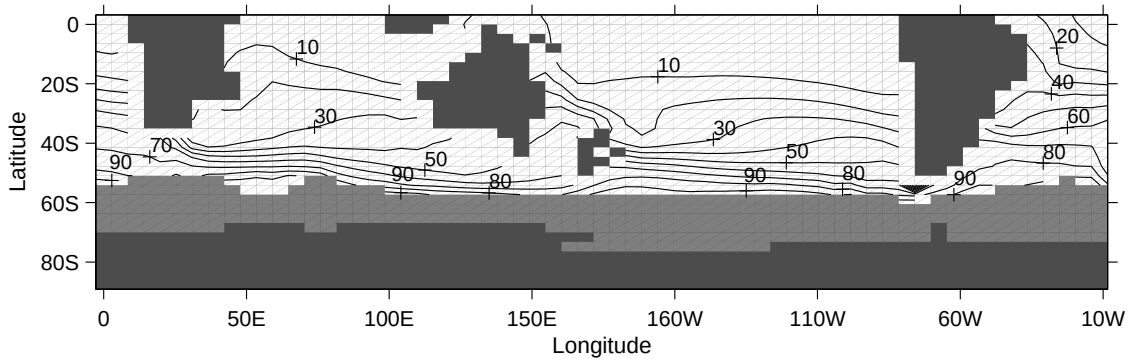

Figure 3: Dye tracer concentration field (as a percentage) on σ_θ=27.2 kg m^{-3} ($\sigma_{27.2}$) after 50 years of tracer release in the coupled climate model. Grey shaded areas are poleward of the $\sigma_{27.2}$ outcrop.

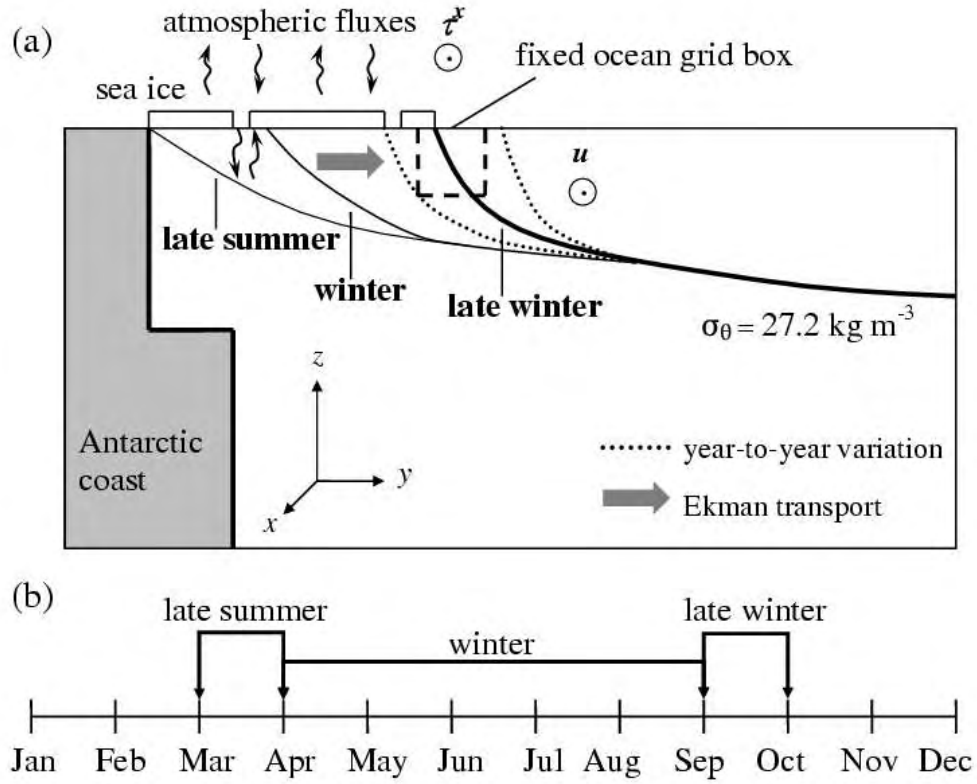

Figure 4: (a) Schematic diagram illustrating processes in the high latitudes of the Southern Ocean which influence the location of the σ_θ=27.2 kg m^{-3} surface ($\sigma_{27.2}$). Note the seasonal and year-to-year displacement of the isopycnal. (b) Conventional season definitions used in the heat and salt budget analyses.

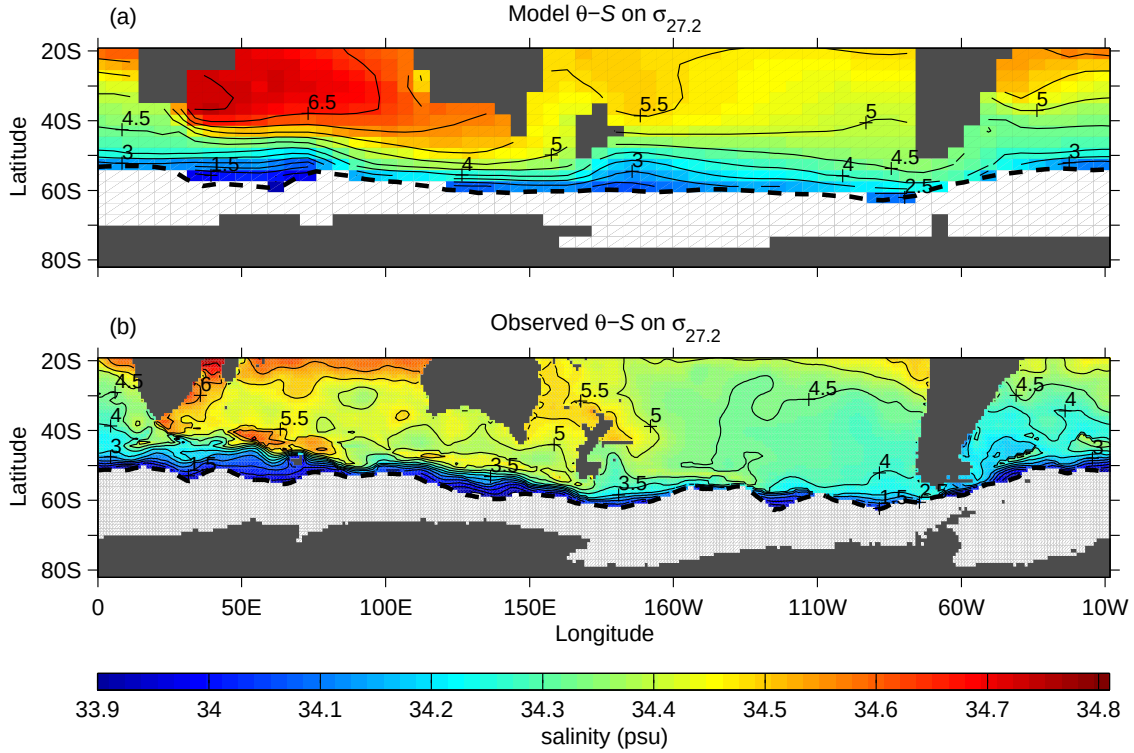

Figure 5: Late-winter potential temperature (shown as contours) and salinity on $\sigma_{27.2}$ in (a) the model and (b) the observed Levitus (1994) climatology. The dashed contour marks the mean location of the $\sigma_{27.2}$ surface outcrop during late winter.

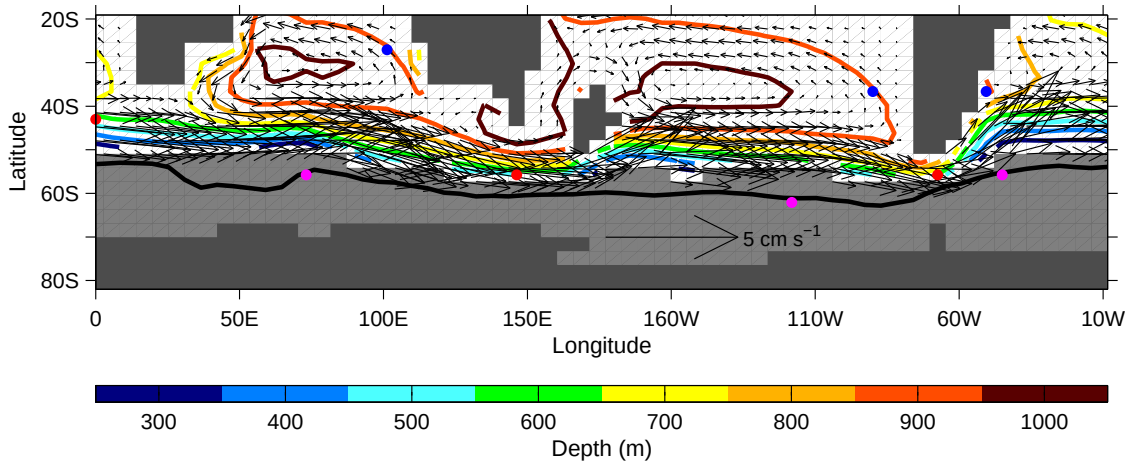

Figure 6: Mean circulation on the $\sigma_{27.2}$ density surface shown by late-winter velocity vectors averaged over 1000 years. Velocity fields are shown only at depths below 200 m. Depth contours are shown in colours. Mean position of the late-winter $\sigma_{27.2}$ outcrop is shown by the black contour. Coloured dots indicate locations of $\theta - S$ scatter plots in Fig. 7.

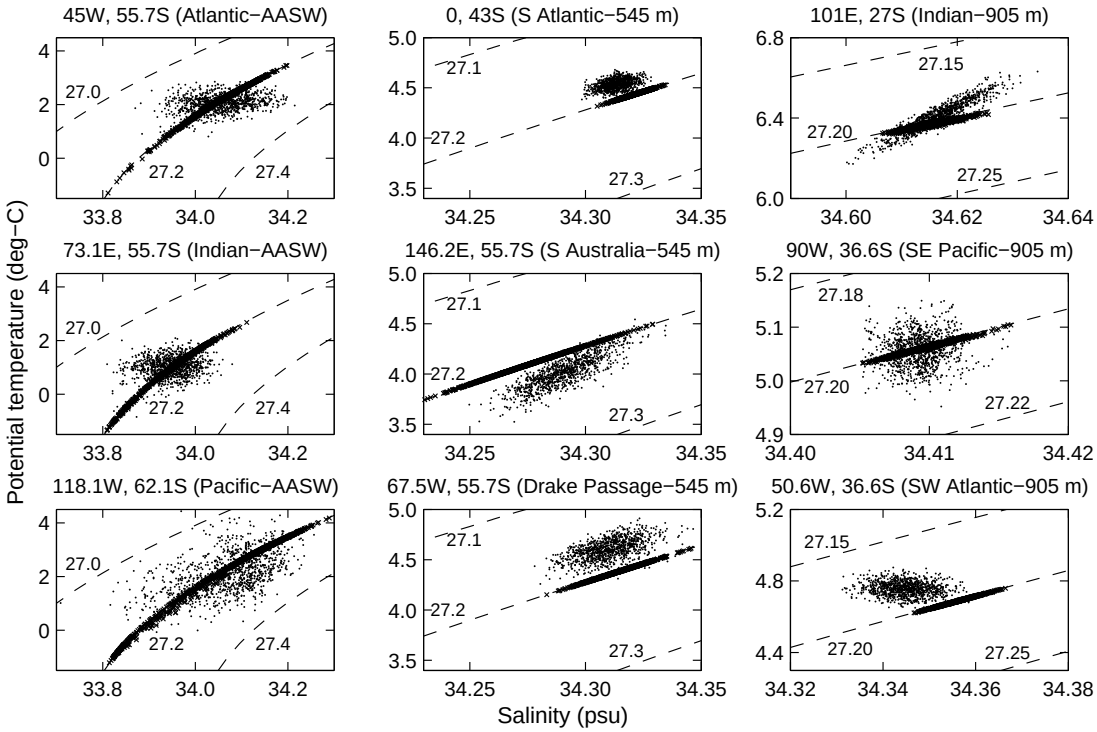

Figure 7: 1000-yr $\theta - S$ scatter plots at specified ocean grid boxes (shown in Fig. 6) having density closest to $\sigma_\theta = 27.2$ kg m^{-3} (marked with dots) and along the isopycnal (marked with crosses), at the surface (left column), 545 m (middle column), and at 905 m (right column). Note that at the surface the scatter plot along the $\sigma_{27.2}$ isopycnal varies with latitude, and in the interior varies with depth.

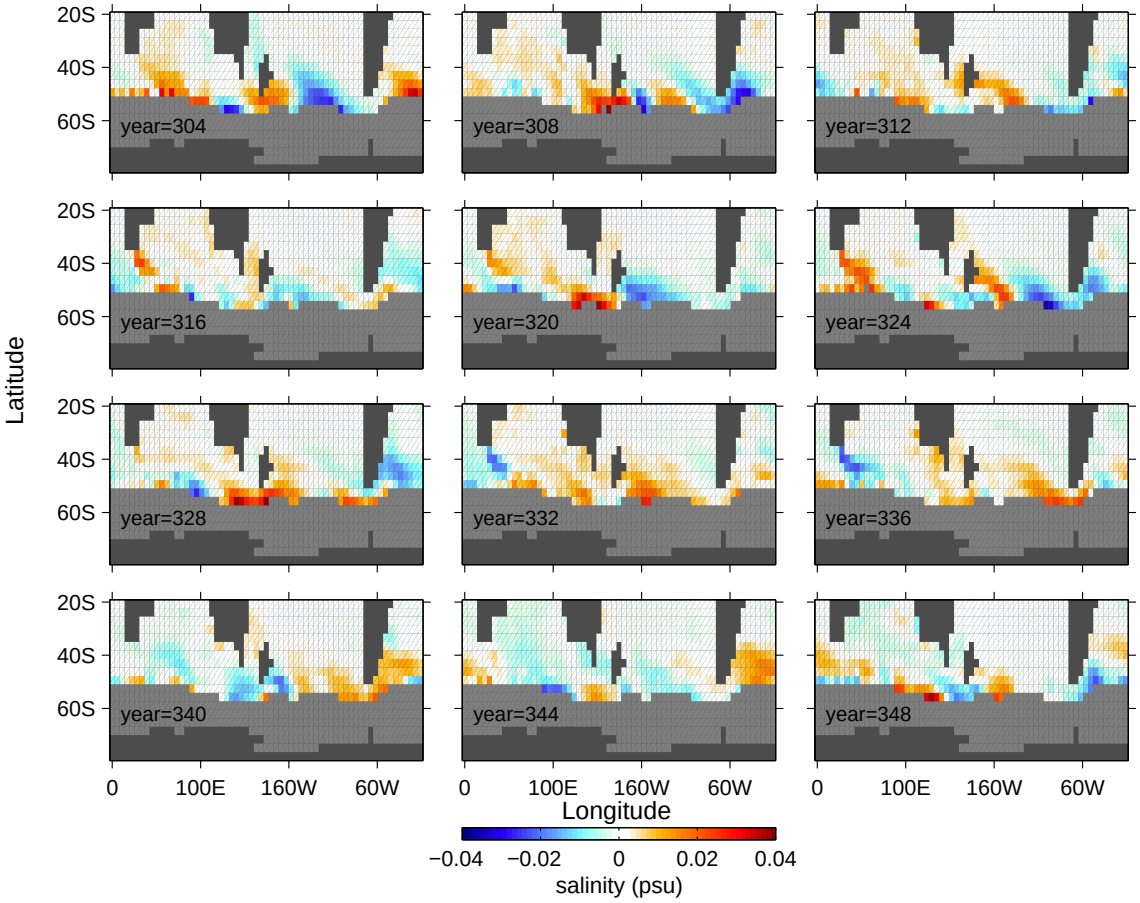

Figure 8: Late-winter salinity anomaly along $\sigma_{27.2}$ from year 304 to year 348 in a 4-yr interval. Grey shaded areas denote regions south of the CEOF domain (base of the $\sigma_{27.2}$ mixed layer).

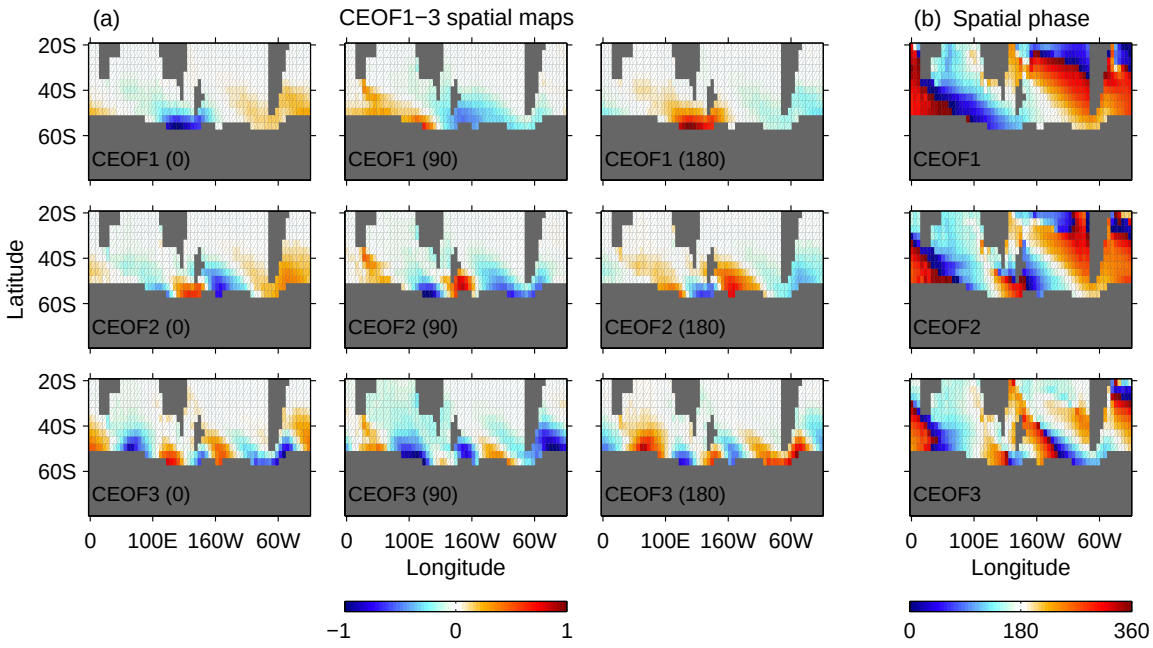

Figure 9: (a) The first three complex EOF modes of salinity shown at 90° phase intervals along $\sigma_{27.2}$. The three modes account for a total of 53% of the net S variance on $\sigma_{27.2}$. The first (CEOF1), second (CEOF2) and third (CEOF3) modes account for 24%, 16%, and 13% respectively. An equivalent CEOF analysis of θ on $\sigma_{27.2}$ shows similar modal structure, so is not shown here. (b) Spatial phase angle of CEOF1-3 indicating the direction of phase propagation of each mode from 0° to 360°. Apparent phase discontinuities occur because the phase is defined only between 0° to 360°.

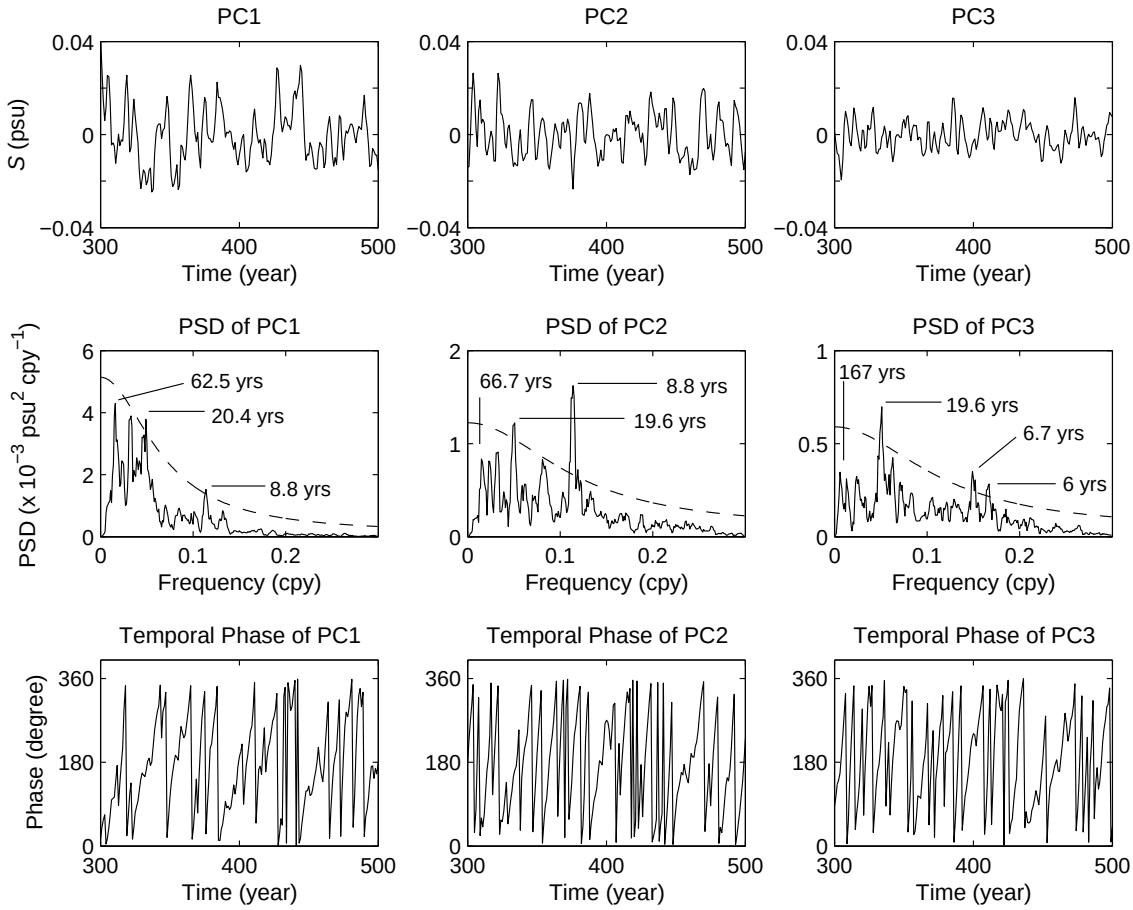

Figure 10: Top row: Principal component timeseries of CEOF1-3 is displayed from year 300-500. Middle row: Power spectral density (PSD) of the principal component timeseries with an estimated AR-1 background spectrum at 95% confidence level (dashed curve). Bottom row: Temporal phases obtained from CEOF1-3 displayed from year 300 to 500. The temporal phase angles in the lower panels are defined between 0° to 360°.

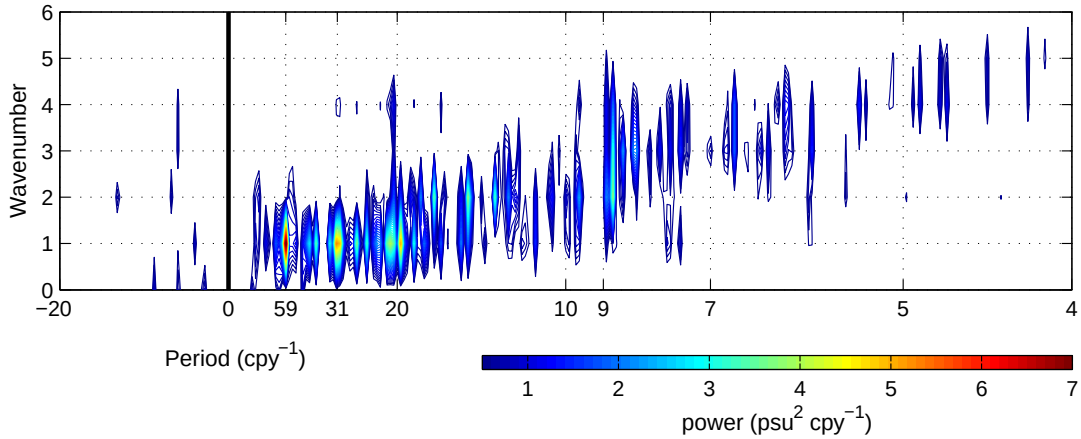

Figure 11: Frequency-wavenumber spectrum of salinity anomaly along the southernmost boundary of the CEOF domain on $\sigma_{27.2}$. The analysis decomposes spatial-temporal signals and shows mostly eastward propagating components (positive frequencies).

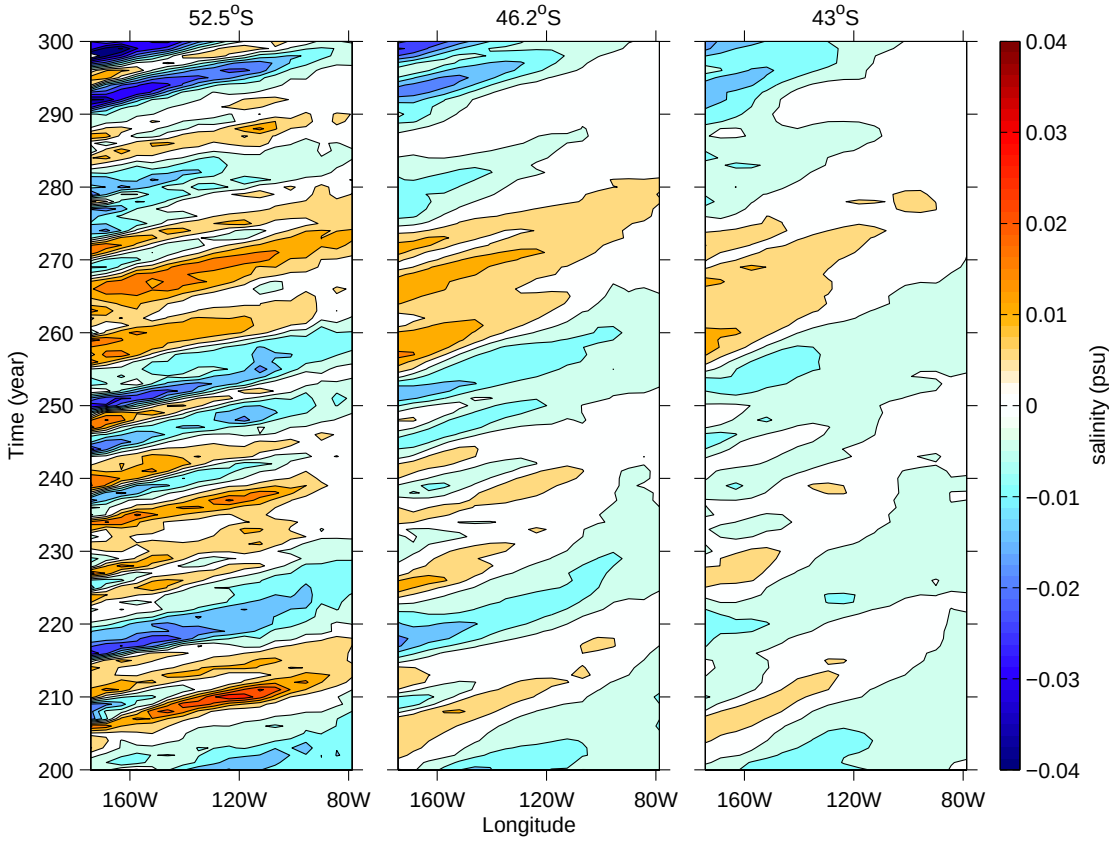

Figure 12: Hovmöller diagram of salinity anomaly on $\sigma_{27.2}$ in the South Pacific between 180°-80°W at 52.5°S, 46.2°S, and 43°S. Note that the depth of the isopycnal increases northward with average depths of 554 m, 884 m, and 963 m for each of the latitudes.

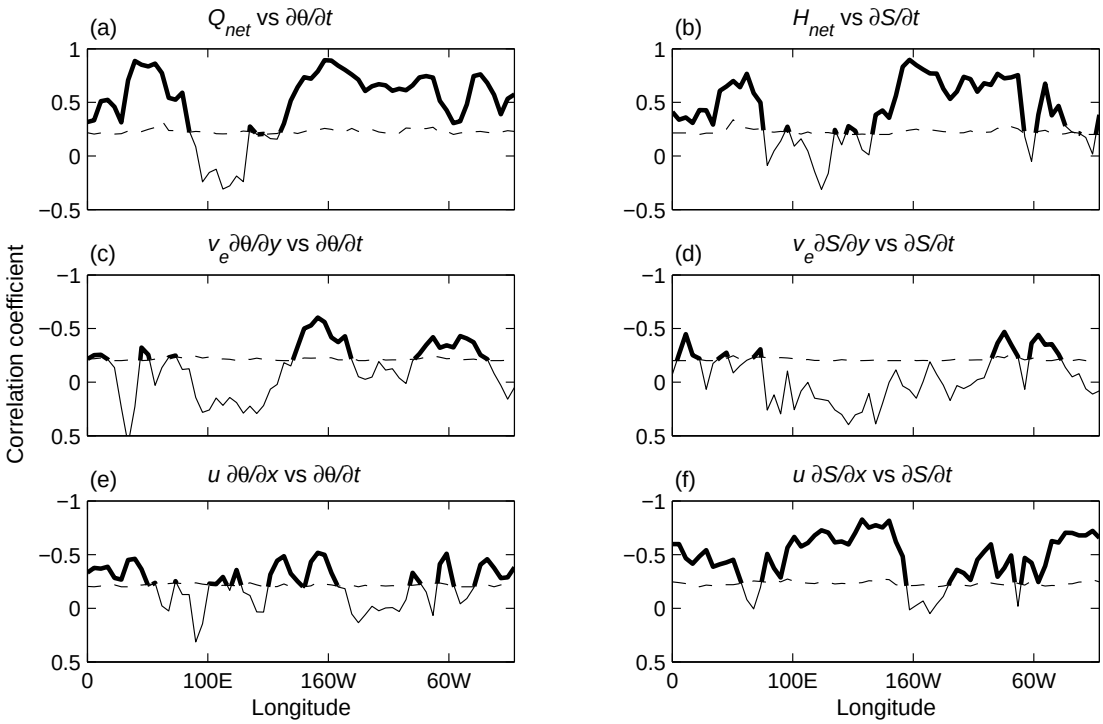

Figure 13: Correlation coefficients of heat and salt storage rate ($\partial\theta/\partial t$, $\partial S/\partial t$) versus winter (a) net air-sea heat flux (Q_{net}), (b) net air-sea equivalent salt flux (H_{net}), northward Ekman heat (c) and salt (d) transports, and zonal heat (e) and salt (f) advection at the $\sigma_{27.2}$ outcrop latitudes. Note that the calculation is based on the first 100 years of the model simulation, and is typical of the full 1000-yr run. Correlation is significant above the dashed line which indicates a 95% significance level and is highlighted for clarity. Note that the advection terms require negative correlations to account for variability in the wintertime AAIW $\theta - S$ properties (refer also to Eqs. 1 and 2). Thus, for convenience, the correlation axes in panels (c)-(f) have been inverted so that the longitudes of significant correlation correspond to those regions above the dashed line.

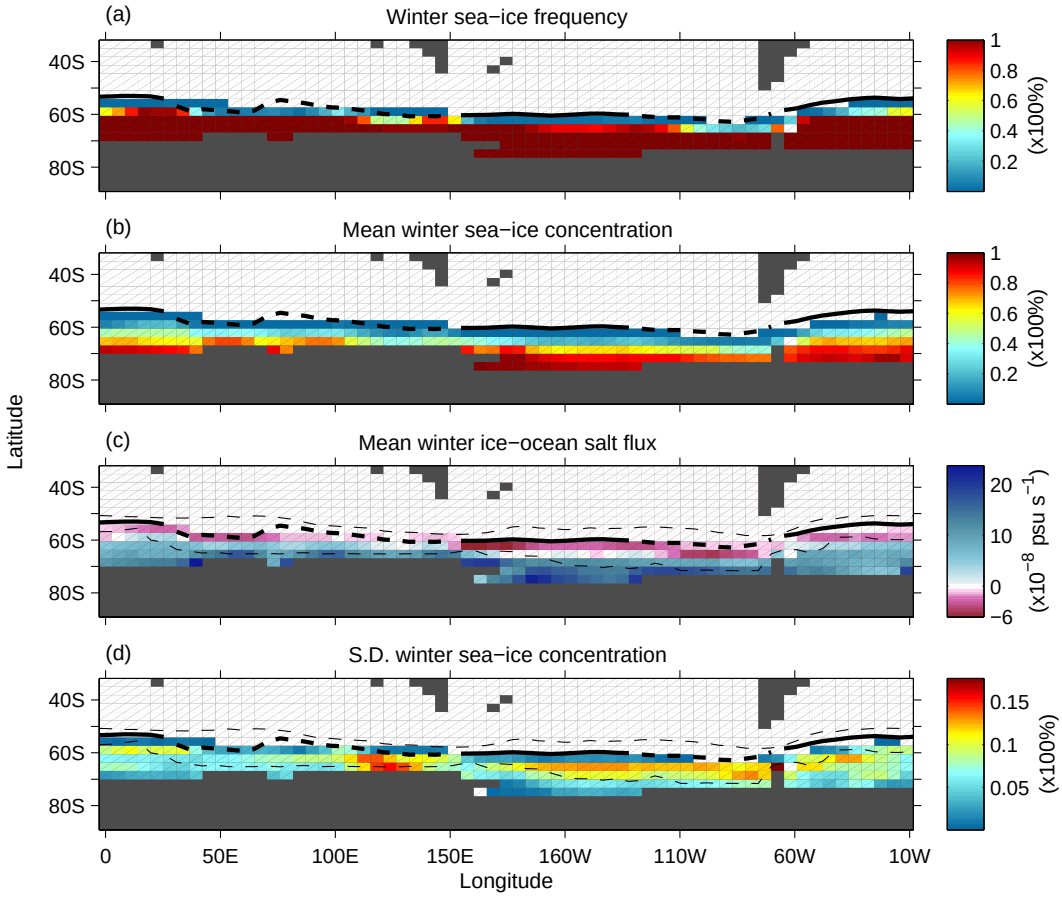

Figure 14: April to September average of ice extent over 1000 years showing (a) frequency of ice coverage, (b) mean ice concentration as a ratio of grid box area, (c) mean winter ice-ocean salt flux (H_{ice}), and (d) the standard deviation of the ice concentration. The mean location of the late-winter $\sigma_{27.2}$ outcrop is indicated by the solid line where the layer exists for the whole 1000 years and by a dashed line otherwise. Dotted lines in (c) and (d) denote maximum and minimum displacement of $\sigma_{27.2}$ outcrop ever attained over the 1000-yr model run (the southern-most extent excludes those years of no outcrop). North of 60°S in (c), sea-ice concentration is generally less than 60% and is marked by negative H_{ice} (freshwater input). Southward excursions of the $\sigma_{27.2}$ outcrop (i.e., low density AASW) generally coincide with years of limited Antarctic sea ice.

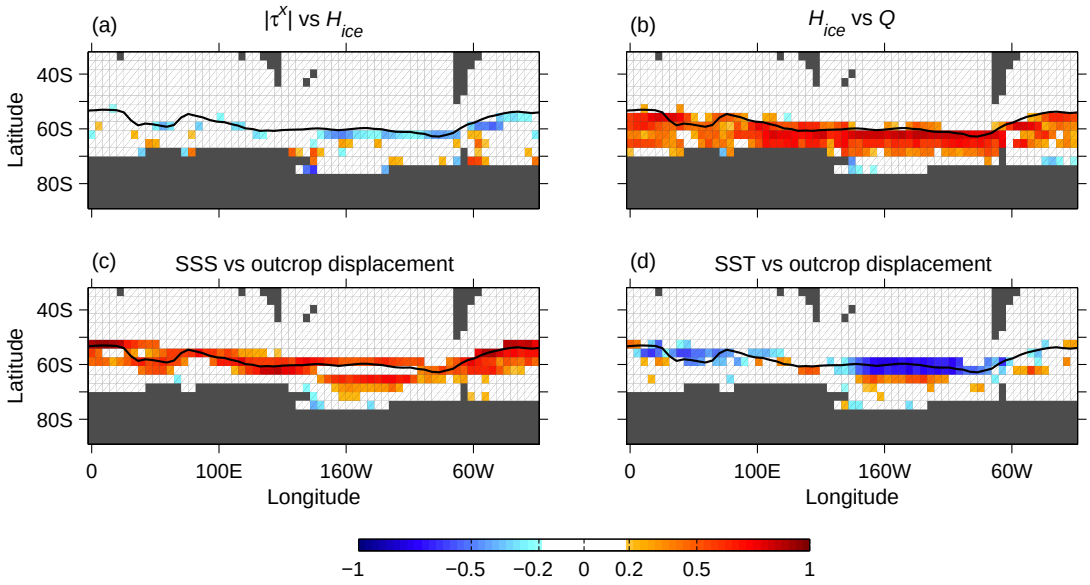

Figure 15: Correlation maps for (a) winter zonal wind stress (τ^x) versus winter ice-ocean salt flux (H_{ice}), (b) winter H_{ice} versus winter surface heat flux (Q, which is dominated by outgoing heat fluxes), and (c) late-winter surface salinity and (d) late-winter surface temperature versus $\sigma_{27.2}$ outcrop displacement. Correlation coefficients are calculated using 100 years of model simulation. The values are displayed when they are above the 95% significance level (refer to colorbar). The contour indicates the mean location of the late-winter $\sigma_{27.2}$ outcrop.

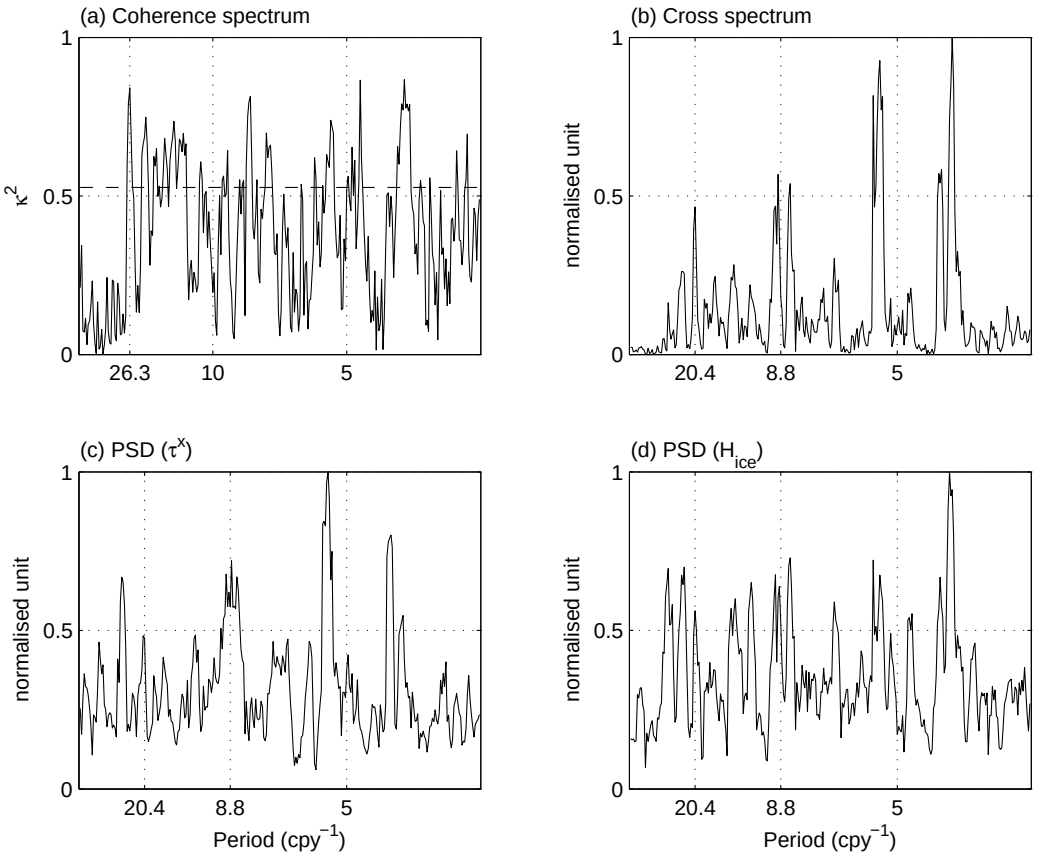

Figure 16: (a) Coherence spectrum, (b) cross spectrum, and the power spectral density of (c) zonal wind stress and (d) meltwater flux zonally averaged at the northern-most winter sea-ice extent near the mean location of the late-winter $\sigma_{27.2}$ outcrop where there is a mean input of ice-to-ocean freshwater (see Fig. 14c). The dashed horizontal line in (a) represents the 95% significance level.

Part II: Circumpolar Deep Water circulation and variability in a coupled climate model

Abstract

The natural variability of Circumpolar Deep Water (CDW) is analysed using a long-term integration of a coupled climate model. The variability is decomposed using a standard EOF analysis into three separate modes accounting for 68% and 82% of the total variance in the upper and lower CDW layers, respectively. The first mode exhibits an interbasin-scale variability on multi-centennial time scales, originating in the North Atlantic and flowing southward into the Southern Ocean via North Atlantic Deep Water (NADW). Salinity dipole anomalies appear to propagate around the Atlantic meridional overturning circulation on these time scales with the strengthening and weakening of NADW formation. The anomaly propagates northward from the midlatitude subsurface of the South Atlantic and sinks in the North Atlantic before flowing southward along the CDW isopycnal layers. This suggests an interhemispheric connection in the generation of the first CDW variability mode. The second mode shows a localised $\theta - S$ variability in the Brazil-Malvinas Confluence Zone on multi-decadal to centennial time scales. Heat and salt budget analyses reveal that this variability is controlled by meridional advection driven by fluctuations in the strength of the Deep Western Boundary and the Malvinas Currents. The third mode suggests an Antarctic Intermediate Water source in the South Pacific contributing to variability in upper CDW. We further find that NADW formation is mainly buoyancy-driven on the time scales resolved, with only a weak connection with Southern Hemisphere winds. On the other hand, Southern Hemisphere winds have a more direct influence on the rate of NADW outflow into the Southern Ocean. The model's spatial pattern of $\theta - S$ variability is consistent with the limited observational record in the Southern Hemisphere. However, some observations of decadal CDW $\theta - S$ changes are beyond that seen in the model in its unperturbed state.

1. Introduction

The absence of any meridional continental boundary in the Southern Ocean allows a global interaction of water masses at these latitudes. Circumpolar Deep Water (CDW), the greatest volume water mass in the Southern Ocean, is a mixture of North Atlantic Deep Water (NADW), Antarctic Bottom Water (AABW) and Antarctic Intermediate Water (AAIW), as well as recirculated deep water from the Indian and Pacific (e.g., Wüst 1935; Callahan 1972; Georgi 1981; Mantyla and Reid 1983; Charles and Fairbanks 1992; You 2000). Besides its role in the stability of the Southern Ocean marine environment (e.g., Prézelin et al. 2000) and in the atmospheric carbon cycle (Sigman and Boyle 2000; McNeil et al. 2001), CDW is an important Southern Ocean water mass as its upper and lower branches, namely Upper Circumpolar Deep Water (UCDW) and Lower Circumpolar Deep Water (LCDW), are further transformed into lighter AAIW and denser AABW respectively (e.g., Döös and Coward 1997; Sloyan and Rintoul 2001a). The formation and circulation of these water masses form an important component of the global thermohaline overturning and thus of the global climate system (for a review see Weaver and Hughes 1992; Schmitz 1995). Understanding the natural variability of CDW is therefore important for improving our knowledge of climate variability and the detection of climate change in the deep ocean.

The southward outflow of NADW through the South Atlantic sector of the Southern Ocean is an important feature of the global thermohaline circulation. A deep western boundary current (DWBC) stretching from the North Atlantic southward into the South Atlantic transports a large volume of NADW from its formation region into the Southern Ocean. Several observational studies have documented the spatial temperature-salinity ($\theta - S$) variation of outflowing NADW and its byproducts in the Indian, Pacific, and Southern Oceans. In the northern North At-

lantic, NADW has a range of $\theta-S$ properties of 1.9−3.6°C and 34.89−34.97 psu contributed from various sources such as Labrador Sea Water, Norwegian−Greenland Sea and the Denmark Strait overflow waters (Talley and McCartney 1982; Swift 1984; Dickson and Brown 1994). As NADW is advected into the South Atlantic, its $\theta - S$ decrease to about 2−3°C and 34.70−34.85 psu between 2000−3000 m depths at approximately 40°S in the southwestern Atlantic, due to mixing with colder and fresher CDW (e.g., Reid et al. 1977; Maamaatuaiahutapu et al. 1992; Tsuchiya et al. 1994).

Once in the Southern Ocean, waters originally from the deep North Atlantic enters the Indian Ocean south of Africa. On the $\sigma_2 = 36.92$ kg m^{-3} density surface, Mantyla and Reid (1995) found that CDW within the Antarctic Circumpolar Current (ACC) has salinity of 34.78 psu at the tip of South Africa. The $\theta - S$ signature decreases further eastward into the Pacific where salinity is found in the range of $34.70 - 34.74$ at $1500 - 2500$-db levels (Reid 1986). After CDW has flowed with the ACC from the Pacific sector through the Drake Passage, some portion of the CDW then joins the deep branch of the Malvinas (Falkland) Current northward into the Brazil-Malvinas Confluence Zone (BMCZ) where the first interaction between CDW and outflowing NADW takes place (e.g., Gordon 1989; Larqué et al. 1997; Stramma and England 1999). The remaining portion of CDW continues to flow eastward with the ACC together with the eastward deflection of the southward DWBC advecting a NADW signature into the Indian sector.

Despite the documentation of $\theta-S$ properties and circulation of CDW, the extent of its variability remains relatively unknown. The short temporal record and sparsity of observations confound existing knowledge of CDW variability, exacerbated by the slow processes characterising the ventilation of the deep water mass. Though deep ocean sediments and isotope samples provide a long temporal record, data coverage

is very sparse so their usage is limited in providing clues on the variability of the thermohaline circulation (e.g., Charles and Fairbanks 1992; Frank et al. 2002). Direct observations of $\theta - S$ variations within the NADW/CDW density class have been documented, in some locations in the Southern Hemisphere (SH), but they are still currently limited to decadal timescales (e.g., Johnson and Orsi 1997; Bindoff and McDougall 2000; Shaffer et al. 2000; Arbic and Owens 2001).

Climate models integrated over millenia featuring realistic climate feedbacks and global water masses are a convenient tool for understanding the dynamics and evolution of deep water properties and circulation. In this paper we analyse CDW variability on decadal to centennial time scales in a fully coupled ocean−atmosphere−ice−land surface model. The signal of NADW propagation into the Southern Ocean in response to the onset of deep water formation in the North Atlantic has been documented by Goodman (1998; 2001) using an ocean only model. Thermohaline oscillations in ocean models have also been studied by Mikolajewicz and Maier-Reimer (1990), Pierce et al. (1995), Osborn (1997), and Weijer and Dijkstra (2003). Our study, however, is the first to assess CDW variability in a fully coupled climate model, focussing on CDW $\theta - S$ variability. While our central goal is to assess CDW hydrographic variability, this naturally requires an analysis of circulation variability along the CDW layers. The rest of this paper is divided as follows. We begin with a description of the model and the methods of analysis in section 2. An overview of model CDW $\theta - S$ properties and circulation is provided in section 3. The CDW variability and the driving mechanisms are described in section 4 and section 5 respectively. Finally, the study is summarised in section 6.

2. Methodology

a. The coupled model

We analyse 1000 years of data from the latter stages of the Commonwealth Scientific and Industrial Research Organisation (CSIRO) 10,000-yr natural pre-industrial CO_2 coupled ocean-atmosphere-ice-land surface model. The model is an updated version of the coupled model described in Hirst et al. (2000). Earlier development and coupling of the model are documented in Gordon and O'Farrell (1997). Recent studies utilising the model can be found, for example, in O'Farrell (2002) and Santoso and England (2004). The atmospheric model has full diurnal and annual cycles, gravity wave drag, a mass flux scheme for convection, semi-Lagrangian water vapour transport, and a relative humidity-based cloud parameterisation. The land component employs the soil-canopy model parameterisation of Kowalczyk et al. (1994). The sea-ice model includes dynamics and thermodynamics and is fully described in O'Farrell (1998). The ocean model is based on the Bryan-Cox code (Cox 1984) with horizontal resolution matching that of the atmospheric component; namely, approximately 5.6° in longitude and 3.2° in latitude. The ocean model has 21 vertical levels of irregular grid box thickness. The parameterization of Gent and McWilliams (1990) and Gent et al. (1995) of eddy-induced transport (GM, hereafter) is included with zero horizontal background diffusivity. Air-sea flux corrections are implemented in the coupling to reduce long-term climate drift.

b. Deep water structure: isopycnal layer definitions

The structure of the model's deep water in the Southern Ocean is shown in Fig. 1 (left column) showing the zonally averaged salinity cross section in each ocean basin poleward from approximately 20°S. The corresponding observed Levitus (1994) salinity is shown in Fig. 1 (right column) for comparison. Despite the

fresher deep water in the model than the real ocean, particularly for the lower NADW (LNADW), the spatial structure is reasonably well reproduced; with realistic ventilation of NADW described in O'Farrell (2002). Weak LNADW formation is a common problem in ocean GCMs, resulting from poor representation of overflow processes south of the Greenland Sea (England and Holloway 1998). This enables stronger than observed AABW intrusion into the North Atlantic. This in turn yields a shallower salinity maximum core layer in the model compared to observations, with fresher than observed deep water. Upper NADW (UNADW), in contrast, is well-resolved by the model; it is this shallower variety of NADW that is of greater interest in the present study. The outflow of relatively saline UNADW in the Atlantic is seen in the model as in the observed with decreasing salinity as it upwells poleward and mixes with the fresher CDW. Traces of the salinity maximum are also observed in the Indian and Pacific sectors. As noted by Hirst et al. (2000), the inclusion of the GM parameterization results in a more realistic CDW density as compared to the model without GM. Eddy fluxes play an important role in the southward flushing of UCDW (Speer et al. 2000).

Our study focuses on the salinity maximum deep-water layer above about 3000 m but at depths below 1000 m isolated from the direct influence of air-sea interactions. The potential density layer referenced to 2000 db $\sigma_2 = 36.70 - 36.90$ kg m^{-3} ($\gamma^n \approx 27.70 - 27.92$) is chosen to inscribe the NADW layer and approximately captures the core of CDW in the model. Note that the locally referenced density at 2000 db is a reasonable approximation of neutral density surfaces for deep water analysis within the $1000 - 3000$-m depth range. This layer corresponds to $\sigma_2 = 36.80 - 37.02$ kg m^{-3} ($\gamma^n \approx 27.82 - 28.07$) in the observed at approximately the same depth levels (Fig. 1; right column), implying insufficiently dense deep water in the model, a problem typical of coarse resolution ocean GCMs (England and Hirst 1997; Hirst et

al. 2000). As also noted in Bianchi et al. (1993), CDW co-exists with NADW within the $\sigma_2 = 36.75 - 37.15$ kg m^{-3} density range (estimated from Reid et al. 1977; their Fig. 6b) which includes our observed CDW density layer $\sigma_2 = 36.80 - 37.02$ kg m^{-3} (Fig. 1; right column).

We further divide the model's CDW layer into an upper and lower part at $\sigma_2 = 36.80$ kg m^{-3} which approximately corresponds to $\sigma_2 = 36.94$ kg m^{-3} in the observations (see Fig. 1; right column). This choice of layer separation is similar to that of Mémery et al. (2000) where UCDW and UNADW in the southwestern Atlantic are observed to overlap over $\sigma_2 = 36.72 - 36.95$ kg m^{-3} above 2000-m depth. Reid et al. (1977) and Sievers and Nowlin (1984), on the other hand, attributed $\sigma_2 = 36.97$ kg m^{-3} as the upper limit of LCDW which is also a separation surface between UNADW and LNADW (Reid et al. 1977). The water below the separation layer is then regarded as LCDW which intercepts, in its upper branch, the core of the salinity maximum of NADW. For example, García et al. (2002) observed a salinity maximum of up to 34.72 psu in the LCDW layer in the Drake Passage. Note that the CDW layers chosen in our analyses also coincide with the salinity maximum in the Indian and Pacific basins (Fig. 1). The position of the isopycnal layers relative to the Atlantic basin meridional overturning streamlines is shown in Fig. 2. Both the UCDW and LCDW layers coincide with the outflowing NADW into the Southern Ocean, with the LCDW layer capturing a small portion of the upper part of the bottom water recirculation cell. The overturning features of the model have been discussed in Hirst et al. (2000) and are thus not elaborated here. However, note that in addition to the deep overturning cell in the North Atlantic, the Atlantic bottom recirculation is also weaker than that inferred from the observations of Sloyan and Rintoul (2001) and Talley (2003).

c. Spatio-temporal variability analyses

We analyse annually-averaged ocean variables since our focus is on deep water depths, where seasonal effects are negligible. The analysed variables include 1000-yr ocean potential temperature (θ), salinity (S), and horizontal velocities $\mathbf{u} = (u, v)$ from the latter part of the 10,000-yr run. We focus mainly on the area south of 20°S which covers the Southern Ocean domain. The ocean variables are linearly interpolated vertically onto discrete potential density surfaces at 0.01 kg m^{-3} intervals between σ_2=36.70 and 36.90 kg m^{-3}, inclusive. Averaged properties along the isopycnal surfaces are obtained for each of the $\sigma_2 = 36.70 - 36.80$ kg m^{-3} and $\sigma_2 = 36.80 - 36.90$ kg m^{-3} layers to represent the UCDW and LCDW, respectively (section 2b). The isolation of CDW from the surface is ensured by applying the layer averaging only when the uppermost surface is at 1000-m depth or deeper (see Fig. 3). The mean position of the UCDW and LCDW isopycnal layers are labelled as σ_{UCDW} and σ_{LCDW}, respectively.

A standard empirical orthogonal function (EOF) analysis is employed to decompose $\theta - S$ variability along σ_{UCDW} and σ_{LCDW} into orthogonal modes, each accounting for a portion of the total data variance. The spatial and temporal evolution of each variability mode are obtained from its eigenvector and expansion coefficient (also known as the principal component), respectively. For a detailed description of the EOF technique, the reader is referred to Preisendorfer (1988). Correlation and spectral analyses are implemented to reveal the temporal characteristics and relationships between variables. The spectral analyses are based on the Thomson multitaper method described in Percival and Walden (1993) and Mann and Lees (1996) for better statistical significance. The computation of correlation confidence level coefficients is described in Sciremammano (1979). We also analyse complex EOFs (CEOF) in order to reveal the propagation of anomalies (see e.g., Horel 1984

for a description of the CEOF technique). Heat-salt budget analyses are conducted to help identify mechanisms controlling CDW $\theta - S$ variability (for details see the appendix).

3. Model CDW: mean properties and circulation

a. Upper layer

Figure 4a, b shows the mean $\theta - S$ on σ_{UCDW} in the model and observed (Levitus and Boyer 1994; Levitus et al. 1994), respectively. The mean circulation and isopycnal layer depth in the model are presented in Fig. 4c (the labelled locations, R1−R4, are used in section 4a to describe the spatial distribution of deep-water $\theta - S$ variability at certain locations). The relatively saline and warm UNADW advected by the southward DWBC in the southwestern Atlantic at $20° - 33°$S shows $\theta - S$ of $\approx 4.0°$C and 34.84 psu in the model. The observed shows colder and slightly fresher UNADW of $\approx 3.0°$C and 34.81 psu. The UCDW layer in this region is found at a mean depth of about 1700 m. The purest concentration of UNADW is confined off the coast of Brazil with $\theta - S$ extrema of 4.1°C and 34.86 psu in the model at about 30°S, 40°W, which is warmer and fresher than the observed $\theta - S$ of 3.7°C and 34.94 psu (see also Reid et al. 1977, their Fig. 3a).

Temperature and salinity along σ_{UCDW} decrease gradually due to mixing as UCDW flows into the Indian and Pacific sectors. In the Agulhas Basin at 22°E, 40°S (around R2), the model's UCDW has average $\theta - S$ of 3.1°C and 34.67 psu which is again warmer and fresher than the observed (2.6°C and 34.73 psu). The UCDW further cools and freshens eastward. The model captures the westward flow from the South Australian Basin towards the east coast of Africa via the Indian Ocean interior, as also suggested by the observations of Mantyla and Reid (1995) on $\sigma_2 = 36.92$.

The spatial $\theta - S$ variations in the Pacific sector are weaker than in the other ocean basins in both model and observations. To the south of New Zealand to Drake Passage along about 53°S, $\theta - S$ decreases less rapidly from $\approx$ 2.2°C, 34.51 psu to 2.1°C, 34.48 psu in the model and from $\approx$ 2.2°C, 34.65 psu to 2.1°C, 34.64 psu in the observed (see also Callahan 1972; Sievers and Nowlin 1984). The UCDW variety in the Pacific sector is the coldest and freshest due to mixing with recirculated interior waters from the Pacific Basin. There is a mean southward flow at the western boundary ($\approx$ 0.3 cm s^{-1}) in the model along the Louisville Seamount Chain ($20° - 40°$S, 170°W) joining the ACC towards the Drake Passage. This flow is observed in the real ocean, for example, by Wunsch et al. (1983), Whitworth et al. (1999), and Wijffels et al. (2001).

As seen in observations, the model captures flow through the Drake Passage being deflected northward in the Malvinas Current into the BMCZ where it meets the southward flowing DWBC. Because of the stronger signature of NADW and the colder and fresher UCDW in the model, the lateral $\theta - S$ gradient in the BMCZ appears to be larger than in the observed (Fig. 4a, b).

b. Lower layer

The $\theta - S$ spatial distribution on σ_{LCDW} is for the most part similar to that on σ_{UCDW} for both the model and observations (Fig. 5a, b). The water along this isopycnal layer is however generally colder and fresher in the model compared to the observed. Similar circulation patterns to the upper layer are also observed on σ_{LCDW} (Fig. 5c), characterised by the convergence of the DWBC and the Malvinas Current in the BMCZ before joining the ACC and flowing into the other Southern Ocean sectors. Topographical obstructions are apparent on σ_{LCDW}. The LCDW flow in the ACC is partially obstructed by the Kerguelen Plateau ($40° - 57°$S, $70° - 80°$E).

Mantyla and Reid (1995) suggest that flow on the $\sigma_2 = 37.00$ surface separates into three streams as it approaches the Kerguelen Plateau. The anticyclonic shear in the South Australian Basin and the northward flow in the Mascarene Basin ($20° - 40°$S, 50°E) are also consistent with the observations of Mantyla and Reid (1995). In the Pacific, northward deflections of the ACC occur along Chatham Rise (southeast of New Zealand) up to 45°S before turning eastward again. This is consistent with the geostrophic flow in Reid (1986) at $2000 - 2500$-db levels. The northward flow into the Tasman Sea as observed in Reid (1986) is also resolved, as well as the large anticyclonic gyre in the South Pacific and the southward eastern boundary flow along the coast of Chile (80°W).

c. Summary

The model mean $\theta - S$ and circulation fields on the density layers corresponding to CDW show good overall agreement with observations. While the salinity of outflowing LNADW is fresher than the observed, rendering LCDW to be too fresh by ≈ 0.2 psu, the spatial $\theta - S$ variations of CDW are qualitatively similar to observed climatologies. In addition, the model's CDW flow pathways are remarkably consistent with available estimates of deep Southern Ocean circulation patterns.

4. CDW variability patterns

a. $\theta - S$ properties

The spatial and temporal variability of the model's CDW on σ_{UCDW} and σ_{LCDW} are described in this section. Figure 6 presents the spread of $\theta - S$ over 1000 years at the selected locations shown in Figs. 4c, 5c on σ_{UCDW} and σ_{LCDW}, respectively. The depths are taken as the mean depth of σ_{UCDW} and σ_{LCDW} at each location. We focus our analysis on the along-isopycnal variability of CDW. Nonetheless, some

reference is also made to the along-isobar variability, as this gives insight into the effect of isopycnal vertical excursions in response to the $\theta - S$ fluctuations (Bindoff and McDougall 1994; see also e.g., Arbic and Owens 2001; Wong et al. 2001).

Variability in both σ_{UCDW} and σ_{LCDW} $\theta - S$ decreases gradually eastward from the Atlantic sector (Fig. 6). This is further illustrated in a standard deviation analysis (Fig. 7), showing a decrease in $\theta - S$ variability into the Indian and Pacific basins. This variability pattern resembles the pathway of NADW outflow into the Southern Ocean (see, e.g., Sen Gupta and England 2004). Note also that the strongest variability in the Southern Hemisphere is localised in the BMCZ.

On σ_{UCDW} (Fig. 6), the along-isopycnal $\theta - S$ range decreases gradually from 0.19°C, 0.036 psu at R1 (Atlantic) to 0.04°C, 0.006 psu at R4 (Pacific). The $\theta - S$ range along isobars decreases from 0.21°C, 0.036 psu at R1 to 0.07°C, 0.008 psu at R4. The magnitude of variability in the lower layer is smaller than in the upper layer (Fig. 6), but with similar geographic trends. An interesting feature of Fig. 6 is that the along-isobar $\theta - S$ variations at R1 (Atlantic Ocean) are in near density compensation. On the other hand, there is a larger diapycnal spread at fixed depth at R2, R3, and R4 (Indian−Pacific Oceans) marked by the dominance of heave effect (see appendix) This spatial distribution of the changes also appears consistent with the observations discussed in section 4b. The changes due to the heave effect are shown by the heat-salt budget analyses (see appendix) to balance the vertical fluxes. On the other hand, changes along isopycnals are mainly attributed to horizontal advection transmitting anomalies over large spatial and temporal scales. It should be noted here that generation of $\theta - S$ anomalies along isopycnals can be attributed to one or a combination of the following mechanisms: 1. air-sea flux variations at water-mass formation regions (e.g., Arbic and Owens 2001), 2. anomalous advection across $\theta - S$ fronts (Schneider 2000; Rintoul and England 2002), and 3. $\theta - S$

and/or volume variability of adjacent water masses (Johnson and Orsi 1997) which also causes heaving of isopycnals. Isopycnal heaving can also result from changes in the rate of gyre spin and baroclinic wave propagation. In the following sections we further examine the modes and mechanisms of CDW variability.

b. Comparison with observations: decadal changes

This section provides a brief overview of the observed decadal changes in CDW in the Southern Ocean. We will compare these changes with the model's largest magnitudes of decadal $\theta - S$ change observed over the course of the 1000-yr model simulations. Note however that a detailed comparison is not straightforward here. Firstly, the model's coarse resolution renders it a more damped system compared to the real ocean with its rich structures of $\theta - S$ variability. Secondly, while the model is run with constant CO_2, the observed changes occur during an era of increasing anthropogenic CO_2. This second factor is perhaps less significant as modern-day CDW is a by-product of water-masses formed as long as centuries ago. In addition, by examining a constant CO_2 run, we can isolate natural, not forced, modes of CDW variability.

Basin-averaged along-isobar warming and salination of ≈ 0.2°C century^{-1} and 0.1 psu century^{-1} were observed at $\approx$ 2000-m depth over 1925 to 1959 along 32°S in the southwestern Atlantic (Arbic and Owens 2001; their Figs. 3, 4). The along-isobar changes consist of mostly changes along isopycnal (their Fig. 9). The corresponding changes in the model at the local mean depth of σ_{UCDW} ($\approx$ 1700 m) display zonally-averaged magnitudes of up to 0.1°C century^{-1} and 0.02 psu century^{-1}. The Arbic and Owens (2001) salinity changes would therefore appear beyond natural variations in CDW.

Temperature-salinity changes between 1962 and 1987 across the Indian Ocean at

$\approx 32°$S have been documented by Bindoff and McDougall (2000). Basin-averaged cooling and freshening along isobars are observed at about 2000-m depth of the order of 0.05°C and 0.005 psu (see their Fig. 6). They suggest that the changes are due to heaving of isopycnals. The corresponding changes in the model are smaller with basin-averaged values on σ_{UCDW} of up to ≈ 0.02°C and 0.002 psu per quarter century. Along-isopycnal change in the model is about half that of the along-isobar change for θ and is comparable in magnitude for S, suggesting that heave effects account for the density difference due to θ change (see also Bindoff and McDougall 2000; their Fig. 10).

In the Pacific, pronounced cooling and freshening of up to 0.07°C and 0.01 psu along deep density surfaces between $40° - 20°$S are found along 170°W between 1968/69 and 1990 (Johnson and Orsi 1997; their Fig. 4). The UCDW layer in the model displays $\theta - S$ differences of up to ≈ 0.06°C, 0.01 psu over 22 yr, concentrated in the southern part of the section. These decrease to ≈ 0.01°C, 0.002 psu on σ_{LCDW}.

Along-isobar warming and freshening of about 0.02°C and 0.002 psu are detected over 28 yr (1967-1995) at about 2000-m depth, zonally averaged from the coast of Chile to $86 - 88°$W at 43° and 28°S (Shaffer et al. 2000; their Fig. 2). The θ change is balanced by heave effect and thus the along-isopycnal change is small (see their Fig. 3). In the model, larger changes can occur at the mean depth of σ_{UCDW} (≈ 1800 m) with up to 0.03°C, 0.001 psu for the corresponding time period. Much smaller changes occur in along-isopycnal space.

It appears from the studies above that along-isopycnal changes are the largest in the South Atlantic, decreasing into the Indian and Pacific sectors where changes due to heave effect become more significant. This is similar to the variability pattern described in section 4a. However, as noted above, the weaker $\theta - S$ changes produced in the model are most likely due to limitations common in coarse resolution climate

models such as reliance on somewhat idealised mixing parameterisation. In addition, the use of surface heat and freshwater flux correction terms might also alter model CDW variability. There is also the possibility that increasing atmospheric CO_2 could be partly responsible for some of the recently observed multidecadal changes in CDW $\theta - S$. Aliasing of modes of the observed $\theta - S$ variability should also be taken into account. This is possible if we have a knowledge of the dominant modes and their spatio-temporal characteristics.

c. Modes of variability: EOF analyses

A standard empirical orthogonal function (EOF) analysis is applied on the CDW $\theta - S$ fields to decompose the variability into orthogonal modes (refer to section 2c). Because the analysis is applied along isopycnals where $\theta - S$ vary coherently to conserve density, the spatial variability patterns and the corresponding temporal characteristics are identical for θ and S. Hence, for simplicity, it is sufficient just to refer to the results for salinity. Here we present the first three leading modes which explain 68% and 82% of the total variance on σ_{UCDW} and σ_{LCDW}, respectively. The proportion of variance represented by each EOF mode for both layers is displayed in Fig. 8. Based on the distance between eigenvalues, only the first and second modes are well separated from their neighboring modes. Higher modes are more likely to be affected by 'effective degeneracy' and 'mixing' (refer to Fig. 8 and caption), thus physical interpretation for these modes can be difficult (North et al. 1982). The spatial patterns of the first three modes are displayed in Fig. 9. The corresponding temporal characteristics are shown in Fig. 10, presented by the principal component (PC) timeseries and their corresponding power spectra.

EOF1 exhibits an interbasin-scale variability of CDW salinity originating from the South Atlantic oscillating on multi-centennial time scales as shown by the char-

acteristic time series (PC1). The UCDW mode has Pacific Ocean salinity anomaly out of phase with the South Atlantic. In both layers the major signature is in the Atlantic sector, decreasing in magnitude eastwards along the ACC. The corresponding power spectra display signals at centennial−milennial time scales with a dominant period of $\approx$ 330 yr. Interdecadal variability is stronger in PC1 for the UCDW layer which is due to the shallow outflow level of NADW. From its spatial characteristics, EOF1 is likely to be related to variability in the NADW properties flowing into the Southern Ocean (discussed further in section 5a).

The spatial pattern of EOF2 (Fig. 9) shows large variance in the BMCZ where UNADW advected by the DWBC mixes with the fresher and colder CDW advected northward by the Malvinas Current. The localised region of the largest variability is marked by a box in Fig. 9 (EOF2) situated at the BMCZ. A weaker and out-of-phase pattern can be seen in the region from the southeastern Atlantic into the circumpolar region south of Australia. The EOF2 mode is characterised by signals at interdecadal−centennial timescales with a dominant variability at 100-yr period on both σ_{UCDW} and σ_{LCDW} (Fig. 10). There is a 30-yr peak in the power spectrum for PC2 in σ_{UCDW} which is virtually absent in σ_{LCDW}. The mechanisms controlling this second EOF mode of variability are described in section 5b.

It is worth emphasising that the two dominant modes persist throughout the thick layer of CDW. This is not the case with the third mode which explains less than 10% of the total variance. EOF3 for σ_{UCDW} reveals variability sourced in the South Pacific spreading northward. In contrast, EOF3 for σ_{LCDW} shows a wavenumber-1 mode of $\theta - S$ variability on interdecadal to multicentennial time scales (Fig. 10). The mechanism for this variability mode is briefly described in section 5c.

The three EOF modes above are retained by complex EOF (CEOF) analyses as shown in Fig. 11a presenting the CEOF spatial maps on σ_{UCDW} at 90° phase

intervals. The CEOF maps for σ_{LCDW} are not presented here as they resemble their EOF counterparts and show similar CEOF patterns as σ_{UCDW}. The spatial phase maps (Fig. 11b) show eastward propagation of anomalies in the Southern Ocean, as well as northward propagation into the Indian and Pacific basins. A more extended EOF analysis of $\theta - S$ fields from a 1600-yr data set taken from earlier model years also captures variability modes with similar spatial and temporal characteristics as the modes described above, although with different amounts of variance explained by each mode (Fig. not shown). Thus, the modes described are robust and are likely to represent physical processes in the model. Finally it may be noted that the combination of the EOF1−EOF3 spatial patterns approximately comprises the overall CDW variability pattern as shown by the standard deviation maps in Fig. 7. This is because the first three EOFs account for a significant component of the total $\theta - S$ variability.

5. Variability mechanisms

a. First mode

The spatial pattern of the first $\theta - S$ variability mode (EOF1; Fig. 9) was seen to be concentrated in the South Atlantic, decreasing eastward into the Southern Ocean. This pattern suggests that the variability may be linked to variations in NADW $\theta - S$, originating from the formation regions in the North Atlantic. To investigate this, we present a correlation analysis between the first principal component (PC1) and the box-averaged salinity anomalies along isopycnals in a region downstream of the Labrador Basin (labeled S_{NA}) and another in the deep tropical region in the South Atlantic (labeled S_{SA}; see Fig. 12 for the respective locations). The timeseries of PC1 and salinity at S_{NA}, S_{SA} are presented in Fig. 12a, b for σ_{UCDW} and σ_{LCDW}, respectively. Note the more prominent interdecadal signals on σ_{UCDW} compared to

σ_{LCDW} because this upper layer is closer to the core of outflowing NADW (Fig. 2). The variability on interdecadal timescales is also more pronounced at S_{NA} compared to S_{SA}, due to the greater damping of NADW variability, via mixing, as these waters are advected away from their source regions.

PC1 and salinity at S_{NA}, S_{SA} are correlated significantly (above 95% confidence level) at different timelags as shown in Fig. 12c, d. This suggests that the first CDW EOF mode is mainly capturing NADW spiked $\theta - S$ variability originating upstream in the North Atlantic. On σ_{UCDW} S_{NA} leads S_{SA} by 51 yr, suggesting that the anomalies travel at ≈ 0.4 cm s^{-1} to cover a distance of 60° latitudes over $\approx$ 50 yr. This is approximately the mean DWBC velocity from S_{NA} to S_{SA}, within the model CDW layer. S_{SA} leads PC1 variability by $\approx$ 13 yr and S_{NA} leads PC1 by $\approx$ 65 yr, again matching the advective timescales for North Atlantic $\theta - S$ anomalies to travel into the Southern Ocean. The LCDW layer exhibits marginally shorter lag times; for example, 49-yr lag from S_{NA} to S_{SA}. This is likely due to different mixing rates in the two CDW layers. For example, the magnitude of variability of S_{NA} is about twice that of S_{SA} on σ_{UCDW}, while the magnitude of the signals at S_{NA}, S_{SA} is comparable on σ_{LCDW}. Thus, more damping occurs along σ_{UCDW}, accounting for the slower phase speed in that layer's EOF1.

The flow of $\theta - S$ anomalies out of the Atlantic can be depicted in Fig. 13 showing a correlation map of the salinity field against S_{NA} on σ_{UCDW} at increasing timelags. The corresponding lag correlation map on σ_{LCDW} is similar to σ_{UCDW}, and is thus not presented here. The diagram suggests a large-scale propagation of anomaly from the North Atlantic southwards in the DWBC then continuing eastward in the ACC (see also Goodman 2001). When S_{NA} is shifted back in time by 20 yr, the lag correlation is significantly high in the region north of S_{NA}, showing that the anomaly signals indeed originate from the NADW formation regions. At

longer time-lags, the correlation peak propagates into the Indian and Pacific basins, but with reduced amplitude as the anomalies have their characteristics damped by mixing. As shown in the appendix, the $\theta - S$ variability is controlled by meridional advection in the South Atlantic where along-isopycnal variability dominates, and by zonal advection in the Southern Ocean where heave processes are more intense.

It should be noted that one half of a cycle of NADW outflow and recirculation involves an outflow of positive anomaly from the South Atlantic into the Southern Ocean, and the ensuing propagation of a negative anomaly in which these anomalies propagate with the ACC and flow northward into the Indian and Pacific basins. A negative anomaly is seen in the South Atlantic to continue the second half of the cycle (see CEOF1 spatial map in Fig. 11a, top panel). We further note that the propagation of anomalies from the North Atlantic to the Southern Ocean takes ≈ 80 yr, corresponding to a quarter cycle, and thus the 330-yr peak shown in the spectra of PC1 (Fig. 10).

Figure 14 presents a series of raw salinity anomaly maps on a meridional-vertical plane along the Atlantic western boundary from year 179−515 in 42-yr intervals (refer to Fig. 15 for the location of the section). A positive S anomaly fills the North Atlantic in year 179 and is flushed southward along σ_{UCDW} and σ_{LCDW} with a decreasing magnitude (year 305). This is then followed by the appearance of a negative anomaly in the north at year 347. The cycle continues at irregular periodicity of approximately 330 yr. This corresponds to a half-cycle of ≈ 160 yr for a North Atlantic anomaly to propagate into the Southern Ocean. The timescale of the propagating anomalous signals seen in Fig. 13, namely the multidecadal transit from the North Atlantic to South Atlantic, is similar to the study of Smethie et al. (2000) using chlorofluorocarbons to trace the outflow of NADW.

Similar periodicity is also found in the Atlantic thermohaline circulation of the

Hamburg Large-Scale Geostrophic ocean-only model, accompanied by a dipole salinity anomaly propagating around the meridional-vertical plane with a dominant period of 320 yr (Mikolajewicz and Maier-Reimer 1990; see their Fig. 10). The oscillation is generated by the Southern Ocean 'flip-flop' oscillator described in Pierce et al. (1995) in which NADW supplies heat to the high latitudes of the Southern Ocean, inducing deep convection there. The convection in turn influences the thermohaline flow through the Drake Passage (Pierce et al. 1995). As a result, the ACC variability has a strong linear relationship with the outflow rate in the Hamburg LSG OGCM (Mikolajewicz and Maier-Reimer 1990). In addition, there is a clear teleconnection between the NH and SH high latitude oceans. In a fully coupled model such as the one used in this study, the NADW−ACC relationship is expected to be less linear. This is confirmed by the low lagged correlation coefficient between the outflow rate (or formation rate) of NADW and the Drake Passage transport in the model (Table 1). The NADW formation rate is however strongly connected to the North Atlantic buoyancy, while the Drake Passage throughflow is tightly linked to the Weddell Sea buoyancy (see Table 1). Osborn (1997) showed that the nature of the oscillation can be altered by a more realistic atmospheric thermal feedback, which is absent in the LSG model, which in turn affects the extent of convection. The inclusion of the GM parameterization which is also known to influence convection, ventilation rates, and thermohaline circulation structure (see e.g., Hirst and McDougall 1996; England and Rahmstorf 1999; Hirst et al. 2000; Kamenkovich and Sarachik 2004), may further enhance the nonlinearity observed in our model.

Whilst the multicentennial periodicity is set by the NADW outflow time scale, it is unclear exactly what sets the $\theta - S$ anomalies in the North Atlantic. Though detailed investigation is beyond the scope of the paper, it is worth commenting that like the LSG model, there seems to be an influence from the Southern Ocean. This

is evident by referring to Fig. 15, which shows a composite map of S anomaly during periods of high and low NADW formation rates (defined as those above/below one standard deviation from the mean). Positive S anomaly occurs in the North Atlantic with high NADW formation rate (Fig. 15a). This is followed by negative anomaly at the subsurface down to intermediate depths in the SH, near 40°S, which then propagates northward (as suggested in Fig. 14, year 179−305). The converse occurs during periods of low NADW formation rate (Fig. 15b; namely, negative S anomaly fills the North Atlantic water column and is accompanied by the occurence of a subsurface positive S anomaly near 40°S see also Fig. 14, year 305−431). Further evidence of the origin and propagation of the subsurface anomalies is provided in Fig. 16 showing the lagged-composite salinity anomaly plots based on the anomalously high North Atlantic overturning. The emergence of negative anomaly south of 50°S in the subsurface is apparent at 50 years prior to the high overturning. Enhancement of the anomaly is evident at the subtropics at the −20 yr time lag. This suggests that at least some portion of the anomaly in the North Atlantic may be sourced from the Southern Ocean [via Subantarctic Mode Water (SAMW) and AAIW]. One possible variability mechanism is through conversion of UCDW to Antarctic Surface Water (AASW) at UCDW outcrop regions, from where AASW is further transformed to AAIW/SAMW via meridional Ekman transport (Rintoul and England 2002; Santoso and England 2004). These water masses eventually flow northward in the Atlantic to close the NADW overturning cell (Sloyan and Rintoul 2001).

While the variability in NADW formation is clearly driven by thermohaline forcing in the North Atlantic, the evidence for a Southern Ocean wind influence as proposed by Toggweiler and Samuels (1995) is not apparent in our model. This is shown by the low correlation between NADW production rate and the northward Ekman transport at the latitude of Cape Horn (labelled as V^{E}_{TS95} in Table 1; with

a mean of about 24 Sv). The relationship would presumably be more apparent if thermal feedbacks were excluded (Rahmstorf and England 1997). This is clearly not the case in a coupled climate model. The relationship between the outflow rate and the wind transport at the southern tip of South America (as calculated according to Toggweiler and Samuels 1995) is also only weak, with a correlation coefficient of 0.14. However, the influence of SH winds is more apparent along a slightly different path integral. In particular, Nof (2003) proposed that the integral of wind stress along a closed integration path, situated north of the ACC, connecting the tips of South America, South Africa, and South Australia ($\int_{Nof03}$; Table 1), gives an estimation of the net transport into the North Atlantic. This transport corresponds to a net northward interior flow, a balance between the western boundary current and the Sverdrup interior. Note that the mean of this calculated integrated transport neglecting friction terms accounts for about 22 Sv which includes the Ekman transport, the geostrophic flow underneath, and the western boundary current transport (Nof 2003). The correlations are now higher between the NADW formation/outflow rates and $\int_{\mathrm{Nof03}}$ as compared to those against $\mathrm{V}^{\mathrm{E}}_{\mathrm{TS95}}$ (Table 1). This analysis suggests that changes in the SH winds have a more direct effect on NADW outflow than on NADW formation, as also suggested by Rahmstorf and England (1997) and Oke and England (2004). Most of these earlier studies refer to equilibrium solutions, whereas the analyses presented here assess the extent of wind influence over decadal−centennial time scales. While wind effects are apparent in NADW outflow variability, buoyancy forcing appears to be of first order importance in controlling the overturning and deep water variability in the model.

b. Second mode

The spatial pattern of the second EOF mode (Fig. 9) shows largest variance confined to the BMCZ where an interaction occurs between NADW and CDW marked by a density-compensated thermohaline front (Fig. 17). Heat-salt budget analyses are performed in the BMCZ to investigate the mechanisms giving rise to $\theta - S$ variability in the UCDW and LCDW layers in the BMCZ (see the appendix for the calculation method). We calculate the mean heat and salt budget terms over the area 28°W−45°W and 37°S−46°S, as denoted in Fig. 17. The magnitude of variability of the $\theta - S$ budget terms on both CDW layers is revealed in their standard deviations given in Tables 2 and 3. The standard deviation of the terms along isobars and due to heave are also presented for reference. The significance of each budget term in its contribution to changes in along isopycnal ($\phi_t|_\sigma$), along isobar ($\phi_t|_z$), and changes due to heave ($\phi_t|_{heave}$) is qualitatively measured by their corresponding correlation coefficients presented in the two tables. The reader may find the materials presented in the appendix helpful in the discussion of the following analyses.

The meridional advection of heat and salt plays an important role in the along-isopycnal $\theta - S$ variability in the BMCZ. This is shown in Tables 2, 3 by the relatively large standard deviation of $v\theta_y$ and vS_y on σ_{UCDW} and σ_{LCDW}. Furthermore, the correlation between the meridional advection and the heat-salt content variations along isopycnals ($\theta_t|_\sigma$, $S_t|_\sigma$) is also large compared to the other advective and mixing terms. Note that although the standard deviation of the vertical advection is also significant, especially $w\theta_z$ in σ_{LCDW}, it does not directly contribute to the variations in $\theta_t|_\sigma$, as suggested by the low correlation value. The vertical advection is instead related to the heave-effect term. This is expected because vertical advection is the major contributor to the buoyancy flux, as mentioned in the appendix, advecting

fluid from above and below the CDW layers. As noted in Wong et al. (2001), $\theta - S$ variations along isopycnals may result from heave effects. This is verified by the significant correlation between $\theta_t|_{heave}$ ($S_t|_{heave}$) and $\theta_t|_\sigma$ ($S_t|_\sigma$). The excess of buoyancy due to vertical advection is balanced by the vertical movement of isopycnals which can in turn amplify or damp the along-isopycnal variations, depending on the vertical gradients of $\theta - S$ (see appendix for further discussion).

It is worth mentioning that when the budget analyses are re-applied to the low-pass filtered data allowing only signals with periods longer than 25 yr, there is a significant reduction in the vertical heat advection and heave-effect terms, most notably in the LCDW layer (Table data not shown). The horizontal advection and along-isopycnal heat-salt content terms in this case become more dominant. Thus, higher frequency fluctuations on σ_{LCDW} are dominated by vertical fluxes and more intense heaving resulting in the 'noisy' fluctuations observed along isobars (as noted by e.g., Johnson and Orsi 1997 in limited observations). In contrast, along-isopycnal advection dominates the variability at longer timescales in the model. Moreover, it is the meridional advection and in particular the meridional velocity, not the $\theta - S$ gradients, that controls the $\theta - S$ variations at these longer time scales (see Fig. A8f at R1). Therefore, deep $\theta - S$ variability in the BMCZ appears to be controlled by oscillations in both the southward DWBC advecting warm-saline NADW, and the northward Malvinas Current advecting cold-fresh CDW.

To explore this further, Fig. 18 presents composite maps for the σ_{UCDW} layer showing velocity anomalies during 'extreme years' in $\theta - S$ properties. By extreme we refer to years when the $\theta - S$ anomalies in the BMCZ are above and below one standard deviation unit, denoted as 'warm-saline' and 'cold-fresh' years, respectively. Warm-saline years in the BMCZ are thus confirmed to occur with an increase in the speed of the DWBC and a coinciding decrease in the speed of the Malvinas Current.

The opposite occurs during cold-fresh years. This pattern also exists on σ_{LCDW} (Fig. not shown). We now denote v_{DWBC} and v_{MC} as the average speeds of the DWBC and Malvinas Current, respectively, over the regions shown in Fig. 18a. These currents fluctuate with $\theta - S$ in the BMCZ on a wide frequency band, with v_{DWBC} (v_{MC}) and $\theta - S$ being positively (negatively) correlated with a significant coefficient of ≈ 0.4 (-0.4). Spectral analyses between v_{DWBC} and v_{MC} are shown in Fig. 19 for frequencies lower than 0.05 cpy (i.e., $>$ 20-yr period); we omit higher frequencies as the cross spectra show little energy for short period variability (Fig. 19b). Coherence spectra in Fig. 19a suggest that there is significant coherence (above 95% confidence level) mainly at periods longer than 50 yr. Note also that the DWBC and the Malvinas Current are shown in Fig. 19c to be approximately out of phase over multidecadal time scales. This implies that when the DWBC strengthens, the Malvinas Current weakens, and vice versa. It is not clear, however, what drives the retreat and extension of the currents. It is possible that the ACC may play a role as suggested by its composite patterns shown in Fig. 18. In summary, an interaction between the DWBC and the Malvinas Current gives rise to $\theta - S$ fluctuations in the BMCZ on multidecadal to centennial timescales via meridional advection of heat and salt. The anomalous $\theta - S$ signals created in the BMCZ are then advected eastward by the ACC into the Southern Ocean (see the eastward propagation shown by CEOF2 in Fig. 11).

c. Third mode

The third mode accounts for a small proportion of the total variance, and some degree of 'mixing' with higher modes is likely to occur (see section 4c). Thus, we only briefly comment on the possible mechanisms at play. The spatial pattern of the third EOF mode of σ_{UCDW} (Fig. 9) suggests variability sourced in the South

Pacific. Heat-salt budget analyses presented in the appendix suggest zonal heat-salt advective fluxes dominate in this region. Oceanic mixing also likely plays a role in distributing the signal into the interior of the Indian and Pacific Oceans, particularly along σ_{UCDW} from AAIW sources. The difference between the structure of mode 3 in the UCDW and LCDW layers suggests a detectable influence from the AAIW layer above (AAIW variability in the model has been presented in Santoso and England 2004). It should be noted that the analyses of Santoso and England (2004) are based on data filtered for periods higher than 200 yr. A low-frequency wavenumber-0 pattern of AAIW variability accounts for 24% of the total variance of the unfiltered AAIW $\theta - S$. This variability mode appears to be strongest in the AAIW outcrop region south of Australia, spreading into the ocean interior over decadal to multi-centennial periodicities (Fig. not shown). A coherence analysis between this AAIW $\theta - S$ mode and PC3 reveals some significant coherence at decadal to centennial timescales, with the cross spectrum between the two timeseries highest at 250-yr period (Fig. not shown). Thus, an AAIW signal is likely transmitted to the UCDW layer (via diapycnal mixing; see Fig. A7e, f in the appendix), and then advected eastward and northward into the Indian and Pacific basins (see CEOF3 maps in Fig. 11). This appears consistent with the decadal cooling and freshening found in the AAIW core which extends to UCDW as documented by Johnson and Orsi (1997) in the South Pacific. The mechanism controlling the EOF3 mode in σ_{LCDW} remains unexplained.

6. Summary and Conclusions

The spatial distribution of CDW properties and the NADW extent in the Southern Ocean was shown to be realistically simulated in the CSIRO climate model. The CDW water mass was divided into an upper and lower isopycnal layer, de-

noted as σ_{UCDW} and σ_{LCDW}, respectively. The variability of CDW $\theta - S$ is large in the Atlantic along the western boundary and decreases gradually eastward into the Southern Ocean. A high $\theta - S$ variability is confined to the BMCZ. Zonal and meridional advection determines the propagation of anomalies along the isopycnal layers, together with the damping effect of mixing. Heaving of isopycnal surfaces driven by variations in θ becomes large in the Southern Ocean due to stronger vertical advection, giving rise to noisy $\theta - S$ fluctuations when viewed along isobars. This spatial pattern of variability appears consistent with recently documented observed decadal $\theta - S$ variations in CDW.

The spatial structure of $\theta - S$ variability in the CDW layers was decomposed via EOF analyses into three dominant variability modes explaining 68% of the total variance in σ_{UCDW} and 82% in σ_{LCDW} (Fig. 9). The first mode shows significant spatial scale $\theta - S$ variability extending at its largest magnitude from the South Atlantic and decreasing gradually as it is advected eastward into the Southern Ocean. This first mode oscillates on multi-centennial time scales with $\approx$ 330-yr periodicity, corresponding to a quarter-cycle of $\approx$ 80 yr for anomalies to transit from the North to South Atlantic via the DWBC to join the ACC. There appears to be an interhemispheric teleconnection in the generation of the first mode of CDW variability in the model. During years of high (low) NADW formation, positive (negative) salinity anomalies propagate southward along the deep-water layer in the Atlantic, followed by northward propagating negative (positive) salinity anomalies at the intermediate depths in the South Atlantic. This salinity anomaly propagation has also been observed on similar time scales in the Hamburg Large-Scale Geostrophic OGCM (Mikolajewicz and Maier-Reimer 1990; Pierce et al. 1995; Osborn 1997). NADW formation is mainly driven by buoyancy forcing on these time scales, with our analyses suggesting only a weak connection between NADW formation and SH

winds (as originally proposed by Toggweiler and Samuels 1995). On the other hand, the SH winds were shown to have a more direct influence on NADW outflow into the Southern Ocean. In particular, following the proposed calculation of Nof (2003) we found a significant correlation between SH winds and NADW outflow.

The second mode of CDW variability is sourced in the BMCZ before being advected eastward by the ACC. It is characterised by interdecadal to centennial timescales of variability, and driven by an interaction between the southward DWBC and the northward Malvinas Current via meridional advective fluxes. When the DWBC accelerates, the Malvinas Current weakens resulting in local warming and salination of CDW. The converse occurs during the cooling and freshening scenario. A similar mechanism has been observed in the upper ocean of the BMCZ on seasonal-annual timescales (Garzoli and Giulivi 1994) and on multidecadal timescales (Wainer and Venegas 2002), under the influence of local atmospheric variability. As far as we are aware there have been no studies of decadal deep water variability in the BMCZ. Our model results suggest that this region is a hub of CDW variability, and thus likely to be a difficult region to analyse with only sparse data coverage.

The third mode of CDW variability showed fluctuations of UCDW sourced in the South Pacific. In the LCDW layer, there was no such source of variability in this region. Thus, AAIW is the most likely source of this mode of UCDW variability. It is noted, however, that this AAIW variability is of lower frequency than that documented in Part I. Vertical mixing and zonal advection were seen to play an important role in the transmission and propagation of the AAIW variability into the UCDW layer.

In summary, this study finds that a large component of CDW variability originates from the North Atlantic via ouflowing NADW. Significant variability also arises due to fluctuations in the Southern Ocean circulation, particularly in the

BMCZ. To a lesser extent, AAIW variability also contributes to the upper layer variability of CDW. Since the model does not simulate the Earth's climate system perfectly, it is of interest to assess the extent of these modes in a range of climate models. For example, it is reasonable to expect a shift in the frequency of the modes as they are determined by the DWBC velocity which is in turn dependent on model resolution. We may also expect a larger amplitude of the modes in models without flux adjustment. A better representation of LNADW may increase the variance explained by the first mode, since this mode explains anomalies originating from the North Atlantic and is more dominant in the deeper layers. Future research should also be carried out using sensitivity experiments and observations to understand the evolution of this deep water mass over a range of time scales and under different climate change scenarios. This is important because CDW is a key component of the global ocean thermohaline circulation, interacting with our climate on long time scales, and influencing the ocean's large-scale redistribution of heat, salt, carbon and nutrients.

APPENDIX

Along-isobar, isopycnal, and heave components of $\theta - S$ changes

a. Heat and salt budget analysis

This section describes the heat-salt budget calculation along isopycnal layers. Referring to Fig. A1, we first consider a volume of fluid with property ϕ (i.e., θ or S) at year $t = n - 1$ along an isopycnal surface at depth $z = h|^{t=n-1}$, where we use $|_{\sigma}^{t=n}$ and $|_{z}^{t=n}$ notations hereafter to denote along-isopycnal and along-isobar processes, respectively, at year $t = n$. As heat and salt fluxes act upon the fluid volume at an isopycnal depth, the property in the following year changes to $\phi|_{z}^{t=n}$ at that depth level while the isopycnal surface has been vertically displaced. The

heat and salt storage rates at a fixed depth at time $t = n$ can be approximately expressed as a function of the advection and total mixing terms:

$$\begin{aligned} \phi_t|_z^{t=n} &= \frac{\phi|_z^{t=n} - \phi|_\sigma^{t=n-1}}{\Delta t} \\ &= -\boldsymbol{u} \cdot \bigtriangledown_\sigma \phi|^{t=n-1} + \phi'_{mix}|^{t=n-1} \ , \end{aligned} \tag{A1}$$

where $\Delta t = 1$ yr, the subscript t denotes the differentiation with respect to time, and $\bigtriangledown_\sigma$ denotes the gradient operator *tracking* along the isopycnal surface. Note that the horizontal advection is calculated based on $\theta - S$ gradients along isopycnals, but the *total* velocities $\boldsymbol{u}$ contain both along-isopycnal and diapycnal components (Bennett 1986). In the ocean interior, the diapycnal components of u and v are much smaller than the along-isopycnal components (Bennett 1986). Thus, diapycnal fluxes are mainly a result of vertical advection which is comparable in magnitude to the horizontal advection due to the much larger vertical than the horizontal $\theta - S$ gradients (McDougall 1984). A change in $\theta - S$ along isobars results in a net shift of buoyancy, which then causes the isopycnal to shoal or deepen, taking a new property $\phi|_\sigma^{t=n}$. Changes along isobars are composed of changes along isopycnals as well as those due to the vertical movement of the isopycnals [Bindoff and McDougall 1994; their Eq. (1)]. The change in along-isopycnal $\theta - S$ with time can be equivalently expressed in terms of $\theta - S$ changes along isobars with an additional term accounting for the $\theta - S$ difference at the old and new isopycnal depths (the so-called 'heave' effect; see also Fig. A2):

$$\phi_t|_\sigma = \phi_t|_z + \phi_t|_{heave} \ , \tag{A2}$$

where the heave-effect term is essentially

$$\phi_t|_{heave} = \left(\frac{h|^{t=n} - h|^{t=n-1}}{\Delta t} \right) \cdot \left(\frac{\phi|_\sigma^{t=n} - \phi|_z^{t=n}}{h|^{t=n} - h|^{t=n-1}} \right) \ .$$

Using the equations above, the heat and salt storage rates along isopycnals can be

written as:

$$\theta_t|_\sigma = -(u\theta_x + v\theta_y + w\theta_z) + \theta'_{mix} + \theta_t|_{heave} \quad \text{(A3)}$$

$$S_t|_\sigma = -(uS_x + vS_y + wS_z) + S'_{mix} + S_t|_{heave} \ , \quad \text{(A4)}$$

where the first term of the right hand side of Eqs. (A3) and (A4) shows the zonal, meridional, and vertical components of the advective flux. The heave term is necessary to balance the *total* advective flux which also contains diapycnal components [c.f. McDougall 1984; his Eqs. (1), (2)]. The same calculation as given above is repeated for each consecutive year over the 1000-yr model integration.

b. Visualizing the heat-salt content terms

Inspired by the work of Bindoff and McDougall (1994), we present here a simple method to visualise the heat-salt storage rate, or content terms in Eq. (A2) over the whole 1000 years of the model run. We first consider the linearised equation of state and its time derivative:

$$\rho = \rho_r \left[1 - \alpha(\theta - \theta_r) + \beta(S - S_r)\right] \quad \text{(A5)}$$

$$\rho_r^{-1}\rho_t = -\alpha\theta_t + \beta S_t \ , \quad \text{(A6)}$$

where ρ_r is density at a reference pressure p_r (i.e., ρ_r =1036.75 kg m^{-3} for σ_{UCDW} and 1036.85 kg m^{-3} for σ_{LCDW} at $p_r = 2000$ db); θ_r and S_r are the reference potential temperature and salinity for the corresponding layer; and α and β are the thermal and haline expansion coefficients at p_r respectively. The influence of heat and salt changes on density is inferred by Eq. (A6), and thus their proportional contribution to changes in density can be deduced by the stability ratio:

$$R_\rho = \frac{\alpha\theta_t}{\beta S_t} \ . \quad \text{(A7)}$$

For example, when warming has a more prominent effect than salination in altering density, R_ρ will be greater than 1. This scenario can be visualised by plotting

$\alpha\theta_t = R_\rho \beta S_t$ (Fig. A2). Note that R_ρ equals 1 for along-isopycnal $\theta - S$ fluctuations as there is no change in density [i.e., $\rho_t|_\sigma$ is always 0; see Eq. (A8)]. Furthermore, it can be shown from the equations above and Eq. (A2) that

$$\rho_t|_\sigma = \rho_t|_z + \rho_t|_{heave} \ , \tag{A8}$$

which implies that density fluctuations along isobars are accompanied by vertical excursions of the isopycnal surface such that density is conserved (i.e., $\rho_t|_\sigma = 0$; marked by $R_\rho = 1$ in Fig. A2).

Although the stability ratio R_ρ reveals the competing contribution of heat and salt changes on density, it does not provide information on the sign of the $\theta - S$ change (i.e., whether the change is related to warming−salination, or warming−freshening, and so on). For this purpose, we use the Turner angle (Tu):

$$Tu = \tan^{-1}(R_\rho) \ , \tag{A9}$$

first described in Ruddick (1983) for diagnosing static stability of the water column due to mixing and stirring (see also e.g., May and Kelley 2002). Tu is used here in terms of density stability as a result of $\theta - S$ temporal evolution. The convention of Tu is shown in Fig. A3 for defining stability quadrants. Density increases occur in the quadrants below the line $R_\rho = 1$; density decreases occur above this line (the quadrants are bound by the lines $R_\rho = \pm 1$). Note that $Tu = 90°$ and $Tu = -90°$ ($R_\rho = \pm\infty$) denote pure warming and pure cooling, and $Tu = 0°$ and $Tu = -180°$ ($R_\rho = 0$) denote pure salination and pure freshening, respectively. The subscripts θ and S in each sector indicate the dominance of either heat or salt on buoyancy. For example, if $\theta - S$ change lies in the WS_θ sector, this denotes that the warming-salination that has occured is dominated by the change in temperature.

The focus of the heat-salt budget analyses described in section a is on the along-isopycnal component. Furthermore, since the sign of the heat and salt content

terms along isopycnals are either both positive (warming-salination) or both negative (cooling-freshening), the visualisation can be presented in terms of either of these two cases. Figure A4 presents the plot of the heat-salt content terms that correspond to warming-salination along the isopycnals for σ_{UCDW} at R1−R4 (see Fig. A6 for R1−R4 locations). The plots for σ_{LCDW} are presented in Fig. A5. The along-isobar and along-isopycnal components are marked with dots and crosses respectively in the top row of the figures, and the corresponding heave-effect component in the bottom row. It can be noted that the along-isopycnal component lies along $R_\rho = 1$ at $Tu = 45°$. Of course, the along-isobar and heave-effect components can occur outside the WS quadrant even when warming-salination occurs along-isopycnal (e.g., Fig. A2). Together with the heat-salt budget analyses, this visualisation method aids with the interpretation of the processes giving rise to the $\theta - S$ variability structure shown in Fig. 6.

c. Heat-salt budget across the ACC

The heat-salt budget analyses are presented along a transect on σ_{UCDW} of the Southern Ocean, passing through R1−R4 (Fig. A6). The standard deviations of the heat-salt content and advection terms along the transect are presented in Fig. A7 [refer to Eqs. (A3), (A4) for the budget equations]. The size of the along-isopycnal variations at R1 (southwestern Atlantic, near the BMCZ) is much larger than that of the heave variations, indicating that only small density variations occur along isobars (Fig. A7a, b). This is confirmed in Fig. A4 showing variations clustered around $Tu = 45°$ in the WS quadrant. Thus, horizontal advection is likely to play a dominant role at R1, since horizontal advection mainly moves fluid along isopycnals. In fact, the meridional advection is shown in Fig. A7c, d to be the dominant term in the South Atlantic and is connected to the along-isopycnal $\theta - S$ variations,

as suggested by the significant correlation in Fig. A8a, b. The influence of the meridional advection decreases into the Indian and Pacific, while the contribution of the zonal advection on the along-isopycnal heat-salt variations becomes more prominent (Fig. A8a, b).

As the magnitude of the along-isopycnal variations becomes smaller compared to the heave variations at R2−R4 (Indian−Pacific), the variations along isobars are seen to be distributed outside the WS quadrant, indicating greater variations in buoyancy (Fig. A4). The vertical advection term is dominant at these locations (Fig. A7c, d) injecting fluid of different densities into the CDW layer. Referring to Fig. A4, the variation spread on σ_{UCDW} at these three locations are seen in the WF and CS quadrants. This can be explained by the $\theta - S$ vertical structure in Fig. A9 in which vertical fluxes inject warmer and fresher water from above, and cooler and more saline water from below, into the σ_{UCDW} surface (refer to Fig. 3 for the definition of the σ_{UCDW} surface). In the process, the vertical displacement of σ_{UCDW} tends to damp the excessive heat content and amplifies the degraded salt content due to the vertical injection. This can be seen in the correlations between the along-isopycnal heat-salt content terms and the heave-effect terms (Fig. A8c, d). Thus, the heave effect modulates the influence of vertical fluxes such that the along-isopycnal heat-salt contents are preserved. The effect of heave on the along-isopycnal variations would be more significant when the vertical $\theta - S$ gradients are density-compensating with large vertical salinity gradient such that S drives the buoyancy perturbation (see also Yeager and Large 2004). Although the vertical $\theta - S$ gradients are of the same sign in the LCDW layer (Fig. A9), θ is more prominent than S on buoyancy (Fig. A4), thus heaving likely acts to damp the vertical fluxes and contributes little to along-isopycnal variability. The vertical $\theta - S$ gradients in the UCDW layer also tend to inhibit the effect of heaving to introduce changes

along isopycnals.

The large along-isopycnal heat-salt content variations at 170°E−160°W (Fig. A7a, b) coincide with the large $\theta - S$ variance seen in the South Pacific in the EOF1 and 3 modes for σ_{UCDW} (Fig. 9). In this region, the standard deviations in the zonal and vertical advective fluxes are large (Fig. A7c, d). However, only the zonal advection term is significantly correlated to the heat-salt content terms (Fig. A8a, b). The $\theta - S$ variability in this region is thus controlled by the zonal advective flux driven by $\theta - S$ gradients rather than the ACC (Fig. A8e; Fig. not shown for S). Furthermore, since this large variability in the South Pacific does not extend down to the LCDW layer (Fig. 7), it is likely that the source of this variability is from the AAIW layer via diapycnal mixing. Note that Fig. A7e, f show large mixing variability in the South Pacific as well as at R1 in the BMCZ. The mixing variability in the South Pacific is in the vertical, whereas it is meridional at the BMCZ. This is consistent with the above physical interpretations.

Table captions

Table 1: Correlation coefficients between the variables used for discussion in section 5a. The time lags mark when the correlations are at a maximum. The correlation is significant at the 95% confidence level when it is above the coefficient displayed within the square brackets. The significant level values are calculated based on the effective degree of freedom described in Sciremammano (1977). The whole 1000-yr data set is used to calculate the correlations. NADW formation denotes the maximum meridional overturning in the North Atlantic. NADW outflow denotes the maximum meridional overturning in the South Atlantic at about 33°S. The ACC is calculated as the integrated zonal transport across the Drake Passage. NA and SA density is defined as the spatially averaged density at 1720-m depth in the North Atlantic (49°N−62°N, 56°W−22.5°W) and in the Weddell Sea (59°S−72°S, 51°W−28°W), respectively. V^{E}_{TS95} is the zonal integrated Ekman transport according to Toggweiler and Samuels (1995) across the Southern Ocean at the latitude of the tip of South America; i.e., $V^{E}_{TS95} = \oint \tau^{x}(\rho f)^{-1} dx$. $\int_{Nof03}$ is the zonal wind integrated transport according to Nof (2003), along an integration path connecting the southern tips of South America, South Africa, and South Australia; i.e., $\int_{Nof03} = \oint \tau^{l}(\rho f)^{-1} dl$, where l denotes the component along the path. Here, ρ is density and f is the Coriolis parameter.

Table 2: Standard deviations (S.D.) of heat budget terms and correlation coefficients for all terms versus heat-content averaged over the Brazil-Malvinas Confluence Zone (BMCZ; 28°W−45°W, 36.6°S−46.2°S; see Fig. 16 for the location). The values are presented for both σ_{UCDW} and σ_{LCDW} in the left and right portions, respectively. Correlation coefficients are shown for 1000 years of model data. The correlation values are significant above $\approx 0.06 - 0.12$

at 95% significance level. The significant level values vary slightly across e ach analysis due to varying effective degrees of freedom (Sciremammano 1977). The standard deviations are calculated for each grid box before spatial averaging. Correlation coefficients are calculated using the spatially averaged variables. Refer to Eq. (A3) for the heat budget equation. The highest standard deviation and correlation values for the advective terms are highlighted in bold-face type.

Table 3: The same as Table 2 but for the salt budget terms in the BMCZ. Refer to Eq. (A4) for the salt budget equation analysed.

Figure captions

Figure 1: Zonally averaged salinity fields below 545 m in the Atlantic, Indian, and Pacific sectors in the model (left column) and Levitus et al. (1994; right column). The σ_2 isopycnal surfaces are shown by the thick dashed contours. The UCDW and LCDW in the model are analysed along isopycnal layers bounded by $\sigma_2 = 36.70 - 36.80$ and $36.80 - 36.90$ kg m^{-3}, respectively. The σ_2 layers in the observed field at isopycnal depths matching the model's isopycnal layers are included in the second column.

Figure 2: Atlantic meridional overturning (Sv) averaged over 1000 model years. The bold dashed contours mark the $\sigma_2 = 36.70 - 36.80$ and $\sigma_2 = 36.80 - 36.90$ kg m^{-3} layers. Contour interval for the meridional overturning is 2 Sv.

Figure 3: Definition of Circumpolar Deep Water layers used in the model analysis. Linear interpolation and averaging are applied for each layer wherever the upper boundary is below 1000-m depth. The core surfaces are labelled as σ_{UCDW} and σ_{LCDW}, respectively.

Figure 4: Mean potential temperature and salinity along σ_{UCDW} in (a) the model and (b) the observed Levitus (1994) and Levitus et al. (1994) climatology. The potential temperature contour interval is 0.15°C. The isopycnal layer is defined over a complete set of discrete σ_2 values with interval of 0.01 kg m^{-3} from $36.70 - 36.80$ kg m^{-3} inclusive for the model data, and $36.80 - 36.94$ kg m^{-3} for the observed data (see Figs. 1, 3). The colour scale for the model output shown in (a) has been adjusted to match the salinity range of the observed (b), however, there remains an offset in the salinity scale in (a) and (b). (c) Mean circulation on σ_{UCDW}. To enhance visibility of the circulation features at depth, the current vectors have been rescaled by $|\log_{10}(\text{speed})|+0.1$.

The mean isopycnal depths are shown by the colour-scaled contours in (c). The locations R1−R4 are marked with filled magenta circles.

Figure 5: As for Fig. 4 only for σ_{LCDW}. Figure 1 shows the layer definition for σ_{LCDW} in the model and observed (see also Fig. 3).

Figure 6: Model 1000-yr $\theta - S$ scatter plots on isopycnal surfaces (crosses) at the specified locations shown in Figs. 4c, 5c (marked as R1−R4) on σ_{UCDW} (left column) and σ_{LCDW} (right column). The corresponding $\theta - S$ properties at fixed depths (taken as the mean depth of the isopycnal layer) are marked with dots.

Figure 7: Standard deviation of salinity (psu) on (a) σ_{UCDW} and (b) σ_{LCDW}.

Figure 8: Percentage of variance explained by each EOF salinity mode in (a) σ_{UCDW} (solid curve) and (b) σ_{LCDW} (dashed curve). The error bars indicate the estimated sampling error for the eigenvalues computation (North et al. 1982). Overlapping error bars between adjacent EOF modes imply modal mixing according to the North et al. criterion. This implies that modes above EOF3 are degenerate.

Figure 9: Spatial maps of the first three EOF modes of salinity on σ_{UCDW} (upper panels) and σ_{LCDW} (lower panels), accounting 68% and 82% of the total S variance, respectively. The values of the eigenvectors have been normalized to unity so that the spatial maps span values between -1 and 1, and hence the principal components (Fig. 10, left column) correspond to the actual magnitude of the variability associated with each mode. The box in the EOF2 map indicates the Brazil-Malvinas Confluence Zone (BMCZ).

Figure 10: Principal component time series of EOF1−3 (PC1 − 3; left column) and the corresponding power spectral density (right column) for σ_{UCDW} (thin

solid line) and σ_{LCDW} (thick solid line). A $\log_{10}$ scale is used in frequency to give more weight to the higher frequency signals and the power spectra are multiplied by frequency to preserve variance.

Figure 11: (a) Spatial maps of the first three complex EOF (CEOF) modes of salinity on σ_{UCDW} shown at 90° phase intervals. The three modes account for $\approx$ 76% of the total salinity variance with CEOF1, CEOF2, and CEOF3 accounting for 44%, 21%, and 10%, respectively. (b) Spatial phase angle for CEOF1−3 indicating the direction of propagation at increasing angle. Phase discontinuities occur at $360° - 0°$ as the phase is defined only between 0° to 360°.

Figure 12: Timeseries of PC1 and box-averaged salinity anomalies at S_{NA}, S_{SA} (defined over the regions indicated at left) in (a) σ_{UCDW} and (b) σ_{LCDW}. Correlation coefficients between the variables are shown in (c) for σ_{UCDW} and (d) σ_{LCDW}. The corresponding 95% confidence levels are also shown for each analysis (the significance curves for S_{NA} vs PC1 and S_{NA} vs S_{SA} are nearly identical).

Figure 13: Correlation maps between global salinity fields and the box-averaged salinity at S_{NA} (indicated by the boxed region) on σ_{UCDW} at different time lags (20-yr interval), showing a propagation of salinity anomaly in outflowing NADW. Correlation coefficients are not shown when they fall below the 95% significance level. Note that the significance level increases with increasing time lags.

Figure 14: Time-series maps of salinity anomaly on a meridional-vertical plane along the Atlantic western boundary (see Fig. 15 for the section location). The dashed contours mark the position of the UCDW and LCDW layers. The

time interval is 42 yr. The color scheme is set to span ± 0.02 psu to enhance the visibility of anomalies at depth. The largest anomaly magnitude is ≈ 0.07 psu which occurs at the surface.

Figure 15: Composite maps of salinity anomaly on a meridional-vertical plane along the Atlantic western boundary shown in the upper-left inset, defined for anomalously (a) high NADW formation rate, and (b) low NADW formation rate. The NADW formation rate is defined as the maximum North Atlantic overturning strength. Extreme years are defined as one standard deviation unit above and below the long-term mean. The timeseries of NADW formation rate is shown in the upper-right inset. The dashed contours mark the position of the UCDW and LCDW layers.

Figure 16: Lagged-composite maps of salinity anomaly on a meridional-vertical plane along the Atlantic western boundary shown in Fig. 15, defined for anomalously high NADW formation rate (see Fig. 15 caption for definition). The time lags are presented at a 10-yr interval starting from 50 years prior to high NADW overturning. The map at 0-yr time lag is essentially the same as in Fig. 15a.

Figure 17: Spatial thermohaline variation of (a) total density, (b) temperature component, and (c) salinity component at 1720-m depth. The total density is derived from the linearised equation of state $\rho = \rho_r \left[1 - \alpha \left(\theta - \theta_r\right) + \beta \left(S - S_r\right)\right]$, where the subscript r denotes a reference value. Dashed (solid) contour indicates negative (positive) density anomaly. The boxed region marks the Brazil-Malvinas Confluence Zone (BMCZ).

Figure 18: Velocity vectors for (a) the mean circulation, (b) composite map of current velocity anomaly on σ_{UCDW} defined for extreme warm-saline years and

(c) cold-fresh years. The extreme events are defined as those above (below) 1 standard deviation unit for the warm-saline (cold-fresh) years. The dashed box in (a) indicates the location of the BMCZ. Solid boxes in (a) indicate the regions defined for averaged values of the DWBC meridional velocity (v_{DWBC}) and the meridional component of the Malvinas Current (v_{MC}).

Figure 19: Spectral analyses for the meridional components of the DWBC (v_{DWBC}) and the Malvinas Current (v_{MC}). Shown are (a) the coherence spectra, (b) the cross spectra, and (c) the phase for the σ_{UCDW} (solid curve) and σ_{LCDW} (dash-dot curve).

Figure A1: Heat-salt budget scheme of Eqs. (A2)−(A4) in the text showing the case of an isopycnal surface deepening at year n relative to year $n-1$ and shoaling at year $n+1$ relative to year n. Advective fluxes upon the fluid cause changes of $\theta - S$ properties at a fixed depth, resulting in the displacement of the isopycnal surface (heave).

Figure A2: $\theta - S$ changes along an isobar, along an isopycnal, and across depths due to heaving of isopycnals in $\beta S_t - \alpha\theta_t$ space.

Figure A3: Quadrants defined by the Turner Angle (Tu) where heat-salt storage changes are shown in $\alpha\theta_t - \beta S_t$ space. The quadrants bound by the lines $R_\rho = 1$ and $R_\rho = -1$ indicate which of θ and S dominates in the resulting density changes. The line $R_\rho = 1$ indicates perfect density compensating variations of $\theta - S$. The line $R_\rho = -1$ indicates density instability as $\theta - S$ changes are out of phase.

Figure A4: Along-isopycnal warming and salination case in $\beta S_t - \alpha\theta_t$ space at R1−R4 along σ_{UCDW} over the 1000-yr model data in terms of Turner Angle (refer to Fig. A3). The along-isobar (black dots) and along-isopycnal (grey

crosses) variations are presented together in the top row. The corresponding heave-effect variations are displayed in the bottom row. The locations of R1−R4 are shown in Fig. A6 (also Fig. 4c). The abbreviations WF, WS, CS, CF indicate the signs of $\theta - S$ change, corresponding to warming-freshening, warming-salination, cooling-salination, and cooling-freshening, respectively.

Figure A5: The same as Fig. A4 but for σ_{LCDW}.

Figure A6: Transect across the Southern Ocean where the heat-salt budget analyses of Figs. A7, A8 are conducted. The locations labeled R1−R4 are taken as examples for discussion, and corresponds to R1−R4 used throughout the text and shown in Figs. 4c, 5c.

Figure A7: Standard deviations of (a) heat content terms, (b) salt content terms, (c) heat advection terms, (d) salt advection terms, (e) heat mixing terms, and (f) salt mixing terms. See the text for definition of the respective terms.

Figure A8: Correlation coefficients for (a) heat advection terms versus $\theta_t|_\sigma$, (b) salt advection terms versus $S_t|_\sigma$, (c) $\theta_t|_{heave}$ versus $w\theta_z$ and $\theta_t|_\sigma$, (d) $S_t|_{heave}$ versus wS_z and $S_t|_\sigma$, (e) zonal heat advection term ($u\theta_x$) versus θ_x and u, and (f) meridional heat advection term ($v\theta_y$) versus θ_y and v. Correlation coefficients which are not significant above the 95% confidence level are not displayed.

Figure A9: Temperature-salinity vertical profiles at R1−R4. The locations of R1−R4 are shown in Fig. A6.

Table 1. Correlation coefficients between the variables used for discussion in section 5a. The time lags mark when the correlations are at a maximum. The correlation is significant at the 95% confidence level when it is above the coefficient displayed within the square brackets. The significant level values are calculated based on the effective degree of freedom described in Sciremammano (1977). The whole 1000-yr data set is used to calculate the correlations. NADW formation denotes the maximum meridional overturning in the North Atlantic. NADW outflow denotes the maximum meridional overturning in the South Atlantic at about 33°S. The ACC is calculated as the integrated zonal transport across the Drake Passage. NA and SA density is defined as the spatially averaged density at 1720-m depth in the North Atlantic (49°N−62°N, 56°W−22.5°W) and in the Weddell Sea (59°S−72°S, 51°W−28°W), respectively. V^{E}_{TS95} is the zonal integrated Ekman transport according to Toggweiler and Samuels (1995) across the Southern Ocean at the latitude of the tip of South America; i.e., $V^{E}_{TS95} = \oint \tau^{x}(\rho f)^{-1} dx$. $\int_{Nof03}$ is the zonal wind integrated transport according to Nof (2003), along an integration path connecting the southern tips of South America, South Africa, and South Australia; i.e., $\int_{Nof03} = \oint \tau^{l}(\rho f)^{-1} dl$, where l denotes the component along the path. Here, ρ is density and f is the Coriolis parameter.

		Maximum correlation coefficient	Time lag (year)
ACC	NADW outflow	0.17 [0.12]	1
ACC	NADW formation	0.17 [0.16]	54
NADW formation	NA density	0.60 [0.25]	1
ACC	Weddell Sea density	0.55 [0.20]	1
NADW formation	V^{E}_{TS95}	0.09 [0.06]	11
NADW outflow	V^{E}_{TS95}	0.14 [0.06]	1
NADW formation	$\int_{Nof03}$	0.10 [0.06]	12
NADW outflow	$\int_{Nof03}$	0.24 [0.07]	0

Table 2. Standard deviations (S.D.) of heat budget terms and correlation coefficients for all terms versus heat-content averaged over the Brazil-Malvinas Confluence Zone (BMCZ; 28°W−45°W, 36.6°S−46.2°S; see Fig. 16 for the location). The values are presented for both σ_{UCDW} and σ_{LCDW} in the left and right portions, respectively. Correlation coefficients are shown for 1000 years of model data. The correlation values are significant above $\approx 0.06-0.12$ at 95% significance level. The significant level values vary slightly across each analysis due to varying effective degrees of freedom (Sciremammano 1977). The standard deviations are calculated for each grid box before spatial averaging. Correlation coefficients are calculated using the spatially averaged variables. Refer to Eq. (A3) for the heat budget equation. The highest standard deviation and correlation values for the advective terms are highlighted in bold-face type.

				σ_{UCDW}				σ_{LCDW}
Budget terms	S.D. ($\times 10^{-10}$ °C s^{-1})	Correlation coefficients			S.D. ($\times 10^{-10}$ °C s^{-1})	Correlation coefficients		
		$\theta_t\|_\sigma$	$\theta_t\|_z$	$\theta_t\|_{heave}$		$\theta_t\|_\sigma$	$\theta_t\|_z$	$\theta_t\|_{heave}$
$\theta_t\|_\sigma$	1.73	1	0.93	-0.50	1.09	1	0.73	-0.35
$\theta_t\|_z$	2.28	0.93	1	-0.78	2.25	0.73	1	-0.90
$\theta_t\|_{heave}$	1.12	-0.50	-0.78	1	1.74	-0.35	-0.90	1
$u\theta_x$	1.55	-0.31	-0.23	0.03	0.85	-0.37	-0.22	0.06
$v\theta_y$	**1.60**	**-0.63**	**-0.54**	0.22	1.02	**-0.59**	-0.37	0.13
$w\theta_z$	1.03	-0.17	-0.34	**0.53**	**1.45**	-0.14	**-0.48**	**0.57**
θ'_{mix}	1.22	0.09	0.15	-0.20	0.73	0.06	0.13	-0.14

Table 3. The same as Table 2 but for the salt budget terms in the BMCZ. Refer to Eq. (A4) for the salt budget equation analysed.

				σ_{UCDW}				σ_{LCDW}
Budget terms	S.D. ($\times 10^{-11}$ psu s^{-1})	Correlation coefficients			S.D. ($\times 10^{-11}$ psu s^{-1})	Correlation coefficients		
		$S_t\|_\sigma$	$S_t\|_z$	$S_t\|_{heave}$		$S_t\|_\sigma$	$S_t\|_z$	$S_t\|_{heave}$
$S_t\|_\sigma$	3.20	1	0.85	0.28	1.92	1	0.92	-0.34
$S_t\|_z$	3.19	0.85	1	-0.26	2.40	0.92	1	-0.68
$S_t\|_{heave}$	1.37	0.28	-0.26	1	1.11	-0.33	-0.68	1
uS_x	2.81	-0.31	-0.33	0.02	1.48	-0.37	-0.31	0.05
vS_y	**2.98**	**-0.63**	**-0.61**	-0.04	**1.82**	**-0.58**	**-0.50**	0.12
wS_z	1.29	0.17	-0.10	**0.49**	0.83	-0.17	-0.37	**0. 56**
S'_{mix}	2.06	0.09	-0.04	0.25	1.29	0.06	0.10	-0.13

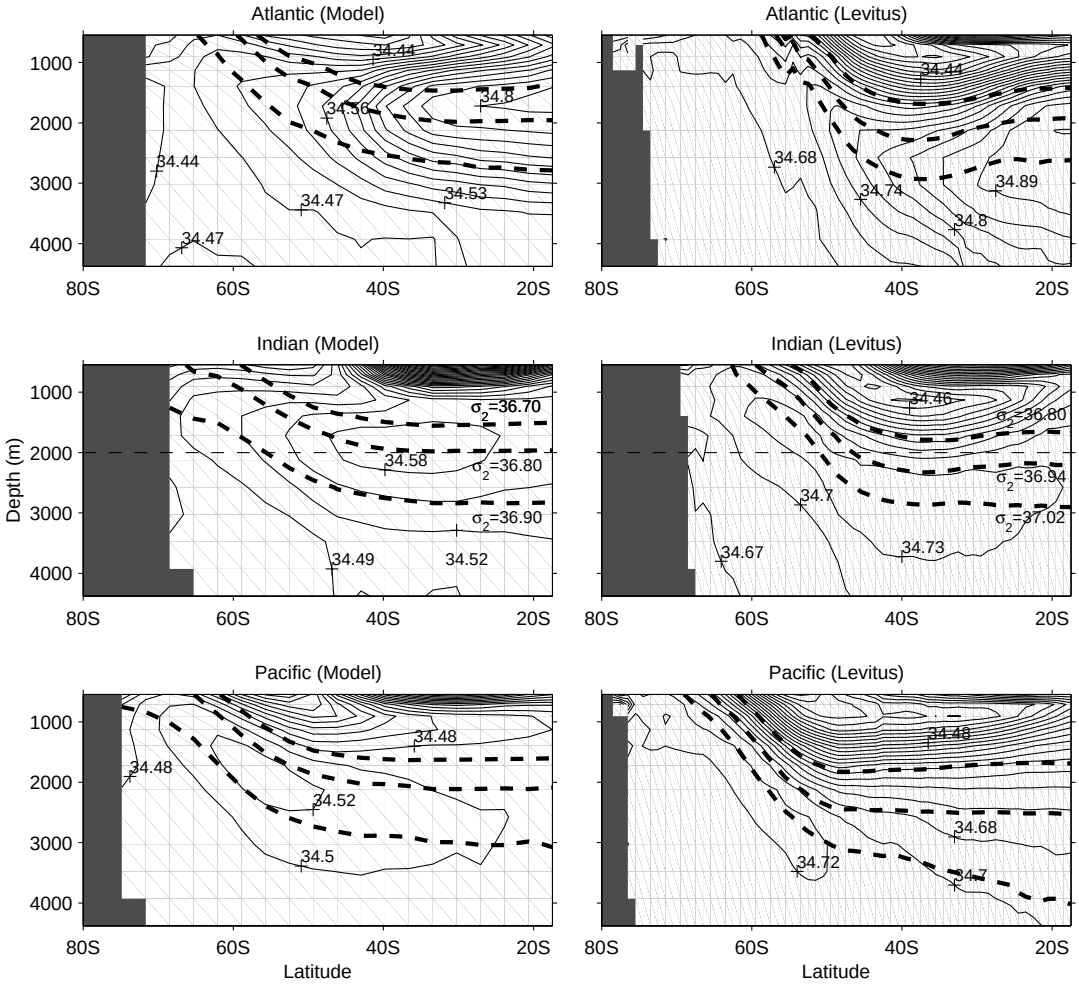

Figure 1: Zonally averaged salinity fields below 545 m in the Atlantic, Indian, and Pacific sectors in the model (left column) and Levitus et al. (1994; right column). The σ_2 isopycnal surfaces are shown by the thick dashed contours. The UCDW and LCDW in the model are analysed along isopycnal layers bounded by $\sigma_2 = 36.70 - 36.80$ and $36.80 - 36.90$ kg m^{-3}, respectively. The σ_2 layers in the observed field at isopycnal depths matching the model's isopycnal layers are included in the second column.

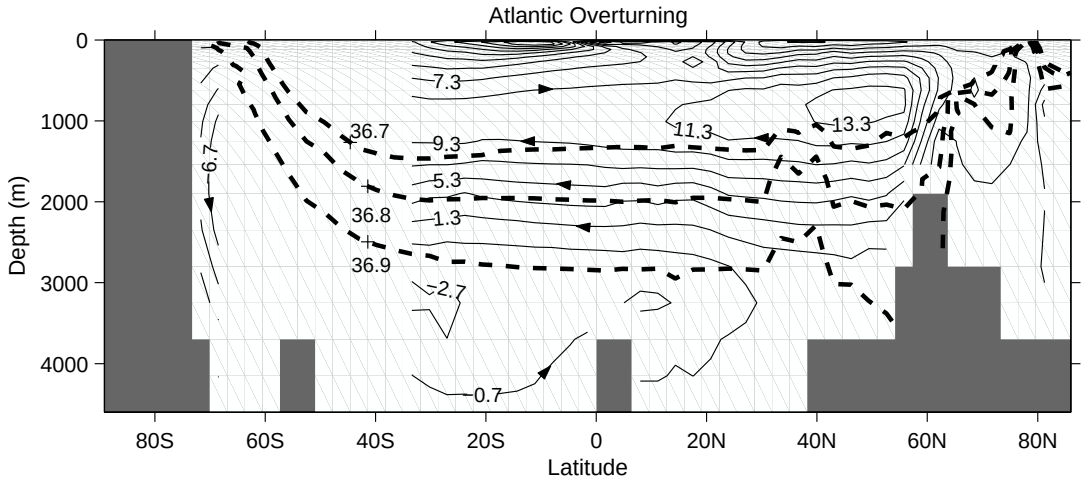

Figure 2: Atlantic meridional overturning (Sv) averaged over 1000 model years. The bold dashed contours mark the $\sigma_2 = 36.70 - 36.80$ and $\sigma_2 = 36.80 - 36.90$ kg m^{-3} layers. Contour interval for the meridional overturning is 2 Sv.

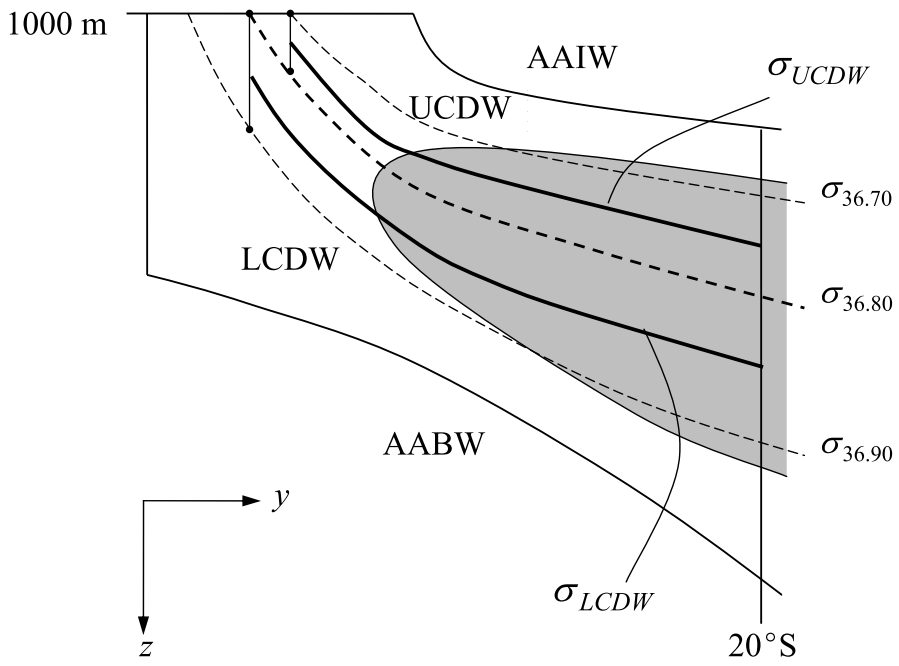

Figure 3: Definition of Circumpolar Deep Water layers used in the model analysis. Linear interpolation and averaging are applied for each layer wherever the upper boundary is below 1000-m depth. The core surfaces are labelled as σ_{UCDW} and σ_{LCDW}, respectively.

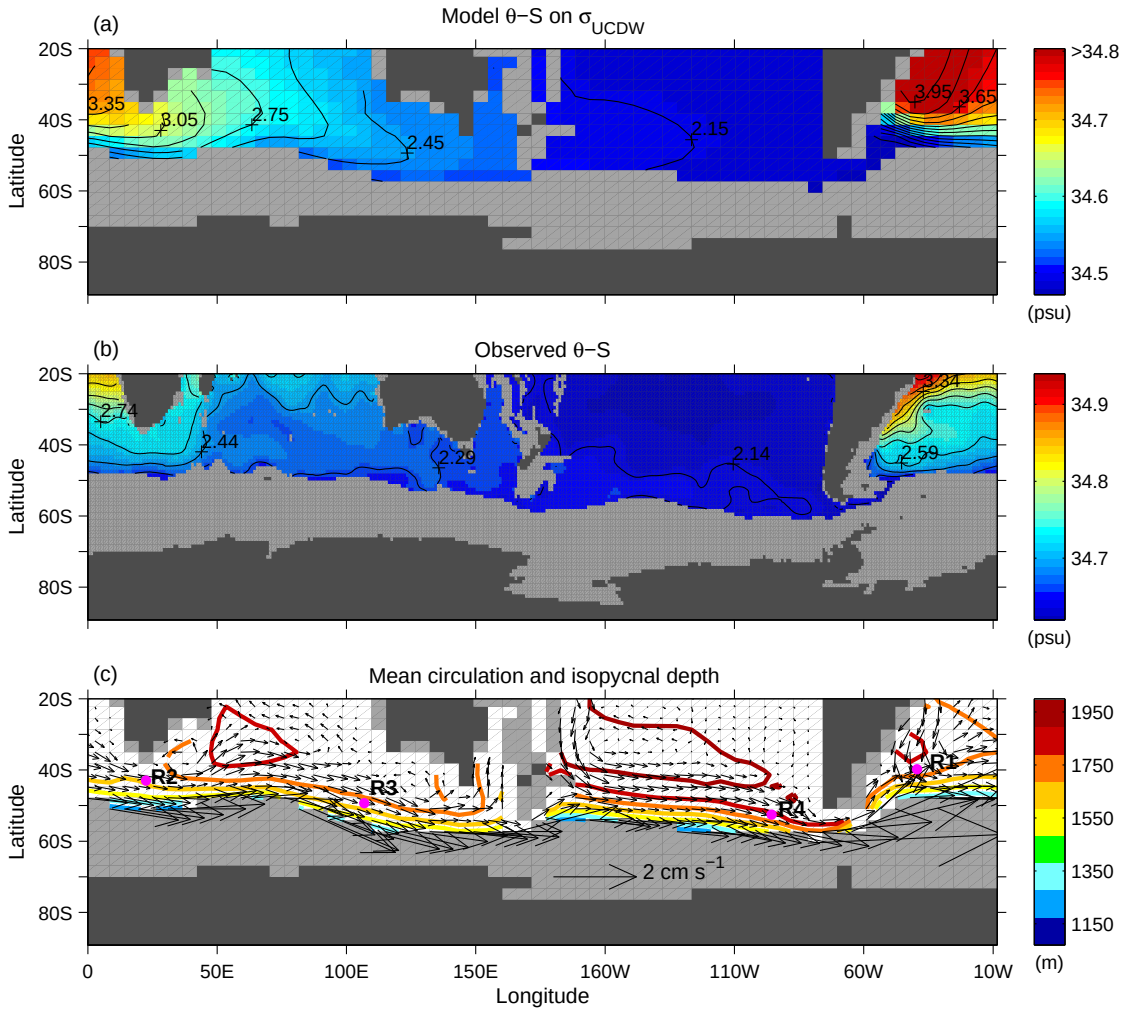

Figure 4: Mean potential temperature and salinity along σ_{UCDW} in (a) the model and (b) the observed Levitus (1994) and Levitus et al. (1994) climatology. The potential temperature contour interval is 0.15°C. The isopycnal layer is defined over a complete set of discrete σ_2 values with interval of 0.01 kg m^{-3} from $36.70 - 36.80$ kg m^{-3} inclusive for the model data, and $36.80 - 36.94$ kg m^{-3} for the observed data (see Figs. 1, 3). The colour scale for the model output shown in (a) has been adjusted to match the salinity range of the observed (b), however, there remains an offset in the salinity scale in (a) and (b). (c) Mean circulation on σ_{UCDW}. To enhance visibility of the circulation features at depth, the current vectors have been rescaled by $|\log_{10}(\text{speed})|+0.1$. The mean isopycnal depths are shown by the colour-scaled contours in (c). The locations R1−R4 are marked with filled magenta circles.

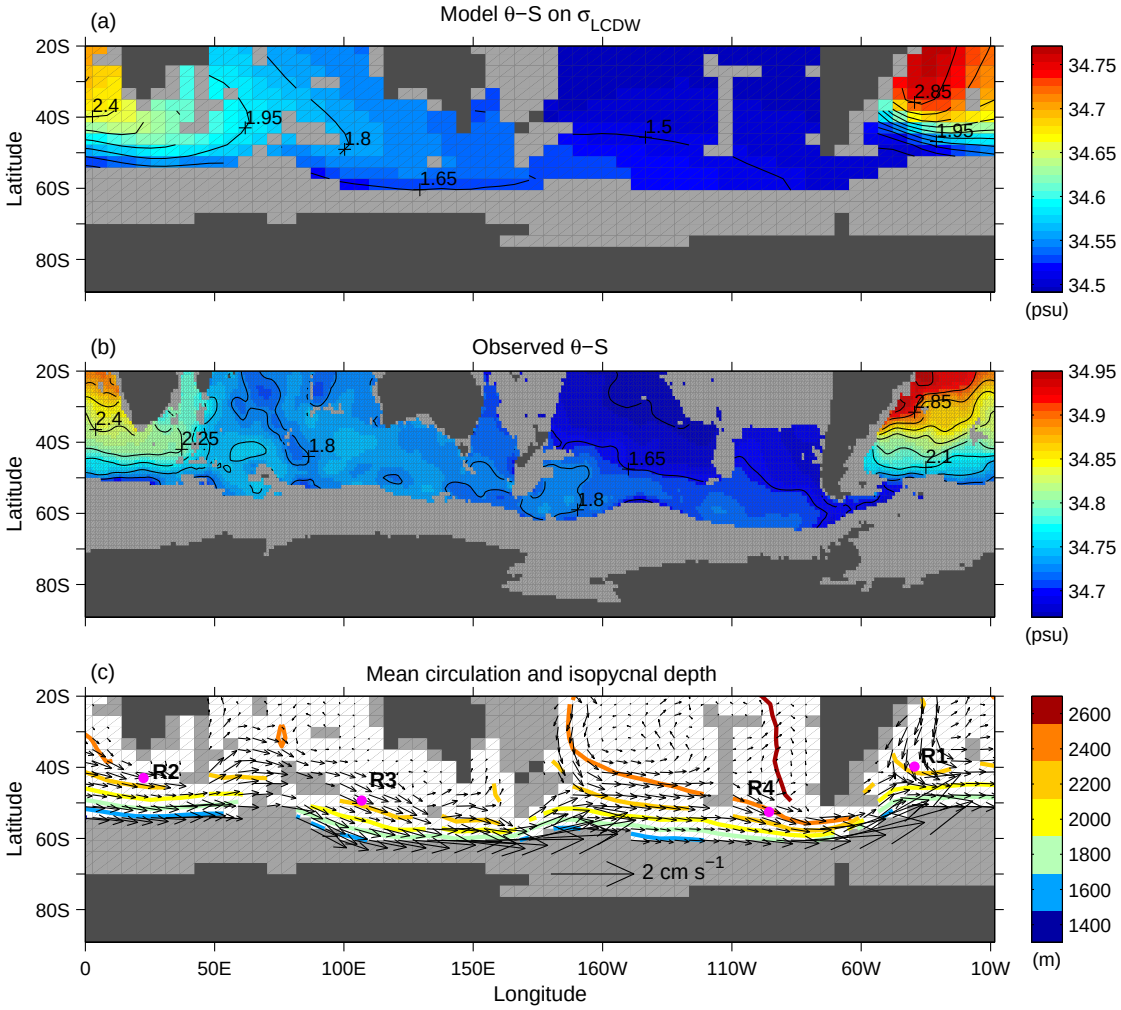

Figure 5: As for Fig. 4 only for σ_{LCDW}. Figure 1 shows the layer definition for σ_{LCDW} in the model and observed (see also Fig. 3).

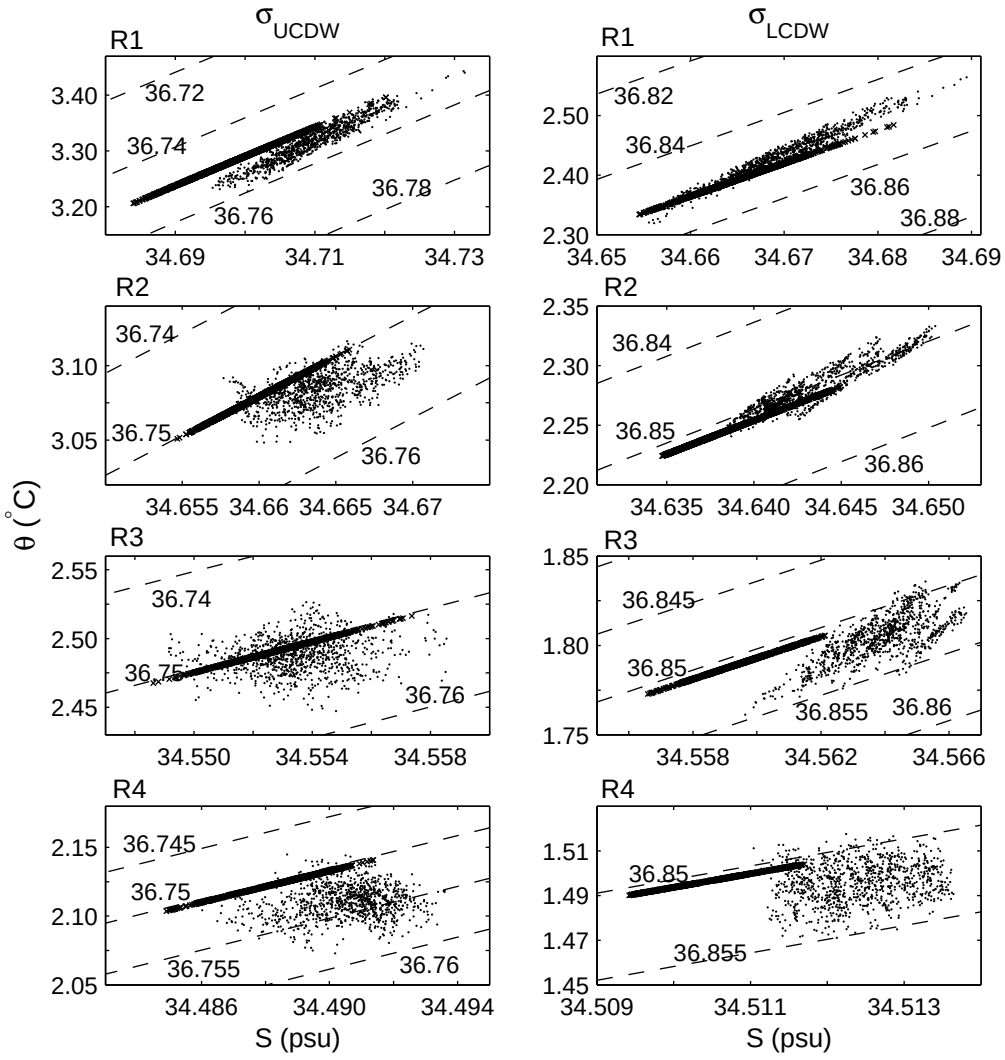

Figure 6: Model 1000-yr $\theta - S$ scatter plots on isopycnal surfaces (crosses) at the specified locations shown in Figs. 4c, 5c (marked as R1−R4) on σ_{UCDW} (left column) and σ_{LCDW} (right column). The corresponding $\theta - S$ properties at fixed depths (taken as the mean depth of the isopycnal layer) are marked with dots.

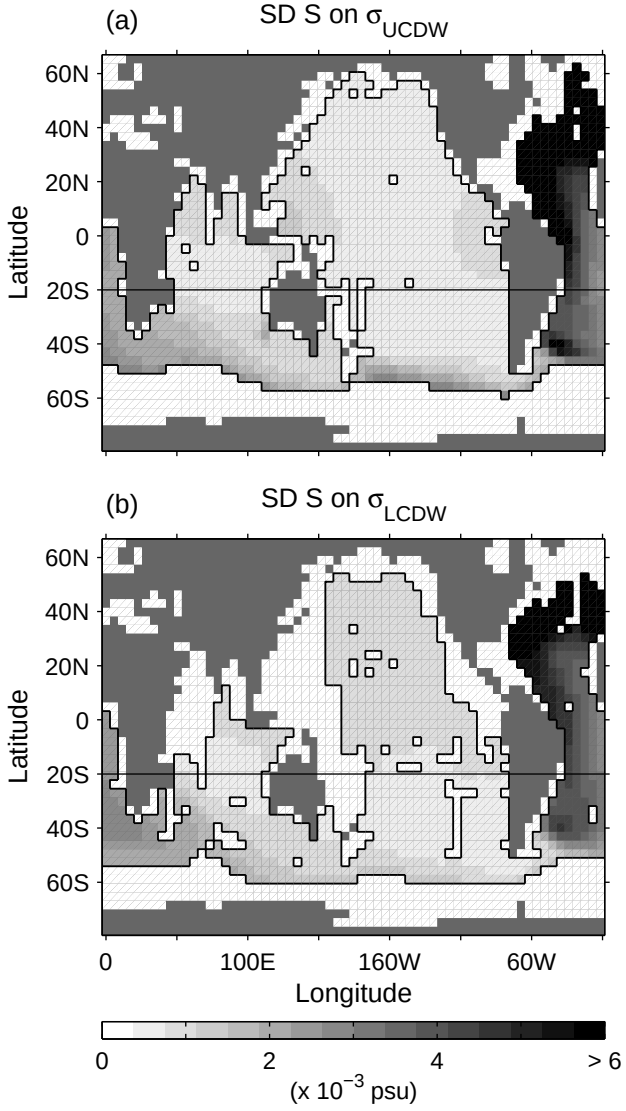

Figure 7: Standard deviation of salinity (psu) on (a) σ_{UCDW} and (b) σ_{LCDW}.

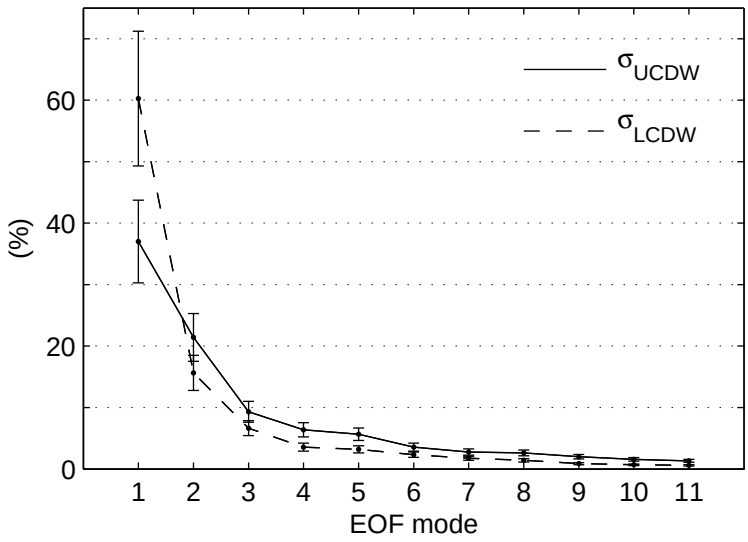

Figure 8: Percentage of variance explained by each EOF salinity mode in (a) σ_{UCDW} (solid curve) and (b) σ_{LCDW} (dashed curve). The error bars indicate the estimated sampling error for the eigenvalues computation (North et al. 1982). Overlapping error bars between adjacent EOF modes imply modal mixing according to the North et al. criterion. This implies that modes above EOF3 are degenerate.

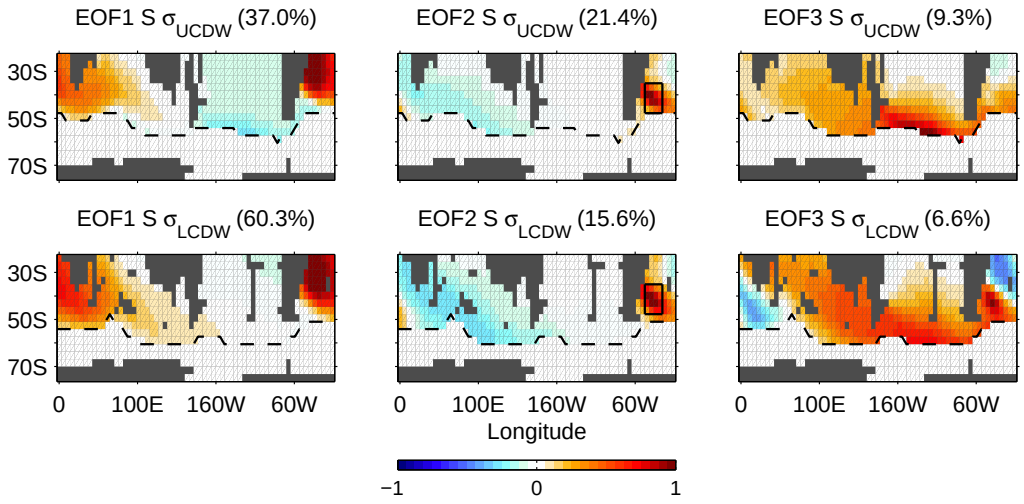

Figure 9: Spatial maps of the first three EOF modes of salinity on σ_{UCDW} (upper panels) and σ_{LCDW} (lower panels), accounting 68% and 82% of the total S variance, respectively. The values of the eigenvectors have been normalized to unity so that the spatial maps span values between -1 and 1, and hence the principal components (Fig. 10, left column) correspond to the actual magnitude of the variability associated with each mode. The box in the EOF2 maps indicates the Brazil-Malvinas Confluence Zone (BMCZ).

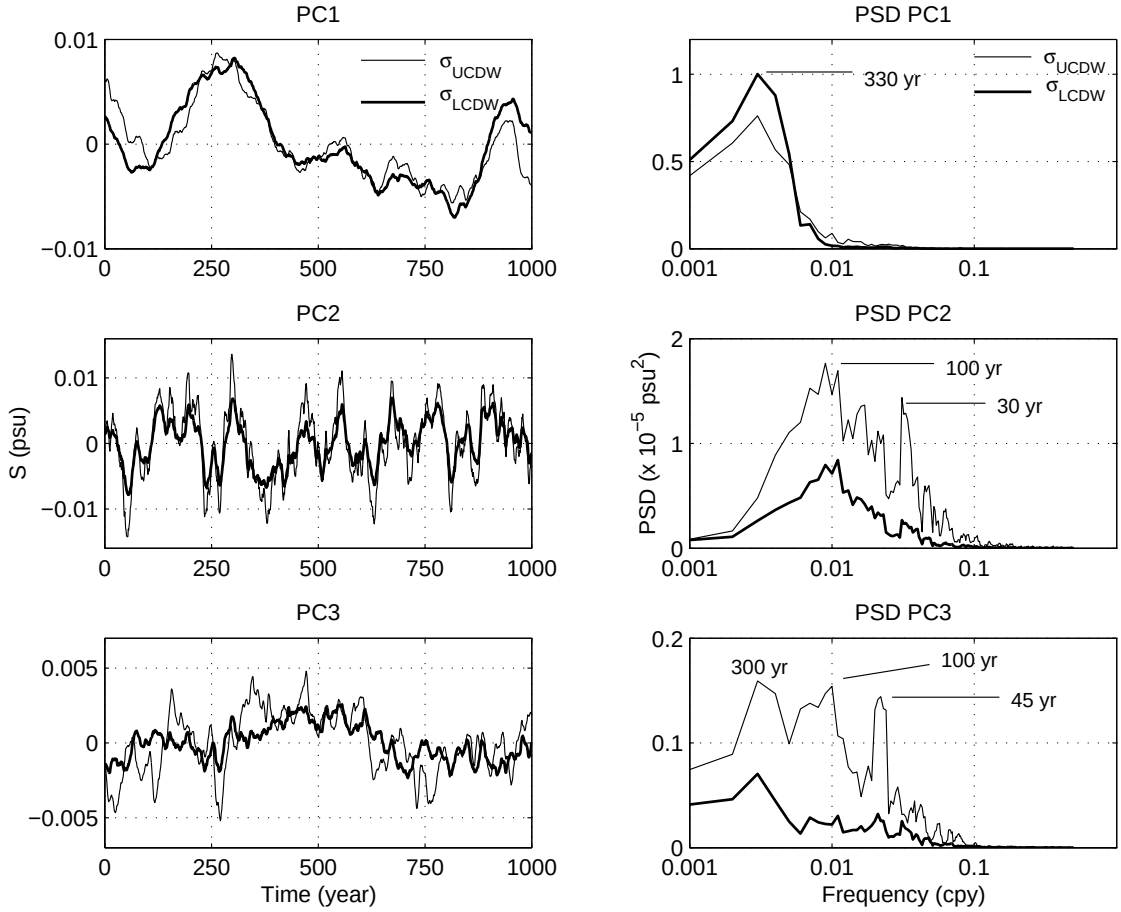

Figure 10: Principal component time series of EOF1−3 (PC1 − 3; left column) and the corresponding power spectral density (right column) for σ_{UCDW} (thin solid line) and σ_{LCDW} (thick solid line). A $\log_{10}$ scale is used in frequency to give more weight to the higher frequency signals and the power spectra are multiplied by frequency to preserve variance.

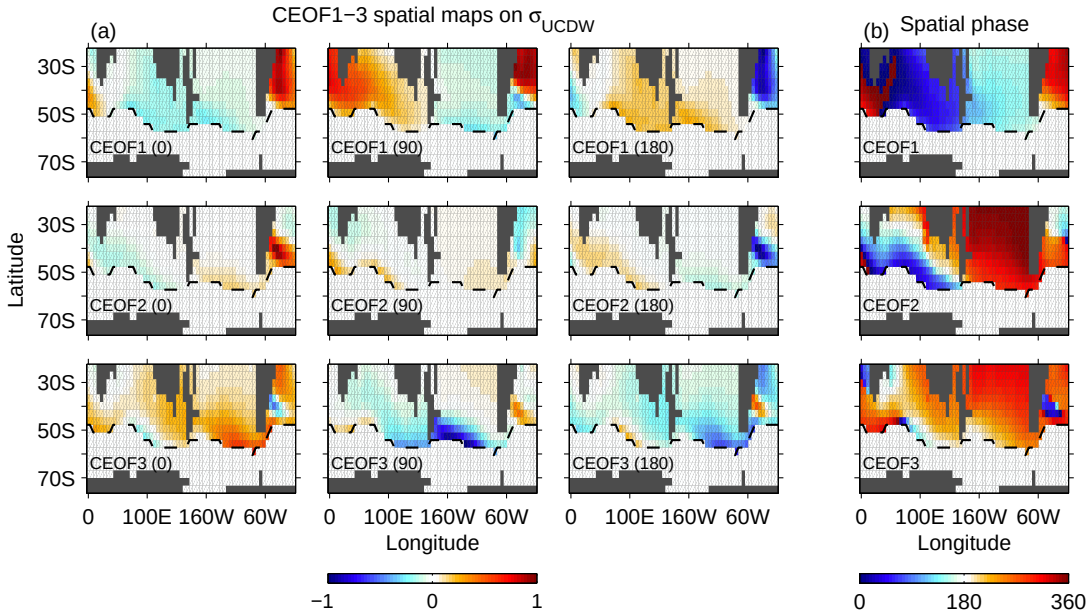

Figure 11: (a) Spatial maps of the first three complex EOF (CEOF) modes of salinity on σ_{UCDW} shown at 90° phase intervals. The three modes account for ≈ 76% of the total salinity variance with CEOF1, CEOF2, and CEOF3 accounting for 44%, 21%, and 10%, respectively. (b) Spatial phase angle for CEOF1−3 indicating the direction of propagation at increasing angle. Phase discontinuities occur at 360° − 0° as the phase is defined only between 0° to 360°.

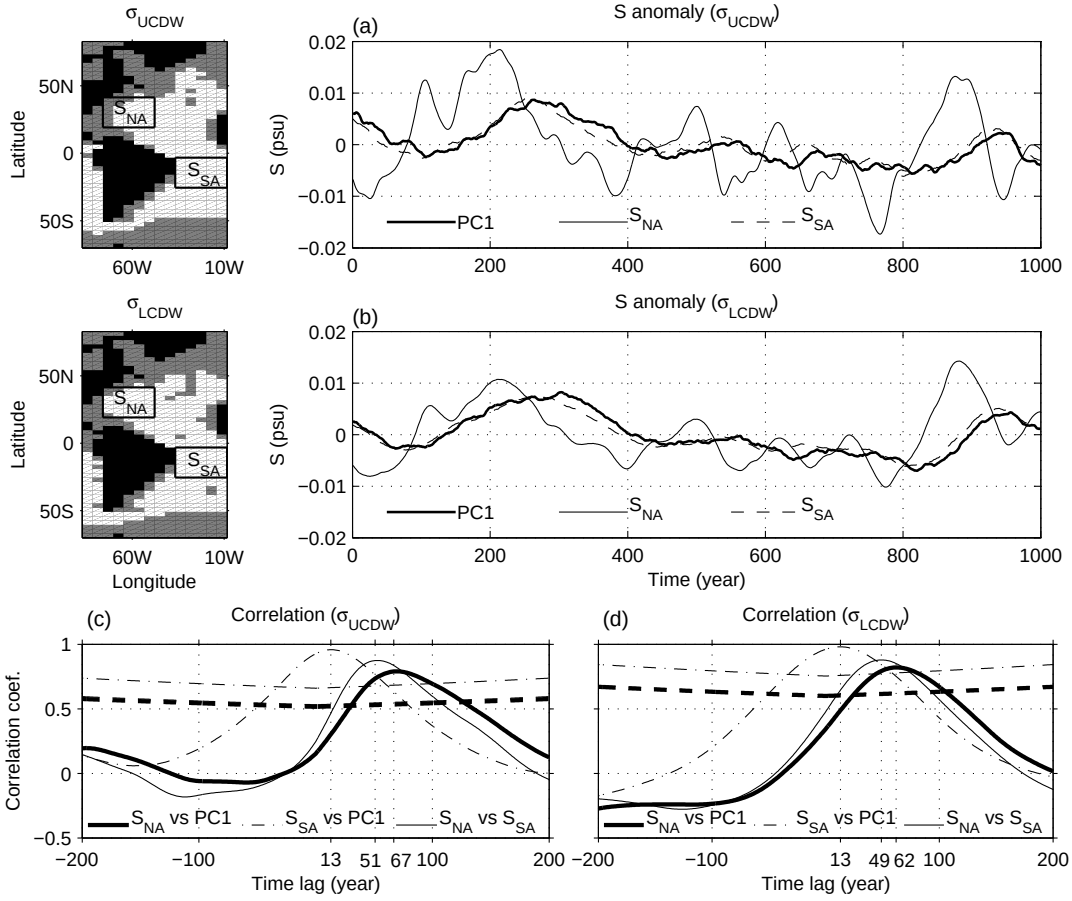

Figure 12: Timeseries of PC1 and box-averaged salinity anomalies at S_{NA}, S_{SA} (defined over the regions indicated at left) in (a) σ_{UCDW} and (b) σ_{LCDW}. Correlation coefficients between the variables are shown in (c) for σ_{UCDW} and (d) σ_{LCDW}. The corresponding 95% confidence levels are also shown for each analysis (the significance curves for S_{NA} vs PC1 and S_{NA} vs S_{SA} are nearly identical).

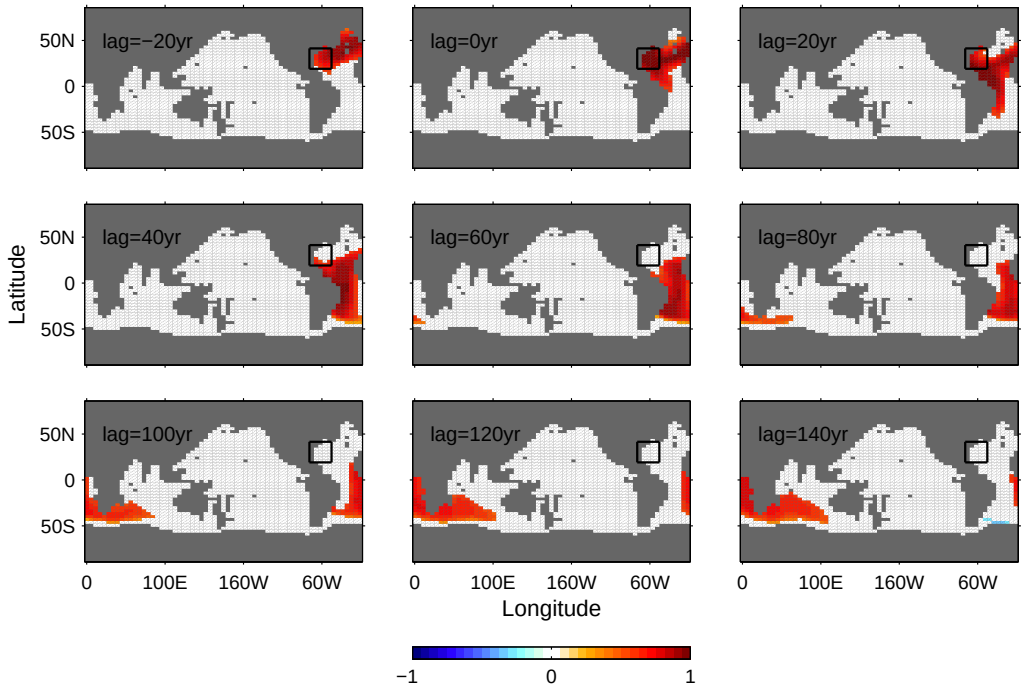

Figure 13: Correlation maps between global salinity fields and the box-averaged salinity at S_{NA} (indicated by the boxed region) on σ_{UCDW} at different time lags (20-yr interval), showing a propagation of salinity anomaly in outflowing NADW. Correlation coefficients are not shown when they fall below the 95% significance level. Note that the significance level increases with increasing time lags.

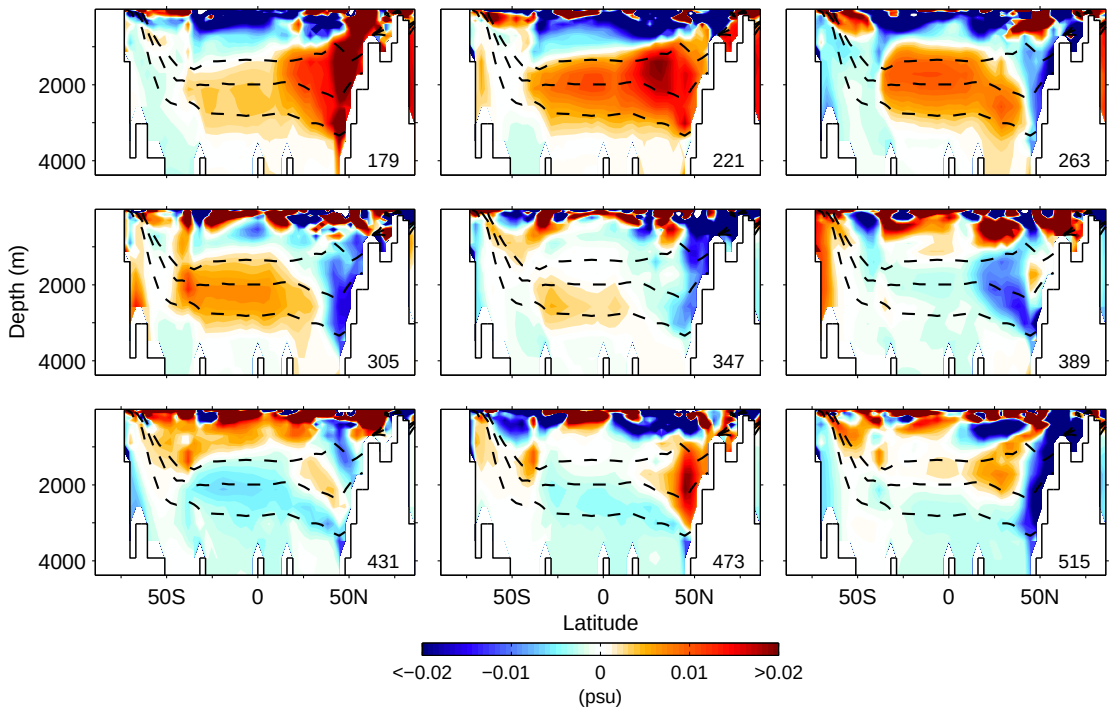

Figure 14: Time-series maps of salinity anomaly on a meridional-vertical plane along the Atlantic western boundary (see Fig. 15 for the section location). The dashed contours mark the position of the UCDW and LCDW layers. The time interval is 42 yr. The color scheme is set to span ±0.02 psu to enhance the visibility of anomalies at depth. The largest anomaly magnitude is ≈ 0.07 psu which occurs at the surface.

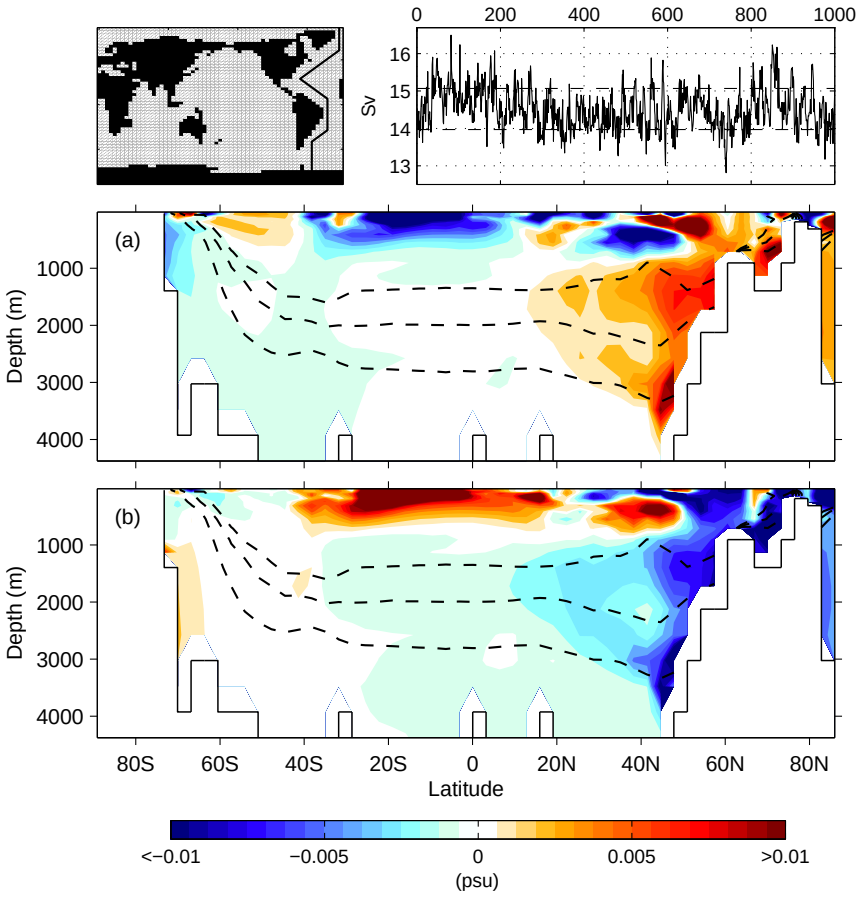

Figure 15: Composite maps of salinity anomaly on a meridional-vertical plane along the Atlantic western boundary shown in the upper-left inset, defined for anomalously (a) high NADW formation rate, and (b) low NADW formation rate. The NADW formation rate is defined as the maximum North Atlantic overturning strength. Extreme years are defined as one standard deviation unit above and below the long-term mean. The timeseries of NADW formation rate is shown in the upper-right inset. The dashed contours mark the position of the UCDW and LCDW layers.

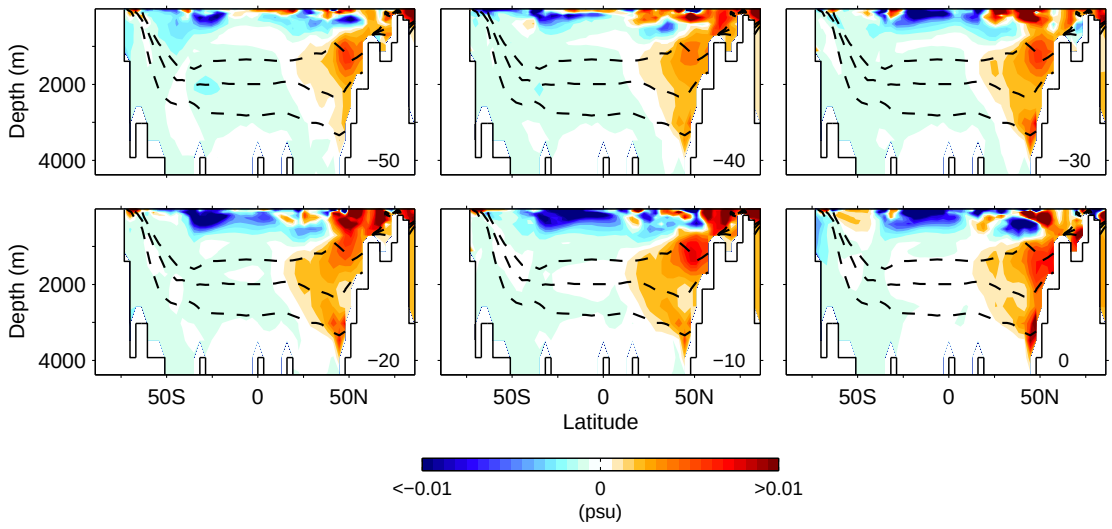

Figure 16: Lagged-composite maps of salinity anomaly on a meridional-vertical plane along the Atlantic western boundary shown in Fig. 15, defined for anomalously high NADW formation rate (see Fig. 15 caption for definition). The time lags are presented at a 10-yr interval starting from 50 years prior to high NADW overturning. The map at 0-yr time lag is essentially the same as in Fig. 15a.

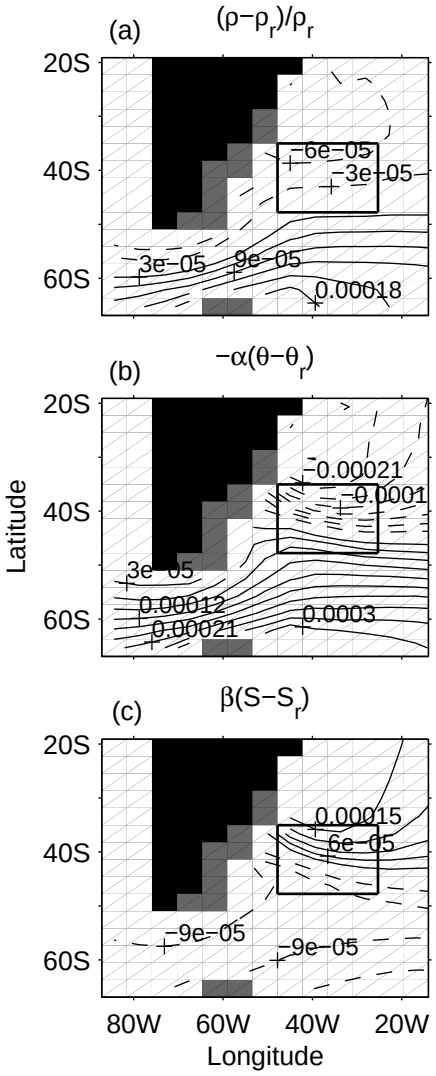

Figure 17: Spatial thermohaline variation of (a) total density, (b) temperature component, and (c) salinity component at 1720-m depth. The total density is derived from the linearised equation of state $\rho = \rho_r \left[1 - \alpha \left(\theta - \theta_r\right) + \beta \left(S - S_r\right)\right]$, where the subscript r denotes a reference value. Dashed (solid) contour indicates negative (positive) density anomaly. The boxed region marks the Brazil-Malvinas Confluence Zone (BMCZ).

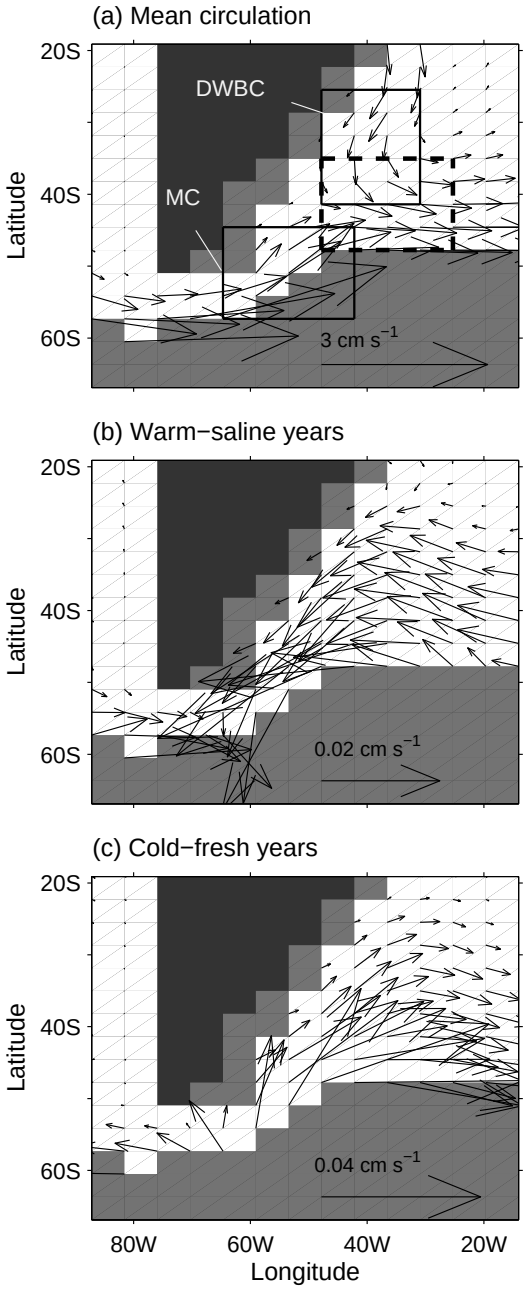

Figure 18: Velocity vectors for (a) the mean circulation, (b) composite map of current velocity anomaly on σ_{UCDW} defined for extreme warm-saline years and (c) cold-fresh years. The extreme events are defined as those above (below) 1 standard deviation unit for the warm-saline (cold-fresh) years. The dashed box in (a) indicates the location of the BMCZ. Solid boxes in (a) indicate the regions defined for averaged values of the DWBC meridional velocity (v_{DWBC}) and the meridional component of the Malvinas Current (v_{MC}).

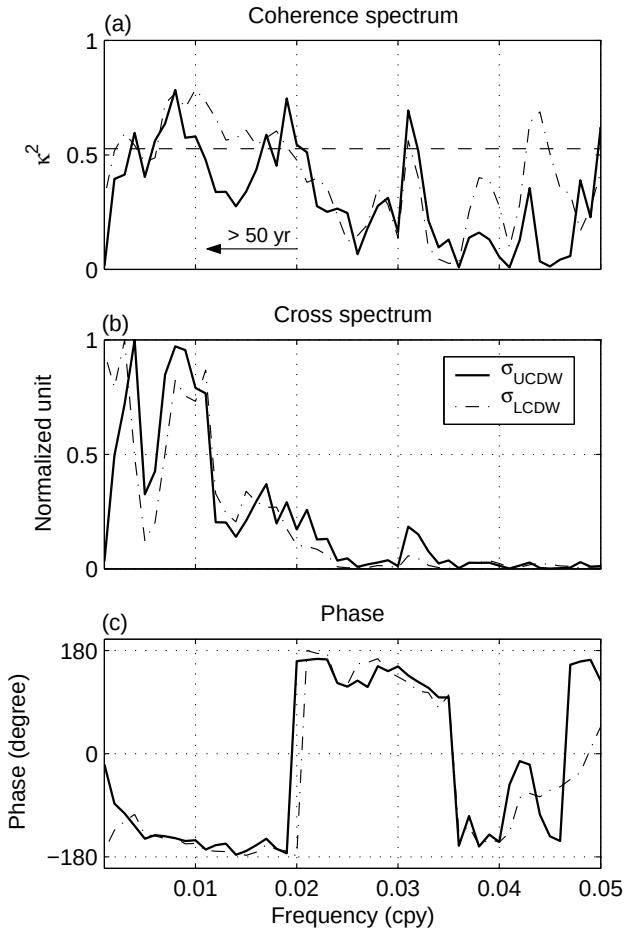

Figure 19: Spectral analyses for the meridional components of the DWBC (v_{DWBC}) and the Malvinas Current (v_{MC}). Shown are (a) the coherence spectra, (b) the cross spectra, and (c) the phase for the σ_{UCDW} (solid curve) and σ_{LCDW} (dash-dot curve).

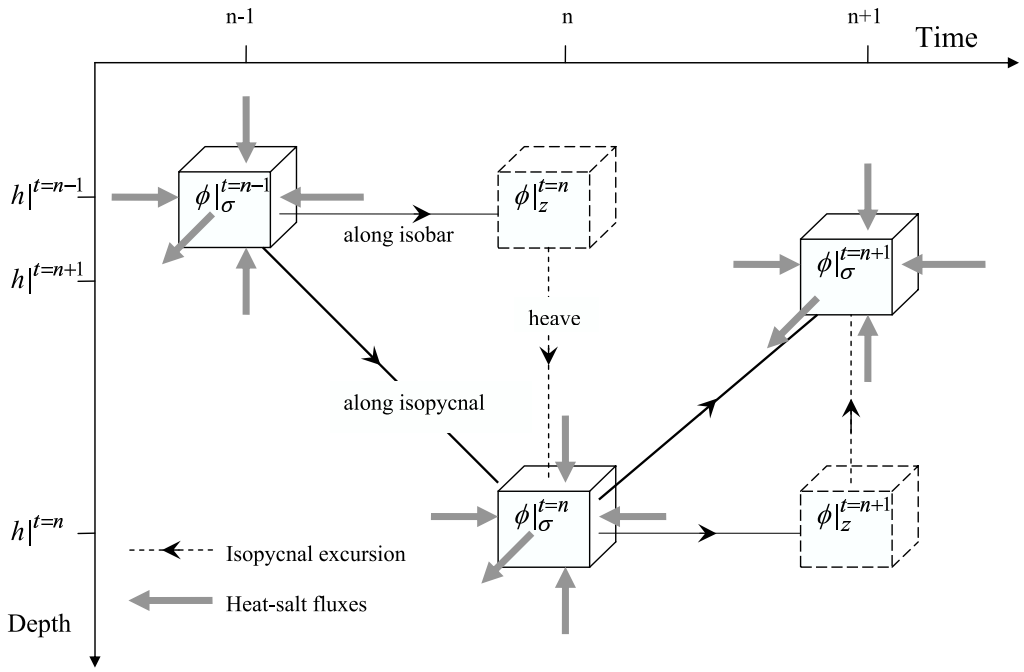

Figure A1: Heat-salt budget scheme of Eqs. (A2)−(A4) in the text showing the case of an isopycnal surface deepening at year n relative to year $n-1$ and shoaling at year $n+1$ relative to year n. Advective fluxes upon the fluid cause changes of $\theta - S$ properties at a fixed depth, resulting in the displacement of the isopycnal surface (heave).

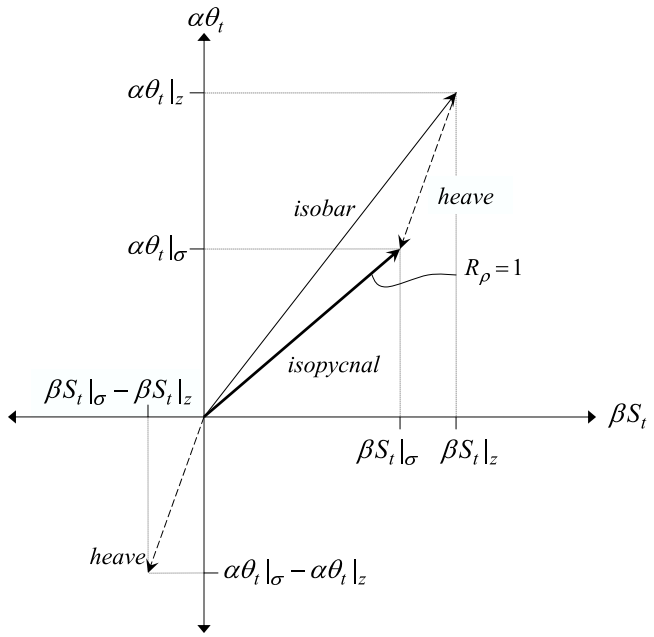

Figure A2: $\theta - S$ changes along an isobar, along an isopycnal, and across depths due to heaving of isopycnals in $\beta S_t - \alpha\theta_t$ space.

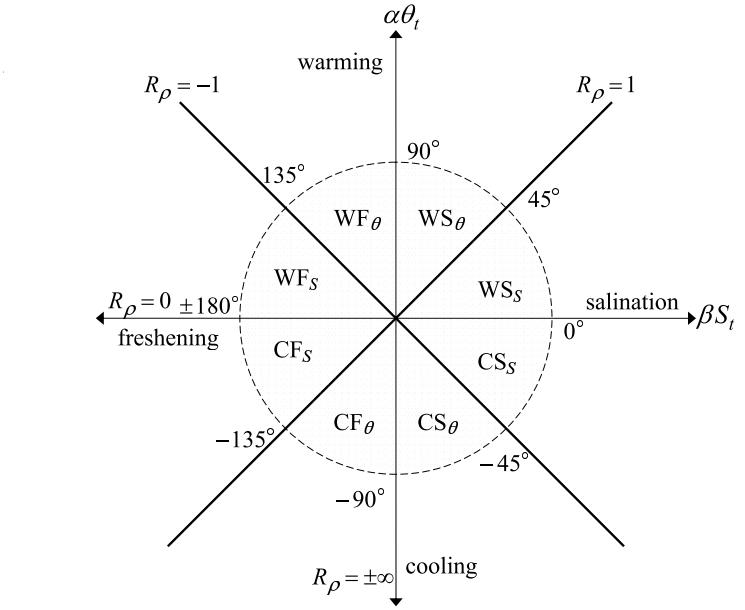

Figure A3: Quadrants defined by the Turner Angle (Tu) where heat-salt storage changes are shown in $\alpha\theta_t - \beta S_t$ space. The quadrants bound by the lines $R_\rho = 1$ and $R_\rho = -1$ indicate which of θ and S dominates in the resulting density changes. The line $R_\rho = 1$ indicates perfect density compensating variations of $\theta - S$. The line $R_\rho = -1$ indicates density instability as $\theta - S$ changes are out of phase.

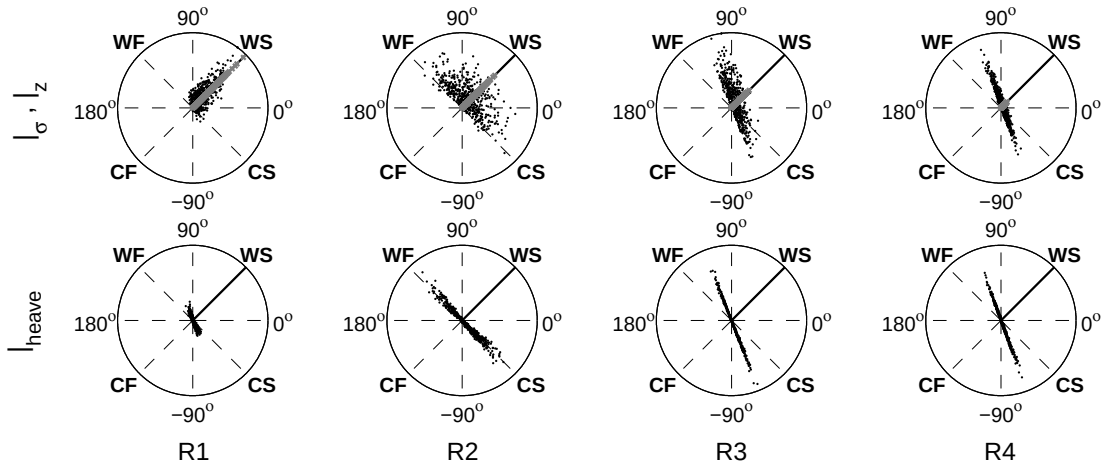

Figure A4: Along-isopycnal warming and salination case in $\beta S_t - \alpha\theta_t$ space at R1−R4 along σ_{UCDW} over the 1000-yr model data in terms of Turner Angle (refer to Fig. A3). The along-isobar (black dots) and along-isopycnal (grey crosses) variations are presented together in the top row. The corresponding heave-effect variations are displayed in the bottom row. The locations of R1−R4 are shown in Fig. A6 (also Fig. 4c). The abbreviations WF, WS, CS, CF indicate the signs of $\theta - S$ change, corresponding to warming-freshening, warming-salination, cooling-salination, and cooling-freshening, respectively.

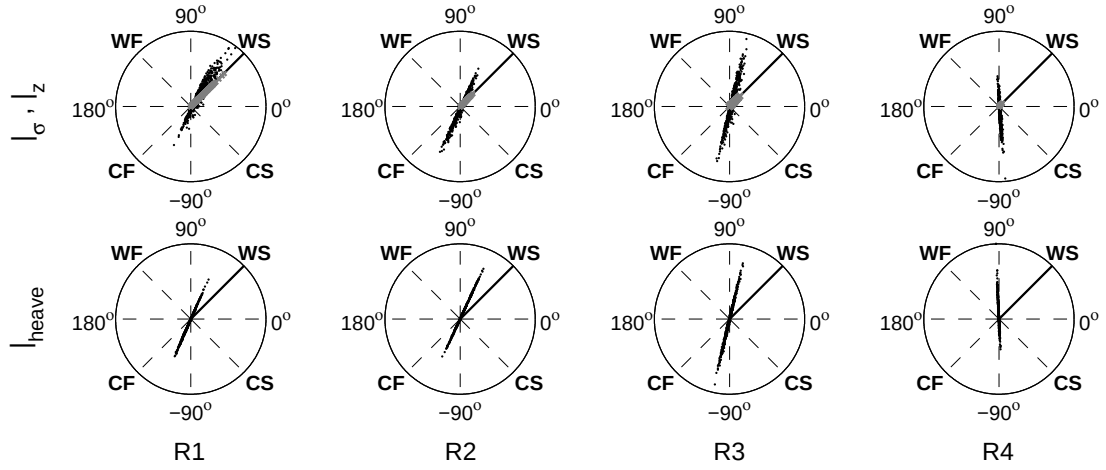

Figure A5: The same as Fig. A4 but for σ_{LCDW}.

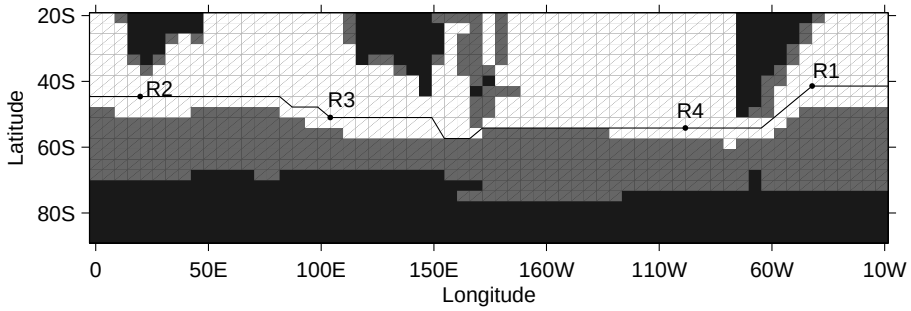

Figure A6: Transect across the Southern Ocean where the heat-salt budget analyses of Figs. A7, A8 are conducted. The locations labeled R1−R4 are taken as examples for discussion, and corresponds to R1−R4 used throughout the text and shown in Figs. 4c, 5c.

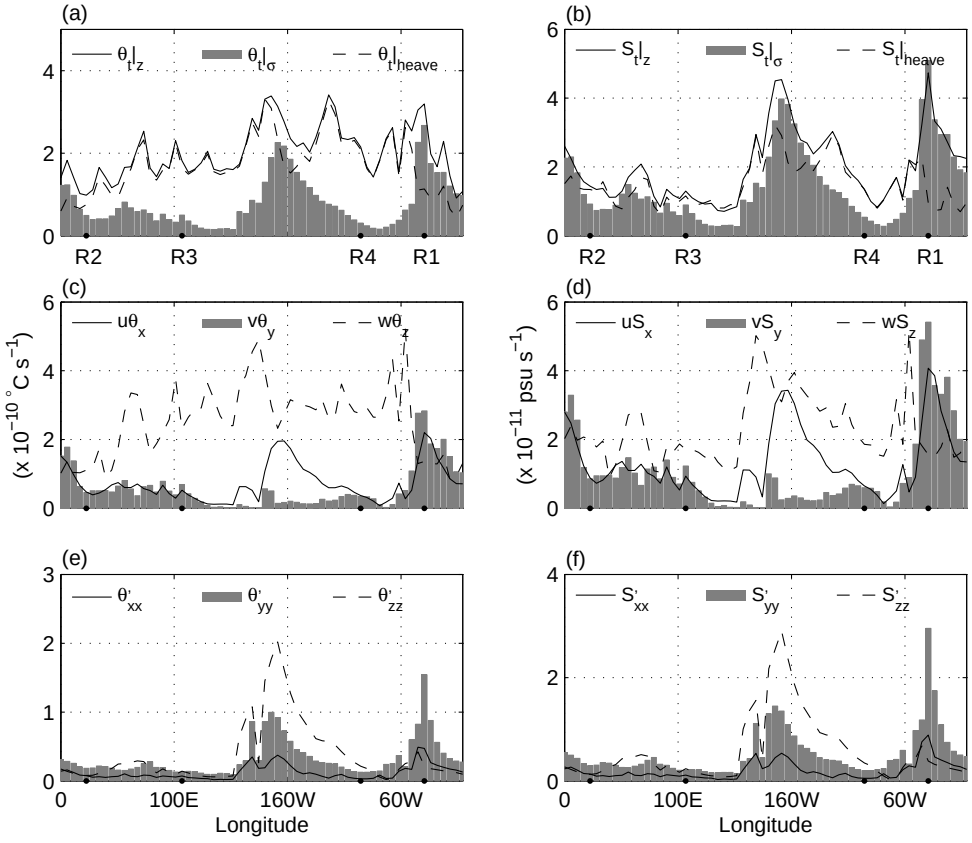

Figure A7: Standard deviations of (a) heat content terms, (b) salt content terms, (c) heat advection terms, (d) salt advection terms, (e) heat mixing terms, and (f) salt mixing terms. See the text for definition of the respective terms.

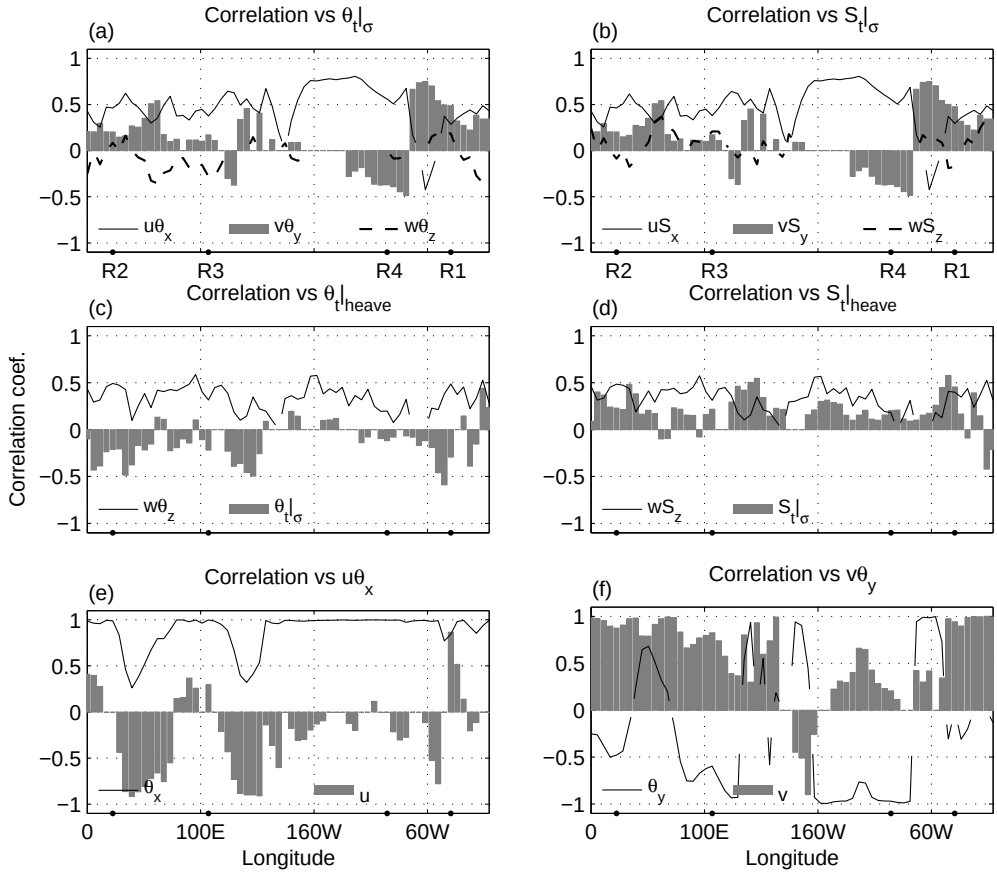

Figure A8: Correlation coefficients for (a) heat advection terms versus $\theta_t|_\sigma$, (b) salt advection terms versus $S_t|_\sigma$, (c) $\theta_t|_{heave}$ versus $w\theta_z$ and $\theta_t|_\sigma$, (d) $S_t|_{heave}$ versus wS_z and $S_t|_\sigma$, (e) zonal heat advection term ($u\theta_x$) versus θ_x and u, and (f) meridional heat advection term ($v\theta_y$) versus θ_y and v. Correlation coefficients which are not significant above the 95% confidence level are not displayed.

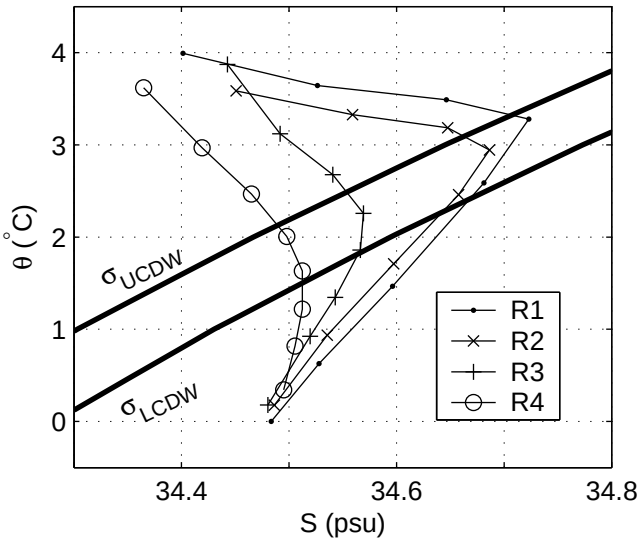

Figure A9: Temperature-salinity vertical profiles at R1−R4. The locations of R1−R4 are shown in Fig. A6.

Part III: Antarctic Bottom Water circulation and variability in a coupled climate model

Abstract

The natural variability of Antarctic Bottom Water (AABW) in a long-term integration of a coupled climate model is examined. Examination of passive tracer concentrations suggests the model AABW is predominantly sourced in the Weddell Sea with injection of Antarctic surface and shelf waters into the interior. Despite the model interior salinity being too fresh, there is still decent agreement between the model and observed AABW pathways and $\theta - S$ distributions. An isopycnal surface corresponding to a potential density $\rho_3 = 1041.50$ kg m^{-3} referenced to 3000 db (hereafter $\sigma_{41.50}$) is selected to mark the separation boundary between AABW and the overlying Circumpolar Deep Water (CDW). Analysis of the propagation of $\theta - S$ anomalies is conducted along $\sigma_{41.50}$ and along a deeper isopycnal surface ($\sigma_{45.95}$; referenced to 4000 db) which is chosen to capture the Weddell Sea Bottom Water in the model. The three leading complex empirical orthogonal function (CEOF) modes of the along-isopycnal $\theta - S$ variability are presented showing propagation of $\theta - S$ anomalies from the southwestern Weddell Sea into the Atlantic interior. The first mode is characterised by fluctuations with 75−90-yr periods which are prominent along $\sigma_{45.95}$. A periodicity of approximately 300 years is notable on $\sigma_{41.50}$ which is the dominant timescale of $\theta - S$ variability in the CDW layer. The higher modes exhibit pronounced interannual to multi-decadal fluctuations.

While salinity variability is dominated by along-isopycnal propagation of S anomalies, θ variability is dominated by heaving of isopycnal surfaces which infers propagation of density anomalies with the speed of baroclinic waves. The matching frequency between the propagation of $\theta - S$ anomalies along isopycnals and the density anomalies suggests coherent variations of $\theta - S$ with convective overturning in the southwestern Weddell Sea region. Sea surface density first increases 2 years prior to the increase in overturning, and the density continues to increase with depth

over the next 25 years. The anomalous state of subsurface advective heat and salt fluxes during anomalous Weddell Sea AABW overturning is described. Warming and salination with an increased density at the surface suggests that salinity, not temperature, largely controls the fluctuations in the surface density. A surface heat-salt budget and composite analyses in the southwestern Weddell Sea suggest that an increased removal of summertime sea ice by enhanced wind-driven northward Ekman transport results in an increased solar radiation absorbed by the ocean. The larger ice-free region in summer eventually leads to enhanced air-sea heat loss, more rapid ice growth and therefore greater brine rejection during winter. This results in surface salination signals that are transmitted along isopycnals into the interior. Preliminary analyses show evidence that modes of climate variability can trigger this mechanism, thus potentially impacting on AABW variability.

1. Introduction

Antarctic Bottom Water (AABW) is the densest water mass originating around the periphery of Antarctica and mixes with the more saline and warmer Circumpolar Deep Water (CDW) as it spreads into the abyssal basins of the world ocean (Mantyla and Reid 1983). AABW further mixes with lighter water masses as it flows equatorward reaching the North Atlantic where interaction with North Atlantic Deep Water (NADW) occurs. AABW variability eventually influences the stability of the global overturning circulation and thus likely exerts an influence on the Earth's climate on decadal to multi-centennial time scales. Better understanding of the spatio-temporal characteristics of AABW natural variability is thus of great importance.

The formation, circulation, and properties of AABW have been studied by several authors (see recent review articles by Orsi et al. 1999; Jacobs 2004). However, the natural variability of AABW, especially on timescales beyond decades, remains poorly known. This study thus aims to provide a picture of the evolution of AABW property anomalies and mechanisms on multi-decadal to centennial timescales.

The term AABW is generally referred to as the northward flowing bottom waters of southern origin found in the abyssal depths of the world oceans. Some studies reserve the term AABW for bottom waters that are exported directly from the Antarctic subpolar regions (e.g., Gordon 1971, 1972; Orsi et al. 1999). As documented by Mantyla and Reid (1983), the abyssal waters of the Atlantic, Indian, and Pacific oceans are not drawn exclusively from the Antarctic waters but also from lighter CDW. CDW itself is derived from the outflow of North Atlantic Deep Water (NADW) into the Southern Ocean where its deeper layer mixes with the fresher and colder bottom waters of the abyssal Antarctic. Orsi et al. (1999) assigned a neutral density surface $\gamma^n = 28.27$ kg m^{-3} (approximately equivalent to $\sigma_2 = 37.16$ kg m^{-3},

$\sigma_4 = 46.04 - 46.06$ kg m^{-3}) to separate AABW from the overlying CDW that flows eastward with Antarctic Circumpolar Current (ACC). Bottom water denser than this $\gamma^n = 28.27$ kg m^{-3} is then referred to as AABW. On the other hand, Naviera Garabato et al. (2002b) assigned a lighter density surface $\sigma^n = 28.26$ kg m^{-3} to separate the Weddell Sea Deep Water (WSDW) from the overlying lower Circumpolar Deep Water (LCDW). The AABW in this study is defined in a similar fashion to that of Naviera Garabato et al. (2002b), although discrepancies remain due to the deviation of the model AABW properties from the observed.

Sources of AABW have been identified as both the contribution from shelf waters at several sites around the Antarctic continental margin and the upwelling of CDW southward of the ACC (see review by Orsi et al. 1999). Despite significant input from the Ross Sea and other regions such as the Adelié land region (Rintoul 1998), the Weddell Sea has been known as the most prominent and active region for bottom water formation (Orsi et al. 1999). The formation of AABW involves complex processes that have been addressed and reviewed in various studies (e.g., Foster and Carmack 1976; Rintoul 1998; Orsi et al. 1999; Meredith et al. 2000; Foldvik et al. 2004). Cyclonic gyres characterise the circulation in the Ross and Weddell seas. Upwelled LCDW enters the Weddell Sea via the eastern flank of the Weddell Gyre at about 30°E (Orsi et al. 1993) where mixing with the overlying colder and fresher winter water occurs. Winter water exists year round in the surface mixed layer as a remnant of the cold layer produced during sea-ice formation (Foster and Carmack 1976). This modified CDW, now referred to as Warm Deep Water (WDW; Whitworth and Nowlin 1987), mixes further with the high salinity southwestern Weddell Sea shelf water (-1.9°C, 34.7) to form Weddell Sea Bottom Water (WSBW; -1.3°C, 34.65). WSBW then mixes with the less dense LCDW as it flows down the continental shelf to form WSDW gaining buoyancy to flow over sills as AABW

(typical $\theta - S$ of ≈ -0.4°C, 34.66). Using chlorofluorocarbon (CFC) data, Meredith et al. (2000) showed that there is contribution to WSDW from the east along the continental margin outside the Weddell Sea. This calls into question the belief that the Weddell Sea is the major AABW source region. Nevertheless, the major ingredient of AABW is CDW as suggested by the analysis of Foster and Carmack (1976) showing that AABW sourced from the Weddell Sea is composed of $\approx 62.5\%$ CDW, 25% shelf water, and 12.5% winter water (see also Whitworth et al. 1998).

A realistic simulation of AABW properties, formation, and pathways in general circulation models (GCMs) is essential for understanding the Earth's climate system. This is a challenging task, requiring a realistic representation of shelf processes (including Antarctic sea-ice and ice-shelves), down-slope flows, and convective overturning. To date there are no climate models capable of simulating the correct properties of the abyssal oceans. However, considerable improvements have been achieved since the early model developments of Bryan (1969) and Cox (1984). For example, one of the most common deficiencies in climate models is that the deep ocean is not sufficiently dense as marked by deep and bottom waters that are too warm and fresh. Corrective fluxes in bottom water formation regions, such as applying a wintertime salinity adjustment, can achieve a better AABW representation (e.g., England 1993). However, for the purposes of studying AABW variability and climatic feedbacks, a realistic representation of the physics of AABW formation is necessary (see also Toggweiler and Samuels 1995). Furthermore, the long ventilation time scales of AABW requires a multi-century integration of a fully coupled GCM, currently only possible at coarse resolution. The newer generation of non eddy-resolving GCMs, such as the one used in this study, rely on the parameterisation of eddy-induced mixing as formulated by Gent and McWilliams (1990) and Gent et al. (1995; referred as the GM parameterisation). This subgrid-scale pa-

rameterisation represents a more physical mixing mechanism and produces a more realistic water mass structure than the early generation models implementing the unphysical background horizontal diffusivity (see e.g., Hirst et al. 2000). However, the drawback of implementing the GM parameterisation is that it supresses convection which then reduces bottom water formation (Doney and Hecht 2002). Coupling the ocean component of the climate models with dynamical sea-ice submodels has the effect of enhancing AABW production rates (Duffy et al. 2001). Other model aspects such as choice of convection scheme, bottom boundary layer scheme (BBL), model resolution, and vertical diffusion require further attention for a more realistic simulation of bottom water formation and pathways (see Doney and Hecht 2002; Stössel et al. 2002).

There have been relatively few studies of the observed variability of AABW and its ingredients on seasonal to decadal time scales. Coles et al. (1996) found AABW cooling and freshening of 0.05°C and 0.008 psu along constant density surfaces in the Argentine Basin over the period 1980−1989. They attribute this $\theta - S$ change to convective events in the Weddell Sea. Warming of WDW and WSDW by $0.1° - 0.2$°C and 0.05°C, respectively, were observed by Meredith et al. (2001) in the eastern Scotia Sea between 1995 and 1999. Changes in the WSDW properties at the shelves of the Weddell Sea, and changes in the wind-driven gyre were listed as possible causes for the warming. Hogg and Zenk (1997) documented warming in the bottom waters of the Vema Channel of about 0.03°C, accompanied by a decrease in the northward bottom water transport. They proposed that these changes are a response to a reduction in bottom water production. More recently, Fahrbach et al. (2004) documented $\theta - S$ fluctuations in the Weddell Sea over 1990 to 2002. A warming trend of WDW is observed from 1992 to 1998 at the prime meridian which is consistent to that documented by Robertson et al. (2002). The warming trend

is then followed by a cooling trend. Changes in the $\theta - S$ of WSDW and WSBW are also documented by Fahrbach et al. (2004) with an amplitude of the order of $0.01° - 0.02°$C, $0.001-0.002$ psu, respectively. They proposed that these changes are caused by variations in atmospheric circulation in response to climate modes such as the Antarctic Circumpolar Wave (ACW) and the Southern Annular Mode (SAM) which impact on the inflow of ACC waters into the Weddell Sea.

Observational studies on the longer-term AABW variability of up to centennial time scales are naturally absent given the short measurement record available. Over such time scales we thus rely on climate models to provide an estimate of temporal and spatial variability. Modelling studies investigating AABW variability on decadal time scales have recently emerged, such as those by Stössel and Kim (1998; 2001). The purpose of this paper is to provide an overview of AABW $\theta - S$ variability on interannual to centennial time scales in a long-term integration of a coupled climate model. Due to limited computing resources, analysis on such long time scales is only possible using non eddy-resolving climate models with known limited capabilities in simulating deep water masses, in particular AABW. The rest of this paper is divided as follows. The coupled model is described in section 2. Section 3 provides an overview of AABW pathways and properties in the model. The $\theta - S$ variability and propagation of anomalies are assessed in section 4. Investigation of the mechanisms leading to AABW variability are presented in section 5. The study is summarised in section 6.

2. The coupled model

The model used in this study is the CSIRO Mark 2 10,000-yr integrated natural pre-industrial CO_2 coupled ocean-atmosphere-ice-land surface model. The atmospheric submodel is discretised on nine levels in a sigma coordinate system with full

diurnal and annual cycles, gravity wave drag, a mass flux scheme for convection, semi-Lagrangian water vapour transport, and a relative humidity-based cloud parameterisation. Parameterisation of land surface interactions follow the soil-canopy model of Kowalczyk et al. (1994). Rainfall runoff occurs after saturation of the surface soil and reaches the sea without a time lag following a path of steepest descent. The sea-ice submodel includes the cavitating fluid rheology of Flato and Hibler (1990), ice thermodynamics (Semtner 1976) and sea-ice dynamics allowing advection and divergence of sea ice by wind stress and ocean currents (see O'Farrell 1998 for a full description).

The ocean model is based on the Bryan-Cox code (Cox 1984) with horizontal resolution approximately 5.6° longitude × 3.2 latitude, matching that of the atmospheric component. In the vertical, the model has 21 levels of irregular grid box thickness. The model features a reasonably realistic topography capturing major landmasses and bottom sills. The Drake Passage extends from 65° to 56°S which is wider than the actual $63° - 57°$S (see also England 1992). The Gent and McWilliams (1990) and Gent et al. (1995) eddy-induced transport parameterisation is implemented with horizontal background diffusivity set at zero. Along isopycnal mixing scheme (Cox 1987; Redi 1982) is implemented with isopycnal tracer diffusivity of 1×10^7 cm^2 s^{-1}. A relatively weak vertical diffusivity is included as a function of static stability. Convection is simulated by applying an enhanced vertical diffusivity in regions of static instability (often also referred to 'convective adjustment'). Constant annual but seasonally varying air-sea flux corrections (heat, freshwater, and stress) are included in the coupling between the ocean and atmosphere (and sea ice) to reduce long-term climate drift. Simmons and Polyakov (2004) have shown that implementation of flux corrections does not have a profound effect on model oceanic variability. There are no flux corrections applied between the atmosphere and sea

ice components. A detailed description of the model can be found in Gordon and O'Farrell (1997) and Hirst et al. (2000).

We analyse 1000 yr of model data from the latter stages of this 10,000-yr run. Note that the model exhibits minimal drift at this late stage of the run. Variables analysed include ocean potential temperature and salinity ($\theta - S$), ocean current velocities (u, v), and air-sea fluxes. Passive tracer concentration data are also analysed to assess the ventilation pathways of AABW in the model, with tracer concentration set to 100% at the sea surface in the Southern Hemisphere (see O'Farrell 2002 for a description of the analogous Northern Hemisphere tracer experiments).

The zonally averaged salinity for each ocean sector is presented in Fig. 1 (left column). For comparison, the corresponding Levitus climatology is shown in Fig. 1 (right column). The density referenced to 2000 db as shown by the thin contours suggests that the model bottom water is lighter than the observed, marked by its salinity that is too low for all of the ocean sectors. However, it can be noted that the Atlantic bottom water is the freshest, coldest, and most dense, while the Pacific bottom water is the most saline, warmest, and least dense. This is consistent with the observations, as described by Mantyla and Reid (1983) and Orsi et al. (1999) among others. Note that the thick red contour marks the mean position of the isopycnal surface chosen in section 3 as the upper-most boundary of the model AABW which captures the bottom portion of the Lower Circumpolar Deep Water. Despite the model limitations in acquiring realistic bottom water properties, some features of the model AABW pathways are consistent with the observed (see section 3b). This motivates us to provide an overview of the bottom water variability and the ventilation of climate anomalies within AABW in the model.

3. AABW definition, properties, and circulation

a. AABW definition

The principal aim of this section is to identify the AABW layer for the variability analysis presented in sections 3 and 4. However, it should be noted that defining AABW in the model is rather problematic as the model bottom density deviates markedly from the observed (section 2a). Nevertheless, the model AABW is captured by considering both of the following aims: 1. to obtain an isopycnal surface separating AABW from the overlying CDW based on the distinct properties and pathways of these water masses; and 2. to capture waters sourced from the Antarctic surface that are eventually found in the deep oceanic basins.

Passive tracer experiments are a useful tool for assessing deep-bottom water ventilation (England 1995), which is in particular relevant to the second aim above. The first aim however presents a problem in relation to deficiencies in using potential density surfaces over a large pressure range as noted, for example, by Lynn and Reid (1968) and Reid and Lynn (1971). Within the high latitudes of the Southern Ocean, constant density surfaces extend from the surface to great depths (see Fig. 1). Ideally, neutral density surfaces (Jackett and McDougall 1997) are implemented for this purpose. However, the labelling of hydrographic datasets with neutral densities involves a comparison against a reference global dataset derived from the Levitus climatology. Since the $\theta - S$ structure and density of the model interior deviate markedly from the Levitus climatology (Fig. 1), labelling the model interior with neutral density results in a distorted AABW density structure. To achieve minimal error due to the compressibility of seawater over a large pressure range, the 'patched' potential density surfaces, though cumbersome in calculation, are used in this study to mark constant density surfaces (e.g., Reid 1994). The potential density surfaces are locally referenced using five pressure levels namely, 0, 1000, 2000, 3000, and

4000 db. Furthermore, Reid (1994) noted geographical dependence for the patched potential density surfaces. For example, a particular density surface in the Indian Ocean sector corresponds to a different density surface in the Pacific region. Thus, the calculation is carried out within the Atlantic, Pacific, and Indian sectors of the Southern Ocean separately.

A patched potential density surface corresponding to the locally referenced potential density at 3000 db, $\rho_3 = 1041.50$ kg m^{-3} (referred to as $\sigma_{41.50}$ surface hereafter) is chosen to contain the AABW beneath. How this isopycnal surface is selected will be apparent via examinations of $\theta - S$, zonal and meridional flows, and passive tracer concentration fields across a few transects in the model Southern Ocean (Figs. 2−4). The corresponding cross sections of Levitus climatology $\theta - S$ are also provided. It may be noted that while the model temperature fields are comparable to the observed, the model salinity values are considerably lower than the observed by > 0.2 psu. A deeper potential density surface corresponding to $\rho_4 = 1045.95$ kg m^{-3} (referenced to 4000 db; $\sigma_{45.95}$ surface hereafter) is chosen for comparison. The density equivalence in each ocean sector referenced at the other pressure levels that corresponds to $\rho_3 = 1041.50$ kg m^{-3} and $\rho_4 = 1045.95$ kg m^{-3} are presented in Tables 1, 2. Figure 2 presents the model $\theta - S$, the tracer concentration after 150 yr of release, and the zonal velocity cross-sectional fields across the Drake Passage at 67.5°W. A thick layer of relatively saline CDW with $\theta - S$ range of approximately $0.2 \leq \theta \leq 1.5$°C, $34.5 \leq S \leq 34.53$ psu (too fresh by about 0.2 psu compared to the observed) can be seen underneath the salinity minimum AAIW north of the Polar Front (60°S) and the cold Winter Water south of the Polar Front (Sievers and Nowlin 1984). At the bottom, the cold and fresh signature below CDW in the southern part is likely derived from WSDW as evidenced by the relatively high tracer concentration there (Fig. 2c). A small volume of the lightest class of WSDW

found in the Drake Passage is observed, for example, by Sievers and Nowlin (1984), Locarnini et al. (1993), and Naviera Garabato et al. (2002a).

The intrusion of WSDW is marked by a weak westward flow over the sill of Drake Passage (at 3475-m model level at 67.5°W) notable in Fig. 2d below the ACC. Note that in contrast to the model, the westward flow in the observed within the Drake Passage is limited to a confined region in the southern portion of the Drake Passage (Naviera Garabato et al. 2002a; see their Fig. 13). This discrepancy, as also noted in Doney and Hecht (2002), is likely common to ocean models with coarse vertical resolution. The artificially wide Drake Passage may also contribute to the discrepancy. Note that the $\sigma_{41.50}$ surface is shown in Fig. 2 to contain the WSDW. This isopycnal surface is used in this study to mark the upper bound of AABW. This is in line with the neutral density surface $\gamma^n = 28.26$ kg m^{-3} (equivalent to σ_4=46.04) used by Naviera Garabato et al. (2002b) to separate WSDW from LCDW, but in contrast to the $\gamma^n = 28.27$ in Orsi et al. (1999) which excludes the highest density water in Drake Passage in their AABW definition.

Along a zonal transect at 62°S, a thick layer of warm and saline CDW is seen across longitudes above $\approx$ 2000 m (Fig. 3a, b). Below CDW, deep and bottom waters of Antarctic origin are detectable by their relatively cold-fresh characteristics (Fig. 3a, b) and high tracer concentration (Fig. 3c). WSDW is distinguishable by its relatively cold and fresh characteristics below the poleward flowing warm-saline WDW, a CDW derivative, at about 1000-m depth (Fig. 3a, b, d). Note also the cold and fresh Winter Water at the surface degrading the warm-saline characteristics of CDW. The $\sigma_{41.50}$ isopycnal is seen in Fig. 3d intercepting the upper part of the northward flowing WSDW and some of the southward flowing WDW. Below the $\sigma_{41.50}$ surface, a thick layer of high tracer concentration ($>$ 50%) in the Weddell Sea (40°W$-$ 40°E) characterises the outflowing cold WSDW and WSBW (Fig. 3b,

c, d). On the other hand, bottom water outflow in the Ross Sea is marked by a lower tracer concentration. This indicates that the dominant source of bottom water is from the Weddell Sea in the model. The tracer concentration minima in the Indian−Pacific sector characterises the old recirculated deep waters from the Indian and Pacific basins. Figure 3c also exhibits a downward injection of surface tracers at about the prime meridian to about 1500-m depth, indicating an area of open-ocean convection in the model. It should also be noted at this point that most coarse resolution ocean models ventilate AABW via open-ocean convection. In reality open-ocean convection is rarely observed in the Weddell Sea with AABW ventilated mainly via along-slope convection. The extent of open-ocean convection in the model is already greatly reduced upon the inclusion of the GM parameterisation as compared to the model version without GM (Hirst et al. 2000). As shown in Hirst and Cai (1994), mixing of surface tracers into the interior also occurs via isopycnal diffusion in regions of steeply sloping isopycnals (e.g., at 68°S; see Fig. 4). Such effect of isopycnal diffusivity acts to partly replace explicit convective mixing in injecting surface tracers to depth (Hirst and McDougall 1996; see also Sijp et al. 2006).

Further south at 68.5°S, the AASW contribution to the Weddell Sea deep waters becomes apparent. This is shown by the deep penetration of high tracer concentration from the surface to depth (Fig. 4c). This is an indication of deep convection occurring near the Antarctic shelf slope which is shown to ventilate the model WSDW with colder and fresher AASW. Meredith et al. (2000) suggested from CFC data that WSDW is not merely a recirculation of WSBW, but is also directly sourced from the continental shelf of the Weddell Sea and from locations along the Antarctic continental margin outside the Weddell Sea. The saltier and colder WSBW underneath WSDW (below the $\sigma_{45.95}$ isopycnal surface; Fig. 4a, b) is contributed from

the high-salinity shelf water due to brine rejection (Gordon et al. 2001). As seen in Fig. 4a, b, the cold and salty water is sourced from the surface of the southwestern Weddell Sea, marked by a local maximum of tracer concentration. The $\sigma_{41.50}$ and $\sigma_{45.95}$ isopycnals shoal steeply towards the surface in the southwestern Weddell Sea which is the main region for WSBW formation (Meredith et al. 2000; Gordon et al. 2001). These outcropping isopycnals act as the path for transmission of climate signals into the interior.

It should be noted however that in contrast to the real ocean with WSBW slightly fresher than WSDW (Figs. 3e, f, 4e, f), the model exhibits saltier WSBW than WSDW. Though injection of high salinity water contributes to WSBW formation, there is also a significant influx of fresher shelf water descending along the continental slope at the northern tip of the Antarctic Peninsula as observed by Gordon et al. (2001). Among other possibilities such as mixing and downslope flow parameterisations, this discrepancy is also likely attributed to the model coarse resolution which does not resolve the proper topographic features of the Antarctic Peninsula. In particular, the actual latitude of the tip of the Antarctic Peninsula is at 63°S, while in the model it is at 67°S. A further northward extent of the tip of the peninsula would likely capture fresher AASW fed by sea-ice meltwater in the region. Furthermore, the reduced extent of open-ocean convection under GM contributes to a more realistic bottom water ventilation and properties. Inclusion of a plume convection scheme, though computationally expensive, would result in further improvements with more reduction in open-ocean convection, while the extent of the near-boundary convection is maintained (Duffy et al. 1999; Stössel et al. 2002).

b. AABW spreading and distributions of properties

The spreading of model AABW is apparent in the passive tracer concentration at the bottom-most cells shown at 50 and 150 yr after release (Fig. 5). The bottom current velocities are also shown in Fig. 5 (top panel). The tracer is highly concentrated within the Weddell Sea and Ross Sea, although there is also very minor contribution from the Amery Ice Shelf at about 70°E. The tracer from the Weddell Sea spreads northward into the Argentine Basin and Angola Basin in the Atlantic. Eastward spreading of the WSBW into the Indian Ocean is apparent with decreasing tracer concentration due to mixing with overlying CDW. The tracer concentration distributions on $\sigma_{41.50}$ and $\sigma_{45.95}$ are shown in Fig. 6, capturing the high tracer concentrations from the Weddell and Ross Seas. Note that tracer concentration increases with depth. This is depicted in Fig. 7 showing a scatter plot of tracer concentration along $\sigma_{41.50}$ (shown with dots) and along the bottom-most cells (shown with crosses) against the tracer concentration along $\sigma_{45.95}$ in the Atlantic sector. Note that the denser layer $\sigma_{45.95}$ only captures bottom waters within the Weddell Sea. Relative to tracer concentrations on $\sigma_{45.95}$, the $\sigma_{41.50}$ contains lower concentration when the tracer concentration on $\sigma_{45.95}$ is lower than 75%. The two layers exhibit comparable concentrations when tracer is higher than 75% (as this indicates the influence of convective overturn and therefore mixed subsurface layers). The opposite holds for the bottom-most cells, with $\sigma_{45.95}$ less ventilated as it overlies the bottom grid cells. This suggests that the model $\sigma_{41.50}$ isopycnal captures the WSDW while $\sigma_{45.95}$ marks the WSBW layer, both of which are well ventilated adjacent to Antarctica. Away from the Antarctic margin, the ventilation on $\sigma_{41.50}$ decreases while bottom layers are more rapidly flushed by the northward spreading Weddell Sea variety of AABW.

The $\theta - S$ distributions on $\sigma_{41.50}$ (Fig. 8a, b) show the cold and fresh bottom

water varieties in the Weddell Sea as compared to those in the Ross Sea. This is consistent with the observed $\theta - S$ distributions despite the unrealistic values of salinity. The mean circulation on $\sigma_{41.50}$ is characterised by the eastward flow of the ACC and the cyclonic Weddell Gyre at about 60°W where isopycnals slope steeply (Fig. 8c). The warm and saline characteristics at the northern flank of the Weddell Gyre suggest the presence of WDW. This class of AABW captures the equatorward flow into the Angola Basin in the eastern boundary of the Atlantic Ocean. An inflow of LCDW is also captured in the Argentine Basin. The AABW does not extend beyond the ridge systems bounding the Australian-Antarctic and the Southeast Pacific basins. Figure 9 shows the difference between $\theta - S$ on the $\sigma_{41.50}$ and $\sigma_{45.95}$ surfaces, revealing that the upper layer is warmer and fresher than the lower layer within the Weddell Gyre. However, outside the Weddell Gyre, the upper layer is warmer and more saline. This implies input from fresh surface water, mixing with CDW in the upper layer within the Weddell Gyre. The lower layer receives its saltier characteristics from brine rejection during sea-ice formation at the shelf. Mixing with the purer form of CDW in the upper layer is more apparent outside the Weddell Gyre, giving it a more saline signature than the lower layer in those regions.

c. Summary

The $\rho_3 = 1041.50$ kg m^{-3} density surface (referred to as $\sigma_{41.50}$) is chosen in this study as the separation boundary between AABW and the overlying LCDW. AABW in the model is therefore defined as the layer beneath $\sigma_{41.50}$, with significant contribution from the Antarctic surface and shelf waters. The model interior is considerably lighter than the observed as characterised by bottom waters that are too fresh. Examination of passive tracer concentration distribution suggests the

model bottom water formation is too restricted in the Weddell Sea with injection of Antarctic surface and shelf waters into the interior. Nevertheless, there is still decent agreement between the model and observed AABW $\theta - S$ distributions and pathways. This sets the motivation to further investigate the AABW variability in the model.

4. Structure and propagation of $\theta - S$ anomalies

A standard deviation analysis of $\theta - S$ along $\sigma_{41.50}$ and $\sigma_{45.95}$ reveals largest magnitude variability within the proximity of the Weddell and Ross Seas where bottom water formation takes place in the model (Fig. 10). The largest standard deviation of $\theta - S$ is of the order of 0.15°C and 0.01 psu. The magnitude of variability is considerably reduced further northward. The apparent obstruction of the AABW pathway eastward from the Ross Sea (near $\approx$ 168°W, not evident in Fig. 8) is an artifact of the analysis over 1000 yr; in particular, in some years the density in the region can be slightly lighter than the potential density $\rho_3 = 1041.50$ kg m^{-3} (and so is excluded in the analysis). On the other hand, the density calculation to define the domain shown in Fig. 8 is based on the 1000-yr averaged $\theta - S$ resulting in a density layer in the region ($\rho_3 = 1041.50$ kg m^{-3}) with fewer topographic obstructions. The 'missing values' in Fig. 10 are not included in the calculation of the variability analyses to ensure temporal continuity. Thus, the Ross Sea region appears to be isolated. Furthermore, since the model AABW is predominantly produced in the Weddell Sea, we focus the rest of our analyses on the AABW variability sourced from the Weddell Sea.

A CEOF analysis is conducted to examine various modes of $\theta - S$ variability along $\sigma_{41.50}$ and $\sigma_{45.95}$. Since $\theta - S$ vary coherently along constant density surfaces, it is sufficient just to present the analyses of S. The propagation of $\theta - S$ anomalies along

$\sigma_{41.50}$ ($\sigma_{45.95}$) are depicted in the CEOF maps in Fig. 11 (Fig. 12) presenting the three leading modes explaining 76.5% (68%) of the total S variance. These modes are well separated according to the North's rule (North et al. 1982). The temporal evolution of the modes represented by the principal component (PC) timeseries and the power spectral density are presented in Fig. 13.

Inspecting Figs. 11 and 12, the CEOF modes on both $\sigma_{41.50}$ and $\sigma_{45.95}$ mainly exhibit large anomalies emerging in the southwestern Weddell Sea which propagate eastward and then northward into the Atlantic. Note that the isopycnal surfaces outcrop near the surface in this region (see Fig. 4). The first mode is characterised by fluctuations with 77−91-yr periods which dominate the variability on $\sigma_{45.95}$. A 333-yr periodicity is also notable on $\sigma_{41.50}$. This multi-centennial periodicity is the dominant timescale of $\theta - S$ variability in the CDW layer (Santoso et al. 2006). On the other hand, the CEOF2 mode captures variability characterised by interannual to multi-decadal fluctuations, with shorter timescale variability more prominent on $\sigma_{45.95}$. The 333-yr signal is evident on both $\sigma_{41.50}$ and $\sigma_{45.95}$ with a relatively weak spectral amplitude. CEOF3 also exhibits interannual to multi-decadal variability, with a pronounced 34.5-yr peak on $\sigma_{45.95}$. The spatial phase of CEOF3 (Fig. 11b) suggests a propagation path following the cyclonic Weddell Gyre. However, overall, the anomalies appear to originate from the southwestern Weddell Sea (marked by the box shown in Fig. 11) where the $\sigma_{41.50}$ and $\sigma_{45.95}$ isopycnals outcrop near the surface.

The advective time scale of the propagation of $\theta - S$ anomalies along isopycnals is apparent in the Hovmöller diagram of $\theta - S$ anomalies presented across 62°S on $\sigma_{41.50}$ (Fig. 14a, b; see Fig. 11a, top panel, for the zonal transect location). The Hovmöller diagram gradients of the anomalies suggest the speed of the travelling signals covering 125° longitude over $\approx$ 50 yr. At 62°S, this corresponds to a speed

of $\approx$ 0.4 cm s^{-1} comparable to ocean current velocities in the region. Low frequency signals are found west of 60°W in the Pacific sector (Fig. not shown) which contribute to the multi-centennial time scale characteristic revealed in the CEOF variability modes.

The shoaling (deepening) of $\sigma_{41.50}$ implies an increase (decrease) of AABW density and thickening (thinning) of the AABW layer. A Hovmöller diagram of the $\sigma_{41.50}$ isopycnal depth anomalies presented in Fig. 14c infers the propagation of density anomalies faster than the propagation of $\theta - S$ anomalies along the isopycnal. Anomalies propagate eastward from 31°W to 25°E before intercepting a westward wave propagation. Inspecting the gradients of the westward signals suggests the time taken to travel 45° of longitude is about 5 years which implies a speed of up to $\approx$ 1.5 cm s^{-1}, matching the speed of baroclinic Rossby waves given by $c = \beta g^{'} H_0 / f^2$, where $g^{'}$ is the reduced gravity, f the Coriolis parameter, β the meridional derivative of f, and H_0 the layer thickness. A scaling analysis yields typical values of the following parameters in the region: $g^{'} = 0.01$ m s^{-2}, $f = -1.3 \times 10^{-4}$ s^{-1}, $\beta = 1.14 \times 10^{-11}$ m^{-1} s^{-1}, and $H_0 = 2000$ m, which yields $c \approx 1.4$ cm s^{-1} at 60° latitude. On the other hand, the speed of the eastward propagating signals is of the order of 0.5 cm s^{-1} which is comparable to the background mean circulation velocity.

Along-isopycnal $\theta - S$ variability is in general accompanied by displacement of the AABW isopycnal surfaces (i.e., heave). Variability of $\theta - S$ along isobars is composed of the along-isopycnal component and $\theta - S$ changes due to heaving of the isopycnals (Bindoff and McDougall 1994). While climate anomalies are transmitted into the ocean interior along isopycnals, heaving of isopycnal surfaces can be attributed to either one or a combination of baroclinic wave propagation, variations in the volume of CDW and AABW, and gyre spin. Inspection of the patterns of Fig. 14a–e

suggests that the propagation of density anomalies is imprinted in the evolution of θ anomalies *along isobars* (Fig. 14e). Note that the along-isobar component is referenced to $\theta - S$ fluctuations along the *1000-yr mean* of the $\sigma_{41.50}$ isopycnal depth. This implies that θ variability along the isobar is related to isopycnal heaving which reflects propagating density perturbations. On the other hand, salinity variability is dominated by along-isopycnal anomalies as suggested by the similarity of the Hovmöller patterns shown in Fig. 14a and 14d.

The propagating $\theta - S$ anomalies away from the Weddell Sea are further masked by baroclinic wave propagation as shown by the the Hovmöller diagrams of $\theta - S$ and isopycnal depth anomalies (h_σ) along a meridional section in the Atlantic sector (Fig. 15; see Fig. 11a, top panel, for the transect location). Along-isopycnal $\theta - S$ anomalies are most notable within the subpolar region south of 40°S, and become less apparent with the northward outflow into the Atlantic interior where variations due to heave become prominent. The opposite sign of θ anomalies along isobars and along isopycnals suggests a dominating effect of isopycnal heaving. For instance, concurrent with a negative θ anomaly (cooling) along isobars, the isopycnal shoaling towards the warmer water above preserves a warming (and salination) signal along the isopycnal. On the other hand, the salinity component of the heave effect appears to be less dramatic than that of θ, because of the relatively weak salinity stratification. Note that the slower northward propagation speed of the along-isopycnal component as compared to h_σ is apparent as shown by the steeper slope of the anomaly patterns in Fig. 15a, b, than in Fig. 15c. The signature of fast baroclinic waves (Fig. 15c) is visible in the along-isobar anomalies (Fig. 15d, e). At about year 200, there is a cooling and freshening signal along the isopycnal. Instead, a warming and less pronounced freshening are observed along isobars which is accompanied by a deepening of the isopycnal surface towards the

colder water below. Thus, the action of isopycnal heaving maintains the structure of the anomalies along the isopycnal. Note that although the wave propagation speed is faster than the advection speed, the frequency of h_σ variability is similar to $\theta - S$ variability. This suggests a variability mechanism at the formation region where $\theta - S$ variability along isopycnals is connected to density fluctuations. The mechanisms for this variability are investigated in the next section.

It is worth mentioning that the magnitude of the maximum decadal $\theta - S$ changes along isopycnals in the model is of the order of 0.1°C, 0.01 psu in the Weddell Sea and 0.01°C, 0.001 psu in the Atlantic interior near 43°S. This seems to be comparable to the magnitude of $\theta - S$ changes in the observations on decadal time scales (see section 1). Note that the magnitude of the decadal $\theta - S$ changes along isobars in the Weddell Sea are of similar order of magnitude as the along-isopycnal components. In the Atlantic interior, however, the along-isobar components are larger than the along-isopycnal components. For instance, the decadal change magnitude of 0.01°C, 0.001 psu along isobars is found further north up to about 27°S. In another modelling study, Stössel and Kim (2001) documented a similar order of magnitude. However, the study by Stössel and Kim (2001) focusses on θ anomalies at a fixed depth and found a propagation speed matching baroclinic Kelvin waves. Here, we have described $\theta - S$ anomalies on both isopycnal and isobaric surfaces.

5. Variability mechanisms

a. Connection with overturning variability

The generation of the $\theta - S$ anomalies in the southwestern Weddell Sea is plausibly linked to AABW formation rates and/or properties, which are in turn linked to density at the near-Antarctic surface layer as set by sea-ice formation and air-sea heat/freshwater fluxes. In this analysis we take the rate of the Antarctic meridional

overturning integrated zonally over the Atlantic sector (see Fig. 2 of Part II) as an indicator of the formation rate of the Weddell Sea component of AABW. The Weddell component of AABW overturning is significantly correlated to the surface density in the southwestern Weddell Sea at 0.59 correlation coefficient with the surface density leading by 2 years (Fig. 21a). The time series of the meridional overturning (Weddell Sea AABW overturning hereafter) is displayed in Fig. 16a exhibiting multi-decadal signals (Fig. 16b). Spectral peaks above the red-noise signal appear at $\approx$ 21 and 35-yr periods. Note that the Atlantic and global AABW meridional overturning are correlated with a coefficient of 0.87, suggesting the dominant role of the Weddell Sea in the total model AABW overturning (see also Fig. 16a).

The connection of $\theta - S$ anomalies with density variability in the Weddell Sea can be assessed in conjunction with the Weddell Sea AABW overturning. Note that there is a significant coherence between Weddell Sea AABW overturning and the CEOF1-3 modes on $\sigma_{41.50}$ and $\sigma_{45.95}$ (see Fig. 17a, b, where the plot has been extended for CEOF4−6; the CEOF1-3 principal components are shown in Fig. 13). Weddell Sea AABW overturning is associated with longer time scale modes of variability on $\sigma_{41.50}$ than the corresponding modes on $\sigma_{45.95}$ (Fig. 17). This is because AABW directly ventilates the abyssal layers of the Southern Ocean, whereas $\sigma_{41.50}$ includes a component of CDW.

Composite analyses are conducted to investigate the anomalous state of $\theta - S$ and density during years of extreme Weddell Sea AABW overturning. High (low) Weddell Sea AABW overturning years are defined as those that exceed one standard deviation above (below) the long-term mean. High (low) AABW overturning in the Atlantic is accompanied by the shoaling (deepening) of the $\sigma_{41.50}$ and $\sigma_{45.95}$ isopycnal surfaces in the Weddell Sea, which implies a density gain (loss) in the region. This is depicted in Figs. 18, 19 (top panel) showing the composite anomalies of

the $\sigma_{41.50}$ and $\sigma_{45.95}$ isopycnal depth during years of extreme AABW overturning. The shoaling (deepening) of isopycnal surfaces is accompanied by warming and salination (cooling-freshening) signals along isopycnal surfaces within the Weddell Sea trailing the cooling and freshening (warming-salination) signals to the east. These dipole anomalies are a combination of the CEOF modes shown in Figs. 11 and 12 which appear to originate from the southwestern Weddell Sea. On the other hand, the composite anomalies along the mean depth of the $\sigma_{41.50}$ surface show an extensive cooling (warming) signal with salinity anomalies retaining the dipole pattern (Fig. 20). This demonstrates the dominance of along-isopycnal characteristics of the salinity variability. The θ variability at depth is dominated by along-isobaric variability which corresponds to density fluctuations, thus the shoaling and deepening of isopycnal surfaces.

The connection between Weddell Sea AABW overturning and density is illustrated in Fig. 21a showing the correlation values of the overturning versus the spatially averaged density field over the southwestern Weddell Sea, from the surface to the deepest level at various time lags (see Fig. 11a, middle panel, for the region used for spatial averaging). This shows that in general, the sea surface density has first increased 2 years prior to the increase in overturning, and that density then continues to increase with depth over the next 25 years. A similar correlation against $\theta - S$ (Fig. 21b, c) reveals positive (negative) $\theta - S$ anomalies created at the sea surface a few years prior to a strengthened (weakened) Weddell Sea AABW overturning. Since salination (freshening) signals correspond to an increase (decrease) in density despite warming (cooling), salinity thus controls the density variations at the surface. The surface density anomaly is then transmitted into the interior via the model convection scheme (see section 2) influencing the overturning rates in the Weddell Sea.

The transmission of surface density anomaly to depth is illustrated in Fig. 22a showing a lagged correlation between surface density and the density throughout the water column, which is in phase with the transmission of SSS anomaly into the interior (Fig. 22b). The salinity and the corresponding θ variability are then transmitted into the interior along isopycnals, resulting in the $\theta - S$ variability patterns captured by the CEOF modes (Figs. 11, 12) and the composite maps shown in Figs. 18 and 19. However, the negative correlation of θ and overturning shown in Fig. 21c and the weak negative correlation between SST and θ at depth (Fig. 22c) indicate diapycnal processes dominating the θ variability in the interior.

Figure 23a-e presents the composite anomalies of $\theta - S$, and ocean current velocities over the southwestern Weddell Sea during the extreme years of AABW overturning. The mean values are presented in the bottom figure panels for reference. Note that the variables are spatially averaged over the region in the southwestern Weddell Sea as indicated in Fig. 11a, except for u which is averaged over the eastern face of the box, and v over the northern face. The cooling (warming) at fixed depths (Fig. 23a) in the interior can be explained by the intensification (suppression) of mean downwelling during high (low) Weddell Sea AABW overturning (Fig. 23e, j), injecting more (less) cold water from above. Note that the reduction (increase) in downward velocity below 2500 m indicates the shallowing (deepening) of the Weddell Sea AABW overturning cell during rapid (slow) overturning years. The anomalous state of the zonal velocity is shown in Fig. 23c, exhibiting increased eastward transport above 1000 m, and a reduction in the weak westward flow at mid-depth. During high (low) overturning, there is an intensification (reduction) of WDW inflow and Weddell Sea deep and bottom waters outflow (Fig. 23d, i). The resulting heat-salt anomalies from this interior circulation tend to be mostly along isopycnals, so they do not perturb density, except near the surface layer where the

heat supplied by WDW inflow may influence sea-ice processes.

Figure 24 presents the correlation between $\theta - S$ and the heat-salt advective fluxes in the upper 500 m. The negative correlation at about 200-m depth between θ and the zonal advection ($u\theta_x$) suggests a decrease in θ due to increased eastward transport, advecting heat out of the region (since $\theta_x > 0$; Fig. not shown). The subsurface heating at 100−300 m is related to the increased influx of CDW as shown by the negative correlation between the meridional advection ($v\theta_y$) since negative $v\theta_y$ implies an increased heat flux ($\theta_y > 0$). This heat is injected upward as suggested by the mean upward velocity in the upper 200 m (Fig. 23j) with a negative vertical θ gradient (Fig. not shown). However, there is a decrease in θ at the upper 100 m, despite the subsurface heating. Furthermore, the corresponding increased upward salt flux ($wS_z < 0$) is related to a decrease in salinity (Fig. 24f). This can be explained by sea-ice melting induced by the inflow of CDW which has the effect of decreasing $\theta - S$ at the surface layer. Furthermore, considering the low-frequency characteristics of $\theta - S$ anomalies within the CDW layer (Santoso et al. 2006), it is most likely that the along-isopycnal $\theta - S$ variations on centennial and longer time scales are contributed from CDW $\theta - S$ variability. The higher-frequency variability is likely contributed from localised air-sea processes that have a direct impact on surface heat-salt fluxes and on interior $\theta - S$ as described above, via changes in ocean circulation.

Finally, it is worth noting that while the AABW overturning responds to the Weddell Sea density variations (Fig. 21a), there is also significant positive correlation between the AABW overturning and the depth integrated ACC transport through the Drake Passage (DP transport; Fig. 25b). Density increase (decrease) in the Weddell Sea enhances (reduces) the meridional isopycnal slope thereby enhancing (reducing) DP transport via geostrophic adjustment. This is shown by the positive

correlation between the DP transport and the southwestern Weddell Sea density, which extends to the surface (Fig. 25a). Hence, variations in the surface density in this region also influence the net transport in the ACC.

b. The role of air-sea and ice-sea fluxes

The importance of sea-ice processes on AABW formation is well established. Stössel et al. (1998) showed using a coupled sea ice-ocean GCM that AABW formation is strongly coupled to local sea-ice processes around the Antarctic margin. They noted the importance of brine rejection and the role of the Southern Ocean winds over sea ice in setting AABW formation rates. Furthermore, there is evidence in the observations to suggest the influence of Southern Ocean climate variability modes such as the Southern Annular Mode (SAM) and the Antarctic Circumpolar Wave (ACW) on bottom water variability in the Weddell Sea (White and Peterson 1996; Fahrbach et al. 2004; Jacobs 2004).

The influence of sea surface density in the southwestern Weddell Sea over the AABW overturning has been demonstrated in section 5a. An increase in AABW overturning is preceded by an increase in the surface density which is accompanied by positive $\theta - S$ anomalies (Fig. 21), implying the dominance of salinity over temperature on density variations. Note that the positive correlation between SST and SSS (Fig. 26) suggests the tendency for $\theta - S$ to vary toward density-compensation over the Southern Ocean (see also Rintoul and England 2002; Santoso and England 2004). Comparisons of the standard deviations of the surface heat and salt budget terms over the southwestern Weddell Sea (Tables 3, 4) suggest that the net surface heat and salt fluxes dominate the annual-mean SST and SSS variability. Shortwave radiation (Q_{solar}) dominates the surface heat flux variability, while the surface freshwater flux is dominated by variations in the sea-ice meltwater rate.

By means of composite analyses, we further provide an overview of the anomalous atmosphere-ocean conditions corresponding to anomalous SSS spatially averaged over the southwestern Weddell Sea (denoted as SSS_{wed}; see the boxed region in Figs. 11, 26 for the location of spatial averaging). We focus here on SSS as salinity, not temperature, dominates in regulating surface density in the Weddell Sea AABW formation region. The composite anomalies of atmospheric variables such as wind stress, ocean current velocities and atmospheric and sea-ice heat-freshwater fluxes are computed based on the years of extreme SSS_{wed} which are defined as years when the salinity exceeds one standard deviation above/below the long-term mean. The time series and power spectrum of SSS_{wed} are presented in Fig. 27. Note the spectral peaks at frequencies of ≈ 0.011, 0.03, and 0.05 cycle per year approximately matching those of the Weddell Sea AABW overturning (Fig. 16) and PC1−3 on $\sigma_{41.50}$ and $\sigma_{45.95}$ (Fig. 13). Seasonality is taken into account by presenting the results for the surface heat-freshwater fluxes in terms of the annual-mean, the summer (averaged over December−March), and the winter (averaged over June−September) composites. Note that the composite anomalies of the variables for the seasons/years of anomalously low salinity are the converse of the high salinity composites. Thus, it is sufficient to focus the discussion on the results of the high salinity composite analysis.

The composite maps for the SSS and SST are displayed in Fig. 28a, b showing warming and salination in the southwestern Weddell Sea (marked by the box in the composite figures). Years of highly saline Weddell surface water are accompanied by a strengthening of zonal winds, driving sea ice northward via Ekman transport as indicated by the anomalous northward meridional flow (Fig. 28f). This is accompanied by an anomalous reduction in the annual-mean sea ice concentration which is mainly dominated by summer-time sea-ice variations (Fig. 29). The winter months

exhibit little anomalous sea-ice concentration in the Weddell Sea, yet they are accompanied by positive ice-ocean salt flux anomalies. This apparent contradiction is explained further below. Note that as would be expected there is a mean sea-ice meltwater flux during summer (Fig. not shown). Thus, the positive summer ice-ocean salt flux anomalies imply a decrease in sea-ice melting, not an increase in brine rejection. Increased northward sea-ice transport by anomalous wind is therefore the most plausible cause of the anomalous decline of the summer sea-ice concentration in the region.

The reduction in the summer sea-ice cover induced by anomalous winds allows enhanced ocean cooling by latent and sensible heat fluxes (Figs. 30, 31, top panel). However, this is also accompanied by an anomalous increase in short-wave radiation absorbed by the ocean over the summer period (Fig. 31, bottom panel), resulting in a positive annual-mean air-sea net heat flux anomaly into the ocean (Fig. 28h). Approaching winter, enhanced atmospheric cooling over the larger than normal ice-free area leads to higher than average brine rejection as shown by the positive anomalies of winter ice-to-ocean salt fluxes (H_{ice}; Fig. 29). This results in a higher than average net salt flux into the ocean, but the ice concentration itself is merely recovering to normal wintertime levels (Fig. 29, top right panel). This indicates that a negative ice-ocean feedback loop is limiting wintertime ice anomalies despite substantial variations in ice-ocean salt fluxes.

Anomalously low summer precipitation (Fig. 30, bottom panel) also partly contributes to the positive net salt-flux anomalies described above. It is worth mentioning that during this unusually high salination period, there is an area of enhanced winter sea-ice meltwater north of 60°S (northern face of the boxed region; Fig. 29), due to the enhanced westerlies. Isopycnal surfaces associated with AAIW outcrop in this region of winter meltwater input (Santoso and England 2004). Just to the south

of this area is a region of higher sea-ice concentration (Fig. 29, top right panel). Together with the resulting anomalous sensible and evaporative cooling during winter (Figs. 30, 31, top panel), the anomalous meltwater flux results in cooling and freshening signals into the AAIW layer. The anomalous winter meltwater and the sensible and evaporative fluxes at the limit of the winter sea-ice margin result in various circumpolar patterns of $\theta - S$ anomalies along the AAIW layer (see Part I).

c. Link to Southern Ocean climate modes

The anomalous atmosphere-ocean conditions described above that result in the SSS variability over the southwestern Weddell Sea (SSS_{wed}) are likely influenced by a combination of climate variability modes in the Southern Ocean. The purpose of this section is to provide a preliminary evidence on such plausibility. A careful and thorough analysis on the Southern Ocean modes and the mechanisms in driving variability of AABW is left for future research. Nonetheless, we present an identification of the Southern Ocean climate modes by conducting EOF analyses of the annual-mean SST. The resulting principal component time series are then correlated with SSS_{wed} (Fig. 33). The spatial patterns of the first six leading EOF modes are displayed in Fig. 32, exhibiting SST responses to well known climate modes such as the SAM (EOF3), the ACW (EOF4), and the Pacific-South American oscillation (PSA; EOF2). A wavenumber-3 pattern exhibited by EOF6 is also referred to as the ACW by Cai et al. (1999) in a similar version of the model. However, caution needs to be taken when attributing physical mechanisms to the above modes. This is because modal mixing is expected as indicated by the closeness of the eigenvalues between the adjacent modes. To test the robustness of the modes, a rotated EOF (REOF) analysis based on the varimax criterion (Richman 1986) is conducted. The first three EOFs are captured by the leading REOFs (Fig. not shown), while

EOF4 − 6 appear to be degenerate. Therefore, we shall put an emphasis on EOF3 in the following analysis.

Figure 33 reveals that the correlation of SSS_{wed} is high against EOF3, 5, and 6 (Fig. 32). The physicality of the modes can be revealed by inspecting the composite anomalies of the wind stress components corresponding to the EOF3, 5, and 6 SST modes shown in Fig. 34. It is apparent that the EOF3 and EOF5 SST modes are a response of a zonally symmetric (or equivalently, a meridional dipole pattern) zonal wind stress which characterises a positive SAM index (e.g., Hall and Visbeck 2002; Sen Gupta and England 2006). The wavenumber-3 pattern of the meridional wind stress composites for EOF3 corresponds to that of the SST mode (see also Cai et al. 1999). Referring to Fig. 28, the SAM signature appears to be the most prominent in the wind stress composites based on extreme phases of SSS_{wed}. The zonal and meridional ocean current velocity composites also exhibit an apparent response to the wind stress during a SAM event (Hall and Visbeck 2002; see their Figs. 4, 5). Therefore, EOF3 may well represent SAM which is shown to correlate to the salinity variability in the southwestern Weddell Sea (Fig. 33). Furthermore, coherence analysis between EOF3 and SSS_{wed} indicates a significant coherence on interannual to interdecadal time scales of $\approx$ 20 years (Fig. not shown). Finally, it is noted that changes in the wind circulation may also impact on the Weddell Gyre which can affect the propagation of $\theta - S$ anomalies and the depth of isopycnals near regions of WSBW formation.

6. Summary

The natural variability of AABW and its mechanisms have been analysed using a 10,000-yr integration of a coupled climate model. Examination of passive tracer concentrations suggests the model AABW is predominantly sourced in the Weddell

Sea, with less contribution from the Ross Sea and insignificant bottom water formation in the Adélie Land region which is in contrast to observations. For example, Rintoul (1998) found that the Adélie coast may be a more substantial source of bottom waters than previously thought. This deficiency is common in coarse resolution GCMs which is likely due to inadequate representation of dense water overflow, convective processes, and surface boundary conditions (see also Doney and Hecht 2002). Despite the unrealistic simulation of salinity and density in the interior, which is also common in GCMs at both high and low resolutions, the model simulates AABW pathways and property distribution that are reasonably consistent with observations. This motivates the analysis of AABW variability in the model.

We analyse 1000 years of model data from the latter stages of the 10,000-yr run, which exhibits very minimal drift at this late stage of the integration. A 'patched' isopycnal surface corresponding to a potential density $\rho_3 = 1041.50$ kg m^{-3} referenced to 3000 db ($\sigma_{41.50}$) is selected to mark the boundary separating AABW and the overlying CDW. The selection criteria involved inspection of $\theta - S$, pathways, and tracer concentrations along a meridional transect across the Drake Passage and zonal transects across latitudes closer to Antarctica. An analysis of the propagation of $\theta - S$ anomalies is conducted along the $\sigma_{41.50}$ and along a deeper isopycnal surface ($\sigma_{45.95}$; referenced to 4000 db) which is chosen to capture the Weddell Sea Bottom Water in the model. Since the density in the Ross Sea region can be lighter than $\rho_3 = 1041.50$ kg m^{-3} over the 1000 years, so breaking up the time series of properties on that surface, we focus our analysis on the Weddell Sea variety of AABW.

The first three dominant CEOF modes of $\theta - S$ variability along the isopycnal surfaces are presented showing propagation of $\theta - S$ anomalies from the southwestern Weddell Sea into the Atlantic interior. The first mode is characterised by fluctuations

with 77−91-yr periods which are more prominent along $\sigma_{45.95}$. A 333-yr periodicity is notable on $\sigma_{41.50}$ which is the dominant timescale of $\theta - S$ variability in the CDW layer (see Part II). Pronounced interannual to multi-decadal fluctuations are captured by the higher variability modes. It may be noted that the magnitude of the maximum decadal $\theta - S$ changes in the model is of the order of 0.1°C, 0.01 psu in the Weddell Sea and reduces to 0.01°C, 0.001 psu in the Atlantic interior. This is comparable to the observed decadal changes documented by Coles et al. (1996), Meredith et al. (2001), and Fahrbach et al. (2004).

Salinity variability was shown to be dominated by along-isopycnal propagation of S anomalies. On the other hand, θ variability is dominated by signatures of isopycnal heaving which exhibits propagation of density anomalies with the speed of baroclinic waves (see also Stössel and Kim 2001). The matching frequency between propagation of $\theta - S$ anomalies along isopycnals and density anomaly propagation suggests that there is a coherent variation of $\theta - S$ with AABW formation rates.

The Weddell Sea AABW overturning in the model was shown to be linked to density at the surface layer in the southwestern Weddell Sea. Sea surface density has first increased 2 years prior to the increase in overturning, and then continues to increase with depth over the next 25 years. This is accompanied by positive $\theta - S$ anomalies created at the surface a few years prior to the strengthened Weddell Sea AABW overturning, suggesting that salinity (not temperature) variations largely control fluctuations in the Weddell Sea component of AABW formation rates. Therefore, during high overturning there is a warming and salination observed along isopycnals in the Weddell Sea region. However, this is accompanied by a cooling and salination along isobars, and shoaling of isopycnal surfaces due to an increase of density. This cooling at fixed depths can be explained by an enhanced mean downwelling which injects more cold waters from the surface during strong overturning.

Furthermore, there is an intensification of CDW inflow and a corresponding increase in outflow of Weddell Sea deep and bottom waters. The resulting heat-salt anomalies due to this anomalous interior circulation are unlikely to perturb density as they tend to be mostly density compensating. However, within the subsurface layer beneath sea ice, the increased influx of CDW induces subsurface heating resulting in sea-ice melting which has the effect of decreasing $\theta - S$ in the surface layer.

The importance of variability in the zonal wind stress in the southwestern Weddell Sea is highlighted. Heat-salt budget analyses in the region suggest the dominance of solar radiation (via sea-ice coverage variability) and ice-sea salt fluxes in driving $\theta - S$ variability. Employing composite analyses, we propose that enhanced westerlies drive lower than average sea-ice concentrations during summer which creates a larger exposed area for enhanced solar heating of the ocean. Approaching winter, the larger than normal ice-free area exposed to atmospheric cooling leads to higher than average ice re-growth and ensuing brine rejection. This mechanism results in a warming and salination signal in the region (characterised by higher densities, hence S effects dominate), leading to years of enhanced Weddell Sea AABW overturning and transmission of positive $\theta - S$ anomalies along isopycnals into the interior.

It is noted that the enhanced westerlies also drive an increased winter sea-ice meltwater north of 60°S where isopycnal surfaces associated with AAIW outcrop. Together with the increased winter wind-driven sensible and evaporative cooling, this results in cooling and freshening signals along the AAIW layer as described in Part I. Preliminary analyses suggest that there is evidence of the Southern Ocean climate variability modes, particularly the SAM, impacting on AABW variability on interannual to interdecadal time scales. This is possible because the enhanced westerlies during positive SAM events can trigger the mechanism described above.

Further studies will be carried out to investigate how the quasi-periodicities observed in the AABW layer and the overturning actually arise. From analyses in this chapter, it appears that the variability on interannual to interdecadal time scales are most likely driven by the SAM (see section 5c). Oceanic mixing would certainly play a role in enhancing the low-frequency signals transmitted from the surface into interior. On the other hand, the multi-decadal signals may be sourced from feedback mechanisms involving the rate of inflow of CDW and sea ice via ocean advection which is in turn connected to the wind gyre (see section 5a, b). These complex mechanisms will certainly be the focus of future research for further understanding of AABW variability.

Table captions

Table 1: Density equivalence at model depth levels corresponding to $\sigma_3 = 41.50$ kg m^{-3} in the three ocean sectors. The values of σ_p are determined based on a matching procedure using a linear fit by least squares in a plot of density values σ_n versus σ_3 at the mid pressure between the corresponding reference pressures, where $n = 0, 1, 2, 4$.

Table 2: As in Table 2 but for $\sigma_4 = 45.95$ kg m^{-3}.

Table 3: Standard deviation of the annual-mean surface heat budget terms over 1000 years spatially averaged over the region indicated in Fig. 29.

Table 4: Standard deviation of surface salinity budget terms. The terms are calculated as for those in Table 3. For consistency of units, evaporation and precipitation have been converted to equivalent salt fluxes (psu s^{-1}).

Figure captions

Figure 1: Zonally averaged salinity fields in the Atlantic (a, b), Indian (c, d), and Pacific (e, f) sectors in the model (left column) and Levitus et al. (1994; right column). The σ_2 density (referenced to 2000 dbar) is shown by thin black contours with an interval of 0.02 kg m^{-3} (0.04 kg m^{-3}) for the model (Levitus climatology). The thick black contour marks 0°C. The thick red contour marks the mean position of $\sigma_{41.50}$ isopycnal defined in the text (section 2b; see Table 1). The grey-scale colour scheme is consistent for all figure panels.

Figure 2: Transect across the Drake Passage in (a-d) the model at 67.5°W showing (a) salinity, (b) potential temperature, (c) passive tracer concentration at 150 yr after release, and (d) zonal velocity. The mean position of $\sigma_{41.50}$ isopycnal is marked by contour. (e), (f) The corresponding cross-sections of $\theta - S$ in the Levitus climatology.

Figure 3: As in Fig. 2 but for a zonal transect across 62.1°S. The dashed contour in (a-d) marks the mean position of $\sigma_{45.95}$ isopycnal surface. The dashed horizontal line in (e), (f) marks the deepest model level.

Figure 4: As in Figs. 2, 3 but for a zonal transect across 68.5°S.

Figure 5: Passive tracer concentration at the bottom-most model level at 50 yr (top panel) and 150 yr (bottom panel) after release at the surface. Mean current velocities at the bottom-most level are shown by the vectors in the top panel. The model bottom relief are presented by thick contours marking the 4000-m depth and thin contours marking 3000-m depth.

Figure 6: Passive tracer concentration on the $\sigma_{41.50}$ and $\sigma_{45.95}$ isopycnal surfaces at 150 yr after release.

Figure 7: Tracer concentration at 150 yr after release for the Atlantic sector on $\sigma_{41.50}$ versus that on $\sigma_{45.95}$ (dots) and for the bottom-most model level versus $\sigma_{45.95}$ concentration (crosses).

Figure 8: Mean potential temperature (a) and salinity (b) along $\sigma_{41.50}$. (c) Mean circulation (current vectors) and the depth of $\sigma_{41.50}$.

Figure 9: Difference of $\theta - S$ on $\sigma_{41.50}$ and $\sigma_{45.95}$.

Figure 10: Standard deviation of $\theta - S$ on (a, b) $\sigma_{41.50}$ kg m^{-3} and (c, d) $\sigma_{45.95}$.

Figure 11: (a) Spatial maps of the three leading complex EOF modes of salinity shown at 90° phase intervals along $\sigma_{41.50}$. The first (CEOF1), second (CEOF2), and third (CEOF3) modes account for 42.4%, 21.9%, and 12.2% of the salinity variance, respectively. An equivalent CEOF analysis of θ shows similar modal structure and so is not shown here. (b) Spatial phase angle CEOF1−3 indicating the direction of phase propagation of each mode from 0° to 360°. Apparent phase discontinuities occur because the phase is defined only between 0° and 360°. The horizontal and vertical lines shown in the CEOF1 map (top row, middle column) mark the position of the transects for the Hovmöller diagrams shown in Figs. 14, 15. The box in the middle and bottom rows (middle column) indicate the southwestern Weddell Sea region for analysis in section 5.

Figure 12: As in Fig. 11, but for $\sigma_{45.95}$. Each mode CEOF1−3 accounts for 34.2%, 18.4%, and 15.4% of the total salinity variance, respectively.

Figure 13: (left column) Principal component time series of CEOF1−3 shown for $\sigma_{41.50}$ (black) and $\sigma_{45.95}$ (grey). (right column) The corresponding power spectral density (PSD) of the principal component time series with an estimated

AR-1 background spectrum at 90% confidence level (dashed curves). A $\log_{10}$ scale is used in frequency to give more weight to the higher frequency signals and the power spectra are multiplied by frequency to preserve variance.

Figure 14: Hovmöller diagram of (a, b) $\theta - S$ anomalies along isopycnal, (c) isopycnal depth anomalies, and (d, e) $\theta - S$ anomalies along isobar on $\sigma_{41.50}$ along a zonal transect at 62° from 60°W to 87°E (see bottom right inset for the transect location; also shown in Fig. 11a). The along-isobar $\theta - S$ anomalies are calculated as deviations from the 1000-yr mean along the mean isopycnal depth of $\sigma_{41.50}$.

Figure 15: As in Fig. 14, but for the meridional transect shown in the bottom right inset (see also Fig. 11a).

Figure 16: (a) Time series of maximum Antarctic meridional overturning rate for the global average (gray) and the Atlantic basin (black). The dashed lines indicate one standard deviation unit above and below the mean for the Atlantic sector overturning. The Atlantic sector overturning is referred to in the text as the Weddell Sea AABW overturning. (b) Power spectral density of the Atlantic sector AABW overturning with the fitted red-noise spectrum at 90% confidence level (dashed curve).

Figure 17: Coherence spectra between the Weddell Sea AABW overturning and the first six leading CEOF principal components of S on (a) $\sigma_{41.50}$ and (b) $\sigma_{45.95}$, only shown here significant at the 95% confidence level. Note that the first three modes account for *approx* 70% and CEOF4−6 account for $\approx$ 20% of the total variance.

Figure 18: Composite anomalies of $\sigma_{41.50}$ (top) isopycnal depth, (middle) potential temperature, and (bottom) salinity for the high (left column) and low (right

column) AABW overturning extremes. High (low) AABW overturning refers to overturning anomalies one standard deviation unit above (below) the long-term mean (see Fig. 16).

Figure 19: As in Fig. 18 but for $\sigma_{45.95}$.

Figure 20: As in Fig. 18 but for the along-isobar $\theta - S$ anomalies tracking along the mean isopycnal depth of $\sigma_{41.50}$.

Figure 21: Lagged correlation between the spatially averaged density in the southwestern Weddell Sea versus the Atlantic sector AABW overturning (Fig. 16). The density is spatially averaged over the region 71.6°S−65.3°S, 61.9°W−39.4°W, as shown by the box in Fig. 11 (middle panel). Negative (positive) time lags indicate density leading (lagging) the overturning.

Figure 22: Lagged correlation between the surface and the regional depth profile of (a) density and (b, c) $\theta - S$ over the southwestern Weddell Sea (boxed region shown in Fig. 11, middle panel). Negative (positive) time lags indicate surface variables leading (lagging) the variables at depth.

Figure 23: (top) Composite anomalies of the spatially averaged $\theta - S$ and velocities over the southwestern Weddell Sea (see Fig. 11 for the boxed region) for the whole depth based on high (black) and low (grey) Weddell Sea AABW overturning extremes. The mean values are shown in the bottom panels for reference. The zonal velocity u is averaged over the eastern face of the boxed region (Fig. 11, middle panel). The meridional velocity v is averaged over the northern face of the boxed region.

Figure 24: Correlation at 0 lag between the southwestern Weddell Sea $\theta - S$ versus advective fluxes for the top 500 m. The dashed lines indicate the 95% confidence level. See text for further details.

Figure 25: (a) Lagged correlation between the depth-integrated ACC transport through the Drake Passage (DP transport) versus the southwestern Weddell Sea density. The cut-off 95% significance level coefficient is from 0.12 at the surface, increasing linearly to 0.2 at the deepest level. Negative (positive) time lags indicate density leading (lagging) the DP transport. (b) Lagged correlation between the ACC transport and the Weddell Sea AABW overturning (the dashed lines indicate 95% significance level).

Figure 26: Correlation map between sea surface temperature (SST) and salinity (SSS) at 0 lag.

Figure 27: (top) Time series of the spatially averaged SSS anomalies over the southwestern Weddell Sea (denoted in the text as SSS_{wed}). Extreme salination (freshening) years are defined as those years when anomalies are above (below) one standard deviation (marked by the dashed horizontal lines). (bottom) The power spectral density of SSS_{wed} with the fitted red-noise spectrum at 90% confidence level (dashed curve).

Figure 28: Composite maps of annual-mean (a) SSS, (b) SST, (c) zonal wind stress, (d) meridional wind stress, (e) zonal ocean current velocity, (f) meridional ocean current velocity, (g) net surface equivalent salt flux, and (h) net surface heat flux, based on the extreme salination years over the southwestern Weddell Sea (see Fig. 27). The boxed region indicates the region used for spatial averaging (as also indicated in Fig. 11a, middle panel). In (g, h), positive (negative) sign indicates increased (reduced) heating and salt fluxes over the ocean, respectively.

Figure 29: Composite maps of (left column) annual mean, (middle column) summer, and (right column) winter ice concentration (top) and ice-ocean salt flux

(bottom), calculated based on the extreme salination years of SSS_{wed} (see Fig. 27; see also Fig. 28 caption). Positive sign indicates an increase in ice concentration and ice-ocean salt fluxes respectively.

Figure 30: As in Fig. 29 but for (top) evaporative and (bottom) precipitative equivalent salt fluxes. Positive sign indicates an increase in evaporation and a decrease in precipitation.

Figure 31: As in Fig. 29 but for (top) air-sea sensible heat flux and (bottom) short-wave radiative flux. Positive sign indicates an increase in sensible heat flux (i.e., increased heat transfer from ocean to atmosphere), and an increased solar radiation (increased heating of the ocean).

Figure 32: The first six EOF modes of annual-mean SST south of 43°S accounting for 42% of the total SST variance.

Figure 33: Lagged-correlation between the spatially averaged SSS over the south-western Weddell Sea (SSS_{wed}) and the principal components of the first six EOF SST modes (Fig. 32). Only correlations significant above the 95% confidence level are displayed. See Fig. 31 for the boxed region used to define the spatially averaged SSS_{wed} (and refer to Fig. 27 for the time series of SSS_{wed}).

Figure 34: Composite anomalies of (top) zonal and (bottom) meridional wind stress components based on the extreme events of EOF3, EOF5, and EOF6 (see text for further explanation).

Table 1. Density equivalence at model depth levels corresponding to $\sigma_3 = 41.50$ kg m^{-3} in the three ocean sectors. The values of σ_p are determined based on a matching procedure using a linear fit by least squares in a plot of density values σ_n versus σ_3 at the mid pressure between the corresponding reference pressures, where $n = 0, 1, 2, 4$.

Model depth level	Reference pressure	Potential density (σ_n)		
(z)	(db)	Atlantic	Pacific	Indian
$z < 500$ m	0 (σ_0)	27.6660	27.6950	27.6601
$500 < z < 1500$	1000 (σ_1)	32.3862	32.3940	32.3843
$1500 < z < 2500$	2000 (σ_2)	36.9961	36.9995	36.9975
$2500 < z < 3500$	3000 (σ_3)	**41.50**	**41.50**	**41.50**
$3500 < z < 4500$	4000 (σ_4)	45.8972	45.8973	45.8988

Table 2. As in Table 2 but for $\sigma_4 = 45.95$ kg m^{-3}.

Model depth level	Reference pressure	Potential density		
(z)	(db)	Atlantic	Pacific	Indian
$z < 500$ m	0 (σ_0)	27.6827	27.7068	27.6617
$500 < z < 1500$	1000 (σ_1)	32.4072	32.4170	32.3984
$1500 < z < 2500$	2000 (σ_2)	37.0278	37.0327	37.0275
$2500 < z < 3500$	3000 (σ_3)	41.5412	41.5433	41.5407
$3500 < z < 4500$	4000 (σ_4)	**45.95**	**45.95**	**45.95**

Table 3. Standard deviation of the annual-mean surface heat budget terms over 1000 years spatially averaged over the region indicated in Fig. 29.

Budget term	std dev ($\times 10^{-8}$°C s^{-1})
$\partial\theta/\partial t$	0.47
Zonal advection ($u\partial\theta/\partial x$)	0.25
Meridional advection ($v\partial\theta/\partial y$)	0.18
Vertical advection ($w\partial\theta/\partial z$)	5.08×10^{-5}
Net surface heat flux (Q_{net})	1.82
Air to ocean solar radiation (Q_{solar})	3.76
Ocean to air long wave radiation (Q_{lw})	1.44
Ocean to air sensible heat flux (Q_{sh})	1.30
Ocean to air evaporative heat flux (Q_{evp})	0.67
Ocean to ice sensible heat flux (Q_{oi})	0.76

Table 4. Standard deviation of surface salinity budget terms. The terms are calculated as for those in Table 3. For consistency of units, evaporation and precipitation have been converted to equivalent salt fluxes (psu s^{-1}).

Budget term	std dev ($\times 10^{-9}$ psu s^{-1})
$\partial S/\partial t$	1.11
Zonal advection ($u\partial S/\partial x$)	0.91
Meridional advection ($v\partial S/\partial y$)	1.40
Vertical advection ($w\partial S/\partial z$)	2.15×10^{-4}
Net surface salt flux (H_{net})	6.47
Evaporative salt flux (E)	0.38
Precipitative salt flux (P)	1.63
Ice to ocean salt flux (H_{ice})	8.96

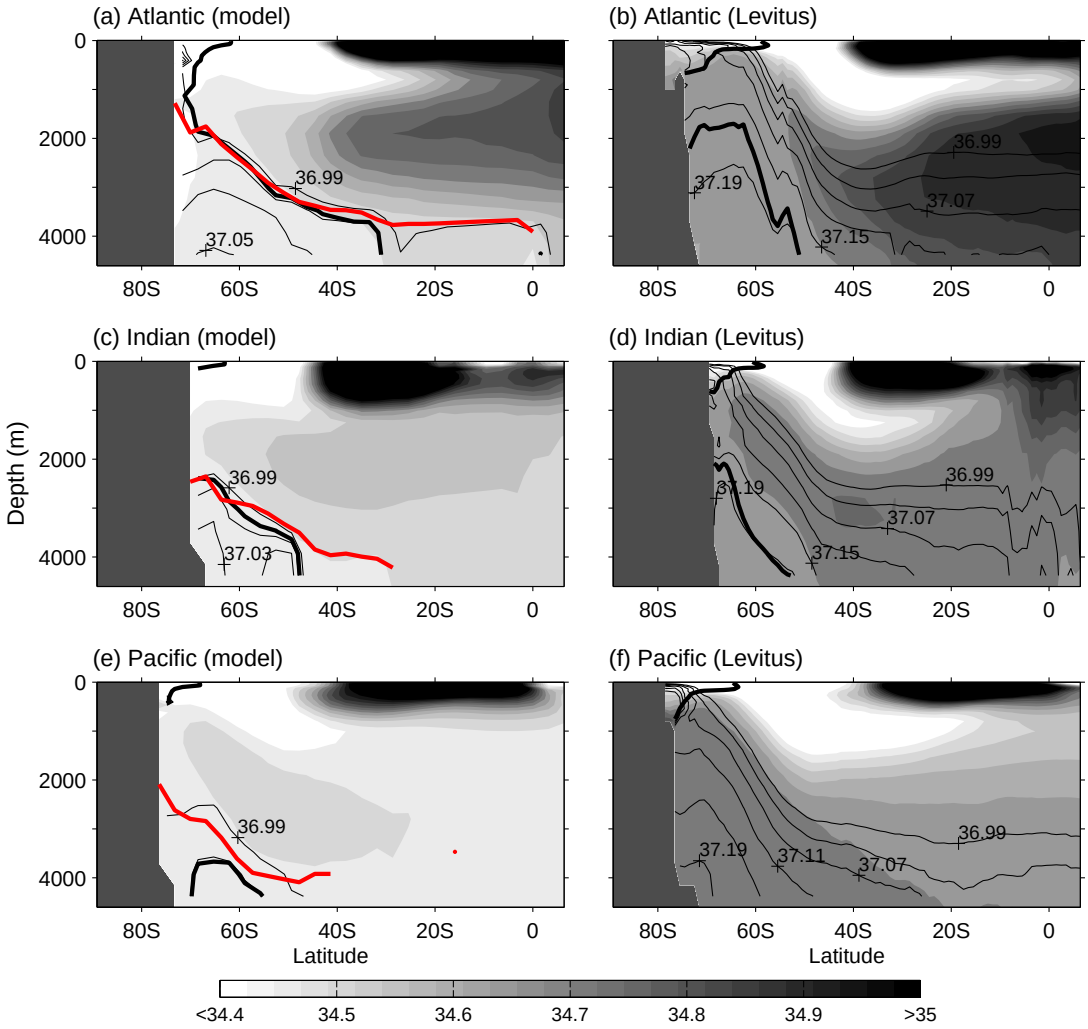

Figure 1: Zonally averaged salinity fields in the Atlantic (a, b), Indian (c, d), and Pacific (e, f) sectors in the model (left column) and Levitus et al. (1994; right column). The σ_2 density (referenced to 2000 dbar) is shown by thin black contours with an interval of 0.02 kg m^{-3} (0.04 kg m^{-3}) for the model (Levitus climatology). The thick black contour marks 0°C. The thick red contour marks the mean position of $\sigma_{41.50}$ isopycnal defined in the text (section 2b; see Table 1). The grey-scale colour scheme is consistent for all figure panels.

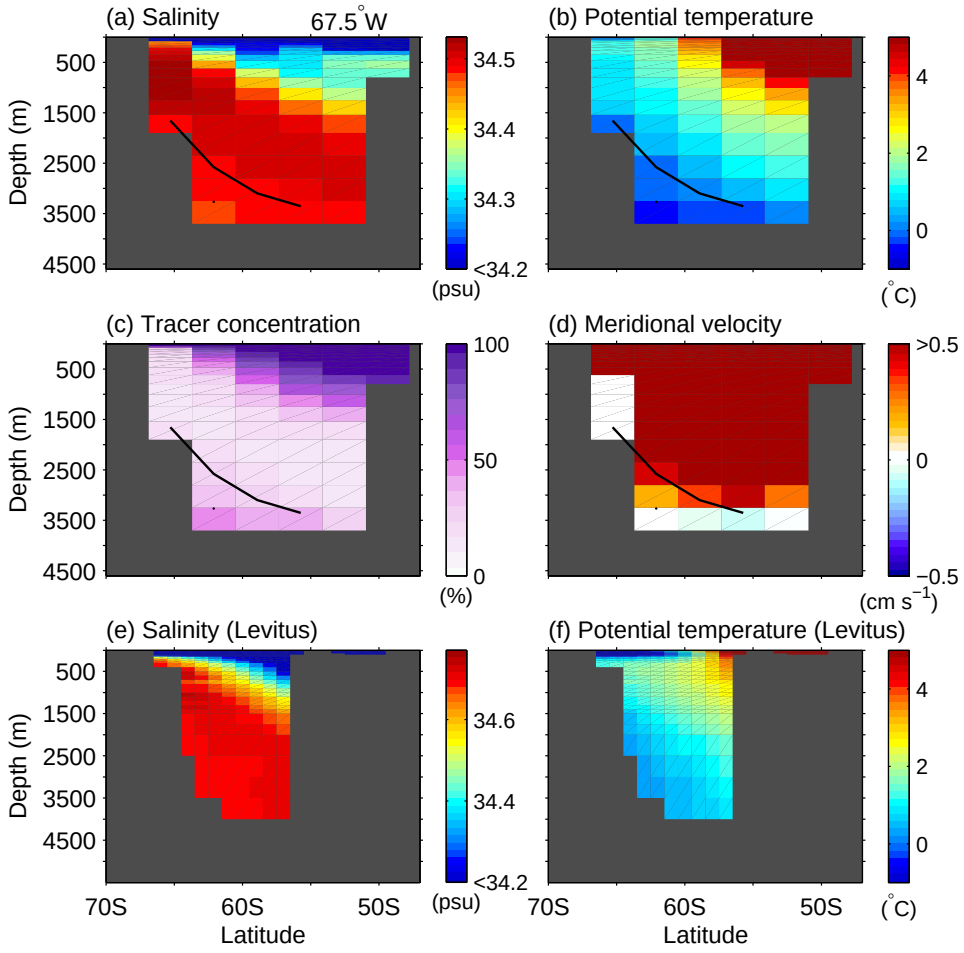

Figure 2: Transect across the Drake Passage in (a-d) the model at 67.5°W showing (a) salinity, (b) potential temperature, (c) passive tracer concentration at 150 yr after release, and (d) zonal velocity. The mean position of $\sigma_{41.50}$ isopycnal is marked by contour. (e), (f) The corresponding cross-sections of $\theta - S$ in the Levitus climatology.

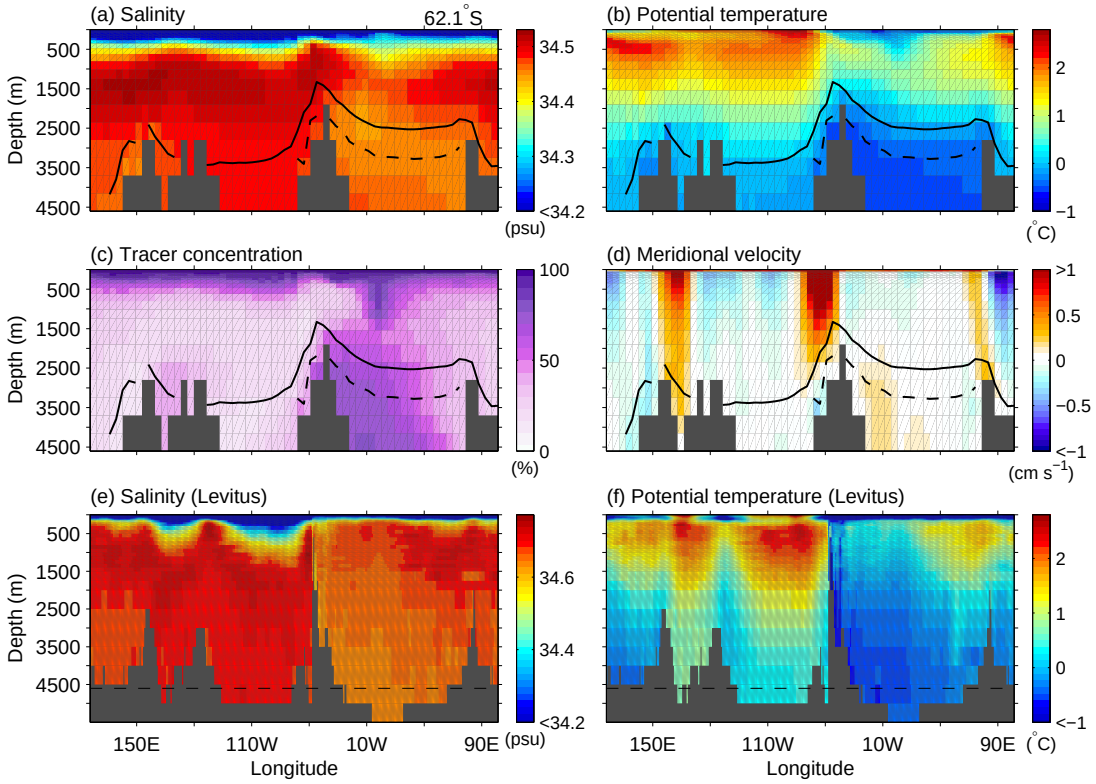

Figure 3: As in Fig. 2 but for a zonal transect across 62.1°S. The dashed contour in (a-d) marks the mean position of $\sigma_{45.95}$ isopycnal surface. The dashed horizontal line in (e), (f) marks the deepest model level.

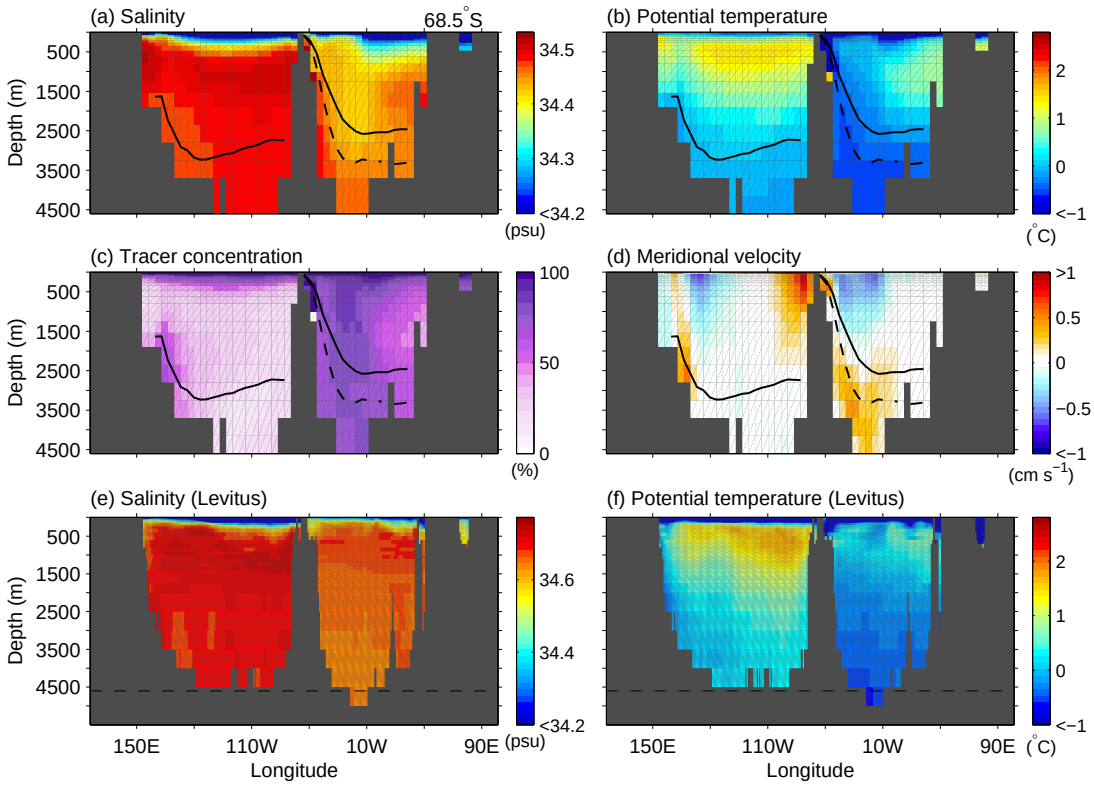

Figure 4: As in Figs. 2, 3 but for a zonal transect across 68.5°S.

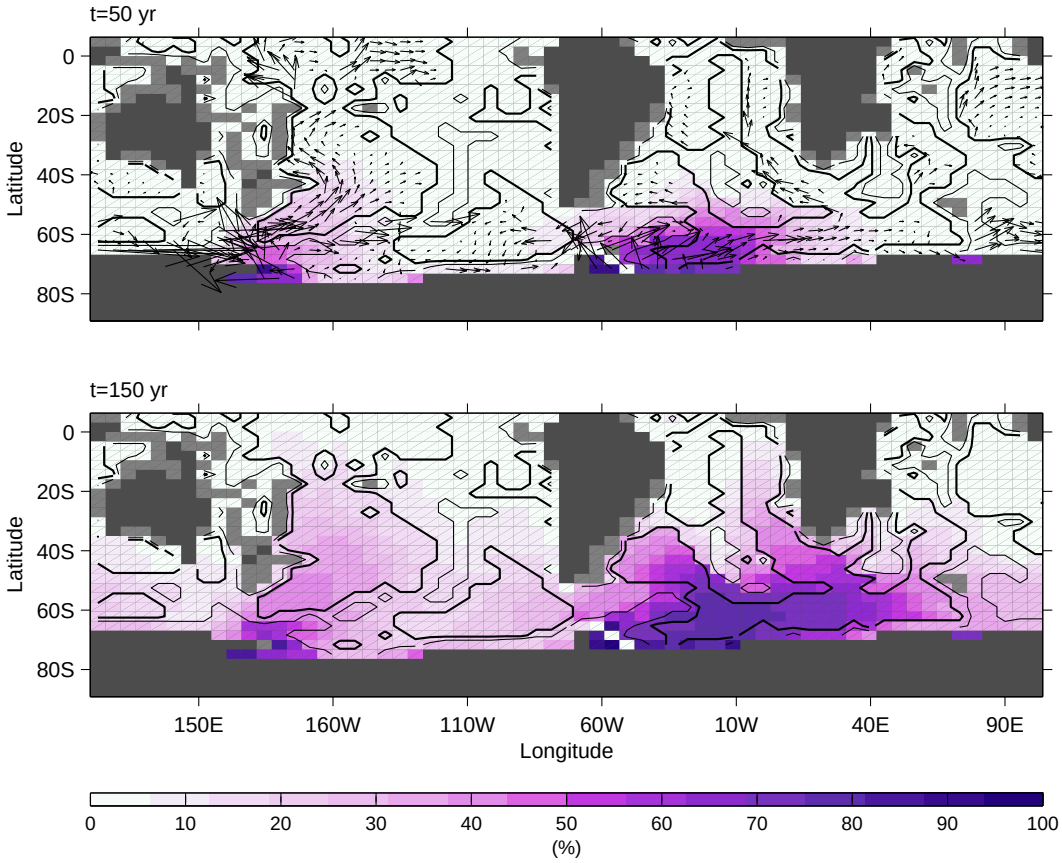

Figure 5: Passive tracer concentration at the bottom-most model level at 50 yr (top panel) and 150 yr (bottom panel) after release at the surface. Mean current velocities at the bottom-most level are shown by the vectors in the top panel. The model bottom relief are presented by thick contours marking the 4000-m depth and thin contours marking 3000-m depth.

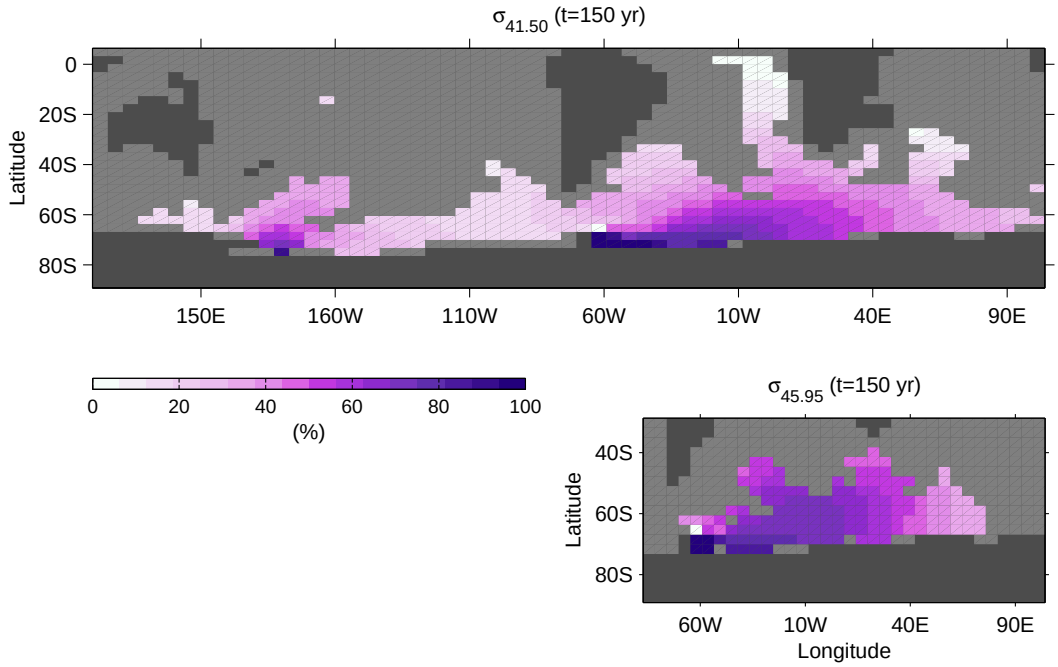

Figure 6: Passive tracer concentration on the $\sigma_{41.50}$ and $\sigma_{45.95}$ isopycnal surfaces at 150 yr after release.

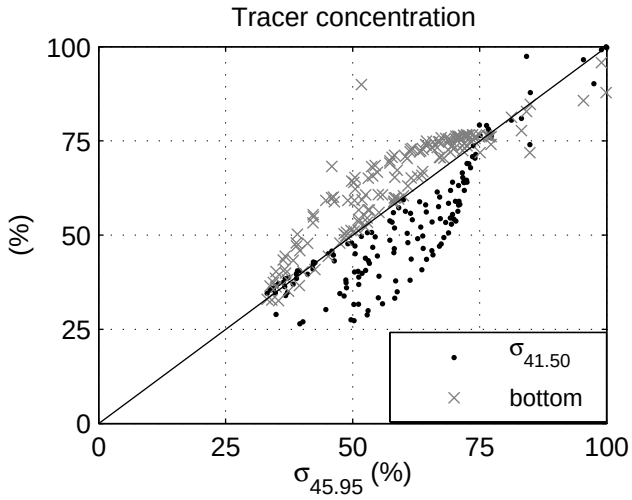

Figure 7: Tracer concentration at 150 yr after release for the Atlantic sector on $\sigma_{41.50}$ versus that on $\sigma_{45.95}$ (dots) and for the bottom-most model level versus $\sigma_{45.95}$ concentration (crosses).

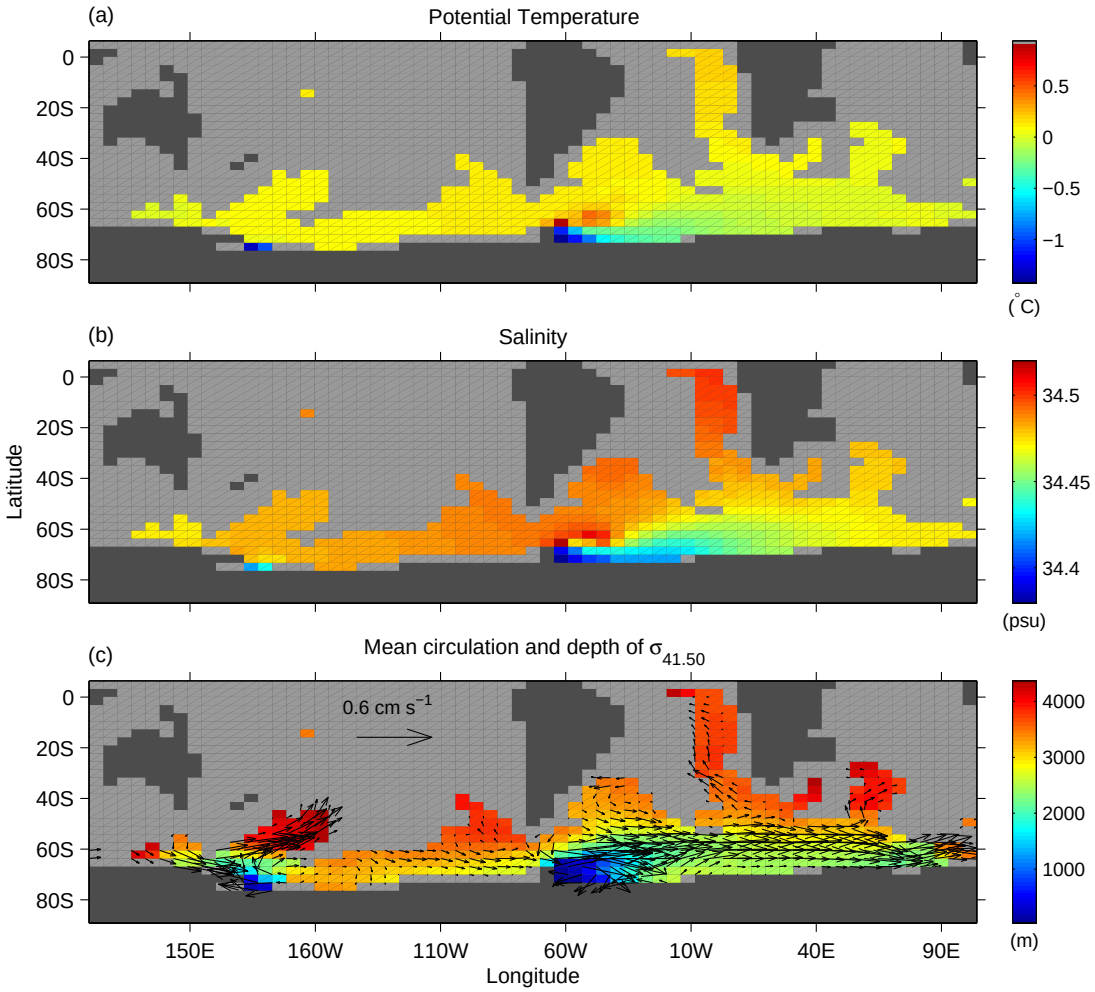

Figure 8: Mean potential temperature (a) and salinity (b) along $\sigma_{41.50}$. (c) Mean circulation (current vectors) and the depth of $\sigma_{41.50}$.

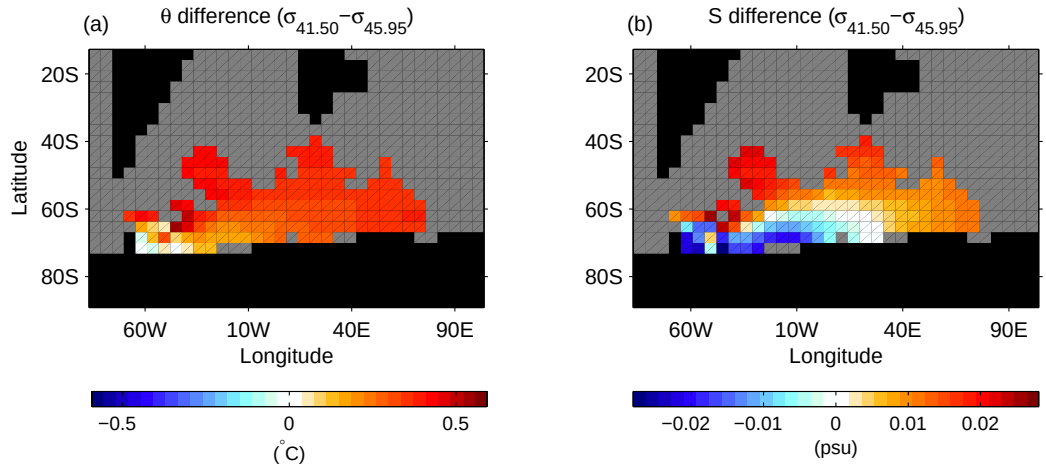

Figure 9: Difference of $\theta - S$ on $\sigma_{41.50}$ and $\sigma_{45.95}$.

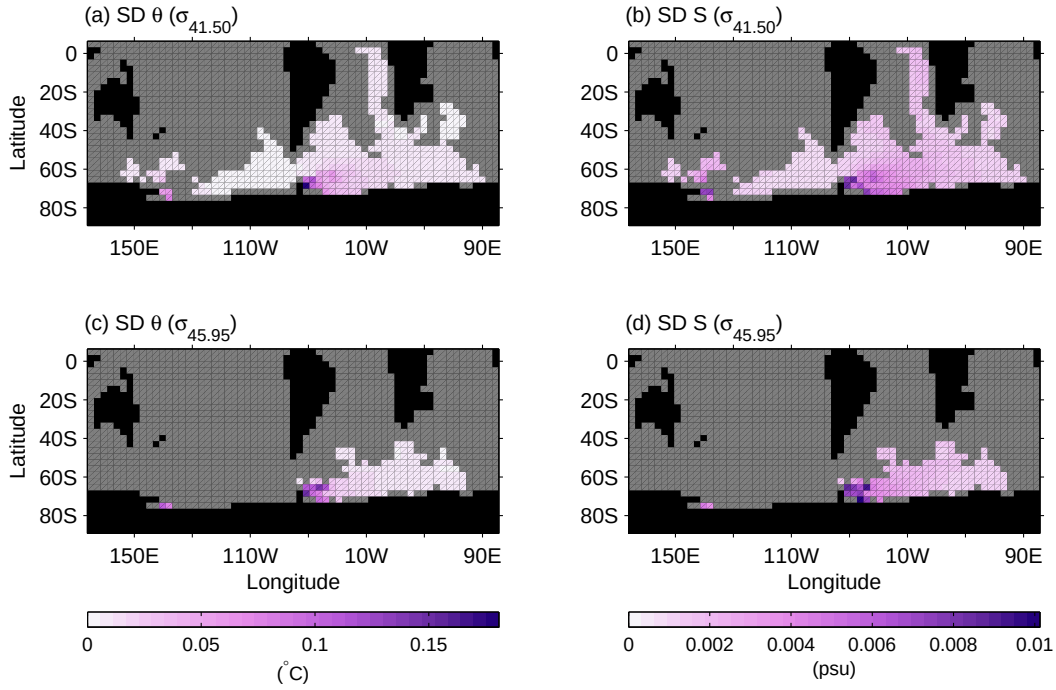

Figure 10: Standard deviation of $\theta - S$ on (a, b) $\sigma_{41.50}$ kg m^{-3} and (c, d) $\sigma_{45.95}$.

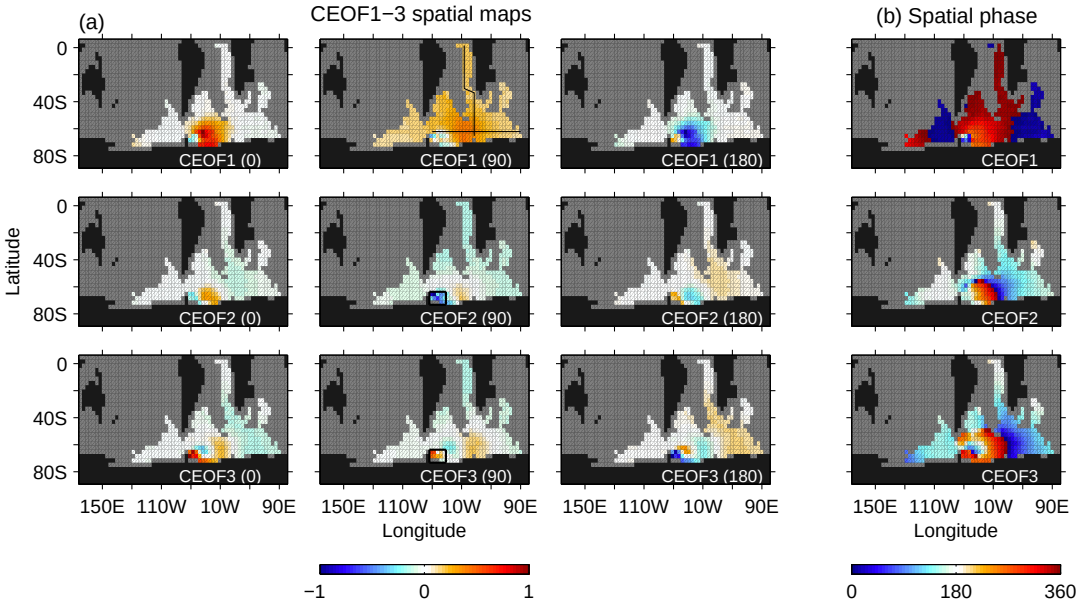

Figure 11: (a) Spatial maps of the three leading complex EOF modes of salinity shown at 90° phase intervals along $\sigma_{41.50}$. The first (CEOF1), second (CEOF2), and third (CEOF3) modes account for 42.4%, 21.9%, and 12.2% of the salinity variance, respectively. An equivalent CEOF analysis of θ shows similar modal structure and so is not shown here. (b) Spatial phase angle CEOF1−3 indicating the direction of phase propagation of each mode from 0° to 360°. Apparent phase discontinuities occur because the phase is defined only between 0° and 360°. The horizontal and vertical lines shown in the CEOF1 map (top row, middle column) mark the position of the transects for the Hovmöller diagrams shown in Figs. 14, 15. The box in the middle and bottom rows (middle column) indicate the southwestern Weddell Sea region for analysis in section 5.

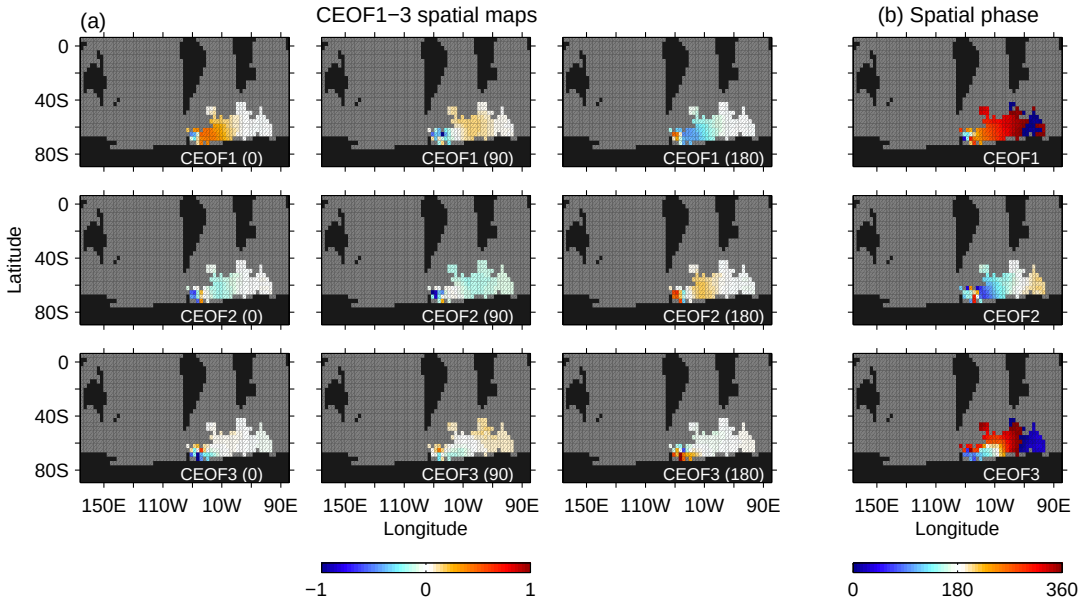

Figure 12: As in Fig. 11, but for $\sigma_{45.95}$. Each mode CEOF1−3 accounts for 34.2%, 18.4%, and 15.4% of the total salinity variance, respectively.

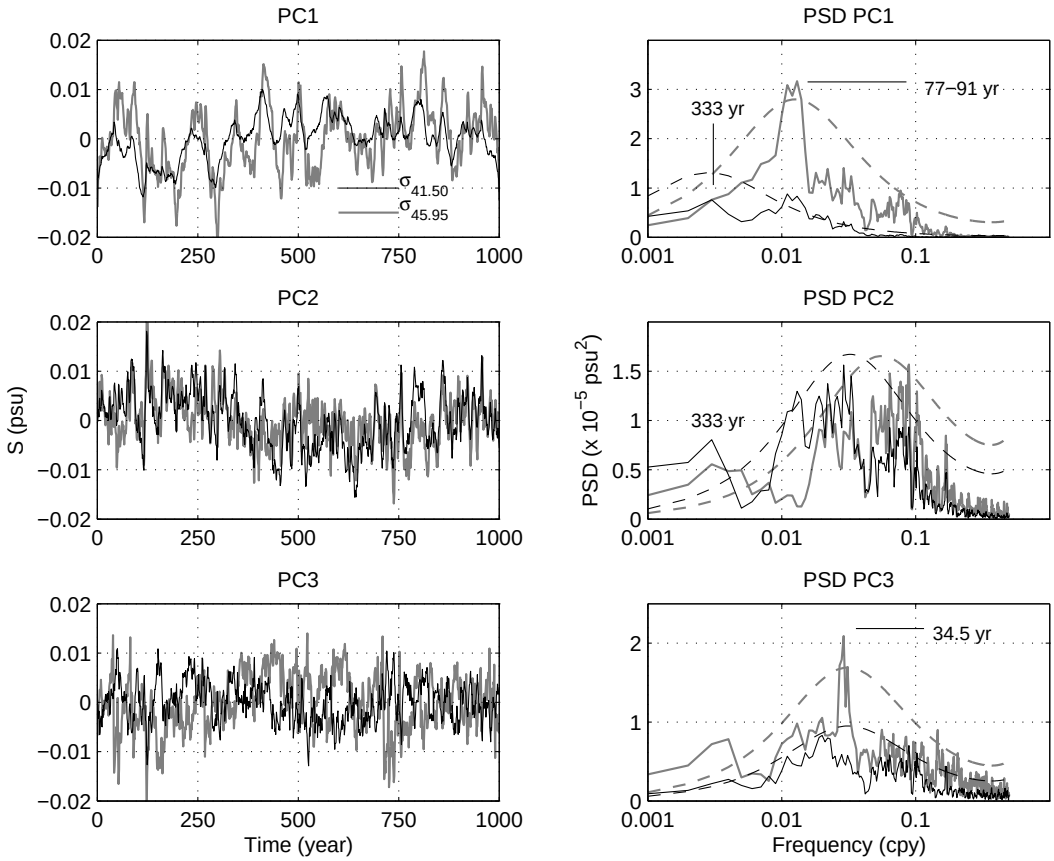

Figure 13: (left column) Principal component time series of CEOF1−3 shown for $\sigma_{41.50}$ (black) and $\sigma_{45.95}$ (grey). (right column) The corresponding power spectral density (PSD) of the principal component time series with an estimated AR-1 background spectrum at 90% confidence level (dashed curves). A $\log_{10}$ scale is used in frequency to give more weight to the higher frequency signals and the power spectra are multiplied by frequency to preserve variance.

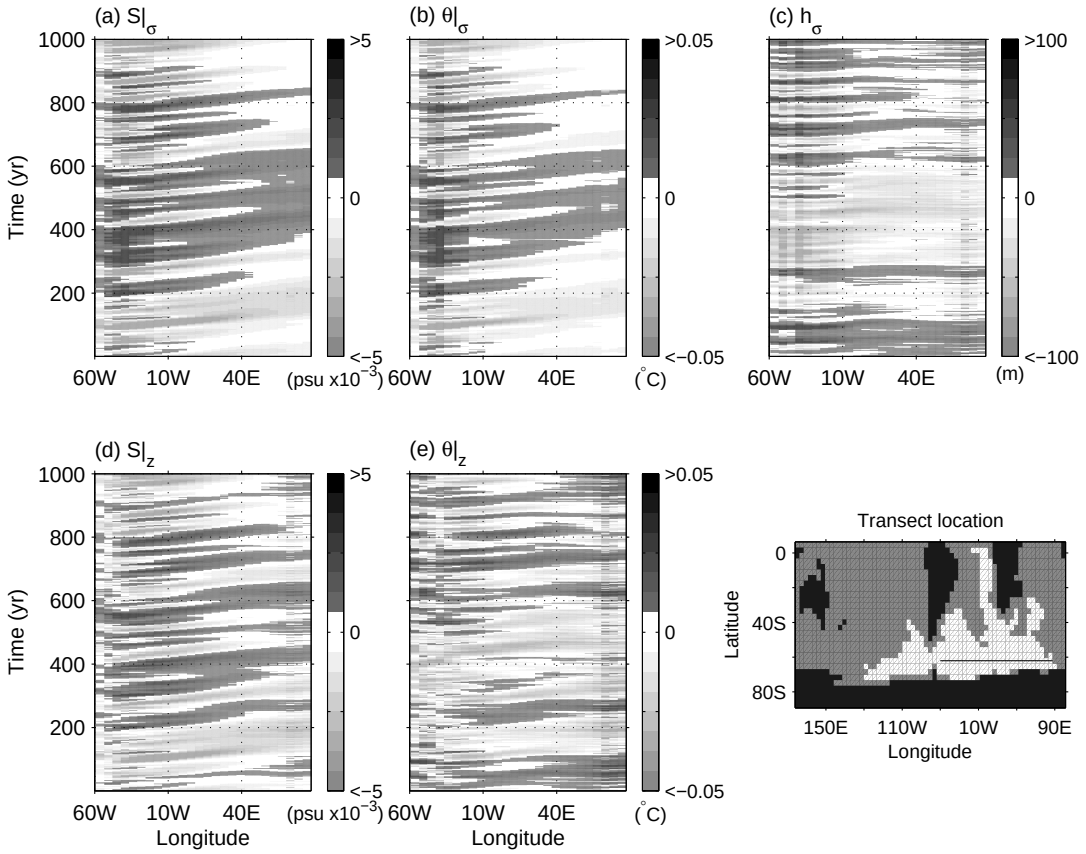

Figure 14: Hovmöller diagram of (a, b) $\theta - S$ anomalies along isopycnal, (c) isopycnal depth anomalies, and (d, e) $\theta - S$ anomalies along isobar on $\sigma_{41.50}$ along a zonal transect at 62° from 60°W to 87°E (see bottom right inset for the transect location; also shown in Fig. 11a). The along-isobar $\theta - S$ anomalies are calculated as deviations from the 1000-yr mean along the mean isopycnal depth of $\sigma_{41.50}$.

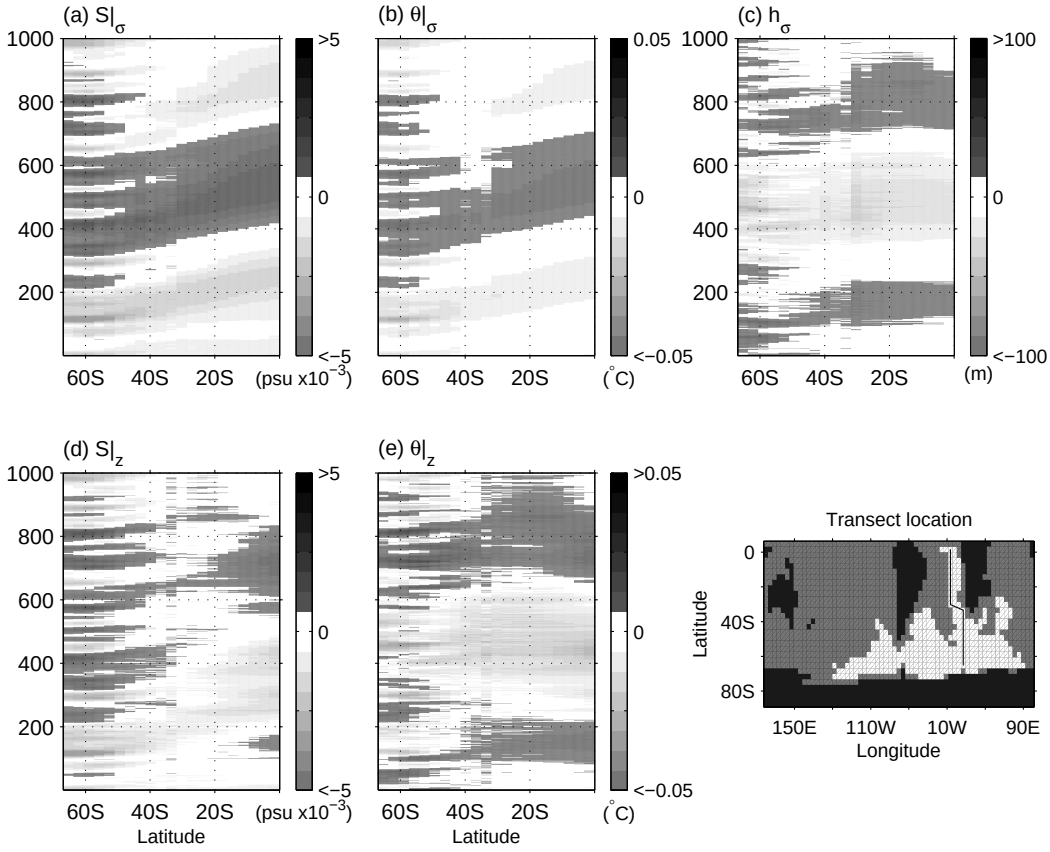

Figure 15: As in Fig. 14, but for the meridional transect shown in the bottom right inset (see also Fig. 11a).

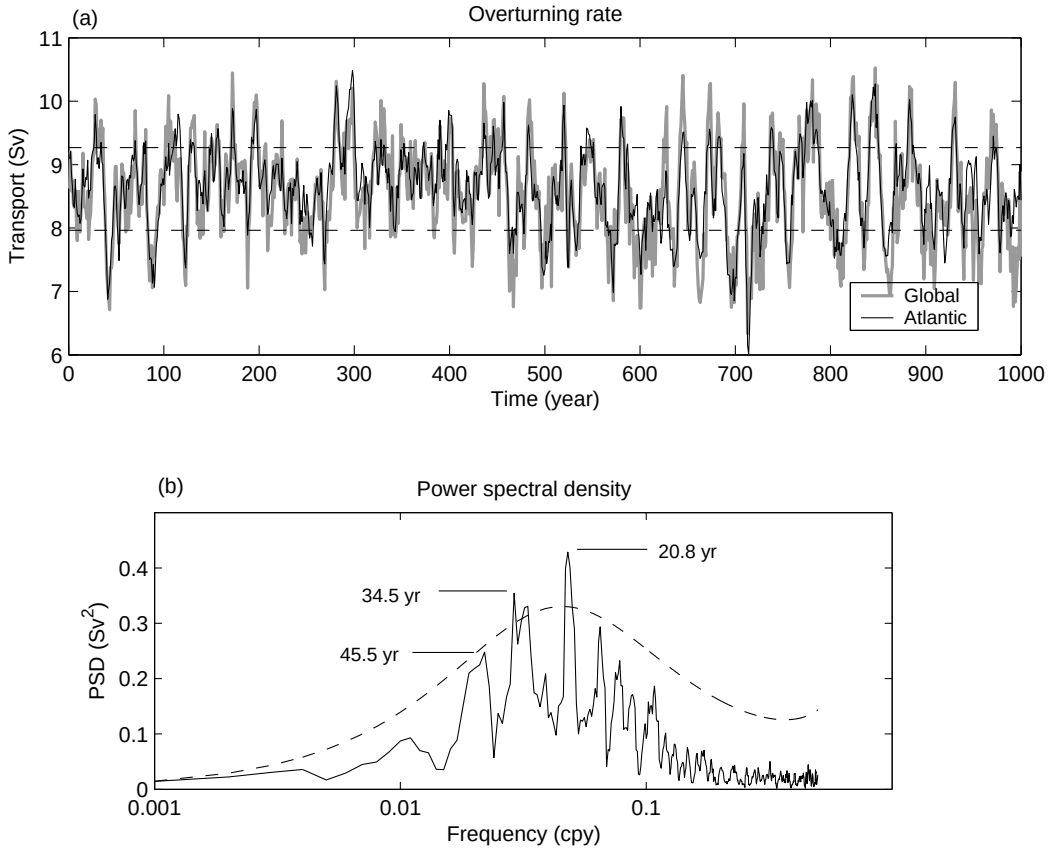

Figure 16: (a) Time series of maximum Antarctic meridional overturning rate for the global average (gray) and the Atlantic basin (black). The dashed lines indicate one standard deviation unit above and below the mean for the Atlantic sector overturning. The Atlantic sector overturning is referred to in the text as the Weddell Sea AABW overturning. (b) Power spectral density of the Atlantic sector AABW overturning with the fitted red-noise spectrum at 90% confidence level (dashed curve).

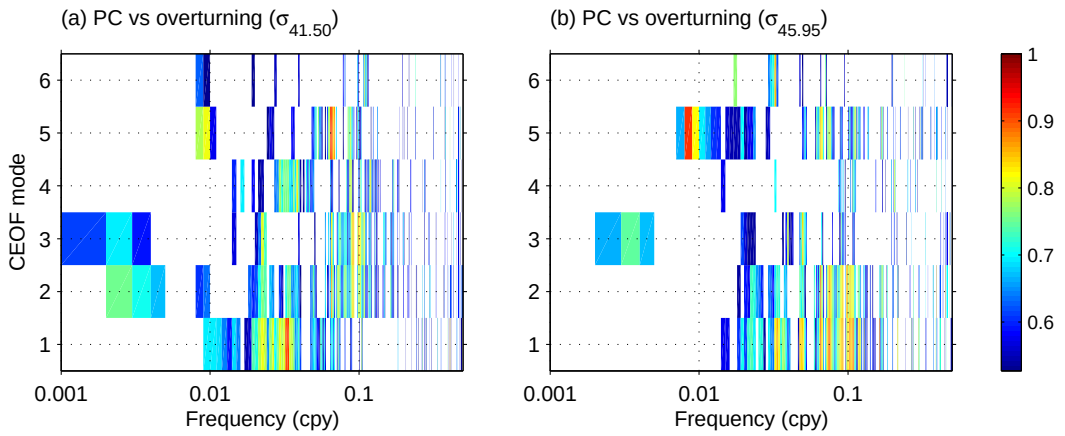

Figure 17: Coherence spectra between the Weddell Sea AABW overturning and the first six leading CEOF principal components of S on (a) $\sigma_{41.50}$ and (b) $\sigma_{45.95}$, only shown here significant at the 95% confidence level. Note that the first three modes account for *approx* 70% and CEOF4−6 account for $\approx$ 20% of the total variance.

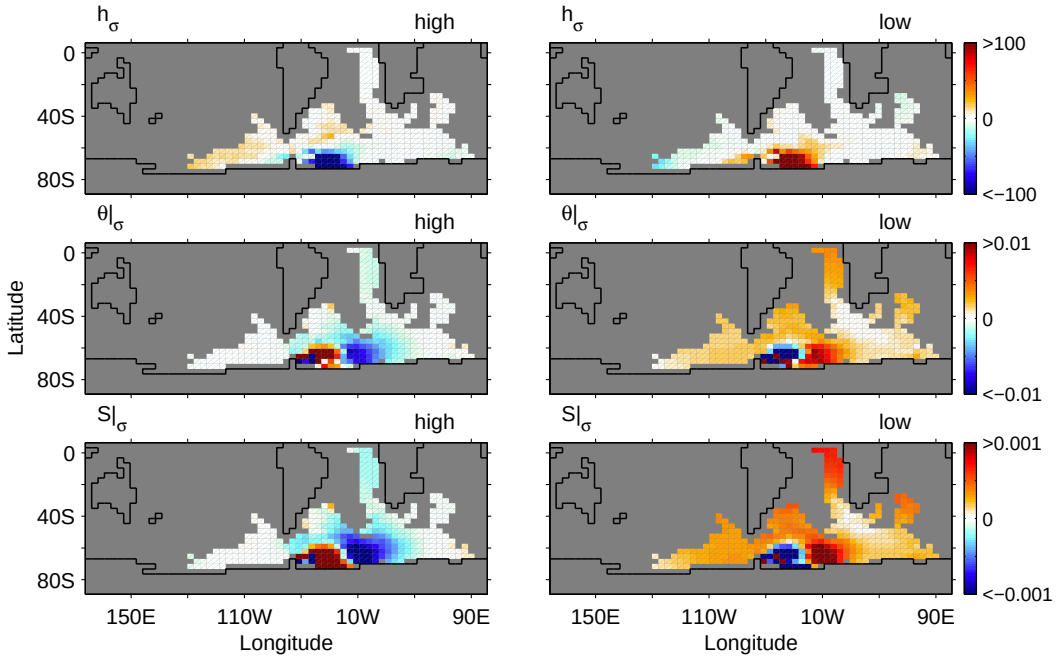

Figure 18: Composite anomalies of $\sigma_{41.50}$ (top) isopycnal depth, (middle) potential temperature, and (bottom) salinity for the high (left column) and low (right column) AABW overturning extremes. High (low) AABW overturning refers to overturning anomalies one standard deviation unit above (below) the long-term mean (see Fig. 16).

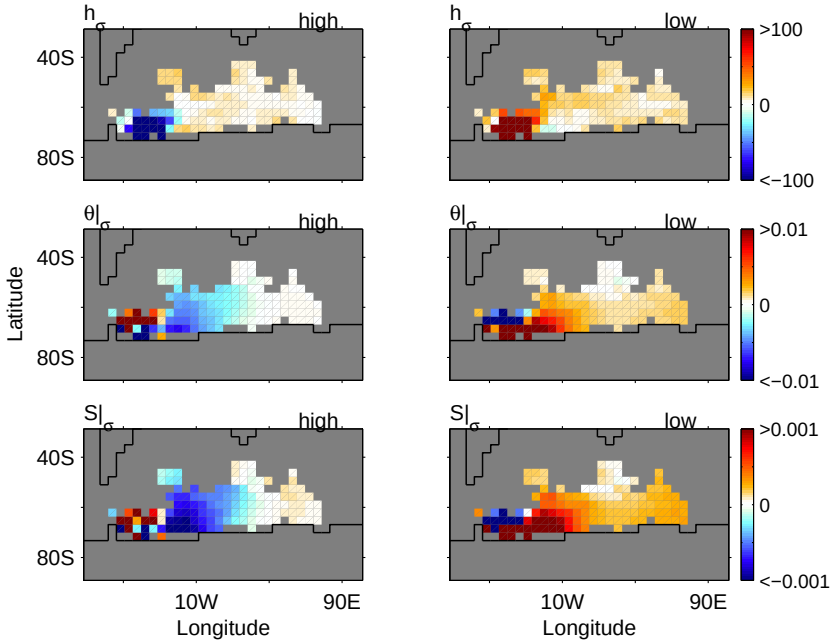

Figure 19: As in Fig. 18 but for $\sigma_{45.95}$.

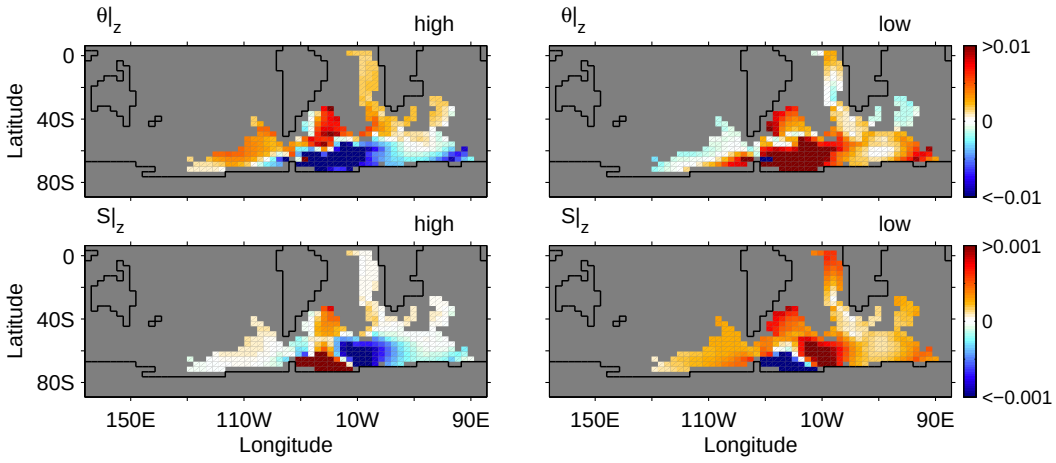

Figure 20: As in Fig. 18 but for the along-isobar $\theta - S$ anomalies tracking along the mean isopycnal depth of $\sigma_{41.50}$.

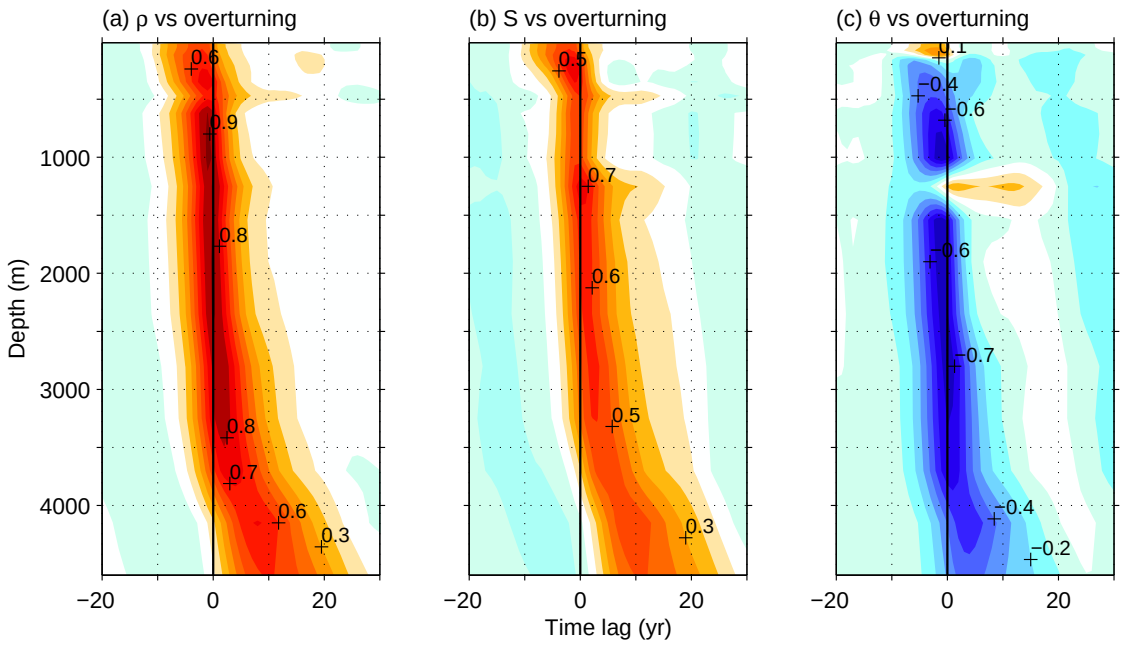

Figure 21: Lagged correlation between the spatially averaged density in the south-western Weddell Sea versus the Atlantic sector AABW overturning (Fig. 16). The density is spatially averaged over the region 71.6°S−65.3°S, 61.9°W−39.4°W, as shown by the box in Fig. 11 (middle panel). Negative (positive) time lags indicate density leading (lagging) the overturning.

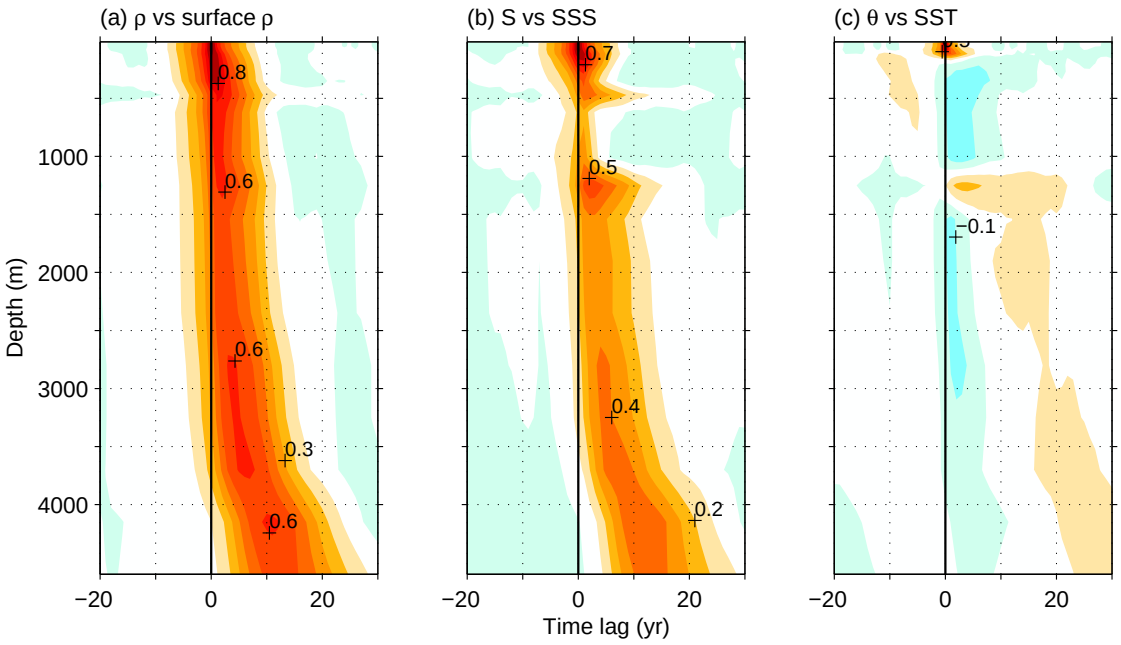

Figure 22: Lagged correlation between the surface and the regional depth profile of (a) density and (b, c) $\theta - S$ over the southwestern Weddell Sea (boxed region shown in Fig. 11, middle panel). Negative (positive) time lags indicate surface variables leading (lagging) the variables at depth.

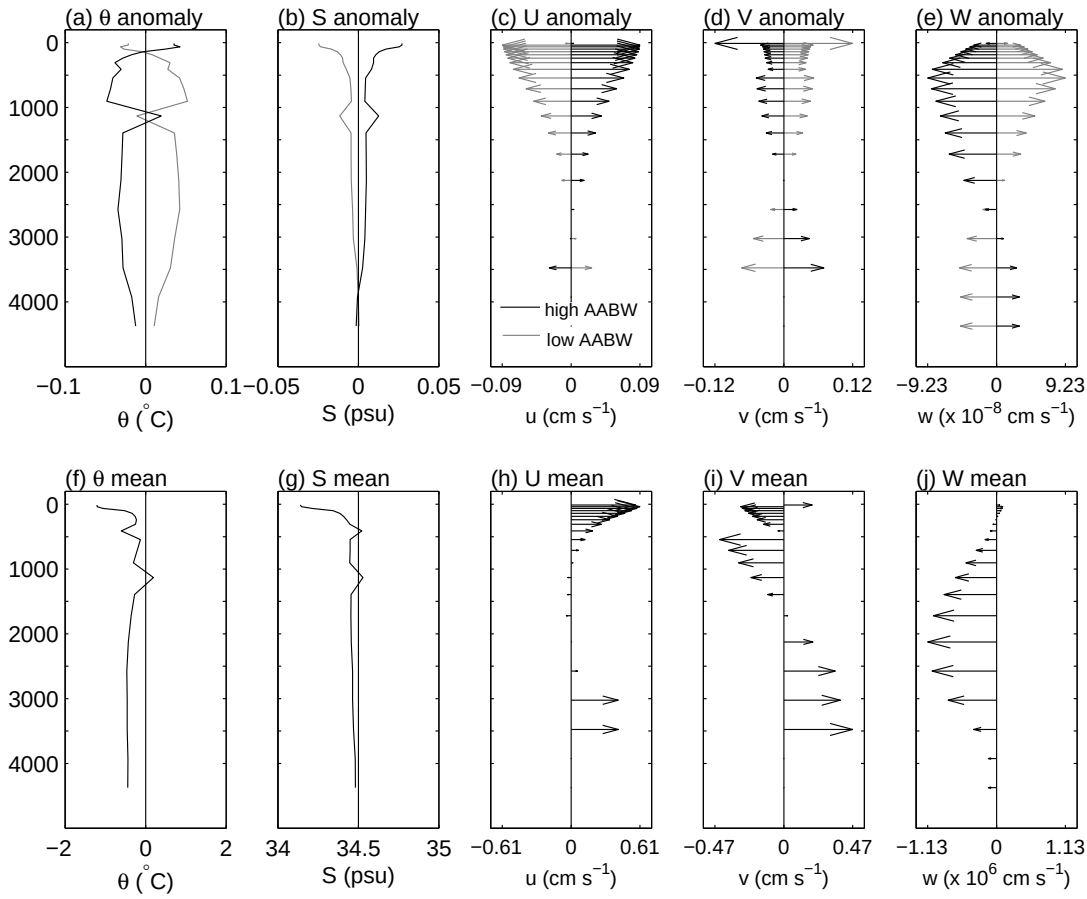

Figure 23: (top) Composite anomalies of the spatially averaged $\theta - S$ and velocities over the southwestern Weddell Sea (see Fig. 11 for the boxed region) for the whole depth based on high (black) and low (grey) Weddell Sea AABW overturning extremes. The mean values are shown in the bottom panels for reference. The zonal velocity u is averaged over the eastern face of the boxed region (Fig. 11, middle panel). The meridional velocity v is averaged over the northern face of the boxed region.

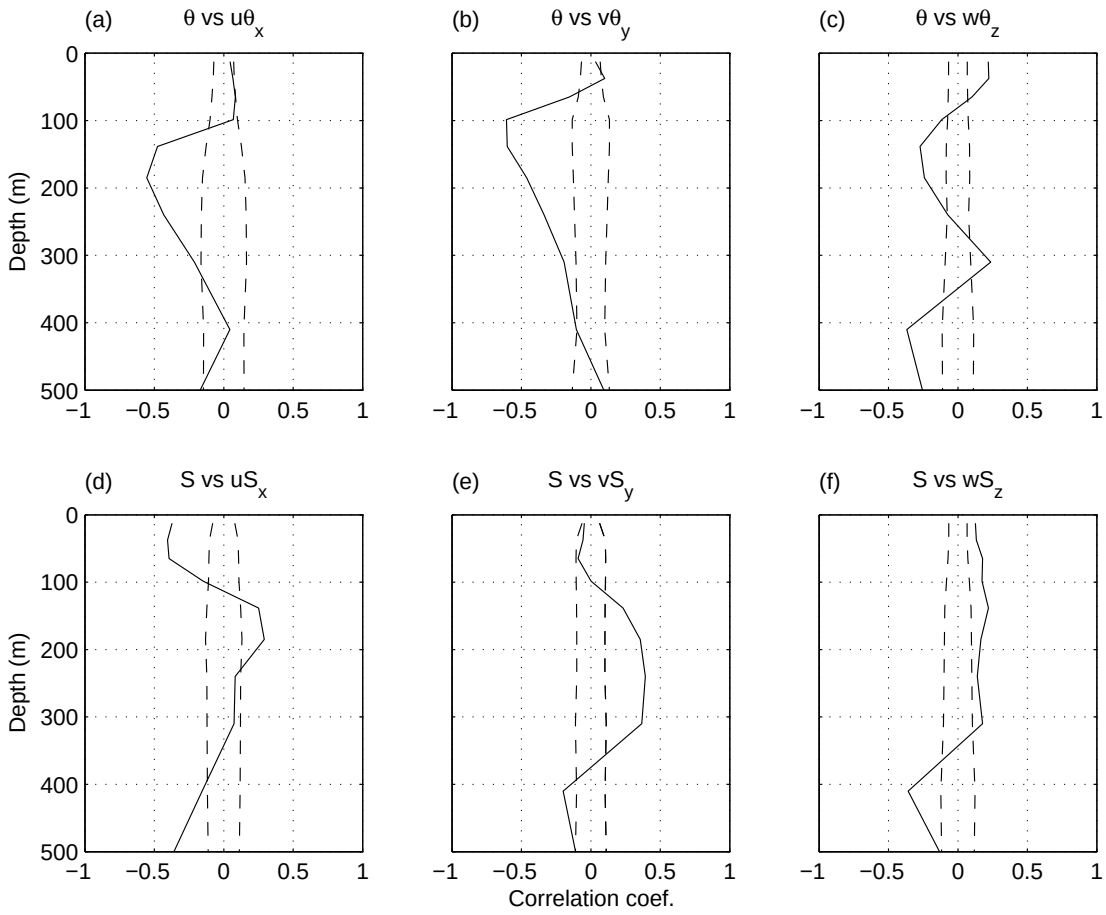

Figure 24: Correlation at 0 lag between the southwestern Weddell Sea $\theta - S$ versus advective fluxes for the top 500 m. The dashed lines indicate the 95% confidence level. See text for further details.

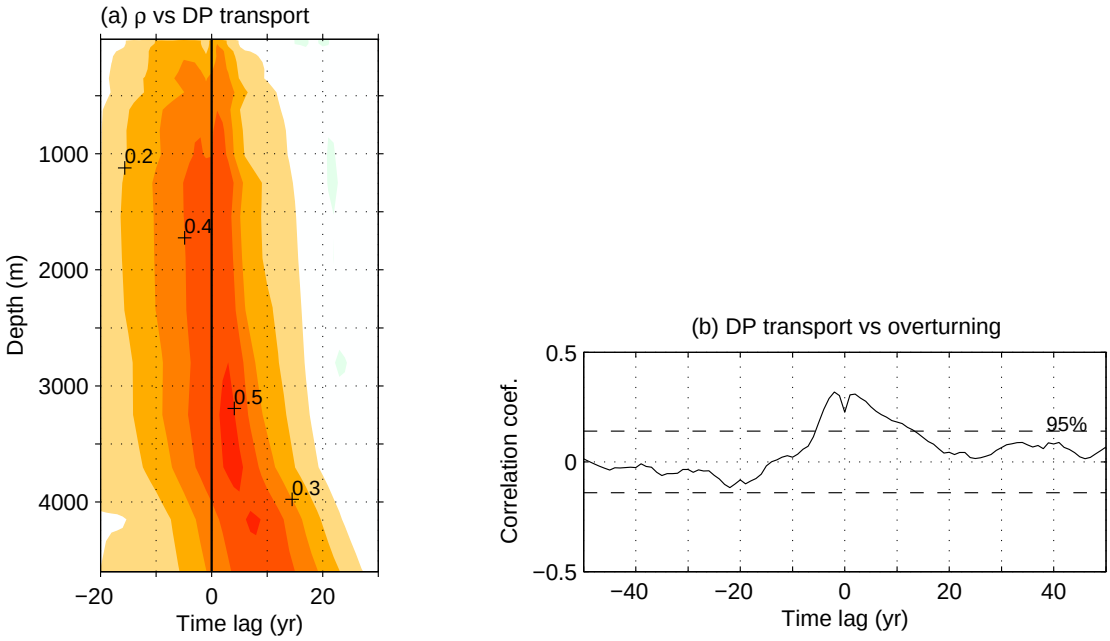

Figure 25: (a) Lagged correlation between the depth-integrated ACC transport through the Drake Passage (DP transport) versus the southwestern Weddell Sea density. The cut-off 95% significance level coefficient is from 0.12 at the surface, increasing linearly to 0.2 at the deepest level. Negative (positive) time lags indicate density leading (lagging) the DP transport. (b) Lagged correlation between the ACC transport and the Weddell Sea AABW overturning (the dashed lines indicate 95% significance level).

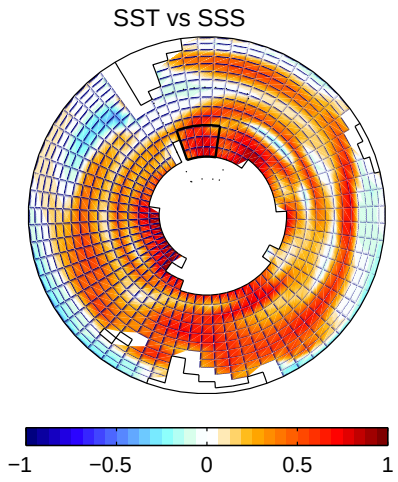

Figure 26: Correlation map between sea surface temperature (SST) and salinity (SSS) at 0 lag.

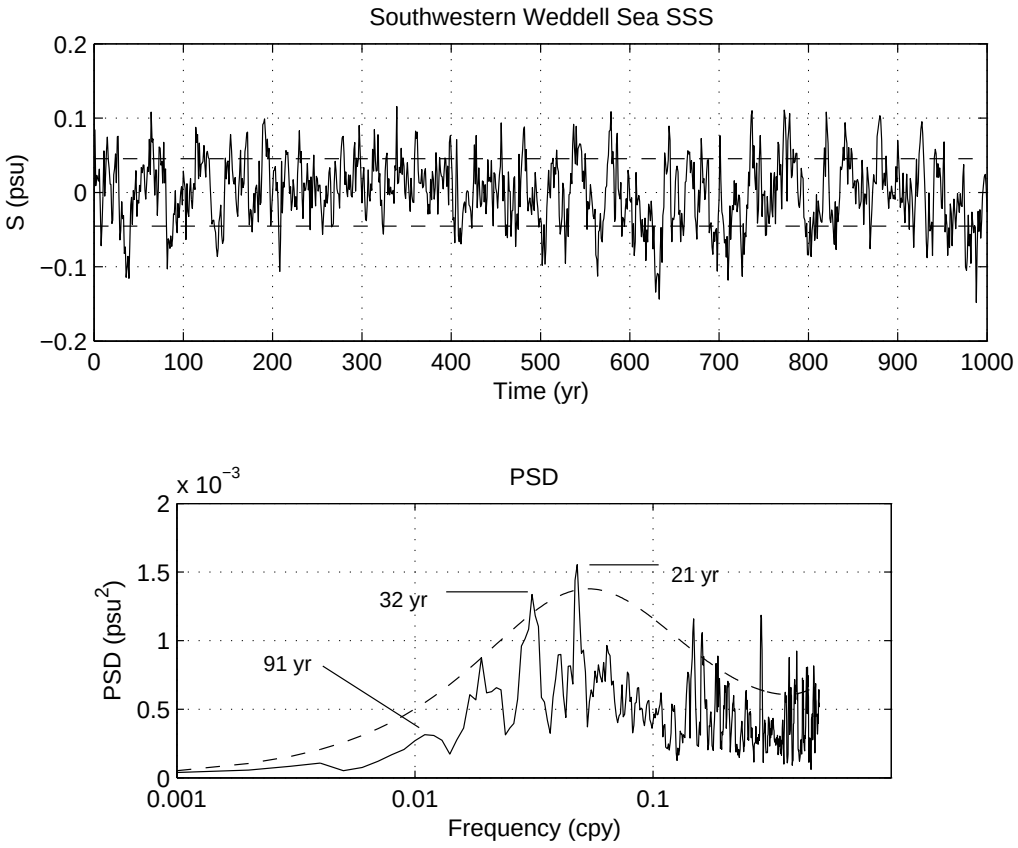

Figure 27: (top) Time series of the spatially averaged SSS anomalies over the southwestern Weddell Sea (denoted in the text as SSS_{wed}). Extreme salination (freshening) years are defined as those years when anomalies are above (below) one standard deviation (marked by the dashed horizontal lines). (bottom) The power spectral density of SSS_{wed} with the fitted red-noise spectrum at 90% confidence level (dashed curve).

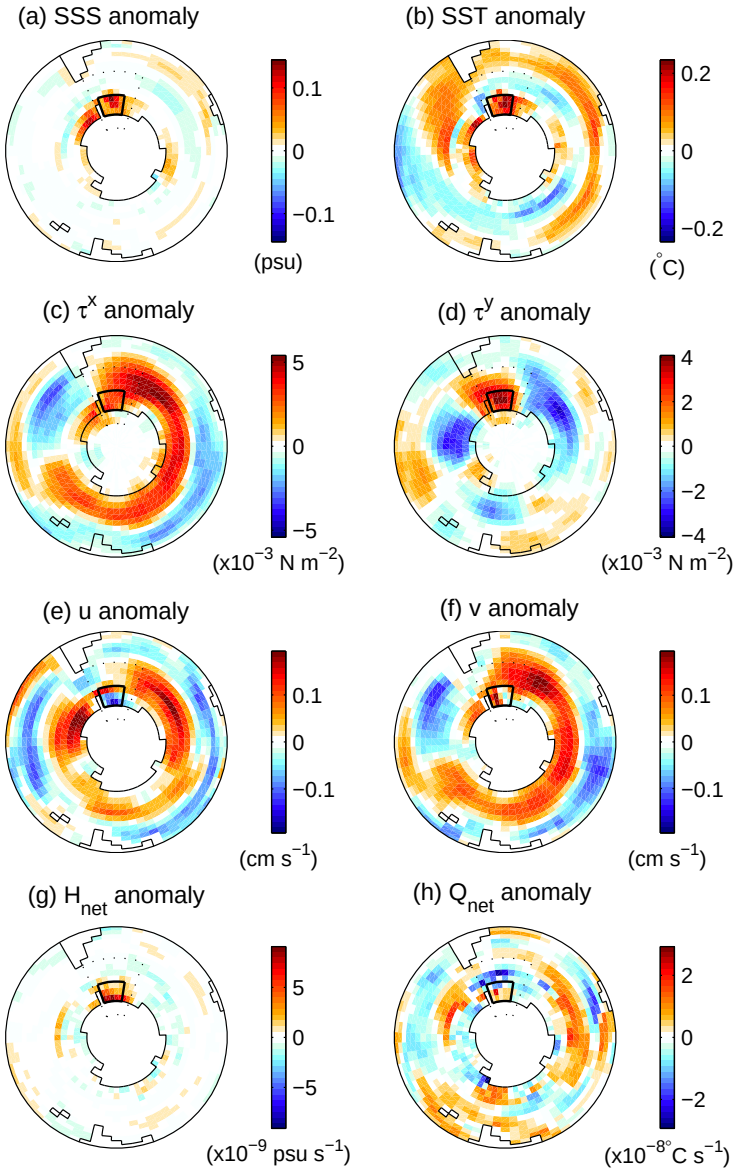

Figure 28: Composite maps of annual-mean (a) SSS, (b) SST, (c) zonal wind stress, (d) meridional wind stress, (e) zonal ocean current velocity, (f) meridional ocean current velocity, (g) net surface equivalent salt flux, and (h) net surface heat flux, based on the extreme salination years over the southwestern Weddell Sea (see Fig. 27). The boxed region indicates the region used for spatial averaging (as also indicated in Fig. 11a, middle panel). In (g, h), positive (negative) sign indicates increased (reduced) heating and salt fluxes over the ocean, respectively.

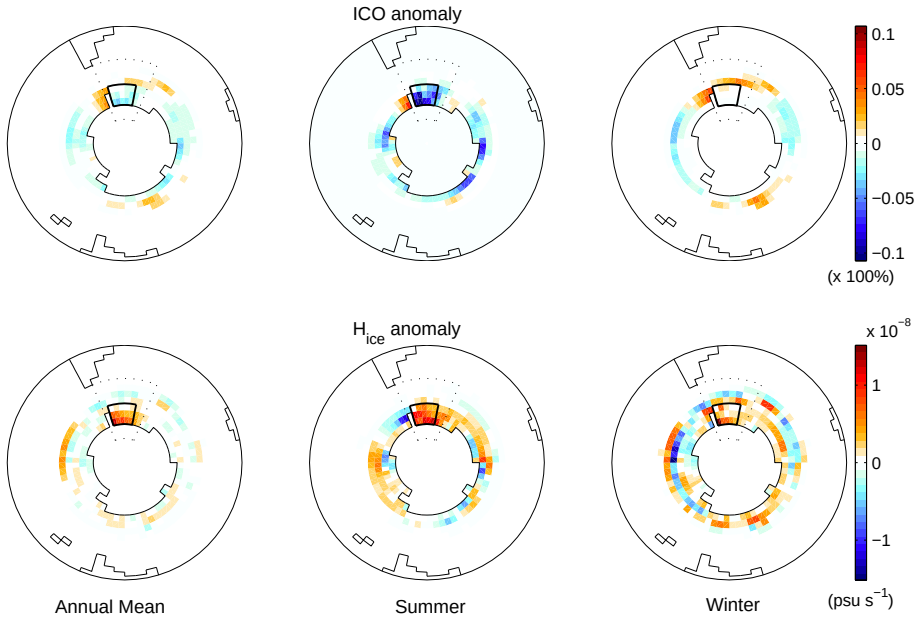

Figure 29: Composite maps of (left column) annual mean, (middle column) summer, and (right column) winter ice concentration (top) and ice-ocean salt flux (bottom), calculated based on the extreme salination years of SSS_{wed} (see Fig. 27; see also Fig. 28 caption). Positive sign indicates an increase in ice concentration and ice-ocean salt fluxes respectively.

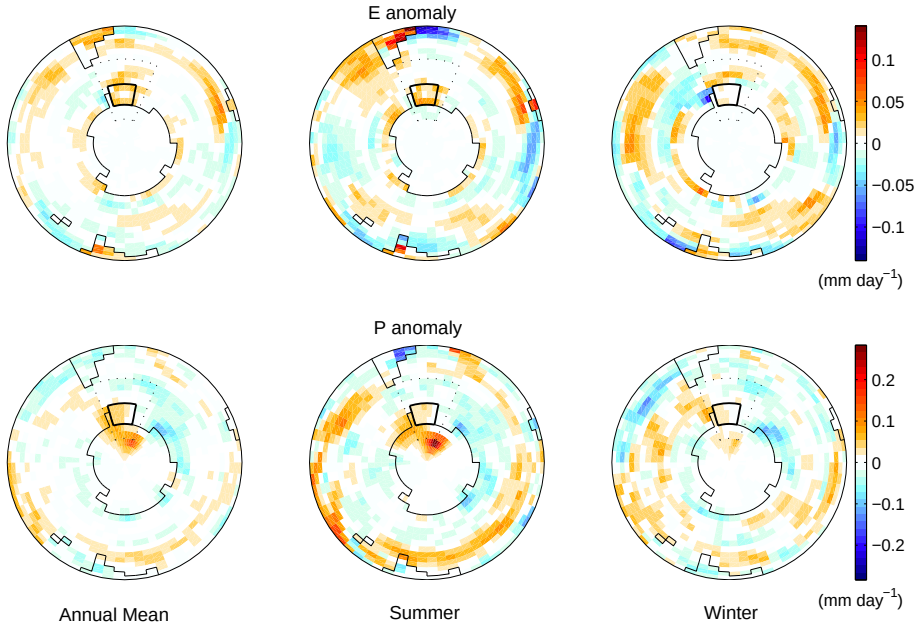

Figure 30: As in Fig. 29 but for (top) evaporative and (bottom) precipitative equivalent salt fluxes. Positive sign indicates an increase in evaporation and a decrease in precipitation.

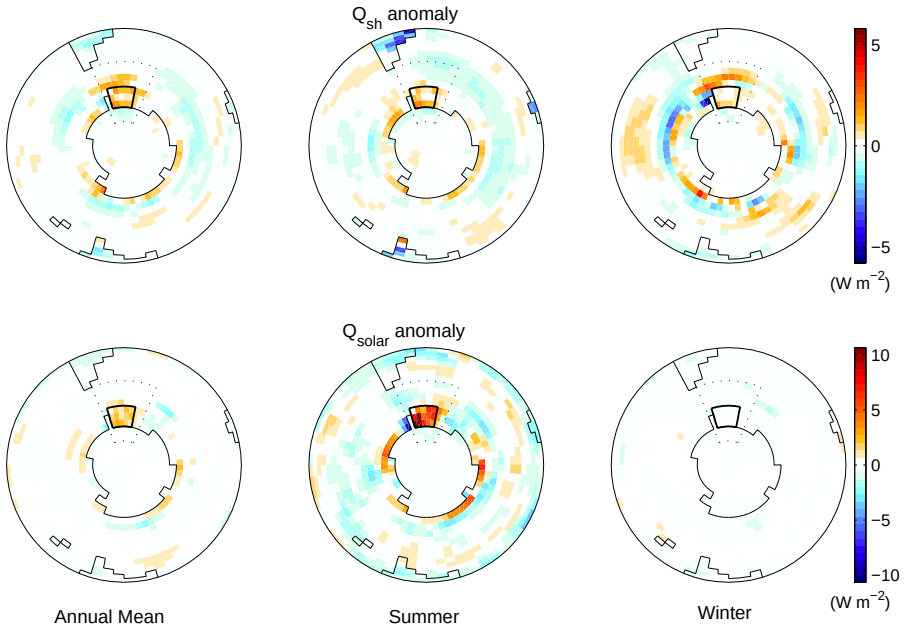

Figure 31: As in Fig. 29 but for (top) air-sea sensible heat flux and (bottom) shortwave radiative flux. Positive sign indicates an increase in sensible heat flux (i.e., increased heat transfer from ocean to atmosphere), and an increased solar radiation (increased heating of the ocean).

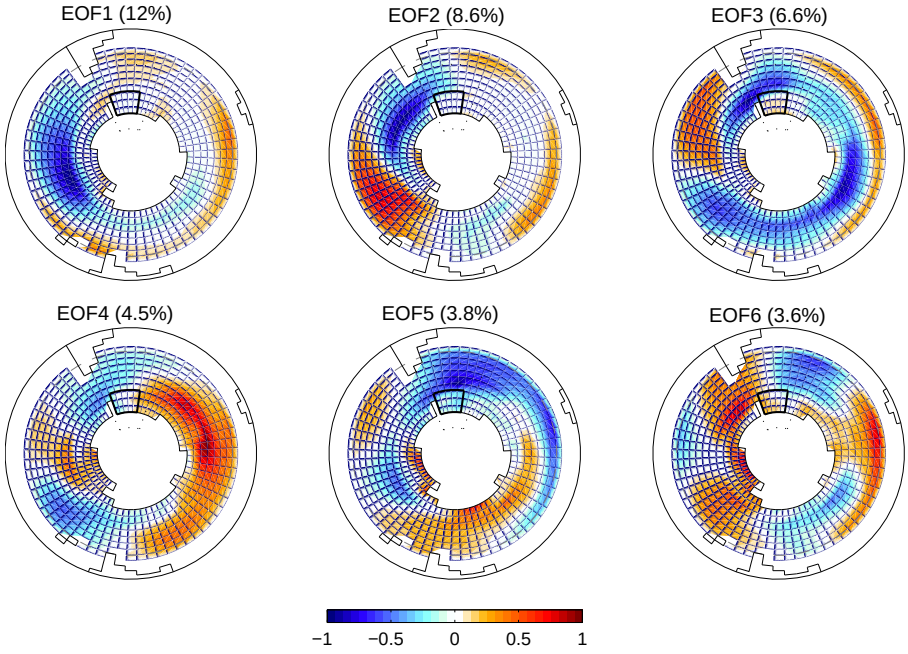

Figure 32: The first six EOF modes of annual-mean SST south of 43°S accounting for 42% of the total SST variance.

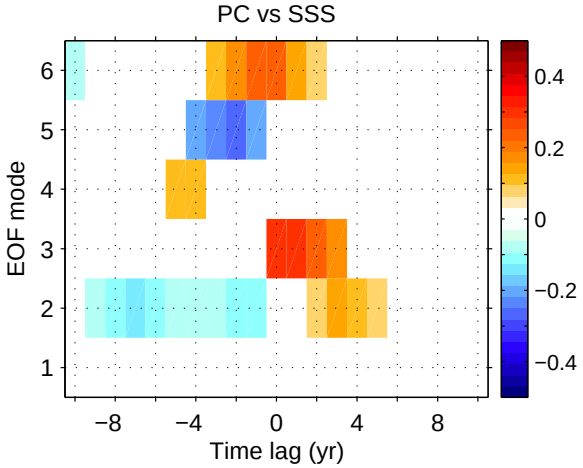

Figure 33: Lagged-correlation between the spatially averaged SSS over the south-western Weddell Sea (SSS_{wed}) and the principal components of the first six EOF SST modes (Fig. 32). Only correlations significant above the 95% confidence level are displayed. See Fig. 31 for the boxed region used to define the spatially averaged SSS_{wed} (and refer to Fig. 27 for the time series of SSS_{wed}).

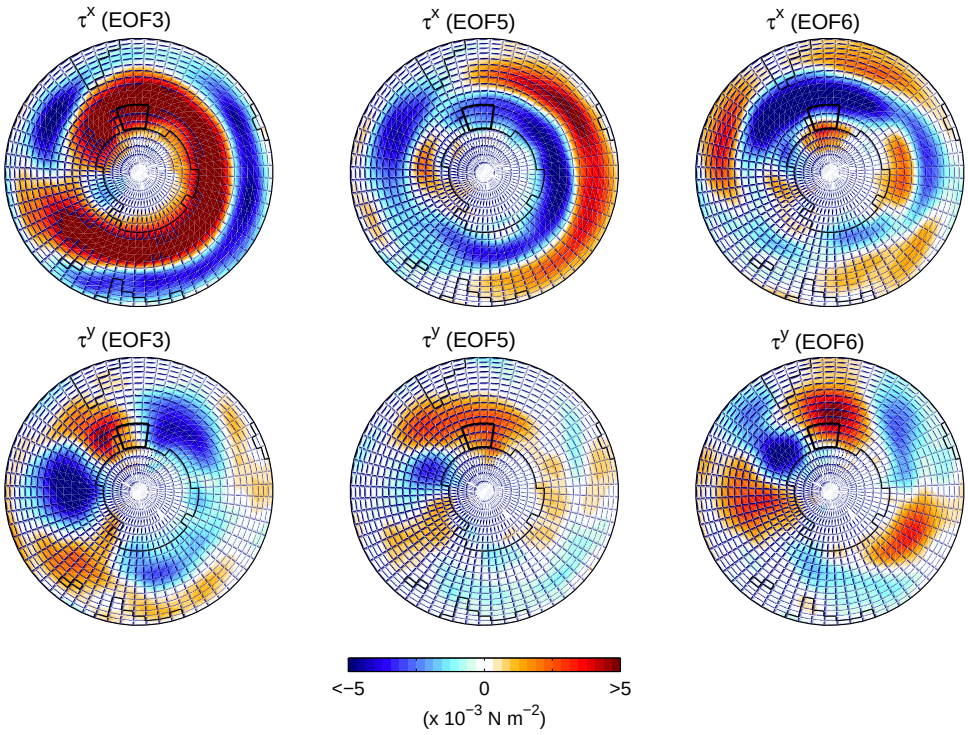

Figure 34: Composite anomalies of (top) zonal and (bottom) meridional wind stress components based on the extreme events of EOF3, EOF5, and EOF6 (see text for further explanation).

Part IV: Indian Ocean variability and links to regional rainfall

Abstract

The Indian Ocean variability on interannual time scales is assessed using a long integration of a climate model and recent observational and reanalysis data. Special attention is given to the Indian Ocean influence on rainfall over southwest Western Australia (SWWA). Empirical orthogonal function (EOF) analyses are conducted to identify dominant large-scale modes of SST variability, with considerations of seasonal preference and spatial domain sensitivity of these modes. As documented in various studies, a basin-wide SST anomaly of uniform polarity over the tropic/subtropical region is found as the dominant mode. A zonally symmetric pattern in the tropics is also detected. These modes are shown in this study to co-evolve along with a subtropical dipole mode. An interesting tripole pattern is detectable as a combination of the tropical and subtropical dipole modes. A Southern Ocean influence on Indian Ocean variability is shown to be moderate and is limited to the subtropical region via the the subtropical dipole mode. Anomalous atmospheric and oceanic conditions during these extreme events are documented, exhibiting anomalous rainfall patterns which appear connected to the SST anomalies.

During years of SWWA rainfall extremes, a meridional SST dipole is established and peaks during austral winter. An SST pole sits in the tropical eastern Indian Ocean off Northwest Australia. Another pole of opposite polarity is found south of the first pole extending northwest towards Central Africa. Our analyses confirm the connection between this pattern and the large-scale tripole mode as identified by the EOF analysis. Thus, we suggest that the SWWA rainfall extremes are linked to a large-scale mode of Indian Ocean SST variability. The evolution of the meridional SST dipole is associated with anomalous atmospheric circulation involving variations of the southeasterly winds over the tropical pole and the generation of an anomalous

anticyclonic/cyclonic wind system near the subtropical pole with variations of the subpolar westerlies. The resulting anomalous latent heat fluxes and ocean Ekman transports control the evolution of the SST dipole. Further examination of the evolution of surface heat flux anomalies confirms that evaporative heat flux is the dominating factor controlling the SST dipole pattern. Ocean transport plays a role in moderating the impact of evaporation and setting the conditions favourable for the next generation phase of an opposite dipole.

1. Introduction

The climate variability over the Indian Ocean and its surrounding regions is known to be influenced by variations in sea surface temperature (SST) on various spatial and temporal scales. Rainfall variability in various regions has been associated with the emergence of spatially coherent Indian Ocean SST anomalies. For example, the Indian Ocean Dipole showing out-of-phase SST anomalies in the tropical eastern and western Indian Ocean (Saji et al. 1999) is shown to influence rainfall variability over Africa (Black 2003; Saji and Yamagata 2003), India (Ashok et al. 2001), Sri Lanka (Lareef et al. 2003), and Australia (Ashok et al. 2003). Other modes of Indian Ocean SST variability have also been recognised, such as the basin-wide monopole pattern (Weare 1979) and the subtropical dipole pattern (Reason 1999; Behera and Yamagata 2001) which have significant impact on regional rainfall. Therefore, improved understanding on the nature of these SST modes and identification of other SST modes that may exist in the Indian Ocean remain an important research area. In particular, it is of great importance to understand how the SST modes are related to extreme rainfall events in the surrounding regions. The focus of this study is on the southwest Western Australian region (hereafter termed SWWA) due to its unique spatial characteristic in terms of its isolated high rainfall over the arid Western Australia (Fig. 1). The SWWA rainfall shows unique temporal variability (Smith et al. 2000) in which its interannual variability remains poorly understood. Thus, it is of particular interest to investigate how the interannual SWWA rainfall extremes are linked to the adjacent Indian Ocean variability.

The tropical Indian Ocean is characterised by the reversal of monsoon winds resulting in seasonally unique atmosphere-oceanic circulation and climate. Interannual variations in monsoon circulation are linked to variations in SST and the intensity of associated rainfall (Saha 1970; Shukla and Misra 1977; Raghavan et

al. 1978; Weare 1979). Previous studies using empirical orthogonal function (EOF) analyses found basin-wide SST anomaly of uniform polarity as the most prominent SST variability mode in the tropical Indian Ocean (e.g., Weare 1979; Behera et al. 2003). Basin-scale warming peaks in austral autumn, which is about 3−6 months following the peak of an El Niño event (Wallace et al. 1998; Klein et al. 1999; Venzke et al. 2000; Lau and Nath 2003; Shinoda et al. 2004). Lau and Nath (2003) presented February−May composites of wind, precipitation, SLP, and SST following years of El Niño Southern Oscillation (ENSO), based on model and observational data (see their Figs. 3, 4). They showed extensive warming over the entire Indian Ocean basin accompanied by anomalous atmospheric conditions such as the weakening of the southeasterly trade winds and lower rainfall over Australia and eastern parts of Indonesia. This anomalous warming in the Indian Ocean is shown to result from variations in heat flux, mainly contributed by latent heat due to weakening of wind; though there is also notable contribution from increased solar input due to reduction in cloud cover (Klein et al. 1999; Venzke et al. 2000; Lau and Nath 2003; Shinoda et al. 2004). These studies mainly focus on atmospheric heat flux forcings associated with the notion of an 'atmospheric bridge' from the Pacific. The role of ocean dynamics in the generation of the SST anomalies has been investigated in further detail, for example, by Chambers et al. (1999) and Murtugudde and Busalacchi (1999). They noted the role of the Indonesian throughflow (ITF) and thermocline variations associated to wind anomalies which alter horizontal and vertical Ekman transports.

Shinoda et al. (2004) demonstrated that zonally out-of-phase SST anomalies in the Indian Ocean develop in austral winter-spring preceding a mature phase of an El Niño (see also Lau and Nath 2003). During developing stages of El Niño, the eastern tropical Indian Ocean exhibits negative SST anomalies while the western part shows

warming. This zonally out-of-phase pattern in the tropical Indian Ocean has generally been referred to as the Indian Ocean dipole (IOD; Saji et al. 1999) and emerges as the second leading EOF of SST variability in the tropical Indian Ocean after the basin-scale uniform polarity mode (e.g., Behera et al. 2003). By early austral summer, the cold anomaly in the eastern tropical Indian Ocean warms rapidly leading to the basin-scale warming over the Indian Ocean. Saji et al. (1999) and Webster et al. (1999), on the other hand, argued that the dipole mode exists independent of ENSO. In the same line of argument, modelling study of Behera et al. (2000) also suggested IOD independence of ENSO based on the low correlation between the Southern Oscillation Index (SOI) and EOF mode exhibiting IOD. Though IOD dependency of ENSO is still a topic of active research, few studies using both observations and models provide evidence that IOD can exist with or without ENSO (e.g., Baquero-Bernal et al. 2002; Li et al. 2003). The emergence of the anomalous SST dipole is strongly associated with anomalous atmospheric circulation during austral spring. The cold anomaly in the east results from the strengthened easterlies which enhance evaporation and the shallowing of thermocline via upwelling. Warming in the west is associated with weakening of the southeasterly trade winds which leads to reduced evaporation and deepening of the thermocline (e.g., Saji et al. 1999; Li et al. 2003). The evaporative effect of winds is highlighted in Behera et al. (2000) who found a dipole-like pattern in the latent heat flux anomalies. Air-sea feedbacks occur to damp the dipole by the austral summer.

SST variability characterised by a dipole pattern has also been discovered in the subtropical region of the Indian Ocean (Reason 1999; Behera and Yamagata 2001). Though the spatial and temporal characteristics of the dipole pattern in Reason (1999) and Behera and Yamagata (2001) differ, in general the dipole is associated with SST anomaly of one sign to the west of Australia and another sign in the

southwest Indian Ocean. This subtropical dipole is visible in austral autumn and dissipates in the following spring. During these events, southern Africa experiences significant anomalous rainfall. These authors suggested that the subtropical dipole events are not related to ENSO. Possible connection with the Antarctic Circumpolar Wave (ACW) is noted by Behera and Yamagata (2001). Recently, Suzuki et al. (2004) confirms the existence of the dipole in a coupled model. Changes in solar radiation and interannual variability of latent heat flux contribute to the generation of this mode (Suzuki et al. 2004), though ocean transport also evidently plays a role (Reason 1999; Behera and Yamagata 2001).

The link of SWWA rainfall to the Indian Ocean SST variability on the interannual scale is not yet fully understood. Relatively few studies have focussed on the natural year-to-year rainfall variability over SWWA. For example, Allan and Haylock (1993), Smith et al. (2000), and Ansell et al. (2000) focus on decadal time scale variability of SWWA rainfall in relation to the recent decline in winter rainfall since the late 1960s. The cause of this multi-decadal change remains a topic of debate, with suggestions on the attributing factor include enhanced greenhouse effect (IOCI 2002) and land clearing (Pitman et al. 2004). The focus of this present study, however, is on the shorter timescale interannual rainfall variability which is strongly influenced by ocean-atmosphere feedback processes.

The use of SST as predictor has received much attention since the traditional Australian rainfall predictor, the SOI, appears to resolve little of the region's variability (Smith et al. 2000; see also Drosdowsky and Chambers 2001). Drosdowsky (1993) found the potential of Indian Ocean SST anomalies for predicting seasonal rainfall in the southern and eastern Australia. However, it was indicated that there appears to be a weak relationship between the SST and SWWA rainfall. Nichols (1989) showed a wide band of rainfall variance from the northwestern Australia

extending through the central to southern Australia to be connected to an Indian Ocean SST dipole. This dipole appears distinct from the IOD and exhibits a reverse SST polarity between the Indonesian archipelago and the central Indian Ocean region. However, Nichols (1989) further demonstrated that the SST difference between the two regions shows little correlation with SWWA rainfall variability. Ansell et al. (2000) used EOF analysis on winter SST in the Indo-Pacific region over the period 1950−1997 and found that SWWA winter rainfall is significantly correlated to the third EOF SST mode. This EOF exhibits an SST anomaly of one sign in the tropical southeast Indian Ocean and another of opposite sign in the south-central Indian Ocean extending north along the eastern coast of Africa (see their Fig. 12). They attributed the decline of rainfall in the late 1960s−1980s to the occurence of cool SST anomalies in the tropical southeast Indian Ocean inhibiting the development of northwest cloudbands which contribute about 25%−40% of winter rainfall in SWWA (Wright 1997). The link between rainfall and Indian Ocean SST is also found by Smith et al. (2000) using EOF analysis of historical monthly SST data for the period 1871−1994. They found SWWA winter rainfall is correlated to the second EOF which shows different structure from that of Ansell et al. (2000).

Currently it is still not clear on the existence of any dominant SST variability mode in the Indian Ocean that is linked to SWWA rainfall interannual variability. Using a multi-century coupled climate model and a more recent observational record, this study attempts to re-assess SST variability modes in the Indian Ocean and investigate the link with SWWA rainfall variability. The rest of this chapter is organised as follows. The model and observational data are described in section 2. Section 3 provides an overview of the Indian Ocean climatology. The Indian Ocean SST variability modes are studied in section 4. The relationship between SWWA rainfall extremes and the Indian Ocean variability is investigated in section 5 with

a description on the evolution of SST and ocean-atmospheric heat flux anomalies. The study is summarised in section 6.

2. Data and data analysis

We analyse 1000-yr output data from the 10,000-yr integrated CSIRO Mark 2 coupled climate model. The model consists of atmosphere, ocean, biosphere, and sea-ice submodels. The atmospheric submodel is discretised on nine vertical levels in a sigma coordinate system and an R21 horizontal resolution. The ocean model horizontal resolution is approximately 5.6° longitude by 3.5° latitude matching to that of the atmosphere model with 21 vertical levels of varying thickness. The model implements seasonally varying but constant year-to-year flux adjustments applied on wind stress, heat and freshwater fluxes between the atmosphere and ocean. The flux adjustments help minimise climate drift in the model. Detailed model specifications can be found in Gordon and O'Farrell (1997), Hirst et al. (2000), and Hunt (2001). The variables analysed in this study include the sea surface temperature (SST), precipitation rate, surface wind stresses (τ^x, τ^y), ocean surface velocities (u, v, w), and air-sea heat fluxes such as the latent and sensible heat fluxes, and the incoming shortwave and outgoing longwave radiation. As the focus of this study is on variability at interannual time scales, a high-pass filter on the frequency-domain is applied to all variables to retain variability with periods shorter than 10 years. A cosine-taper is implemented in the filtering process to reduce the effect of ringing (Emery and Thomson 1998).

The spatial domain of interest is the entire Indian Ocean basin north of 50°S. Because of the sparsity of direct observations over the extratropical oceans, we employ reanalysis climatologies which combine available data with reanalysis techniques to provide a hindcast estimate of parameters over the entire domain of interest. The

reanalysis data for the atmospheric variables discussed in this study [wind velocities and sea level pressure (SLP)] are from the National Center for Environmental Prediction (NCEP) and National Center for Atmospheric Research (NCAR) reanalysis project (Kalnay et al. 1996). The NCEP/NCAR reanalyses use a global spectral model with a horizontal resolution of T62 ($\approx 2^\circ$ lat $\times$ 2° long) and 28 unequally spaced vertical sigma-levels in the atmosphere. Assimilation of *in situ* and satellite measurements is incorporated into the model with parameterisations of all major physical processes. The NCEP/NCAR reanalyses data is the most extensive reanalysis record available to date. The reanalysis SST data set used in the study is the National Oceanic and Atmospheric Administration (NOAA) reconstructed SST which has a resolution of $\approx 2^\circ$ latitude by 2° longitude. We analyse the observed data over the period 1970 to 2003, as open-ocean data coverage is sparse prior to 1970.

The CPC Merged Analysis of Precipitation (CMAP; Xie and Arkin 1996) climatology is used to analyse rainfall variability over large spatial scales. The CMAP data set consists of monthly averaged precipitation rates on $\approx 2.5^\circ$ latitude by 2.5° longitude over the period 1979−2003. Note that the CMAP data are used instead of NCEP/NCAR reanalysis rainfall as the latter exhibits deficiencies on regional scales as revealed by Janowiak et al. (1998).

The observed SWWA rainfall record over the period 1970−2003 is obtained from the gridded Australian Bureau of Meteorology (BoM) rainfall data sets, averaged over 30−35°S and 115−120°E (see Fig. 1 for location). The model SWWA rainfall is also averaged over the same spatial domain. As there are only two model grid points wholly enclosed by the SWWA box, the spatial averaging is conducted using an area-weighted linear interpolation involving a total of 12 model grid points that span the domain of interest. The mean of the model and observed monthly SWWA

rainfall is shown in Fig. 2. Both model and observed show peak rainfall over June-July-August (JJA) with a gradual decline to a minimum over December-January-February (DJF). It may be noted that the model displays lower precipitation rates than the observed which is partly due to the smoothing that takes account of grid points outside the region in the spatial averaging. Simulating rainfall accurately has long been a problem in climate models as it involves small-scale processes unresolved by the model resolution. Nonetheless, the CSIRO Mark 2 model does a reasonable job at representing SWWA rainfall over the annual cycle (see also Hunt 2001).

The observed data sets above are linearly detrended to exclude long-term trend in the analysis. We refer to the reanalysis data sets as the 'observations' throughout the study, although it is acknowledged that in some regions data are sparse and the reanalysis fields may well differ from reality. Monthly anomalies are defined as departures from the long-term monthly mean. Statistical techniques such as correlations, composite analyses, and empirical orthogonal function (EOF) techniques are implemented for our analyses. The EOF analysis is a common and powerful tool in climate research to investigate spatial and temporal characteristics of climate variability (e.g., Venegas et al. 1997; Mo 2000). The EOF technique extracts a set of eigenvectors and eigenvalues from the SST covariance matrix. A spatial map and principal component time series for each mode can then be obtained to describe the mode's associated spatial pattern and how it changes with time. For further detailed description of EOF techniques, the reader is referred to Preisendorfer (1988). The power spectral density (PSD) of a time series is estimated using the Thomson multitaper method described in Percival and Walden (1993) and Mann and Lees (1996). The computation of significance level described in Sciremammano (1979) is adopted for the correlation analyses, which is based on the effective number of degrees of freedom calculated from the decorrelation time scale of the time series.

3. Indian Ocean climatology

a. Annual-mean state: comparison of model and observations

The model and NOAA extended reconstructed SST exhibit similar spatial patterns (Fig. 3a, b). For a coarse resolution model such as this, the structure of the annual mean SST is well reproduced. The model SST is actually centred at 12.5 m to represent the upper 25 m of the model's top layer. Thus, the model SST in the tropical region appears to be about ≈ 0.5°C colder than the observed.

The model wind stress and the NCEP/NCAR reanalysis wind velocities are shown in Fig. 3c, d, respectively. The model captures atmospheric circulation features as in the observed in general, such as the southeasterly trade winds (at $\approx$ 30°S−10°S, 50°E−100°E), the westerly monsoon (north of the Equator), and the prevailing subpolar westerlies ($\approx$ 40°S). Some differences between the model and observations occur over continents, such as over northeastern Africa and southern Africa. These differences may be due to land surface processes not resolved in the model.

The annual mean rainfall in the model and the CMAP rainfall are presented in Fig. 3e, f. Looking at the overall spatial rainfall distribution, the model performs reasonably well, exhibiting high precipitation rates over the tropical region, and lower rainfall over northern Africa and in the Australian region. Some regions of the model display lower annual-mean rainfall than observed such as over Western Australia and in the central Indian Ocean. Over the tropics, the highest mean rainfall value in the model is about 4100 mm yr^{-1} which is low compared to the observed 5800 mm yr^{-1}. The model also displays higher rainfall than the observed in some regions, for example, over the Bay of Bengal ($\approx$ 10°S, 90°E) and to the southwest of India. Accurately simulating precipitation rates is a common problem in climate models, even in models with much higher spatial resolution. This is due to

our present lack of understanding of cloud physics and their representation in models, especially in the tropics where convective processes dominate cloud formation (Robinson and Henderson-Sellers 1999).

b. Indian Ocean monsoon: atmospheric conditions

The Indian Ocean climate is characterised by seasonally reversing winds, termed the monsoon climate. The primary cause of monsoon circulations is the difference in the rate of heating over land and sea leading to development of pressure gradients. To describe the monsoon processes, the observed SLP for each season is shown in Fig. 4a-d with the wind vectors overlaid. The influence of the monsoon winds on precipitation is demonstrated using the model monthly mean rainfall shown in Fig. 5a-d. The model wind stress is overlaid in each figure panel showing atmospheric circulation consistent with the observed. Note that despite the underestimation of precipitation over the tropics by the model, the monsoonal influence in the simulation is clearly apparent.

During boreal winter (DJF), high pressure develops over the Asian land mass leading to northeasterly jets over the tropics (Fig. 4a). These winds advect dry air into South Asia characterising the region with dry conditions during this season. The occurrence of the northeasterlies terms this season as the *Northeast Monsoon*. Strong pressure gradients are seen in the subtropics with a low pressure over the Australian continent and a high pressure over the South Indian Ocean causing the branching out of the southeasterly trade winds eastward and westward. The northern part of Australia and Indonesia experience a high rainfall season during the Northeast Monsoon.

Approaching boreal summer (June-July-August; termed JJA), the high pressure system over the Asian continent attenuates in MAM (March-April-May; Fig. 4b)

with a developing low pressure system over India and the surrounding regions due to northern hemisphere summer heating. This is accompanied by dissipation of the northeasterly winds which reverse to southwesterlies in JJA when the low pressure system fully develops (Fig. 4c). Rainfall starts to increase in MAM over South Asia (Fig. 5b) and peaks in JJA (Fig. 5c). On the other hand, the southwesterlies over the northwest of Australia switch to southeasterlies due to a pressure increase over Australia as a result of southern hemisphere winter cooling. Northern parts of Australia and Indonesia experience dry conditions during the *Southwest Monsoon*. The intensification of the mid-latitude anticyclonic high pressure system strengthens the southeasterly trade winds. This is accompanied by the shifting of rain bearing fronts eastward along the western rim of Australia. The Southwest Monsoon conditions ease off in austral spring which is a transition period prior to the onset of the Northeast Monsoon (Fig. 5d).

c. Indian Ocean monsoon: ocean surface circulation

The associated seasonal ocean surface circulation response to the monsoon climate in the model is shown in Fig. 6a-d. During the Northeast Monsoon, there is a broad westward flow of the South Equatorial Current in the latitudinal band of $\approx 10°S - 20°S$ which has a southward Ekman component in response to the southeasterly trade winds. The South Equatorial Countercurrent is seen just to the south of the equator supplied by the southward-flowing Somali Current and northward-flowing East African Coast Current (Schott and McCreary Jr. 2001) Note that the model shows weak downwelling along the path of the South Equatorial Countercurrent. The Somali Current is fed by the North Equatorial Current (NEC) which flows westward and splits into southward and northward branches. As a result, downwelling is seen against the coast of Somalia, as well as upwelling north of the

equator due to the divergence of the North Equatorial Current. The branching out of the southeasterly winds over the northwestern coast of Australia (see Fig. 5a) creates a divergence in the region which forces a weak but extensive upwelling. The upwelling over this region during the Northeast Monsoon has been inferred in the observational study of Qu and Meyers (2005). South of 20°S is marked by surface downwelling for all seasons.

During southern hemisphere autumn (MAM; Fig. 6b), the NEC reverses its direction in response to the reversal of the northwesterlies in transition to southwesterly winds in JJA. Consequently, there is notable surface downwelling developing against the western coast of Sumatra. The upwelling in the northwest of Australia is reduced and downwelling develops. In the Southwest Monsoon season, there is southward flow across the equator joining the SEC. At the same time the downwelling along western Sumatra strengthens. The strengthening eastward flowing NEC is followed by the northward flowing Somali Current. This creates surface divergence along the coast of Somalia and draws colder water upwards during the northern summer (Tomczak and Godfrey 2003). As seen in Fig. 6c, strong coastal upwelling is observed. Upwelling on the southern side of the equator is limited to the north of $\approx 15°$S, as also observed by Qu and Meyers (2005) for the southeastern tropical Indian Ocean. The transport of the ITF appears to be large during this season (Schott and McCreary Jr. 2001). In spring, the circulation shows similar patterns to that of autumn. Overall, the simulated Indian Ocean mean seasonal climate shows an excellent agreement with observations given the model's coarse resolution.

4. Indian Ocean climate variability

a. Modes of SST variability: EOF analysis

EOF analysis has been used widely to identify modes of interannual SST variability over the tropical and subtropical Indian Ocean (see section 1). These SST variability modes are not merely statistical artefacts, as actual physical mechanisms have been shown to explain the evolution of the modes and their influence on the surrounding climate (see also Behera et al. 2003). In this study an EOF analysis is applied on the model and observed SST data over an extensive spatial domain spanning meridionally from $\approx 50°$S to 30°N and zonally from 20°E to 150°E, to cover the entire Indian Ocean basin. While allowing identification of spatially large-scale modes, this approach also re-evaluates the co-evolution of the already documented local modes, such as the IOD, as part of a more global picture of climate variability. Though variability in the annual-mean climatic state and associated dynamical processes are the focus of this study, seasonal stratification is also noted in the following EOF analyses. This is because the Indian Ocean climate is strongly influenced by the monsoons (see section 3a). A more detailed analysis involving seasonality will be made in section 5 which investigates the ocean-atmospheric variability connected to SWWA annual rainfall extremes. Having prior knowledge of the dominant SST modes in the model and observations will help in connecting any anomalous SST patterns that emerge during the SWWA rainfall extremes to the identified dominant modes.

The first three leading EOFs of the annual mean SST in the model and observed (the latter for the period 1970−2003) are presented in Figs. 7, 8 showing the spatial patterns (top panel), the principal component time series (middle panel), and the power spectra (bottom panel). The first EOF of the model annual SST (Fig. 7, upper panel; hereafter referred as the *model Mode-1*) exhibits a basinwide SST

anomaly of uniform polarity over the tropical Indian Ocean (north of 20°S) and an anomaly of the opposite sign in the southwest Indian Ocean (30°S−50°S, 20°E-70°E). The first EOF of the NOAA reanalysis SST over period 1970−2003 (Fig. 8, lower panel) also displays a very similar structure to that of the model (hereafter referred as the *observed Mode-1*). It can be noted, however, that the observed Mode-1 explains more variability in the western tropical region than the model. The contrast in spatial distribution of anomalies in the model and observed can be inferred from the standard deviation maps of the model and observed data shown in Fig. 9a, b. In both observed and model, large SST variability is concentrated in the region of northwestern Australia and in the southwestern Indian Ocean. However, the observed exhibits large variability in the tropical western and eastern Indian Ocean, which is absent in the model. As shown by the principal component time series (Figs. 7, 8; middle panel), the model Mode-1 generally corresponds to a maximum SST anomaly of ≈ 0.8°C, which is comparable to the observed 0.9°C. The power spectra for the model and observed (Figs. 7, 8, bottom panel) show markedly different spectral structure with the model displaying peak variability at about 7-yr period, and the observed at 4-yr period.

The second and third EOFs in the model (Fig. 7) exhibit a dipole pattern in the tropics (referred as Mode-2 and Mode-3, respectively). Like Mode-1, these modes are accompanied by a distinct anomalous pattern in the southwestern Indian Ocean which may be linked to a subtropical dipole signal as found, for example, by Reason (1999). The tropical dipole displayed by the model Mode-2 and Mode-3 is different from the IOD as described in Saji et al. (1999) which, on the other hand, is captured by the observed Mode-2 (Fig. 8). In the observed, IOD is an out-of-phase SST anomaly in the equatorial Indian Ocean which is not apparent in the model EOFs of annual-mean SST variability. The principal component time

series of the model Mode-2 and Mode-3 (Fig. 7, middle panel) shows that these modes are related to SST anomalies of up to about 0.6°C, which is comparable to the observed Mode-2. Note that the model Mode-2 and Mode-3 explain almost an equal percentage of variance ($\approx 9\%$) suggesting that their eigenvalues are close to each other. This implies the possibility of 'effective degeneracy' as described by North et al. (1982). Thus, modal mixing between Mode-2 and Mode-3 is expected which will be discussed in the following sections.

The most prominent feature of the observed Mode-2 is the tripole pattern with the first pole occurring in the northwestern region of Australia and extending northwest to the region off Sumatra. The second pole of opposite sign which lies to the southwest of the first pole, extends north against the eastern coast of Africa to the south of India. A weaker subtropical pole occurs in the southwestern Indian Ocean. The spatial pattern of the observed Mode-2 looks similar to the model Mode-3, though the central pool of SST anomaly in the model lies slightly further north to that in the observed. The temporal variability of the model Mode-3 and observed Mode-2 share similar spectral peaks at 3 and 8-yr periods, despite the richer spectral structure in the model.

Though the model variability is comparable to the observed, overall it is weaker as deduced by the model maximum standard deviation value of ≈ 0.41°C compared to the observed 0.54°C. As mentioned above, apart from some discrepancies in the spatial structure of the model and observed EOFs, differences are also notable in their temporal structures. Furthermore, the model annual-mean SST variability modes account for a smaller percentage of variance as compared to the observed. For example, the model Mode-1 explains only 16% of the model data variance, while the observed accounts for 31%. These differences are expected because the model 1000-yr data consists of a greater variety of signals as compared to the observed 34-

yr record. The weaker model variability may be associated with the damping effect of the implemented surface flux adjustment terms. The coarse model resolution is also likely to contribute to the discrepancy in the spatial structure of the modes. A climate change imprint in the observed SST over the period 1970−2003 may also contribute to the differences between the model and observations. This is an interesting topic for future research.

a.1. Spatial mixing

Variability modes identified over large spatial scales can be a combination of modes defined over smaller regions. In this case, the identified SST variability modes above may be composed of tropical and subtropical modes. An EOF analysis applied on the model and observed SST over the tropical (north of 20°S) and subtropical (south of 20°S) regions separately shows a basin-scale uniform polarity in the tropics and a subtropical dipole pattern as the first EOFs (denoted as EOF1-N20 and EOF1-S20, respectively; Figs. not shown). The second EOF exhibits a tropical dipole pattern (Fig. not shown; denoted as EOF2-N20). Using the principal component timeseries of the EOFs, a correlation analysis is conducted to reveal the connection between the large-scale modes and the regional modes. The correlation coefficients and the corresponding cut-off values at 99% significance level are displayed in Table 1.

Mode-1 is highly correlated to EOF1-N20 with a correlation coefficient of 0.92 and 0.95 for the model and observed, respectively. The correlation against EOF1-S20 is also significant however with a weaker correlation coefficient of 0.55 in the model and 0.64 in the observed. Thus, it is confirmed that Mode-1 is composed of the uniform polarity and subtropical dipole modes which co-evolve as a large-scale mode of the Indian Ocean interannual SST variability.

The model Mode-2, Mode-3, and the observed Mode-2 are all significantly cor-

related to EOF2-N20 and EOF1-S20, suggesting that these modes are composed of the tropical dipole and the subtropical dipole. However, note that the model and observed tropical dipoles have different spatial patterns (see Figs. 7 and 8 for the dipole pattern north of 20°S). The observed dipole exhibits an IOD while the model exhibits a dipole which looks different from an IOD as already noted in the previous section.

a.2. Seasonal mixing

The SST variability mode is also expected to have some seasonal preference, since the Indian Ocean is characterised by a monsoonal climate. To demonstrate this, an EOF analysis is performed on the seasonal-mean SST anomalies. The principal components of the seasonal EOFs are then correlated with the principal component of the annual-mean EOFs. The correlation coefficients and the 99% significance level cut-off values are presented in Table 2. The spatial patterns for the seasonal modes are shown in Figs. 10, 11 for the model and observed, respectively.

Correlation values in Table 2 show that the seasonal EOF1 in the model are all correlated significantly with the model Mode-1. EOF1-DJF and EOF1-MAM exhibit the Mode-1 uniform polarity pattern which becomes less extensive in JJA (see Fig. 10, upper panel). EOF1-SON exhibits an IOD-like pattern in the tropics (see also e.g., Shinoda et al. 2004). Though the summer and winter stratification in the observed Mode-1 is similar to the model, the winter and spring modal characteristics are slightly different. The observed EOF1-JJA and EOF1-SON are instead correlated to Mode-2, while the EOF2-JJA and EOF2-SON exhibits the Mode-1 pattern (Fig. 11), as also supported by the high correlation values between EOF2-JJA, -SON, and Mode-1 (Table 2). On the other hand, none of the model seasonal EOF2 patterns exhibit any Mode-1 pattern (Fig. 10), despite the weak correlations between EOF2-JJA and EOF2-SON against Mode-1. The correlation values for the

model seasonal EOF2 versus Mode-2 and Mode-3 suggest that the model Mode-2 is dominated by summer-autumn SST variability, while Mode-3 is dominated by winter-spring variability.

a.3. Summary

The above analyses demonstrate the seasonal stratification in the annual-mean SST variability modes. There are slight differences in seasonal stratification of the model and observed modes. The basin-scale uniform polarity mode (Mode-1) in the model is prominent in the austral summer to winter. On the other hand, the observed Mode-1 is only dominant from summer to autumn. In winter and spring, the observed tripole SST pattern (Mode-2) is dominant with an IOD signature in the tropics. The IOD-like signal in the model occurs only in spring and is less dominant than the observed.

The analyses on spatial mixing show that local SST variability modes such as those already identified in previous studies (see section 1) can co-evolve and manifest as a larger mode of variability. For example, the model large-scale Mode-1 is composed of the basin-wide mode and the subtropical dipole. The model Mode-2 and Mode-3 and the observed Mode-2 consist of tropical and subtropical dipoles. These analyses demonstrate the different nature of modal mixing and decompositions in the model and observed data, which are subjected to differences in record length, spatial domain, and seasonal stratification. These factors need to be considered when interpreting large-scale variability in the annual mean as presented in the following section.

b. Anomalous conditions related to extreme events

The similar characteristics shared between the model Mode-1 and the observed Mode-1, and the model Mode-3 and the observed Mode-2 motivate us to look at

the atmosphere-ocean processes associated with these modes. Composite analyses of annual-mean climate parameters in the model and observed such as rainfall, wind stresses/velocities, SLP, SST, and ocean surface currents, are presented based on the principal component timeseries of the identified EOFs. The composites based on the observed Mode-1 and Mode-2 are presented with the former exhibiting the Indian Ocean monopole pattern and the latter exhibiting the SST tripole pattern in the central Indian Ocean basin. Both have been shown to co-evolve with the Indian Ocean subtropical dipole. The model composite analyses are presented based on the first and third EOFs (model Mode-1 and Mode-3) whose patterns resemble the observed Mode-1 and Mode-2, respectively.

b.1. Observed Mode-1/Model Mode-1

Figure 12 presents composite anomalies of the observed annual mean SST, rainfall, atmospheric circulation, and sea level pressure (SLP) during Mode-1 related events. During a warm (cold) event, basinwide ocean surface warming (cooling) is observed over much of the tropical and subtropical regions of the Indian Ocean accompanied by cooling (warming) off southeastern Africa. Similar SST composite patterns are also seen in the model (Fig. 13a, b), although the regions of more intense anomalies in the model are concentrated in the central Indian Ocean to the northwest of Australia. During the warm (cold) years, positive (negative) SLP anomalies develop over the tropical region of the western Pacific to eastern Indian oceans (Fig. 12). Negative (positive) SLP anomalies are seen over a vast area south of 30°S. Consequently, this anomalous positive (negative) meridional SLP gradient forces southeastward (northwestward) geostrophic winds around 20°S thus weakening (enhancing) the southeasterly trade winds in the region. On the other hand, while the observed southeasterly trade winds over the southwest of Sumatra strengthens (weakens), the model shows weakening (strengthening). The prevailing

westerlies at $\approx 40°$S strengthen (weaken) during the warm (cold) years in both the observed and model.

The influence of winds evidently plays a role in the generation of the basinwide anomaly via latent heat fluxes and ocean Ekman transports. Enhanced winds may induce anomalously strong latent heat flux. Thus, the weakening of atmospheric flow during warm years reduces the rate of evaporation. However, in some regions such as near the equator, enhanced winds occur during warm years. Induced warming in the region may instead result from a reduction in cloud cover, thus allowing higher input of solar radiation (see also Klein et al. 1999). The cold (warm) anomaly in the southwestern subtropical region can arise from both increased (reduced) evaporation from an enhanced (weakened) wind field as well as an increased (reduced) northward Ekman transport advecting colder water into the region (Fig. 13).

The rainfall patterns associated with anomalous SST are shown in Figs. 12e, f, and 13e, f. It may be noted that there is an ENSO signature in the patterns. During warm (cold) years there is a latitudinal band of higher (lower) annual mean precipitation extending from southeast Asia to the south Indian Ocean in both the observed and model. A band of opposite sign and stronger rainfall anomalies occurs in the western Pacific whereby the northern and eastern parts of Australia generally experience dry (wet) conditions. However, the dry (wet) anomalies over Western Australia as shown in the observed are not apparent in the model. The southeast African continent experiences drought (enhanced precipitation) during the warm (cold) years in response to the surrounding anomalous cooling (warming) of subtropical waters. This anomalous SST in the southwestern Indian Ocean is associated with the subtropical dipole (IOSD).

b.2. Observed Mode-2/Model Mode-3

The observed composite patterns based on Mode-2 are shown in Fig. 14. The composite SST anomalies show a tripole structure over the tropical-subtropical region. The model composites are shown in Fig. 15 based on the model Mode-3 which exhibits similar structure as the observed Mode-2, despite some slight differences in the location of the poles as already discussed in the EOF analyses section. For the following discussion, a positive (negative) Mode-2 event refers to the SST composite pattern shown in Fig. 14a corresponding to cold (warm) anomaly off the northwestern Australia, a warm (cold) SST pool in the central subtropical Indian Ocean, and a cold (warm) SST pole in the southwestern Indian Ocean.

During a positive Mode-2 event, anomalously high pressure fills a vast region of the domain. A weak low SLP in the southwest subtropical region forces an anomalously cyclonic wind flow (Fig. 14c). This anomalous pressure system weakens the southeasterly trade winds over the pool of warm water in the subtropical region ($\approx$ 40°S, 90°E). In the model, the anomalous southeasterly trades occur further north than in the observed. The occurence of anomalously high SLP west of the western coast of Australia induces an anomalous anticyclonic system enhancing the southeasterly trades in the eastern part of the Indian Ocean basin. In the model, however, this anomaly occurs further east at the pool off northwestern Australia. The northward extension of the SLP anomaly to the equatorial western Indian Ocean causes a suppression of the westerlies at the equator. Enhancements of the prevailing westerlies at $\approx$ 40°S are observed during the positive Mode-2 event, as also seen in the model, for the longitude band 20°$-$70°E and to the east of 100°E. This enhances the mean northward Ekman transport (Fig. 15c; see Fig. 6 for the annual-mean current vectors) in the corresponding longitude bands, forcing colder water northward. The anomalous oceanic current response to the wind anomalies is also

apparent in other regions. For instance, northward Ekman transport is favoured over the i warm SST pool in the central Indian Ocean, during the positive event. Anomalously westward oceanic flow at the equator accompanies the anomalously westward winds there. Anomalous southward Ekman transport is also seen over the northern-most cold SST pool. The reverse conditions to those described above occur during the negative events.

The observed rainfall composites during a positive (negative) Mode-2 event shown in Fig. 14e (Fig. 14f) exhibit dry (wet) condition over the Indonesian archipelago and the southwest Western Australia, and wet (dry) condition over western Indian Ocean and the equatorial Pacific Ocean. It may be noted that the model rainfall composites (Fig. 15e, f) also exhibit similar spatial distribution of anomalies to that of the observed. There appears to be a positive correlation between rainfall and SST over the tropics. Since convection is strong over the tropics, higher SST corresponds to higher convective processes which result in higher precipitation rates.

c. Remote forcings on the Indian Ocean SST variability

c.1. ENSO influence

External influences on the Indian Ocean SST variability have been mainly attributed to ENSO (see section 1). The extensive basin-scale warming or cooling, described here as Mode-1, has been associated with the manifestation of ENSO in the Indian Ocean (e.g., Wallace et al. 1998; Chambers et al. 1999; Klein et al. 1999). The emergence of IOD signal during ENSO events has also generated debates on the extent of remote influence from the Pacific Ocean (e.g., Saji et al. 1999; Baquero-Bernal et al. 2002). It is thus worth commenting on the extent of ENSO forcing on the Indian Ocean SST variability in the 1000-yr run of the CSIRO Mk2

climate model and the reanalysis SST over the period 1970 to 2003.

To demonstrate the manifestation of ENSO in the Indian Ocean, SST composite anomalies are constructed based on the temporal evolution of ENSO which is represented by the principal component of the first EOF for the tropical Pacific Ocean SST (denoted as EOF1-Pacific). The spatial pattern of EOF1-Pacific is presented within the boxed region in Figs. 16a and 17a for the model and observed SST, respectively, showing a mature El Niño phase. The model SST composite anomaly for the El Niño (La Niña) years is shown in Fig. 16b (c) exhibiting warming (cooling) over the tropical Indian Ocean which intensifies and becomes more widespread in the following year (Fig. 16d, e). The observed composites show similar patterns in the Pacific as the model (Fig. 17b-e), though exhibiting some differences in the Indian Ocean. Note that the observed composite anomalies during the ENSO years (Fig. 17b, c) display some signature of Mode-2 (refer to Fig. 8, upper panel). On the other hand, the extensive anomalous warming/cooling following the ENSO years (Fig. 17d, e) exhibits similar spatial patterns as Mode-1.

Table 3 presents correlation values of model and observed EOF1-Pacific (ENSO) versus the model and observed annual-mean SST variability modes at 0-yr and 1-yr time lags (i.e., ENSO leads the modes by 1 year). The model (observed) Mode-1 is significantly correlated to ENSO at 1-yr lag at 99% (90%) significance level with a correlation coefficient of only 0.32 (0.40). There are no significant correlations for the model Mode-2 and Mode-3 versus ENSO at the 99% significance level. However, the observed Mode-2 is significantly correlated to ENSO. Note that when seasonal stratification is taken into account, the degree of correlation is higher for the model EOF1-DJF versus ENSO at 1-yr lag with a coefficient of 0.43 significant at the 99% level (see Fig. 10 for the spatial map of the model EOF1-DJF). As for the observed, the correlation is highest for EOF1-MAM with a significant correlation coefficient

of 0.50 above the 95% level. At 0-yr lag, ENSO is best correlated to the observed EOF1-SON with a correlation coefficient of 0.56 above the 95% significance level. The correlation coefficient for the model EOF1-SON is 0.24 significant at the 99% level.

It can be noted that the model underestimates the SST anomalies associated with ENSO (see also Hunt and Elliott 2003). The magnitude of the model EOF1-Pacific SST anomaly is $\approx 1°$C and the observed is $\approx 2°$C (Figs. 16a, 17a). Thus, it may also contribute to the weaker correlations between ENSO and the SST modes in the model. In addition, the magnitude of the SST composite anomalies due to ENSO (Figs. 16b-e, 17b-e), is smaller than that associated with the SST modes (see earlier Figs. 7, 8). For example, Mode-1 is associated with an SST anomaly of about 0.8°C, however, the basin-scale anomalous warming/cooling associated with ENSO corresponds to an SST anomaly of only the order of 0.1°C. Furthermore, since the correlations between ENSO and the SST modes are only modest, these suggest that the influence of ENSO on the Indian Ocean SST variability is limited, and that there must be mechanisms unique to the Indian Ocean that give rise to the SST variability modes.

c.2. Southern Ocean influence

As shown in section 3b, the subtropical dipole mode (described as EOF1-S20) contributes to the large-scale SST variability modes (see Table 1). Forcing of ENSO on the subtropical dipole is likely to be weak or negligible as suggested by Behera and Yamagata (2001) and the weak correlation between the model/observed ENSO (EOF1-Pacific) and EOF1-S20 (correlation coefficients of near 0 for the model and 0.31 for the observed - only marginally significant at 90% level). On the other hand, because of the close proximity of the subtropical dipole to the Antarctic Circumpolar Current (ACC) region, it is likely that the Southern Ocean SST variability may have

a more important influence. The influence of the ACW on the subtropical dipole was also suggested by Behera and Yamagata (2001), however, without demonstrating the connection. Here, we attempt to document the Southern Ocean influence on the Indian Ocean SST variability via the subtropical dipole.

EOF analyses are conducted on the SST over the circumpolar region within the latitude band of $\approx 40^\circ - 60^\circ$S (indicated by the dashed lines in Fig. 18, top panel). To capture a range of SST modes in the region, the first six EOFs in the model are displayed in Figs. 18a-c (EOF1−3), 19a-c (EOF4−6), showing anomalous patterns of SST with a variety of wavenumbers. The corresponding composite anomalies constructed based on the principal component of the EOFs are shown in Figs. 18d-f, 19d-f respectively. Figures 20, 21 present the corresponding analyses for the observed SST.

Table 4 presents correlation coefficients of the Southern Ocean modes (EOF1, 2, 3, 4, 6 -SO) versus the subtropical dipole (EOF1-S20) for the model and observed. The subtropical dipole in the model is shown to be significantly correlated at 99% significance level to some of the Southern Ocean modes, namely EOF1-SO, EOF2-SO, EOF3-SO, and EOF5-SO. The observed subtropical dipole is correlated to EOF1-SO, EOF4-SO, and EOF6-SO at the 95% level. It can be noted that these significantly correlated Southern Ocean modes exhibit an apparent SST dipole pattern in the region south of 20°S with one pole in the southwestern Indian Ocean and another one of opposite sign in the eastern side. This analysis shows that there is a Southern Ocean signature in the Indian Ocean variability. However, with only modest correlation coefficients, the influence of the Southern Ocean SST variability, for example via the ACW and/or the Southern Annular Mode, is only moderate, and is confined to the subtropical Indian Ocean.

5. SWWA rainfall extremes linked to Indian Ocean variability

a. SWWA rainfall variability and extreme events

Figures 22a, 23a show the timeseries of SWWA annual rainfall anomaly for the 1000-yr coupled model integration and the BoM observations, respectively, after the removal of a long-term mean of 369 mm yr^{-1} in the model and 520 mm yr^{-1} in the observed. Despite the relatively low precipitation rate in the model (about 120 mm yr^{-1} lower than the observed), the model produces rich interannual variability structure with periods of dominant variability approximately matching the observed (as inferred from comparing Figs. 22b and 23b). The power spectral density (PSD) of the SWWA rainfall anomaly in the model (Fig. 22b) shows variability occuring over a broad range of periods with peaks at about $3-4$ years and 8.5 years (significantly different from a white noise signal at 95% confidence level). The PSD analysis of observed rainfall (Fig. 23b) shows much less spectral structure given the short data record. However, the observed peaks at 2.4, 3.9, and 8 years are in good agreement with three of the significant peaks shown in the model analysis. It can be noted that the magnitude of the model SWWA rainfall variability is weaker than that in the observed, with a standard deviation of 44 mm yr^{-1} as compared to the observed 66 mm yr^{-1}. This is typical of coarse resolution climate models wherein extreme events tend to be weakly damped compared to observations.

SWWA rainfall extremes are defined as those in which the rainfall anomaly exceeds one standard deviation above and below the long term mean, resulting in approximately 160 instances in the model for each of anomalously wet and dry years. On the other hand, the observed rainfall over the period $1970-2003$ shows only six dry SWWA years comprising of 1972, 1977, 1979, 1987, 1994, and 2002;

and five wet years in 1973, 1974, 1988, 1992, and 1999 (see Fig. 23a). To reveal the corresponding anomalous state of the Indian Ocean climate during these extreme years, a composite analysis of some climate parameters is performed based on the pre-defined dry and wet years.

b. Surface anomalies during SWWA rainfall extremes

Figure 24 presents composite anomalies for the model annual mean rainfall, wind stress, SST, and surface ocean current velocity. The composite plots for the observed annual mean rainfall, SLP, wind velocity, and SST are shown in Fig. 25. For the model plots, anomalies are only shown where they exceed 90% significance level as estimated by a two-tailed t-test.

Anomalous rainfall extends from SWWA and the eastern Indian Ocean into Asia, as well as in the southern part of Australia, with a reversal in sign in the western Pacific Ocean and in some parts of the western Indian Ocean (Fig. 24a, b). The composite patterns of model precipitation exhibit similar distribution patterns as in the observed 1979−2003 CMAP rainfall climatology, however with notable differences (compare Figs. 24, 25). The highest anomalies in the model occur over SWWA not Asia in contrast to the observed. For the observed rainfall, stronger anomalies also fill the western Pacific and a vast area of the western Indian Ocean. It should be mentioned that if a significance test were not used to produce the model composite maps, more anomalies can be seen over the western Indian Ocean, Asia, and the Pacific regions. This indicates a greater variety of rainfall scenarios over these regions in the model during dry and wet SWWA years.

An SST dipole emerges during dry and wet SWWA years (Figs. 24c, d). During dry years, a cold SST anomaly sits in the tropical eastern Indian Ocean off Northwest Australia (referred hereafter to as P1) extending northward into the western Pacific

region. A pole of anomalously warm SST (P2) is found to the south of P1, centered at ≈ 25°S, 90°E, extending northeast towards Central Africa. Reversal in sign of the dipole occurs during wet years, with the SST dipole nearly a mirror image of the dry year scenario. This tropical-subtropical dipole pattern matches the observed (Fig. 25c, d) with anomalies reaching peak amplitude in the tropical and subtropical eastern Indian Ocean, adjacent to Western Australia. Note that some differences in the model and observed anomaly patterns exist. First, the magnitude of the model peak anomalies is weaker than the observed (± 0.1°C versus ± 0.4°C, respectively). Second, in the observed, there is an SST cold (warm) pool in the southwestern Indian Ocean centered at about 40°S, 50°E during dry (wet) years which is absent in the model. These differences may result from a combination of the model's coarse resolution, the model flux adjustment terms, and the size of sample used for the composite analysis (≈ 160 events in the model versus only ≈ 6 in the observed). It can also be noted that the IOD signature is stronger during dry years than wet years as inferred by both the model and the observed.

The composite patterns of the wind stress anomalies show significant changes in direction over the SST poles (Fig. 24c, d) during the extreme years. Figure 3c, d (see section 3a) shows mean southeasterly winds over SST P1 and P2. During dry (wet) years, these southeasterly winds accelerate (decelerate) over P1 driving stronger (weaker) southward surface Ekman transport (Fig. 24e, f). Winds over the southeast Indian Ocean SST pole (P2) are anomalously southwestward (northeastward) during warm (cold) phases resulting in anomalously southeastward (northwestward) Ekman transport. There is also a strengthening (weakening) of the subpolar westerlies during dry (wet) SWWA years with the corresponding increase (decrease) in the annual mean northward Ekman transport. These features of the wind vector anomalies match those in the observed (Fig. 25c, d).

It can be seen in Fig. 25e and f that the wind anomalies are a response of anomalous SLP. During dry years, SLP over the Australian continent is higher than average. A band of anomalously low pressure stretches across the subpolar region forcing an intensified westerly wind field at 40°S. The reverse anomalous SLP condition occurs during wet years, however the anomalously low SLP across Australia stretches southward to the subpolar region near 60°E. The changes in wind stresses and surface currents induce variability in the surface heat fluxes, thus perturbing the mean state of SST in the regions. Intensity in atmospheric latent heat flux is influenced by the strengthening and weakening in wind stresses. Variability in the wind stresses then drives Ekman transport variability which in turn influences the ocean surface heat budget via advective heat fluxes. These mechanisms in the model are elaborated in more detail in sections 5c and 5d taking seasonality into account.

Finally, it is of particular interest to address the following question: To what extent does this tropical-subtropical SST dipole that emerges during SWWA extreme years fit into the Indian Ocean climate system? In other words, can this dipole be identified as one of the leading modes of the Indian Ocean SST variability? By inspection, the observed and model SST composite patterns shown in Fig. 24c, d and Fig. 25c, d resemble the observed Mode-2 and model Mode-3, respectively (see Figs. 7, 8). Furthermore, there is a significant correlation between the SWWA rainfall versus these EOFs. The observed rainfall is correlated to the observed Mode-2 with a correlation coefficient of 0.53 (above the 99% significance level). The model rainfall is correlated to model Mode-3 with correlation coefficient of 0.24 (significant at the 99% significance level). Figure 26 shows the observed SWWA rainfall timeseries against the principal component timeseries of Mode-2. Note that all anomalously high (low) precipitation rates [i.e., those exceeding one standard

deviation above (below) the mean] coincide with negative (positive) Mode-2 events, except for year 2002. In the model, a correlation analysis between the rainfall and Mode-3 timeseries taking account of only the extreme years shows a coefficient of 0.40, and 0.72 for the observed. Therefore, the SWWA rainfall extremes and their associated climate anomalies are part of a well-defined Indian Ocean dominant mode of variability.

c. Seasonal evolution of climate anomalies

A composite analysis of the mean seasonal SST and wind anomalies in the model is presented to investigate the mechanisms leading to the development of the SST dipole. Figure 27 presents the composite plots illustrating the seasonal evolution of SST and wind stress anomalies during years of SWWA extreme. During dry (wet) SWWA years, cold (warm) SST anomaly at P1 is seen to develop off Northwestern Australia in DJF accompanied by an emergence of a weak SST anomaly at P2. The SST anomaly at P2 becomes more notable in fall (MAM) and intensifies alongside P1 to peak in JJA. The development of the anomalous atmospheric flow in DJF is less apparent than that of SST anomalies, though there is a slight acceleration (deceleration) in the wind field around P1 and deceleration (acceleration) around P2 during dry (wet) SWWA years (for comparison with the mean DJF wind stress refer to Fig. 5). Acceleration of the mean southeasterly wind over P1 during dry years becomes more prominent in MAM with developing anticyclonic gyre forcing anomalously southward flow over P2 (i.e., a reduction in wind strength). These wind anomalies intensify in JJA with the strengthening of the SST dipole. It can be noted that this is accompanied by the weakening of the southerly winds over the western Indian Ocean. The amplitude of the SST dipole and wind anomalies ease off in spring (SON) marked with a significant weakening of the southeasterlies in the

central Indian Ocean during the dry years. These anomalous conditions are reversed during the wet years. Changes in the wind intensity may then drive the anomalous SST via latent heat fluxes and Ekman transports. The similarity of JJA composite patterns to the annual counterpart (see section 5b) suggests that the wintertime anomalies dominate the annual mean variability. It is worth noting that the SWWA is a winter rainfall region (see section 2; Fig. 2).

Figure 28 shows the composite anomalies of latent heat flux and wind strength patterns in DJF to SON. Latent heat anomalies around P1 have already developed in DJF, gradually strengthening to a peak in JJA. During dry (wet) SWWA years from DJF to JJA, the cold (warm) SST pole P1 is a region characterised by increased (decreased) evaporation with the reverse occuring in P2. Note the striking feature of the latent heat composite anomalies over P1 in JJA which corresponds to strengthening (weakening) winds and increased (decreased) SST over P1. Though evident, the pattern over P2 is less apparent compared to P1. Thus, it seems that the effect of wind cooling is more prominent in developing the SST anomaly at P1. By austral spring, there is a sudden switch in sign in the latent heat flux anomaly over P1 which acts to damp the SST anomaly. Consequently, the SST anomaly at P1 is reduced in magnitude, however, without immediate reversal in polarity. Other features to note is the effect of wind strength in creating an SST anomaly via evaporation which is apparent in the western Indian Ocean during JJA. The negative (positive) anomaly over land in the SWWA region indicates the dry (wet) condition there. It is also worth mentioning that the warming (cooling) of the surface water in the equatorial central Indian Ocean in SON occurs with the weakening (strengthening) of the mean eastward equatorial wind, decreasing (increasing) evaporation during dry (wet) years (compare Fig. 27g, h with Fig. 5d). This particular anomalous wind flow is observed during an IOD event (Saji et al. 1999) which sug-

gests further that these SST dipole events, related to SWWA rainfall extremes, may coincide with the IOD in SON when the IOD is most intense.

The surface current velocity composite anomalies (Fig. 29) indicate anomalous Ekman transport in response to the anomalous wind stress shown previously in Fig. 27 (i.e., to the left of the wind vector). As mentioned in section 3a, the most distinctive seasonal characteristics in the mean surface circulation over the year is during summer when circulation at P1 is characterised by surface divergence induced by the occurence of westerly anomalies north of Australia. Consequently, there is an upwelling of colder water from below (see Fig. 6a). During the summer of dry (wet) SWWA years, this divergence and upwelling at P1 are enhanced (suppressed) along with the strengthening (weakening) westerly anomalies. Approaching winter, these wind anomalies switch to an easterly-southeasterly anomaly, thus enhancing the South Equatorial Current via southward Ekman transport. Downwelling is seen to develop along the western coast of Australia (see section 3, Fig. 6) which also corresponds to some part of P1. On the other hand, P2 is characterised by year-round surface convergence and downwelling (Fig. 6). Anomalous surface circulation over P2 during the extreme years (Fig. 29) shows a fluctuation and extension of the South Equatorial Current and South Indian Ocean Current, thus altering the downwelling location. As the southeasterly wind weakens (strengthens) dramatically (Figs. 27g, h, and 28g, h), the tropical upwelling weakens (intensifies), and the subtropical downwelling intensifies (weakens) during dry (wet) SWWA years. JJA is characterised by an enhanced (reduced) southwestward flow over P1 with a strengthening (weakening) Leeuwin Current and anomalous southward (northward) flow over P2 during dry (wet) SWWA years. Since the meridional temperature gradient over much of the Indian Ocean is positive (i.e., waters in the north are warmer than in the south) the anomalous southward (northward) currents thus seem to have

a damping effect on the SST anomaly at P1 which contrasts to the effect of latent heat. On the other hand, anomalous meridional transport has an enhancing effect on the development of the SST anomaly at P2. This is examined further in the following sections.

d. Evolution of heat flux anomalies

The large heat capacity of the ocean and the presence of climate fluctuations over interannual timescales suggest that the generation of the SST anomalies may begin months or even a few years before peaking. Thus, in order to get a clearer picture of the effect of ocean and atmospheric heat fluxes on the evolution of the SST dipole on interannual timescales, we inspect the composite anomalies of the ocean surface advection and air-sea heat fluxes spatially averaged over P1 and P2 (see Fig. 30 for P1, P2 locations). The composite anomalies are shown for the two years leading up to the extreme year. To view the damping anomalous structures after peaking, the analysis is extended to the following year. Shorthand notations: $var{-}2$, $var{-}1$, $var{+}0$, $var{+}1$, where var is year or season (e.g., DJF, MAM), are used when referring to the years referenced to the SWWA rainfall extreme years (at year+0).

The seasonal surface heat flux composite anomalies at P1 and P2 during both dry and wet SWWA years are presented in Figs. 31 and 34, respectively. The heat flux variables adopted in the analysis include ocean advective heat fluxes: zonal ($u\theta_x$), meridional ($v\theta_y$), and vertical advection ($w\theta_z$) and the surface air-sea interface fluxes which includes net atmospheric heat flux (Q_{net}), latent heat flux (Q_{evp}), sensible heat flux (Q_{sh}), incoming short-wave radiation (Q_{solar}), and outgoing long-wave radiation (Q_{lw}). For reference when making deduction on the sign of the anomalies, the seasonal mean values for the ocean advection and net air-sea heat flux at P1

and P2 are shown in Fig. 32 and Fig. 35, respectively. For simplicity, we limit our discussion to the case of dry SWWA years since the wet year case is more or less the converse of the dry years. To comprehend the effect of anomalous heat fluxes on the evolution of temperature anomalies, we present composite anomalies of potential temperature (θ) from the surface down to about 550-m depth, spatially averaged over P1 (Fig. 33) and P2 (Fig. 36). The presentation of subsurface θ anomalies may provide an indication of vertical transport of heat anomalies.

The purpose of this analysis is to determine the heat fluxes which contribute to the development of negative SST anomalies at P1 towards peak condition in JJA+0 dry years. For P2, we seek heat fluxes whose temporal evolution support the development of positive SST anomalies. It is also of interest to identify the heat fluxes which contribute to the damping of anomalies following the peak anomalies in JJA.

d.1. Heat flux composite anomalies at P1

During the two years prior to SWWA dry years (i.e., year-2, year-1), variations in $u\theta_x$ and $v\theta_y$ are shown to have an adverse effect on the development of the negative SST anomalies at P1 (Fig. 31a, b). As the mean circulation for all seasons shows westward flows (see Fig. 6), the negative mean zonal advection implies positive zonal temperature gradient (i.e., warmer on the eastern side). This indicates an input of heat which is generally enhanced throughout this period preceding the dry years. The mean meridional advection is negative for all seasons (Fig. 32b) with mean southward velocities advecting warmer northern waters southward since $\theta_y > 0$. Thus, the negative anomaly of $v\theta_y$ also implies an increase of heat into P1 during dry years. On the other hand, anomalous $w\theta_z$ and Q_{net} generally tend to induce anomalous cooling (Fig. 31c, d). Since $\theta_z > 0$ (i.e., upper layer is warmer than lower layer; Fig. not shown), the positive mean vertical advection at P1 (Fig. 32c)

implies upwelling in each season. Thus, the positive anomalies in Fig. 31c suggest an enhanced advection of colder water from depth. While the effect of $w\theta_z$ on SST anomalies seems to be fairly small, it may have a more significant influence at the subsurface. It can also be noted that θ anomalies at depth lead θ anomalies at shallower depths (Fig. 33a). This is an indication of vertical transport of anomalies which may be sourced from variations in the rate of upwelling at P1 during seasons preceding the dry years.

The negatively enhanced Q_{net} implies reduced net heating in DJF and MAM, and an enhanced cooling in JJA and SON (refer to Figs. 31d, 32d), thus having a constructive effect toward the development of the negative SST anomalies at P1. Note that Q_{net} is the dominant term, as the magnitude of its anomalies is large compared to that of the oceanic heat fluxes (Fig. 31). Consequently, anomalous cooling occurs despite the prevailing warming effect of the meridional and zonal advective fluxes in some seasons during year−2 to year−1. Figure 33a shows progressive cooling from DJF−2 to SON−1 in the top 300 m, with an exception of a warming shift from MAM to JJA in year−2. This warming shift occurs as the Q_{net} anomaly is positive in MAM−2 and not significant in JJA−2 (Fig. 31d). The negative anomalies of Q_{net} during year−2 to year−1 are contributed mainly by a reduction in the Q_{solar} term, with contribution to a lesser extent from an increase in Q_{sh} and Q_{evp} (Fig. 31e−g). The rapid shift of SST anomaly towards the negative in SON−1 (Fig. 33a) is accompanied by an apparent increase in net heat loss to the atmosphere (Fig. 31d). This net heat loss is solely due to increased Q_{evp} (Fig. 31e). This accumulation of negative SST anomalies via air-sea heat fluxes and vertical advection during this period sets the favourable conditions for the generation of peak negative SST anomalies during the extreme dry years.

The shift of θ anomalies towards cooler values prevails to year+0 in the upper

150 m (Fig. 33b). Changes in evaporation and ocean surface circulation due to the reorganisation of the wind field force anomalous heat fluxes into P1 (see section 5c; Figs. 27, 28). During the dry SWWA years (year+0), negative SST anomalies are already seen at P1 in DJF (refer to Fig. 27a) despite the anomalous warming due to Q_{net} (Fig. 31d). These negative SST anomalies in DJF are a remnant from SON−1 when enhanced atmospheric heat loss cools the water at this time (Fig. 31d). Vertical advection is also increased in DJF which may aid further development of the negative anomalies in the coming seasons. Apparent increases in net heat loss from the ocean surface at P1 occur in MAM+0 and JJA+0 (Fig. 31d). This is largely due to the dramatic increase in evaporation rate during these seasons (Fig. 31e; see also Fig. 28) which is larger than the warming effect of the anomalous solar influx (Fig. 31g; i.e., implying a clear sky condition).

The reversal of anomalous zonal advection in JJA+0 and SON+0 introduces cooling at P1. The warming effect due to increased southward advection remains until JJA+0 which likely has a prolonged effect in the following seasons. Note that upwelling is reduced from MAM to SON, as well as the cooling effect of Q_{net} in SON. This is mainly due to the reduction in Q_{evp} as well as Q_{sh} which tends to shift the cool SST anomalies from JJA+0 to SON+0 towards the positive (Fig. 33b). The dispersion of the negative SST anomalies in year+1 is accompanied by net oceanic heat gain which is dominated by a reduction in Q_{evp} and Q_{sh} (Fig. 31e, f). However, the cooling effect of the anomalous zonal advection along with the reduced southward transport since SON+0 (Fig. 31a, b), tends to moderate the effect of anomalous Q_{net}, allowing gradual dispersion of the negative SST anomalies (Fig. 33b). Again, it can be noted in Fig. 33b that the subsurface warming leads the surface shift towards the positive. These processes set the warming condition toward the anomalously warm SST in the ensuing SWWA extreme wet years.

d.2. Heat flux composite anomalies at P2

Referring to Fig. 36b, the warm SST anomaly at P2 has only started to become visible in DJF+0. Prior to the dry years, the composite SST anomalies at P2 are still of negative sign (Fig. 36a). Anomalous air-sea heat fluxes impact upon SST to shift the anomalies towards the positive. Most apparently, the warming is caused by anomalous atmospheric net heat gain (Q_{net}) which starts to appear in MAM−1 and persists through JJA in year+0 (Fig. 34d). This progression is most notably seen in the anomalous Q_{evp} which dominates the other heat flux terms (Fig. 34). At some instances during this period, the atmospheric warming is also partly contributed by anomalous Q_{sh} and Q_{solar}.

The composite anomalies of zonal ocean advection (Fig. 34a) exhibit large spatial uncertainties over P2 and an erratic seasonal pattern. Thus, zonal advection does not play a significant role in the generation and build-up of SST anomalies at P2. On the other hand, meridional advection shows notable positive anomalies during JJA−1 to DJF+0, implying a reduced mean southward transport of heat into P2 (see Fig. 35b for mean values of $v\theta_y$ indicating input of heat in P2). Thus, like at P1, the role of $v\theta_y$ is to moderate the effect of reduced evaporation in generating the positive SST anomaly.

The seasonal shift in θ anomalies in Figure 36 indicates that surface anomalies lead the subsurface with a mean downwelling throughout the year (Fig. 35c). This suggests that anomalies are created at the surface and get advected/mixed downward. In SON−1 to JJA+0, there is an increased downwelling in response to weakened wind strength which at the same time causes a reduction in the evaporation rate (see section 5c; Fig. 28). This transports positive θ anomalies to depth. In year+1, the downwelling is reduced with increased atmospheric cooling. As in P1, the anomalous shift in Q_{net} occurs from SON+0 onwards, which acts to cool

the waters at P2 inducing the dispersal of the positive SST anomalies, and thereby preconditioning the waters towards the SWWA extreme wet year scenario.

6. Summary

The Indian Ocean variability on interannual time scales and its link to regional rainfall have been analysed using 1000-yr of output data from the CSIRO coupled climate model as well as recent observational data sets. Modes of Indian Ocean SST variability in the model and observations have been re-assessed with a particular interest on the link between Indian Ocean variability and the rainfall variability in the southwest Western Australian region (SWWA). A knowledge of existing dominant SST modes aids in the detection and definition of anomalous SST patterns that emerge during SWWA rainfall extremes.

An overview of the annual-mean and seasonal state of the Indian Ocean climate was provided. Comparisons between the model and the observed mean climate were made to assess the model's performance in the region. Given the coarse resolution, the model simulates the Indian Ocean climate with excellent agreement with the observations, although some discrepancies remain presumably due to unresolved fine-scale physical processes in the model. It should be mentioned here that the variability analyses reveal the model under represents ENSO and IOD. Though this may be due to the use of flux adjustment in the model to achieve stable climates, the model's coarse resolution and other various factors, such as cloud physics parameterisations, are also likely to play a role.

Modes of annual-mean SST variability were identified using an EOF analysis over the entire Indian Ocean basin north of 50°S. A basinwide SST anomaly of uniform polarity over the tropical Indian Ocean and an anomaly of the opposite sign in the southwest Indian Ocean (Mode-1) emerges as the leading mode in both the model

and observations. Some differences in the spatial and temporal characteristics exist between the model and the observed Mode-1. The observed Mode-1 explains more variability in the western tropical region than in the model. The spectral structure of the model and the observed Mode-1 exhibits a peak at 7-yr and 4-yr periods, respectively. Furthermore, the model Mode-1 was seen to occur during austral summer to winter, while the observed is only dominant from summer to autumn. Since this mode is shown to be linked to ENSO (Table 3), there is an implication that these differences are partly due to the weak equatorial Pacific Ocean SST anomalies and the longer periodicity of ENSO in the model as compared to the observed (Hunt and Elliott 2003).

Similarities are shared between the model Mode-3 and the observed Mode-2. Both exhibit a tripole pattern with the first pole occurring in the northwestern region off Australia and extending northwest to the region off Sumatra, the second pole of opposite sign lies to the southwest of the first pole, and a weaker subtropical pole is found in the southwestern Indian Ocean. The model Mode-3 and observed Mode-2 exhibit spectral peaks at 3 and 8-yr periods and are dominant in the austral winter to spring. The model Mode-3 and observed Mode-2 thus appear to be linked. They were shown to be associated with similar atmosphere-oceanic processes as demonstrated by the composite analyses presented in section 4b. It may be noted that these modes also exhibit a tropical dipole pattern. The model tropical dipole, however, appears different from the IOD described in Saji et al. (1999) which is otherwise captured by the observed Mode-2. The IOD-like signal in the model appears in spring and is less dominant than the observed IOD which emanates in the annual-mean spatial pattern. The model Mode-2 on the other hand exhibits a tropical dipole pattern distinct from an IOD signal and does not exhibit a tripole pattern such as that of Mode-3. This mode explains a similar portion of SST variance

as Mode-3 but it is prevalent during austral summer to autumn. Furthermore, since the model Mode-2 pattern is not seen in the observations, this mode is possibly an artificial feature of the model.

An EOF analysis applied over the tropical and subtropical regions separately showed that the anomalous SST pool in the southwestern Indian Ocean (exhibited in all of the EOFs) is a manifestation of the subtropical dipole as observed by Reason (1999) and Behera and Yamagata (2001). This subtropical dipole mode is thus shown to co-evolve with the mode exhibiting basin-wide uniform polarity and the tropical dipole modes. It is also shown that there is a Southern Ocean influence in the Indian Ocean variability but confined to the subtropical region contributing to the subtropical dipole mode, likely via variability in the meridional ocean Ekman transport. Regional rainfall variability patterns were shown to be linked to these large-scale modes.

During extreme rainfall events in the SWWA, an anomalous SST pole appears in the tropical eastern Indian Ocean off Northwest Australia (P1) extending northward into the western Pacific region. A pole of opposite sign (P2) occurs to the south of P1 extending northeast towards Central Africa (Figs. 24c, d, and 25c, d). The similarity of this meridional dipole pattern in the model and observed is remarkable. Differences, however, remain in the stronger magnitude of the observed anomalies and the emergence of a third pole in the southwestern Indian Ocean in the observations. These differences may result from a combination of the model's coarse resolution, the model's flux adjustment terms, and the size of sample used in the analysis (i.e., the fact that we use 1000-yr of model data versus a 34-yr observational record). The dipole pattern that emerges during extreme SWWA rainfall events was shown to be associated to the EOF-defined observed Mode-2 and the model Mode-3. This suggests that the SWWA rainfall extremes and their related climate anomalies

are linked to a well-defined large-scale mode of Indian Ocean variability.

The evolution of the SST dipole anomaly during the SWWA extreme rainfall events is induced by large-scale anomalous atmospheric circulation driving variability in atmosphere-ocean heat fluxes. During dry (wet) SWWA years, a cold (warm) SST pool (P1) starts to develop off Northwestern Australia in the austral summer with an acceleration (deceleration) of the southeasterly wind over P1, driving stronger (weaker) southward Ekman transport and higher (lower) evaporation rates. By austral autumn, an anomalous anticyclonic (cyclonic) wind gyre system develops over P2 with a strengthening (weakening) of the subpolar westerlies due to the positive (negative) meridional SLP gradients, forcing anomalously southward (northward) oceanic flow with an emergence of a warm (cold) anomaly. These anomalous atmosphere-ocean conditions peak in austral winter and abate during spring.

Finally, we analyse the evolution of surface heat flux anomalies at P1 and P2, two years prior and a year following the peak dipole in winter during years of extreme SWWA rainfall. We conclude that the SST dipole is created chiefly by anomalous wind-driven evaporation and partly by anomalous upwelling/downwelling. Interestingly, the resulting anomalous ocean Ekman transport plays a role in moderating the effect of atmospheric heat fluxes. Together with the reorganisation of the wind system after a peak dipole, the ocean Ekman transport preconditions the waters favourable for the next generation phase of an opposing dipole. There is also evidence of a contribution from variations in the incoming solar radiation involving a cloud feedback mechanism. For instance, the development of a Northwest cloud band during a wet SWWA year tends to reduce the amount of incoming solar radiation which contributes to a cold SST anomaly toward dry conditions over SWWA.

The SST dipole is shown to be driven by wind anomalies which at the same time can influence the SWWA rainfall variability via divergence/convergence of moisture

over the region (England et al. 2006). As noted in Smith et al. (2000), it is not clear, however, what causes the atmospheric variations in the first place. This is left as an open question for future investigations. Nevertheless, the analysis presented in this study implies a potential for using the dipole pattern in the prediction of SWWA rainfall extremes. For example, if we can detect both a continuing development of negative SST anomalies at P1 and a sudden warming at P2 between spring and the following summer, and if this trend is maintained through autumn, then there is a possibility of a maturing dipole which is linked to a low winter rainfall in SWWA. The ocean in this case acts like a recording device which monitors the development of anomalous atmospheric condition towards a full blown anticyclonic/cyclonic anomalies over the SWWA region.

Table captions

Table 1: Correlation coefficients between the principal components of the model Mode-1, Mode-2, and Mode-3 (see text for definition of the modes) against the principal components of the first EOF SST mode calculated over the tropical Indian Ocean north of 20°S (EOF1-N20), the subtropical region south of 20°S (EOF1-S20), and the second EOF SST mode for the tropical region (EOF2-N20). The correlation values for the NOAA extended reconstructed SST (referred to as the 'observed') are shown in the right hand side portion. The correlation coefficients for the model case are calculated using year 400−600 of the time series. Correlation coefficients significant at 99% significance level are highlighted.

Table 2: The same as Table 1 but for the principal components of the first and second EOF SST modes calculated for each season versus the model Mode-1, -2, -3 and the observed Mode-1, -2. Correlation coefficients significant at 99% significance level are highlighted.

Table 3: The same as Table 1 but for the principal component of the first EOF SST mode in the Pacific region representing ENSO (EOF1-Pacific; see text and Figs. 16a, 17a for definition) against the model Mode-1, -2, -3, and the observed Mode-1, -2. Correlation coefficients significant at 99% significance level for the model and 90% for the observed are highlighted. The 1-yr time lag implies ENSO leading the modes by 1 year.

Table 4: The same as Table 1 but for the first EOF SST modes over the subtropical region (south of 20°S; EOF1-S20) representing subtropical dipole mode versus the SST modes in the Southern Ocean region (see Figs. 18-21, upper panel). Correlation coefficients significant at the 99% significance level for the model

and 95% for the observed are highlighted.

Figure captions

Figure 1: Australian annual mean rainfall (mm yr^{-1}) from the Australian Bureau of Meteorology (BoM) gridded rainfall climatology, with the study region in southwest Western Australia indicated (115−120°E, 30−35°S).

Figure 2: Monthly mean rainfall spatially averaged over southwest Western Australia (in mm $month^{-1}$) in the model and observed. The observed rainfall is derived from BoM gridded rainfall climatology during 1970−2003. The model seasonal cycle is derived from the 1000-yr integration of the CSIRO Mk2 climate model.

Figure 3: Annual mean of sea surface temperature in (a) the model (b) NOAA extended reconstructed SST, (c) the model wind stress, (d) NCEP/NCAR reanalysis wind velocity, (e) model rainfall and (f) CMAP rainfall climatology. The mean values are obtained by averaging annual mean values over the 1000-yr model integration and over the period 1970−2003 in the observed (except for the rainfall climatology which spans 1979−2003).

Figure 4: NCEP/NCAR reanalysis wind velocity (arrow vectors) and SLP (colour shading) mean values for (a) December−February, (b) March−May, (c) June−August, and (d) September−November. The seasonal mean is obtained by averaging over the period 1970−2003.

Figure 5: As in Fig. 4 but for the model wind stress (vectors) and rainfall (b/w shading).

Figure 6: As in Fig. 4, but for the model ocean surface horizontal velocity (vectors) and vertical velocity (colour shading).

Figure 7: Empirical orthogonal function (EOF) analysis of the 1000-yr integra-

tion annual-mean SST in the model presenting the spatial maps of the first three leading EOF modes in dimensionless unit (top panel), the principal component timeseries of each corresponding EOF mode (middle panel) with a true anomaly magnitude, and the corresponding power spectral density of the principal components (bottom panel). The dashed line in the bottom panels indicates the estimated white noise spectrum at 95% confidence level. The gray shading in the top panels indicates land regions and the Pacific sector excluded in the EOF calculation.

Figure 8: As in Fig. 7, but for the NOAA extended reconstructed SST.

Figure 9: Standard deviation of the annually averaged SST in the (a) model (b) NOAA extended reconstructed SST.

Figure 10: EOF analysis of model SST for each season showing spatial maps of the first EOF mode for each season (top panel), and the corresponding second EOF mode (bottom panel). The colour scale indicates true anomaly magnitude inferred by each EOF.

Figure 11: As in Fig. 10 but for the NOAA extended reconstructed SST.

Figure 12: Composite analysis based on the *observed* Mode-1 (see text for definition) showing (a-b) SST anomalies, (c-d) SLP (colour shading) and wind velocity anomalies (vectors), and (e-f) rainfall anomalies. Left (right) panel shows the composites based on the positive (negative) values of the Mode-1 characteristic timeseries. The observed parameters refer to NOAA extended reconstructed SST, NCEP/NCAR wind velocity and SLP, and the CMAP rainfall climatology.

Figure 13: As in Fig. 12 but for composite analysis based on the *model* Mode-1

(see text for definition) showing (a-b) SST and wind stress anomalies, (c-d) ocean surface current velocity anomalies, and (e-f) rainfall anomalies.

Figure 14: As in Fig. 12 but for the *observed* Mode-2 (see text for definition).

Figure 15: As in Fig. 13 but for the *model* Mode-3 (see text for definition).

Figure 16: (a) Spatial map of the first EOF SST mode over the region marked by the box, showing a mature phase of El Niño. (b-c) SST composite anomalies calculated based on the positive (b) and negative (c) values of the principal component of the first EOF mode (shown in a). (d-e) as in (b-c) but calculated with the EOF1 principal component leading by 1 year.

Figure 17: As in Fig. 16 but for the NOAA extended reconstructed SST.

Figure 18: (a-c) the first three leading EOF SST modes in the model over the Southern Ocean region bounded by the dashed lines. (d-f) composite anomalies corresponding to the principal components of the EOF modes shown in (a-c).

Figure 19: As in Fig. 18 but for the fourth, fifth, and sixth leading EOF modes.

Figure 20: As in Fig. 18 but for the NOAA extended reconstructed SST.

Figure 21: As in Fig. 19 but for the NOAA extended reconstructed SST.

Figure 22: (a) Time series of annual rainfall anomaly (mm yr^{-1}) in SWWA over the 1000-yr climate model simulation. The dashed lines indicate one standard deviation (44 mm yr^{-1}) above and below the 1000-yr mean, which is used to define anomalously dry and wet years. The model SWWA rainfall is defined as the average over the area indicated by the box at 115−120°E, 30−35°S (see Fig. 24a, b for the location). (b) Power spectral density (PSD) of the

model SWWA rainfall. The dashed line represents the estimated white noise spectrum at 95% confidence level.

Figure 23: (a) Detrended time series of the observed annual rainfall anomaly (mm yr^{-1}) for SWWA for 1970−2003. The dashed lines indicate one standard deviation (66 mm yr^{-1}) above and below the 34-yr mean with years of rainfall extremes above and below these lines are marked with filled circles. (b) Power spectral density (PSD) of observed SWWA rainfall. The dashed horizontal line represents the estimated white noise spectrum at 90% confidence level.

Figure 24: Composite maps of (a-b) rainfall anomaly, (c-d) SST (colour shading) and wind stress anomalies (vectors), and (e-f) ocean surface current anomalies during dry (a, c, e) and wet (b, d, f) years in the climate model. Anomalies are shown where they exceed a 90% significance level as estimated by a two-tailed t-test. Anomalous wind stress and surface current velocities below the significance level are displayed as grey vectors in (c-f). Wind anomaly vectors of magnitude less than 0.5×10^{-3} N m^{-2} are not shown. The highlighted box in (a-b) marks the SWWA location used to define years of anomalous model rainfall.

Figure 25: Composite maps of (a-b) rainfall anomaly, (c-d) SST anomaly, (e-f) SLP (colour shading) and wind velocity (vectors) anomalies in the observational and reanalysis data for the dry (a, c, e) and wet (b, d, f) years. The highlighted box in (a-b) marks the SWWA location used to define years of anomalous rainfall.

Figure 26: Time series of the observed rainfall anomaly overlaid on the principal component time series of the *observed* Mode-2 (see text for definition). Horizontal lines indicate one standard deviation of the observed rainfall anomaly

above/below the long term mean.

Figure 27: Seasonal evolution of SST and wind stress anomalies presented as composite maps based on extreme years of SWWA annual rainfall in the coupled climate model. Anomalies are shown where they exceed a 90% significance level as estimated by a two-tailed t-test. Anomalous wind stress below the significance level is displayed as grey vectors. Wind anomaly vectors of magnitude less than 0.5×10^{-3} N m^{-2} are not shown.

Figure 28: Seasonal evolution of latent heat flux (colour shading) and wind strength (contour) anomalies presented as composite maps based on extreme years of SWWA annual rainfall in the model.

Figure 29: As in Fig. 28 but for ocean surface velocities. Horizontal velocities are presented as vectors. Vertical velocities are presented in colour shading.

Figure 30: Location of P1 and P2 shown in grey shading, corresponding to the SST dipole shown in the model composite maps in Fig. 24c, d.

Figure 31: Seasonal evolution of composite anomalies of model atmosphere-oceanic heat fluxes spatially averaged over P1 (see Fig. 30 for the location) from two years prior to one year following the SWWA rainfall extreme years (indicated by the dark vertical lines at year+0). The oceanic heat flux variables are (a) zonal advection ($u\theta_x$), (b) meridional advection ($v\theta_y$), and (c) vertical advection ($w\theta_z$). The atmospheric heat fluxes at the air-sea interface include (d) net downward heat flux (Q_{net}), (e) upward latent heat (Q_{evp}), (f) upward sensible heat (Q_{sh}), (g) downward solar radiation (Q_{solar}), and (h) outgoing long-wave radiation (Q_{lw}). Composite anomalies corresponding to dry and wet years are displayed in red and blue, respectively. The red and blue horizontal lines corresponding to the dry and wet year composites mark

the upper and lower cut-off values of the 95% significance level as determined by a two-tailed t-test indicating sampling spread of the composite estimates due to spatial averaging over P1.

Figure 32: Seasonal mean of (a) zonal advection ($u\theta_x$), (b) meridional advection ($v\theta_y$), (c) vertical advection ($w\theta_z$), and (d) net air-sea heat flux Q_{net} spatially averaged over P1 (see Fig. 30 for location). The sampling spread at 95% significance level is indicated by the upper and lower horizontal lines.

Figure 33: Depth profile of potential temperature (θ) anomalies from the surface to $\approx$ 550-m depth showing seasonal evolution during (a) two years preceeding SWWA dry years (referred to as year-2, year-1 in text). Solid line indicates θ anomalies during year-2, dashed lines indicate anomalies during year-1. (b) Depth profile of θ anomalies during SWWA dry years (year+0; solid lines) and one year following the extreme year (year+1; dashed lines). The colour indicates the seasons. The arrows illustrate the temporal shift of the anomalies.

Figure 34: As Fig. 31 but for P2.

Figure 35: As Fig. 32 but for P2.

Figure 36: As Fig. 33 but for P2.

Table 1. Correlation coefficients between the principal components of the model Mode-1, Mode-2, and Mode-3 (see text for definition of the modes) against the principal components of the first EOF SST mode calculated over the tropical Indian Ocean north of 20°S (EOF1-N20), the subtropical region south of 20°S (EOF1-S20), and the second EOF SST mode for the tropical region (EOF2-N20). The correlation values for the NOAA extended reconstructed SST (referred to as the 'observed') are shown in the right hand side portion. The correlation coefficients for the model case are calculated using year 400−600 of the time series. Correlation coefficients significant at 99% significance level are highlighted.

	Model (99%)			Observed (99%)	
	Mode-1	Mode-2	Mode-3	Mode-1	Mode-2
EOF1-N20	**0.92**	0.22	0.22	**0.95**	0.13
EOF1-S20	**0.56**	**0.60**	**0.60**	**0.64**	**0.58**
EOF2-N20	0.12	**0.56**	**0.61**	0.01	**0.58**

Table 2. The same as Table 1 but for the principal components of the first and second EOF SST modes calculated for each season versus the model Mode-1, -2, -3 and the observed Mode-1, -2. Correlation coefficients significant at 99% significance level are highlighted.

	Model (99%)			Observed (99%)	
	Mode-1	Mode-2	Mode-3	Mode-1	Mode-2
EOF1-DJF	**0.70**	0.02	0.01	**0.83**	0.05
EOF1-MAM	**0.88**	0.23	0.10	**0.84**	0.03
EOF1-JJA	**0.84**	0.06	**0.29**	0.46	**0.75**
EOF1-SON	**0.52**	**0.24**	**0.26**	0.15	**0.45**
EOF2-DJF	0.03	**0.73**	**0.27**	0.06	**0.53**
EOF2-MAM	0.11	**0.83**	**0.30**	0.39	0.10
EOF2-JJA	**0.34**	**0.35**	**0.51**	**0.69**	0.38
EOF2-SON	**0.35**	0.15	**0.65**	**0.70**	0.09

Table 3. The same as Table 1 but for the principal component of the first EOF SST mode in the Pacific region representing ENSO (EOF1-Pacific; see text and Figs. 16a, 17a for definition) against the model Mode-1, -2, -3, and the observed Mode-1, -2. Correlation coefficients significant at 99% significance level for the model and 90% for the observed are highlighted. The 1-yr time lag implies ENSO leading the modes by 1 year.

	Model (99%)						Observed (90%)			
	Mode-1		Mode-2		Mode-3		Mode-1		Mode-2	
	0-yr	1-yr	0-yr	1-yr	0-yr	1-yr	0-yr	1-yr	0-yr	1-yr
EOF1-Pacific	0.12	**0.32**	0.27	0.08	0.12	0.10	0.29	**0.40**	**0.44**	0.05

Table 4. The same as Table 1 but for the first EOF SST modes over the subtropical region (south of 20°S; EOF1-S20) representing subtropical dipole mode versus the SST modes in the Southern Ocean region (see Figs. 18-21, upper panel). Correlation coefficients significant at the 99% significance level for the model and 95% for the observed are highlighted.

	EOF1 -SO	EOF2 -SO	EOF3 -SO	EOF4 -SO	EOF5 -SO	EOF6 -SO
EOF1-S20 (Model, 99%)	**0.33**	**0.32**	**0.44**	0.05	**0.50**	0.07
EOF1-S20 (Observed, 95%)	**0.37**	0.03	0.27	**0.56**	0.17	**0.38**

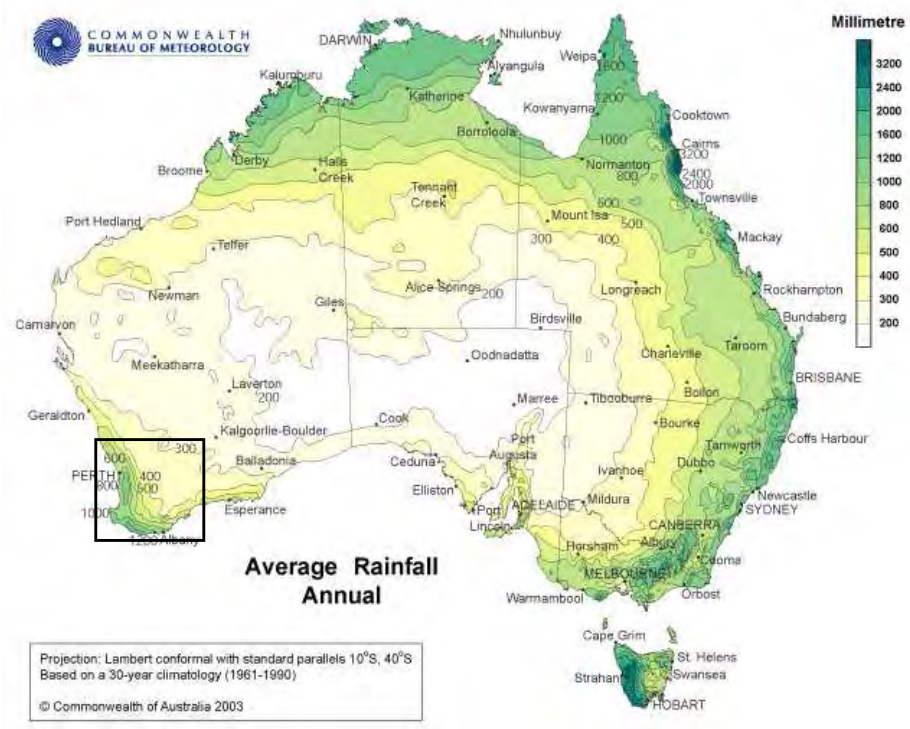

Figure 1: Australian annual mean rainfall (mm yr^{-1}) from the Australian Bureau of Meteorology (BoM) gridded rainfall climatology, with the study region in southwest Western Australia indicated (115−120°E, 30−35°S).

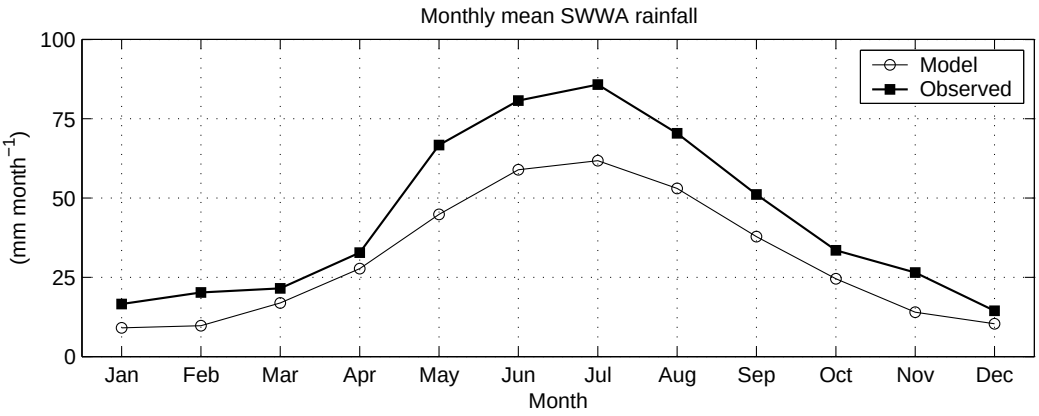

Figure 2: Monthly mean rainfall spatially averaged over southwest Western Australia (in mm $month^{-1}$) in the model and observed. The observed rainfall is derived from BoM gridded rainfall climatology during 1970−2003. The model seasonal cycle is derived from the 1000-yr integration of the CSIRO Mk2 climate model.

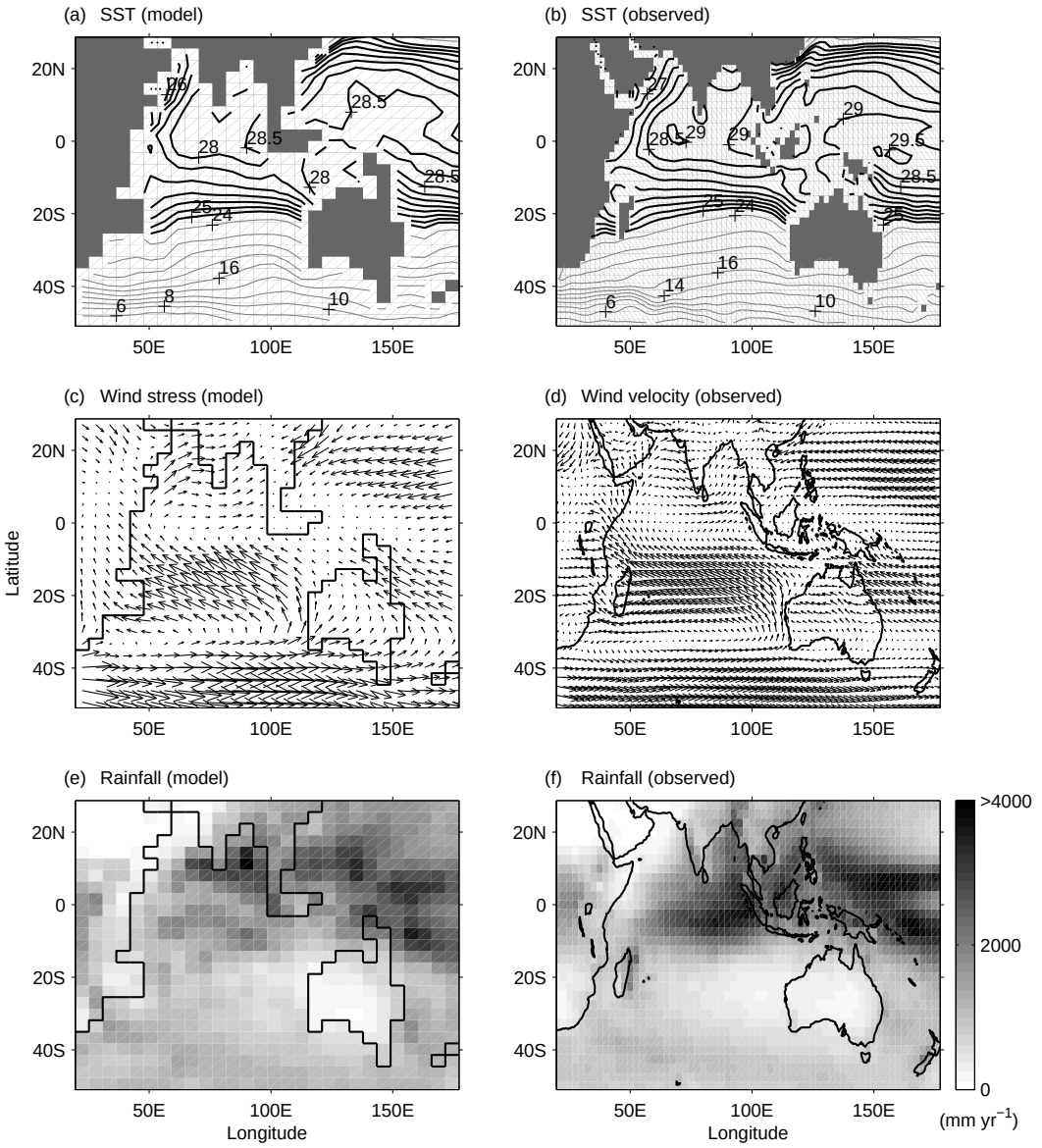

Figure 3: Annual mean of sea surface temperature in (a) the model (b) NOAA extended reconstructed SST, (c) the model wind stress, (d) NCEP/NCAR reanalysis wind velocity, (e) model rainfall and (f) CMAP rainfall climatology. The mean values are obtained by averaging annual mean values over the 1000-yr model integration and over the period 1970−2003 in the observed (except for the rainfall climatology which spans 1979−2003).

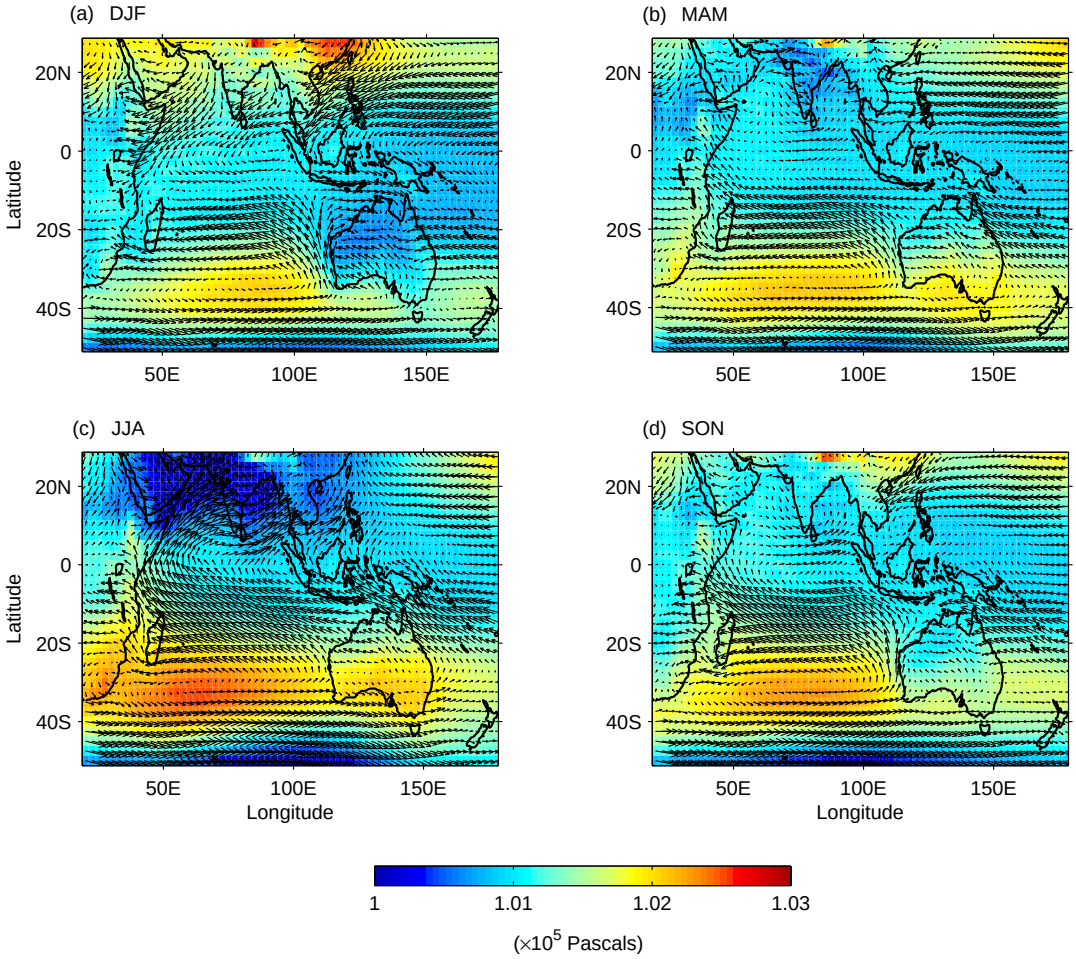

Figure 4: NCEP/NCAR reanalysis wind velocity (arrow vectors) and SLP (colour shading) mean values for (a) December−February, (b) March−May, (c) June−August, and (d) September−November. The seasonal mean is obtained by averaging over the period 1970−2003.

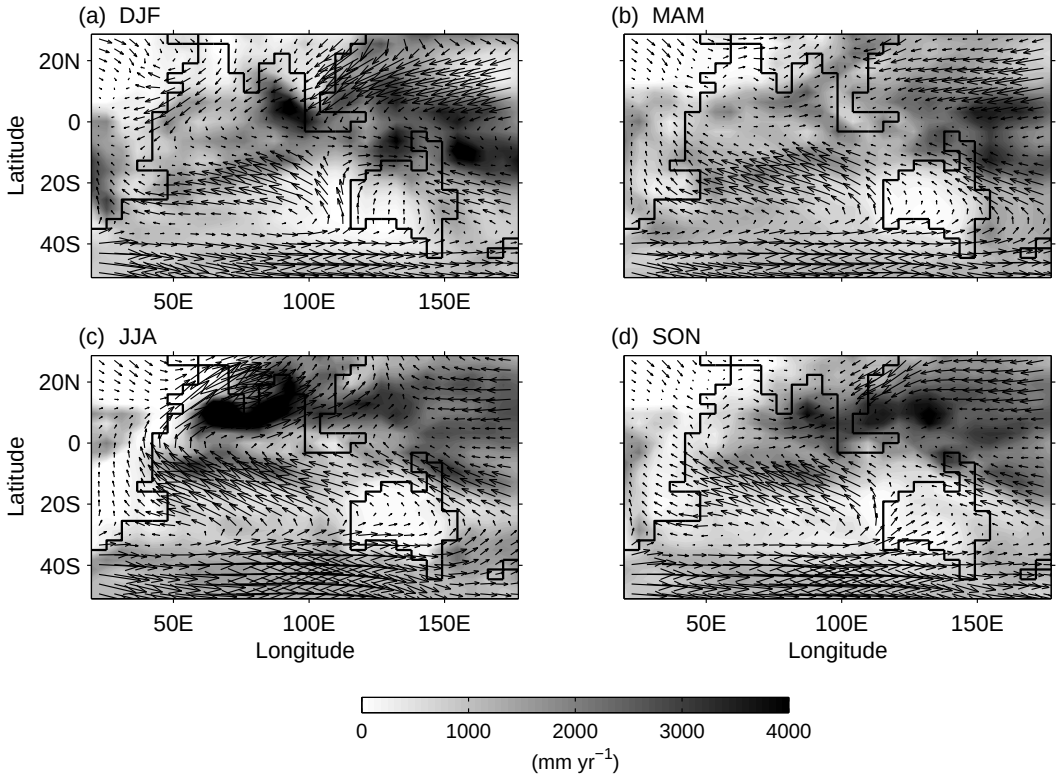

Figure 5: As in Fig. 4 but for the model wind stress (vectors) and rainfall (b/w shading).

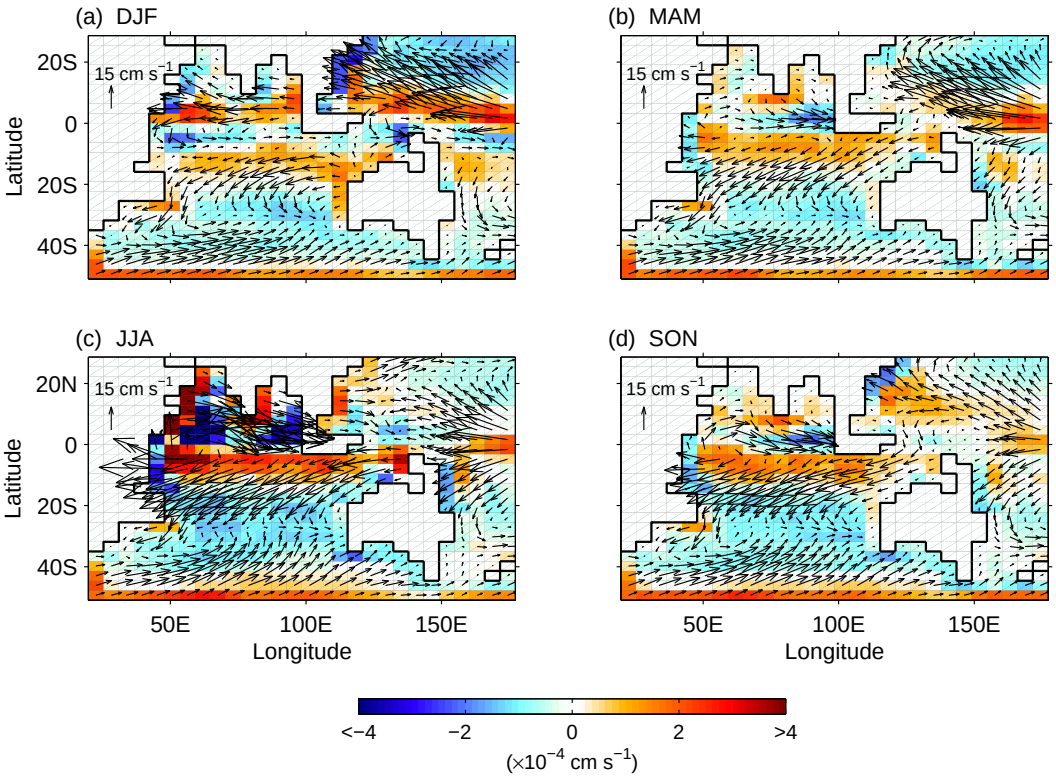

Figure 6: As in Fig. 4, but for the model ocean surface horizontal velocity (vectors) and vertical velocity (colour shading).

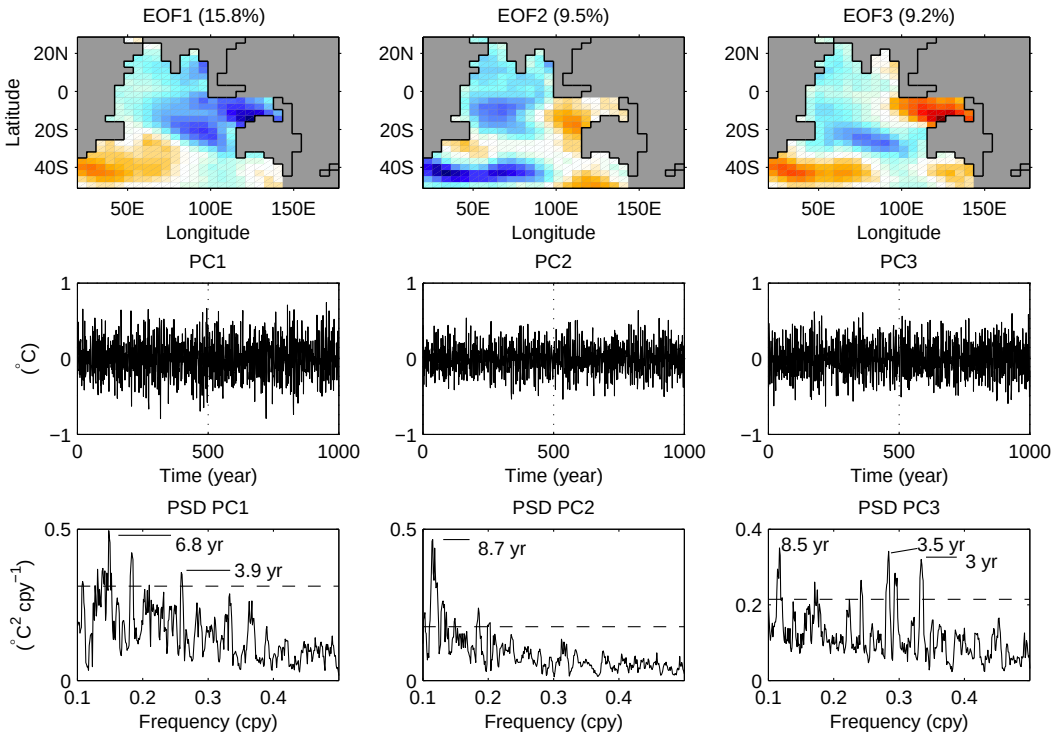

Figure 7: Empirical orthogonal function (EOF) analysis of the 1000-yr integration annual-mean SST in the model presenting the spatial maps of the first three leading EOF modes in dimensionless unit (top panel), the principal component timeseries of each corresponding EOF mode (middle panel) with a true anomaly magnitude, and the corresponding power spectral density of the principal components (bottom panel). The dashed line in the bottom panels indicates the estimated white noise spectrum at 95% confidence level. The gray shading in the top panels indicates land regions and the Pacific sector excluded in the EOF calculation.

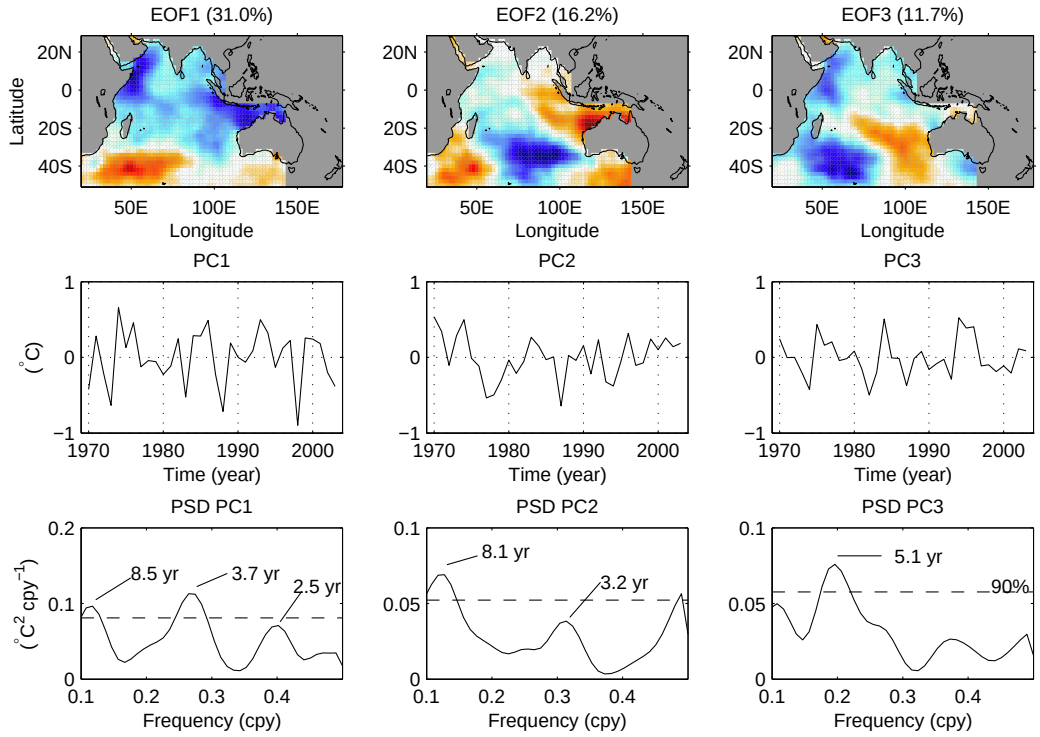

Figure 8: As in Fig. 7, but for the NOAA extended reconstructed SST.

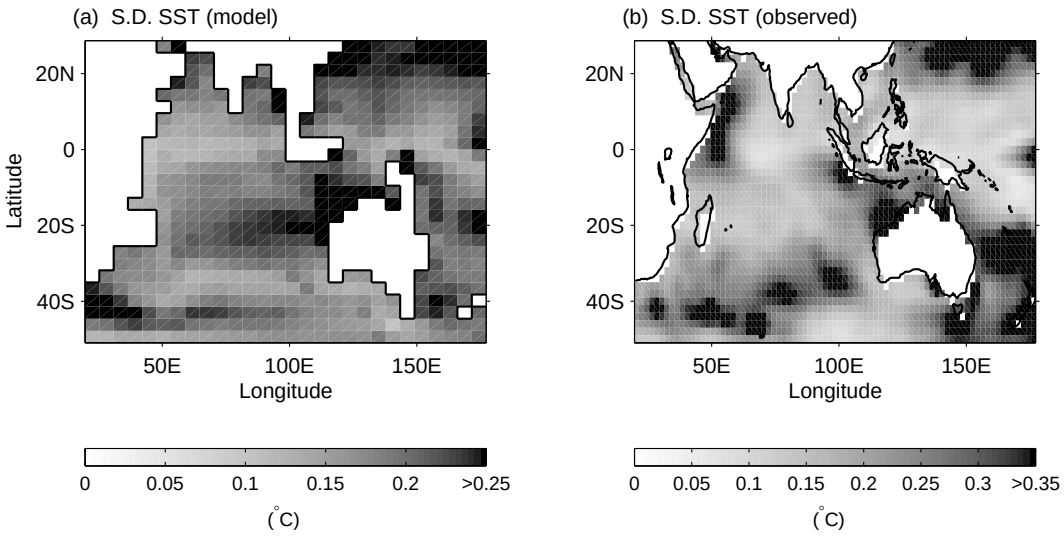

Figure 9: Standard deviation of the annually averaged SST in the (a) model (b) NOAA extended reconstructed SST.

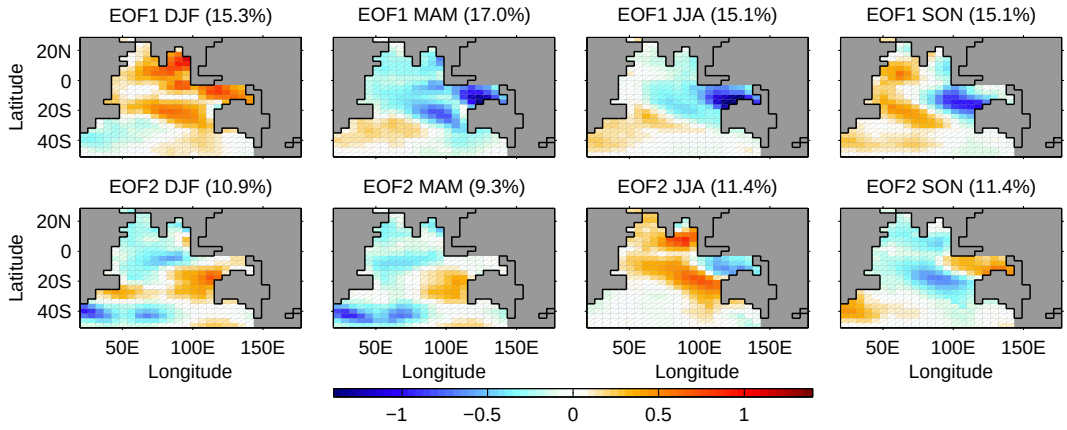

Figure 10: EOF analysis of model SST for each season showing spatial maps of the first EOF mode for each season (top panel), and the corresponding second EOF mode (bottom panel). The colour scale indicates true anomaly magnitude inferred by each EOF.

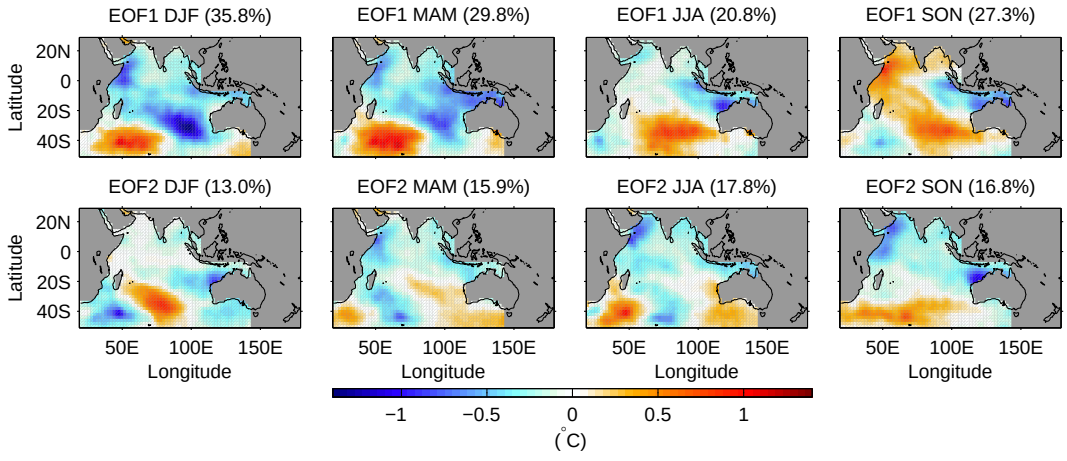

Figure 11: As in Fig. 10 but for the NOAA extended reconstructed SST.

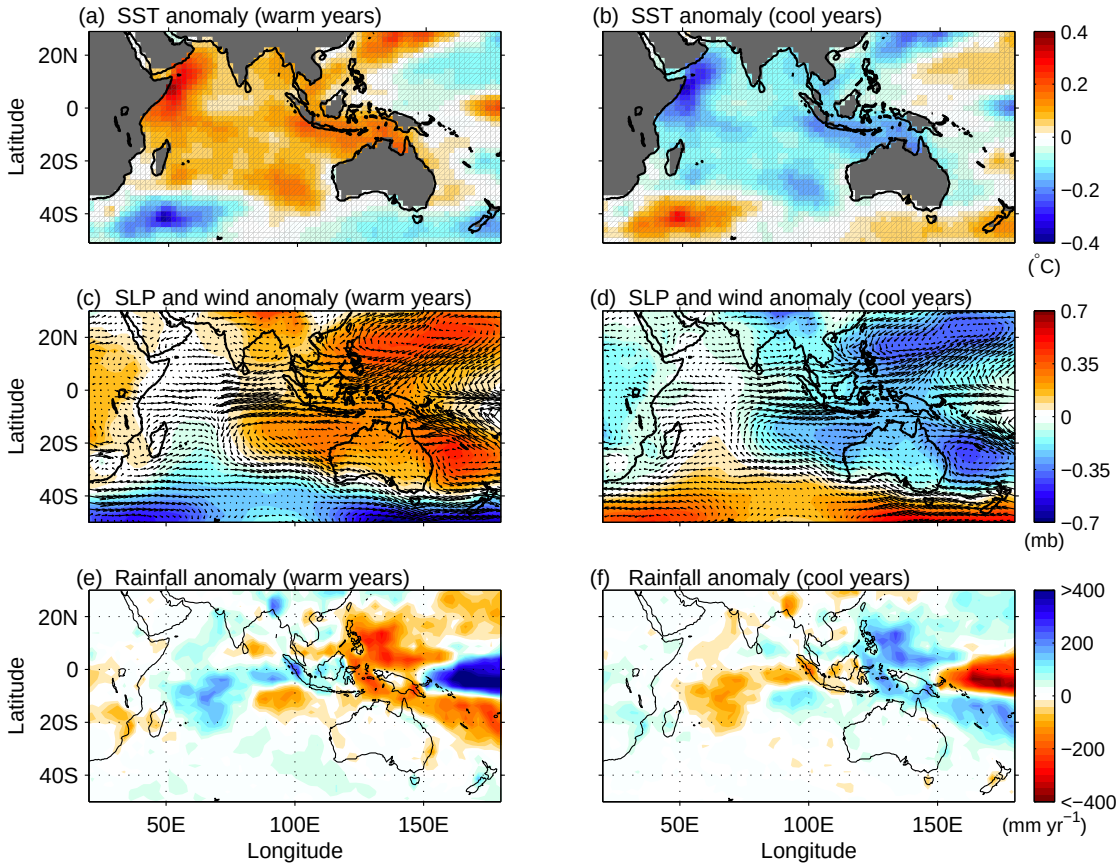

Figure 12: Composite analysis based on the *observed* Mode-1 (see text for definition) showing (a-b) SST anomalies, (c-d) SLP (colour shading) and wind velocity anomalies (vectors), and (e-f) rainfall anomalies. Left (right) panel shows the composites based on the positive (negative) values of the Mode-1 characteristic timeseries. The observed parameters refer to NOAA extended reconstructed SST, NCEP/NCAR wind velocity and SLP, and the CMAP rainfall climatology.

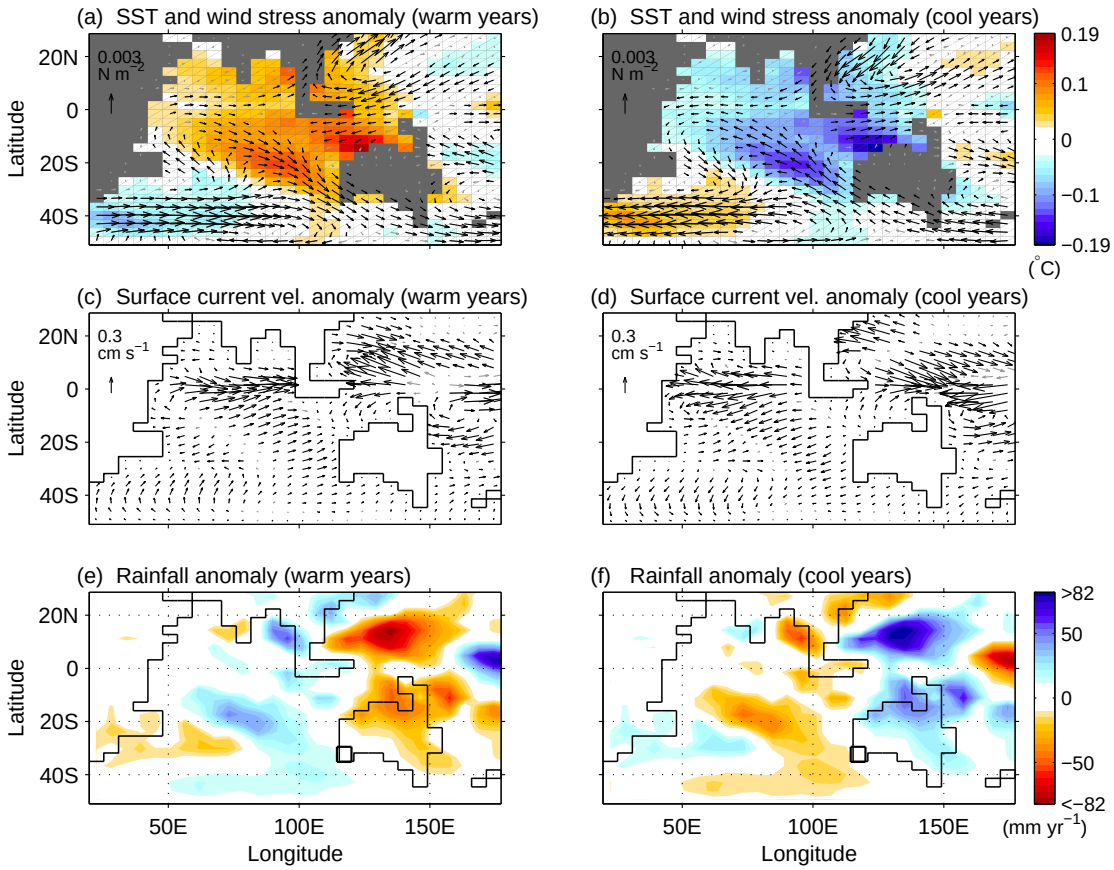

Figure 13: As in Fig. 12 but for composite analysis based on the *model* Mode-1 (see text for definition) showing (a-b) SST and wind stress anomalies, (c-d) ocean surface current velocity anomalies, and (e-f) rainfall anomalies.

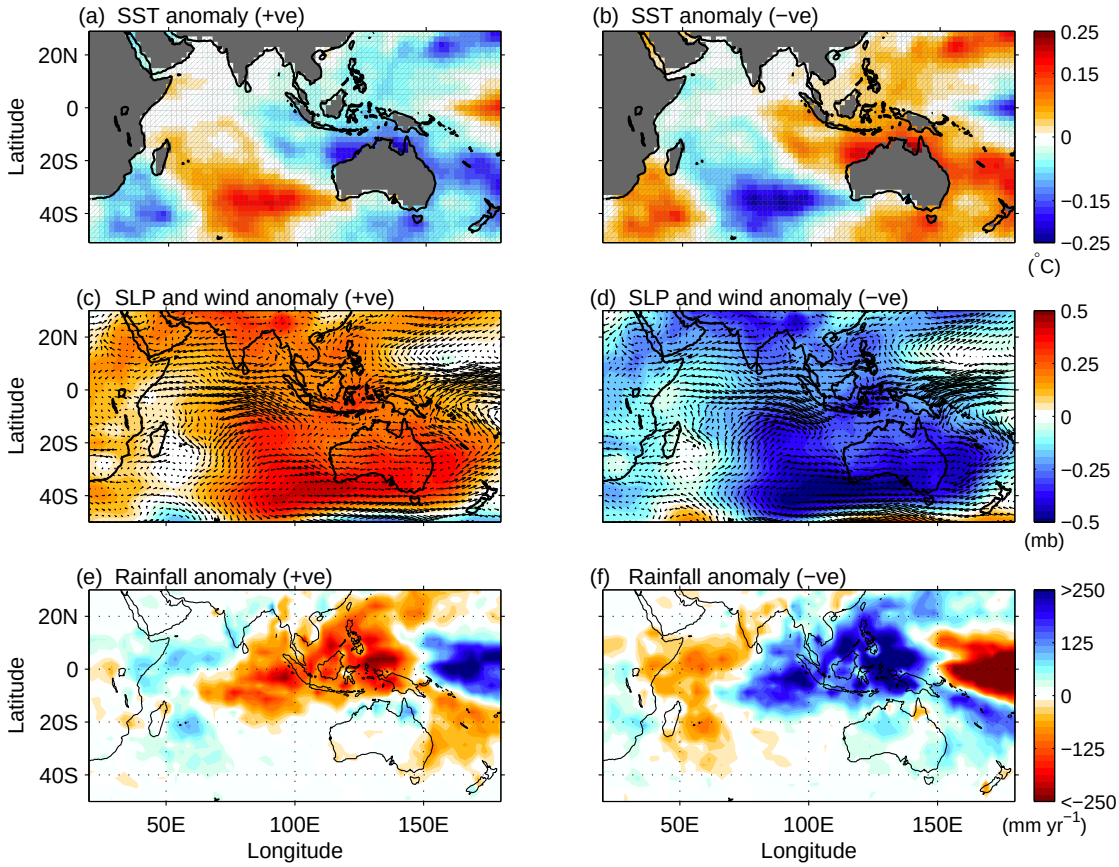

Figure 14: As in Fig. 12 but for the *observed* Mode-2 (see text for definition).

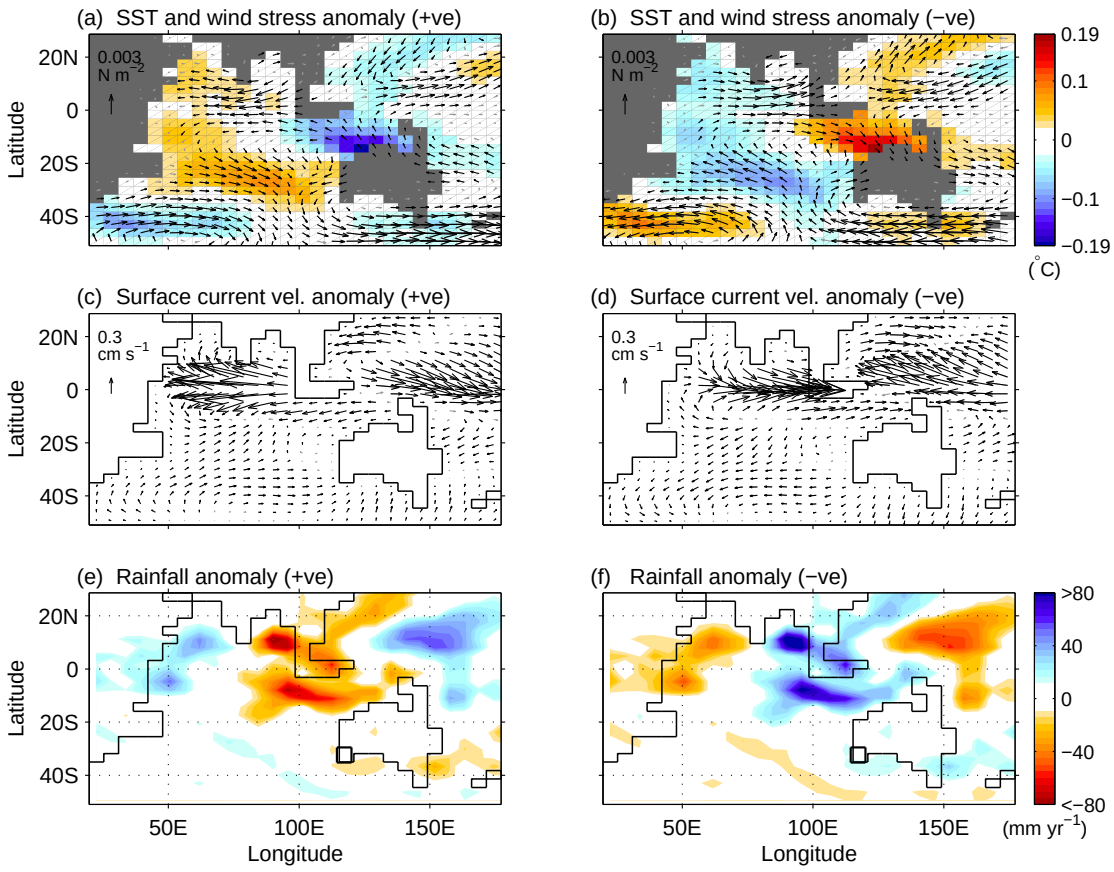

Figure 15: As in Fig. 13 but for the *model* Mode-3 (see text for definition).

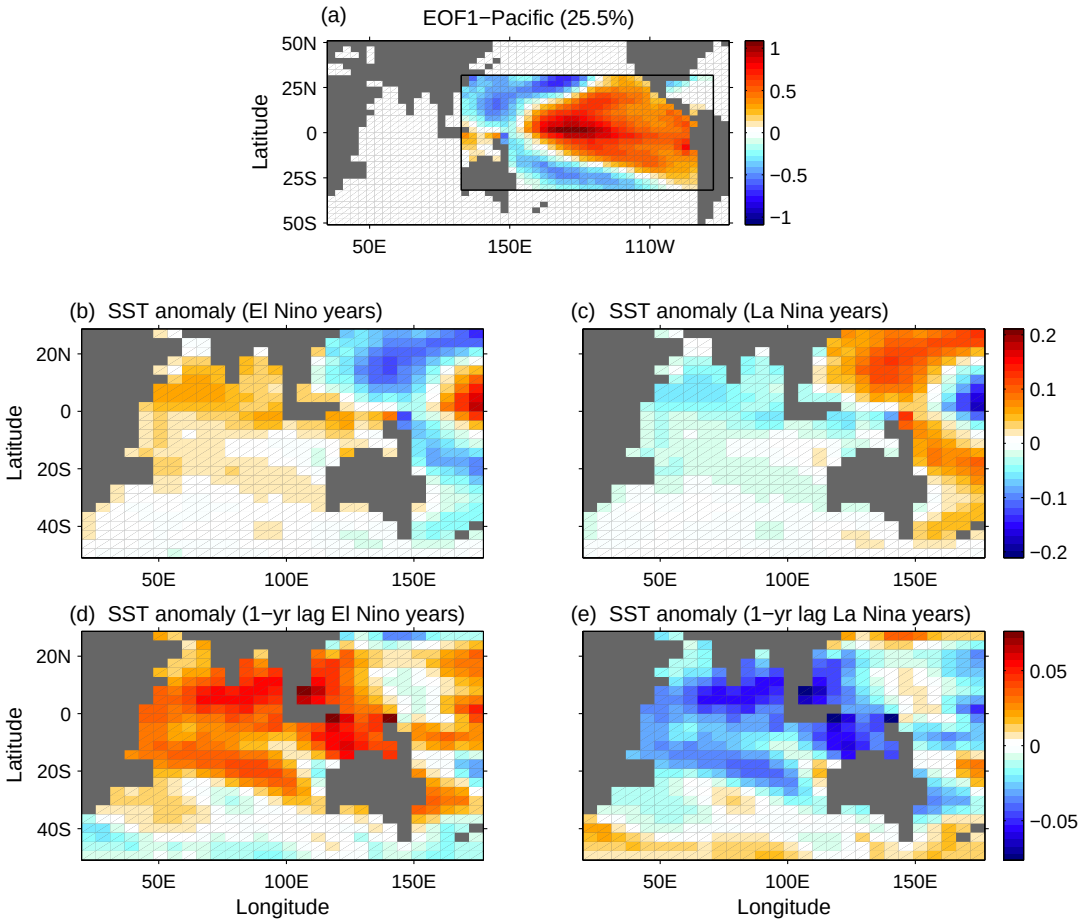

Figure 16: (a) Spatial map of the first EOF SST mode over the region marked by the box, showing a mature phase of El Niño. (b-c) SST composite anomalies calculated based on the positive (b) and negative (c) values of the principal component of the first EOF mode (shown in a). (d-e) as in (b-c) but calculated with the EOF1 principal component leading by 1 year.

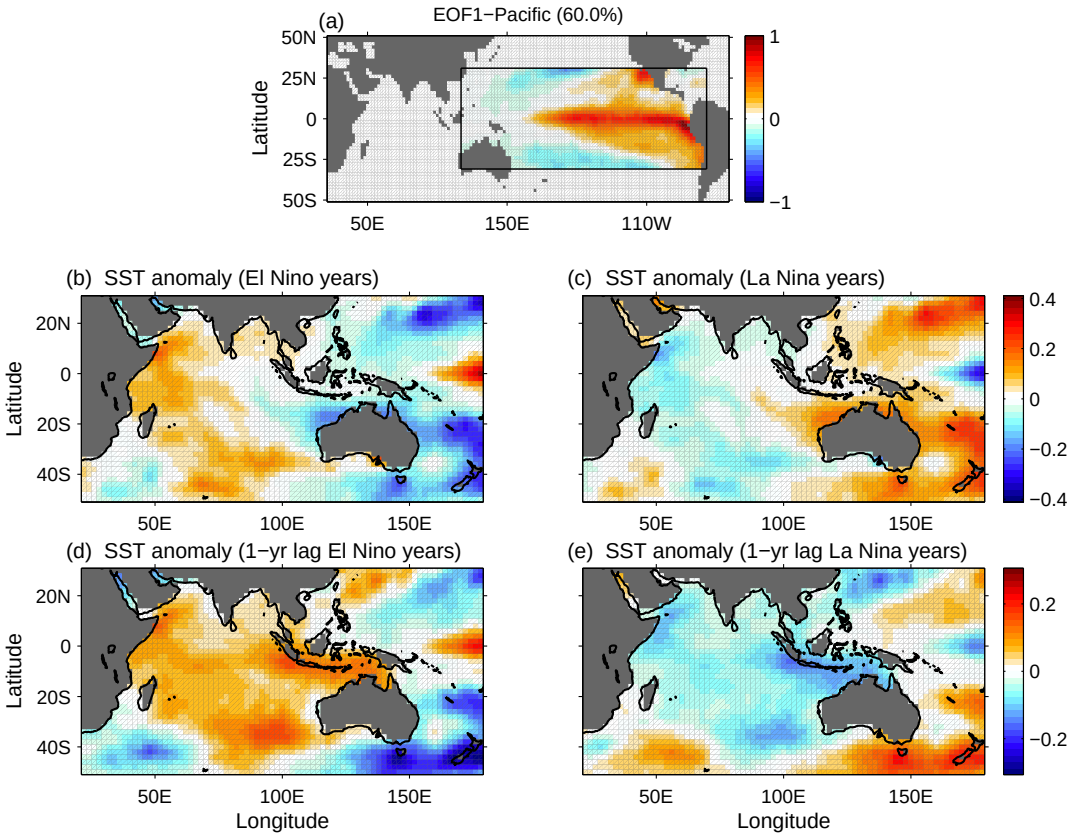

Figure 17: As in Fig. 16 but for the NOAA extended reconstructed SST.

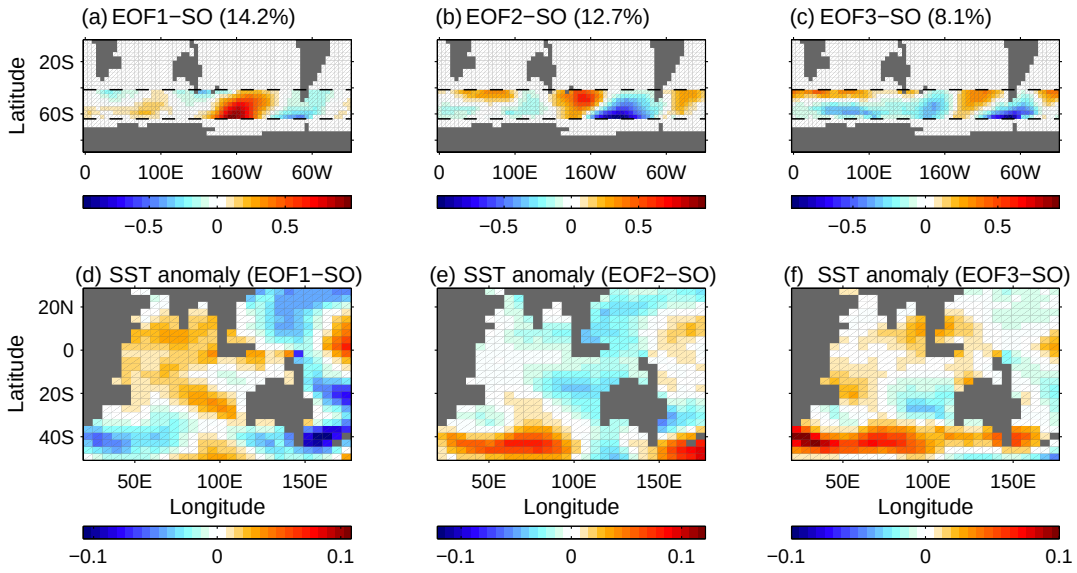

Figure 18: (a-c) the first three leading EOF SST modes in the model over the Southern Ocean region bounded by the dashed lines. (d-f) composite anomalies corresponding to the principal components of the EOF modes shown in (a-c).

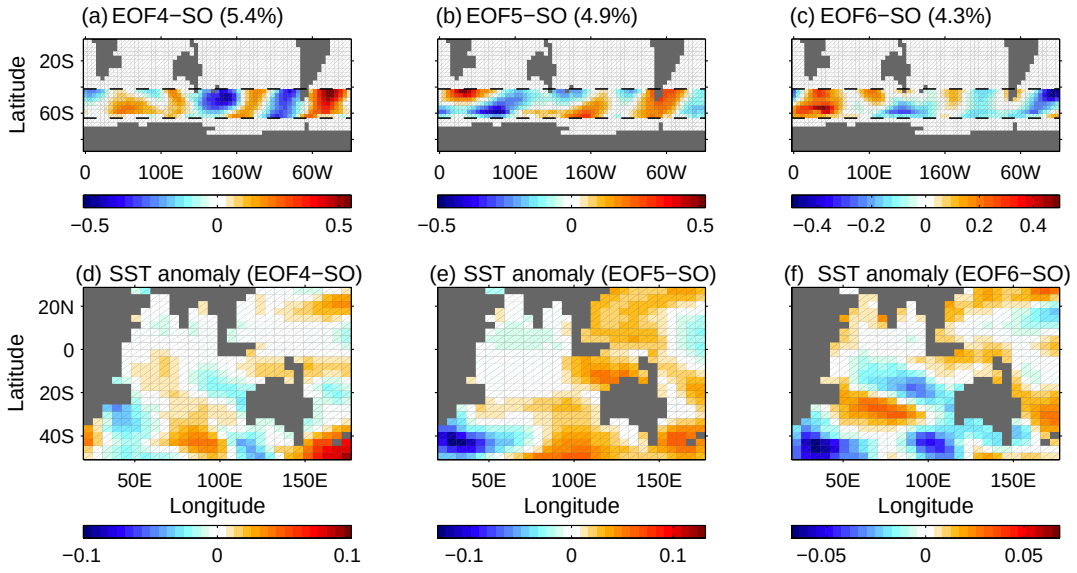

Figure 19: As in Fig. 18 but for the fourth, fifth, and sixth leading EOF modes.

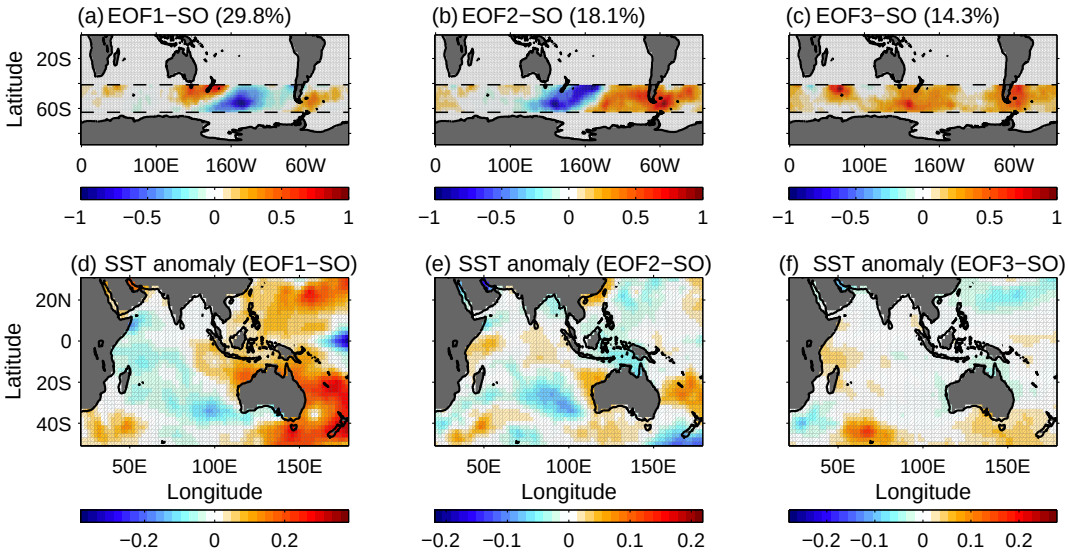

Figure 20: As in Fig. 18 but for the NOAA extended reconstructed SST.

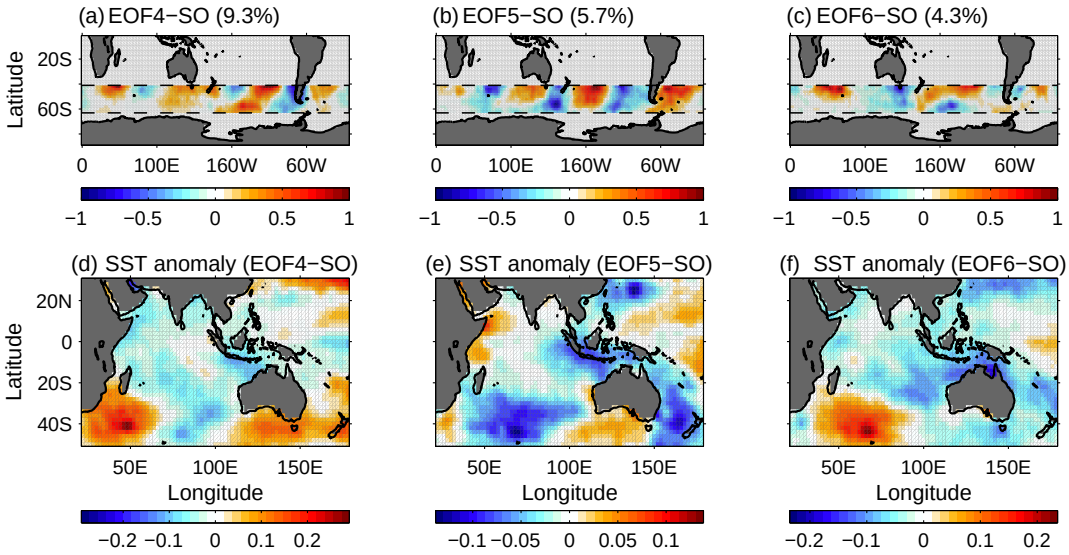

Figure 21: As in Fig. 19 but for the NOAA extended reconstructed SST.

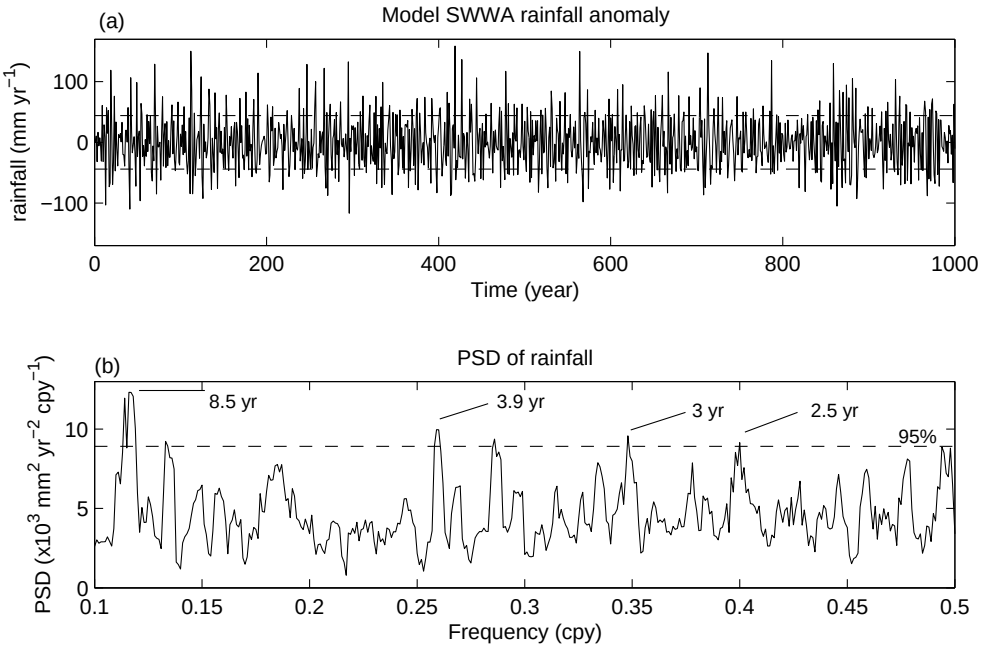

Figure 22: (a) Time series of annual rainfall anomaly (mm yr^{-1}) in SWWA over the 1000-yr climate model simulation. The dashed lines indicate one standard deviation (44 mm yr^{-1}) above and below the 1000-yr mean, which is used to define anomalously dry and wet years. The model SWWA rainfall is defined as the average over the area indicated by the box at 115−120°E, 30−35°S (see Fig. 24a, b for the location). (b) Power spectral density (PSD) of the model SWWA rainfall. The dashed line represents the estimated white noise spectrum at 95% confidence level.

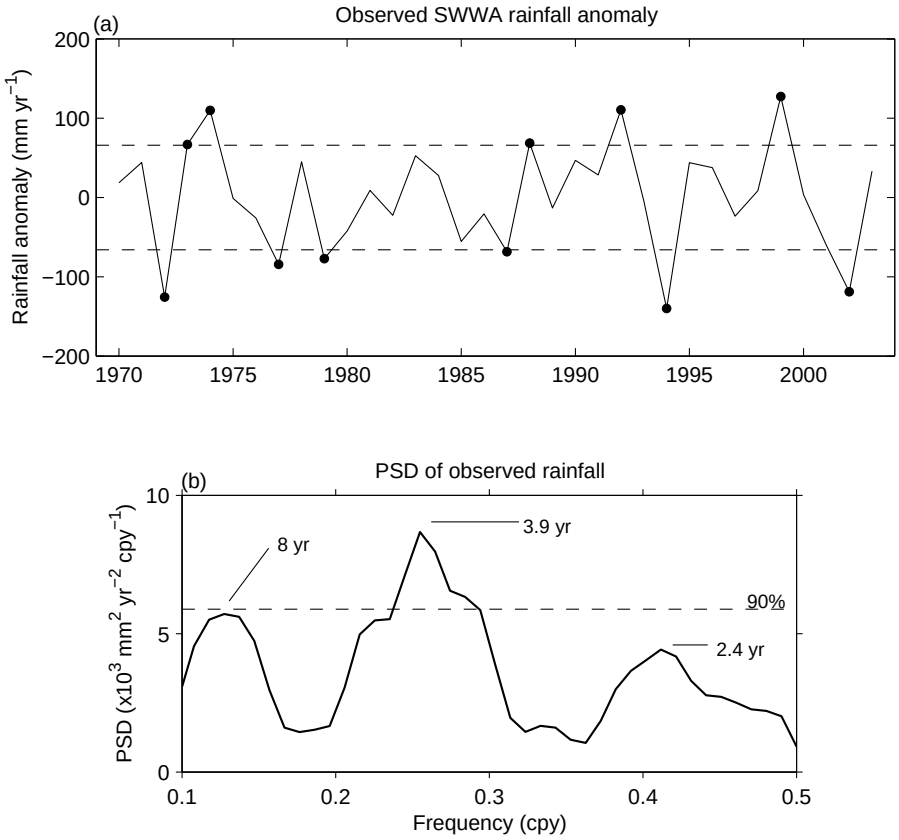

Figure 23: (a) Detrended time series of the observed annual rainfall anomaly (mm yr^{-1}) for SWWA for 1970−2003. The dashed lines indicate one standard deviation (66 mm yr^{-1}) above and below the 34-yr mean with years of rainfall extremes above and below these lines are marked with filled circles. (b) Power spectral density (PSD) of observed SWWA rainfall. The dashed horizontal line represents the estimated white noise spectrum at 90% confidence level.

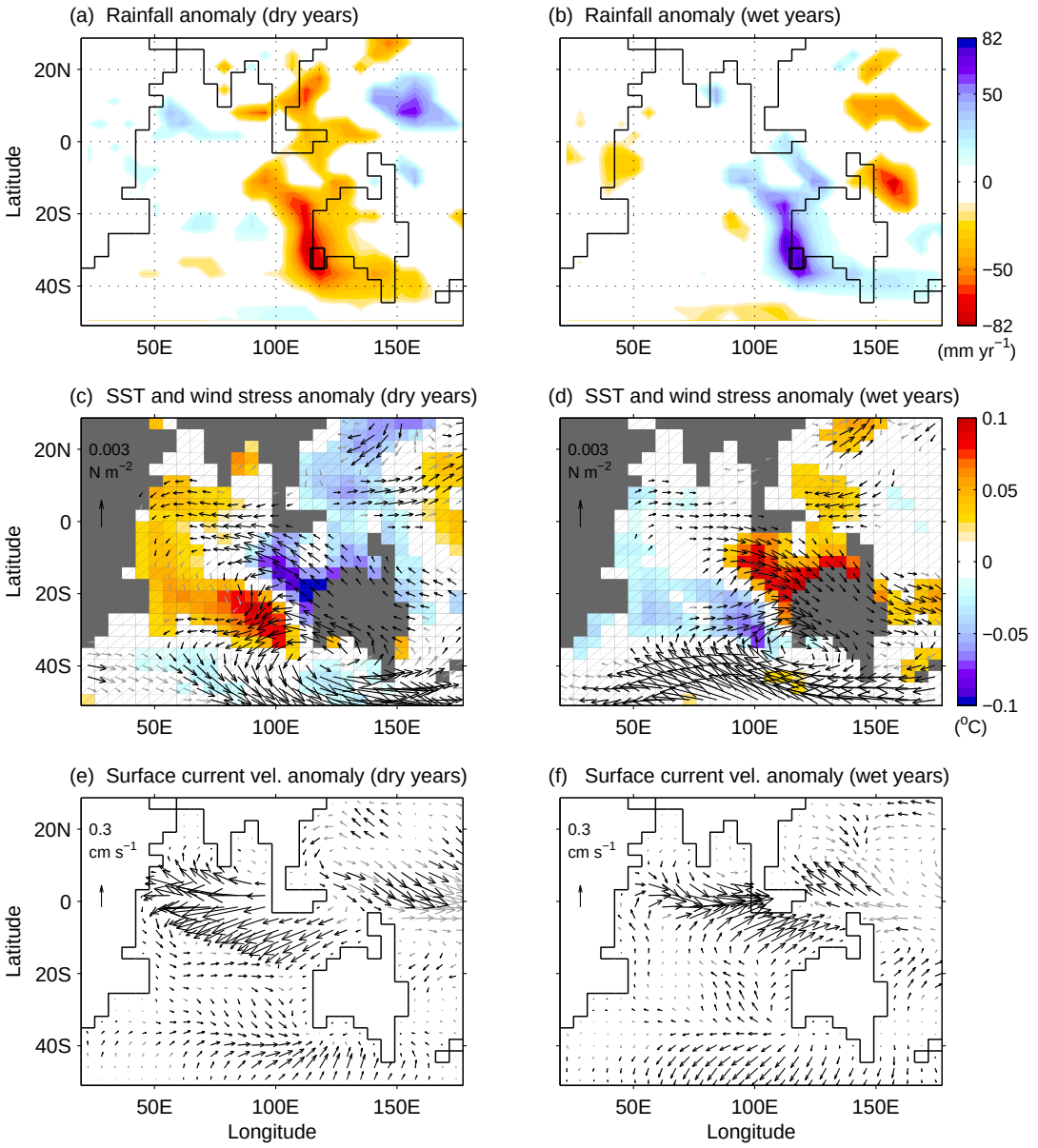

Figure 24: Composite maps of (a-b) rainfall anomaly, (c-d) SST (colour shading) and wind stress anomalies (vectors), and (e-f) ocean surface current anomalies during dry (a, c, e) and wet (b, d, f) years in the climate model. Anomalies are shown where they exceed a 90% significance level as estimated by a two-tailed t-test. Anomalous wind stress and surface current velocities below the significance level are displayed as grey vectors in (c-f). Wind anomaly vectors of magnitude less than 0.5×10^{-3} N m^{-2} are not shown. The highlighted box in (a-b) marks the SWWA location used to define years of anomalous model rainfall.

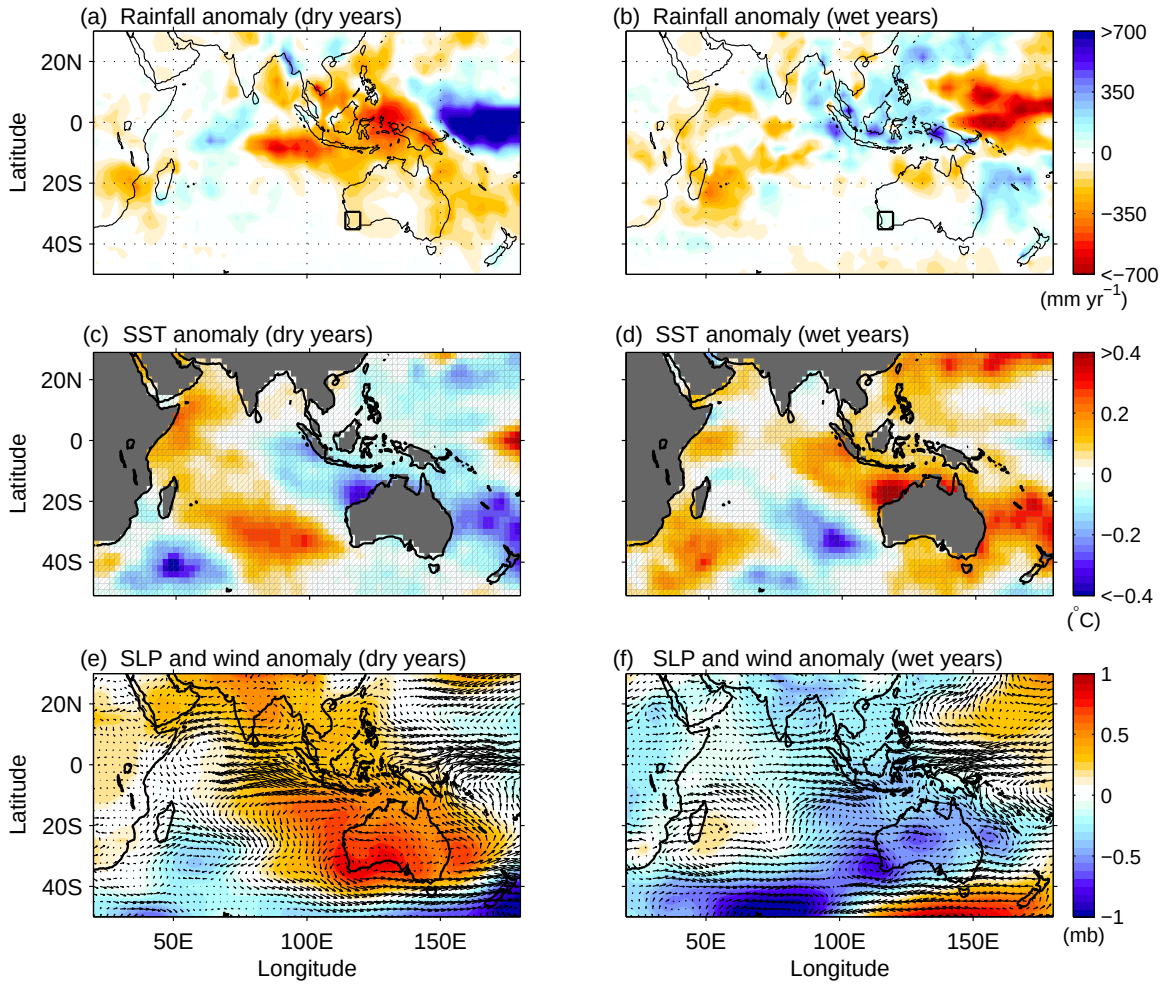

Figure 25: Composite maps of (a-b) rainfall anomaly, (c-d) SST anomaly, (e-f) SLP (colour shading) and wind velocity (vectors) anomalies in the observational and reanalysis data for the dry (a, c, e) and wet (b, d, f) years. The highlighted box in (a-b) marks the SWWA location used to define years of anomalous rainfall.

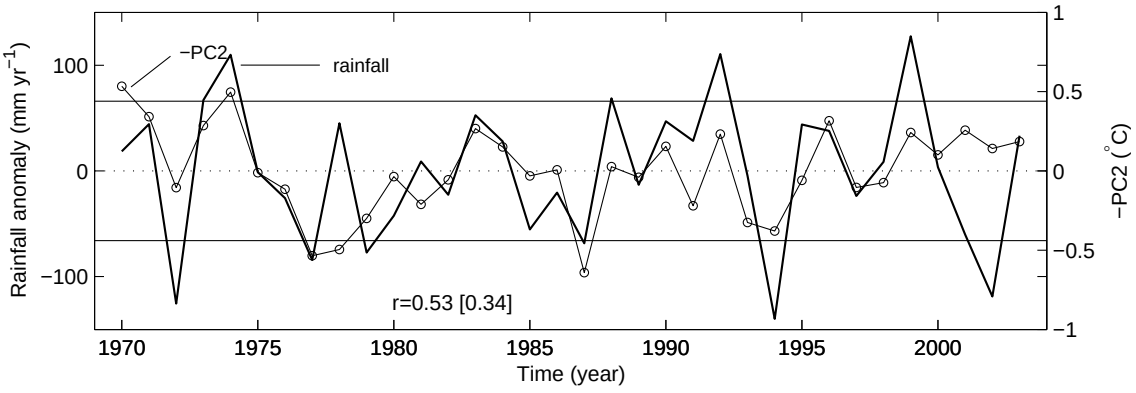

Figure 26: Time series of the observed rainfall anomaly overlaid on the principal component time series of the *observed* Mode-2 (see text for definition). Horizontal lines indicate one standard deviation of the observed rainfall anomaly above/below the long term mean.

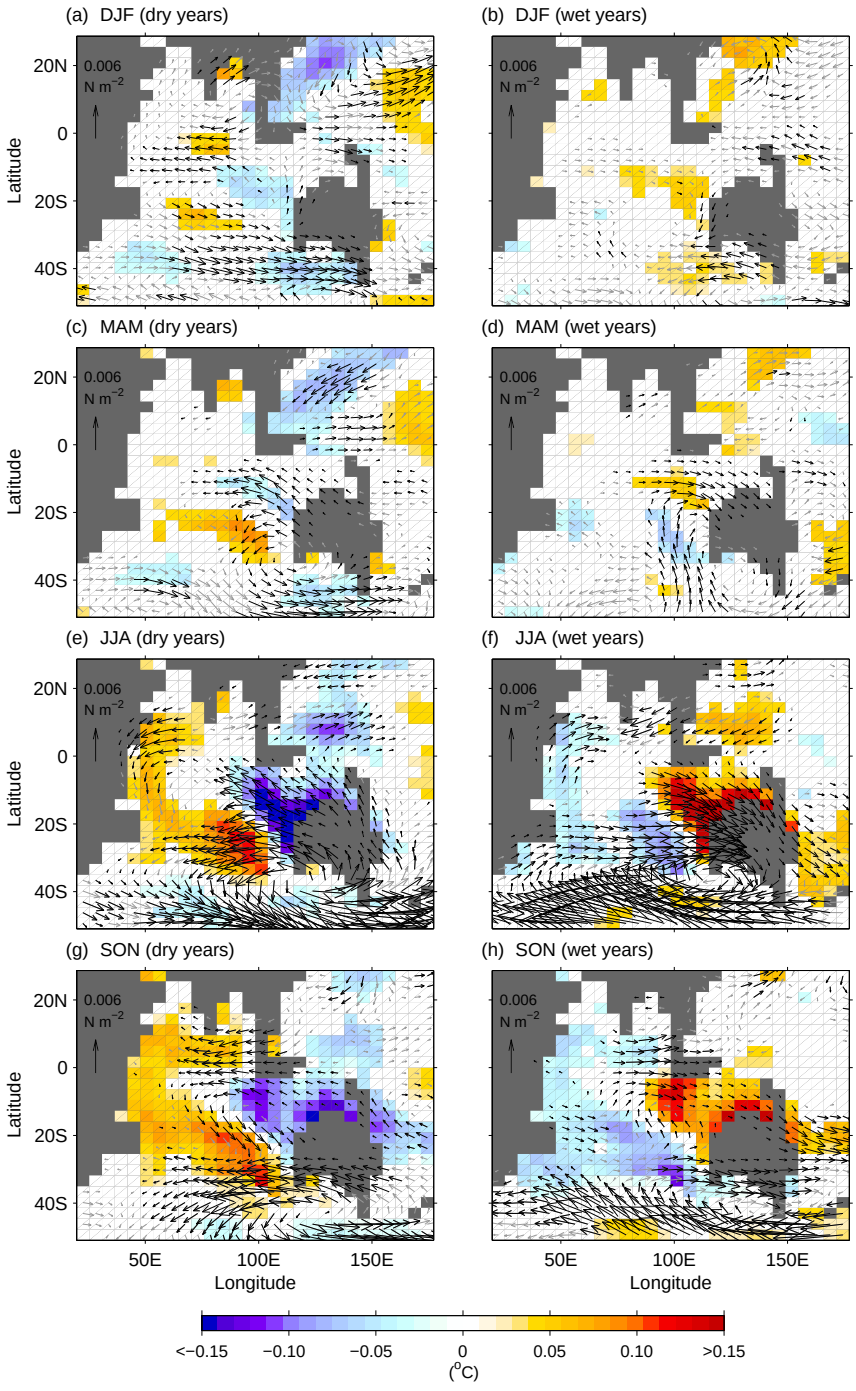

Figure 27: Seasonal evolution of SST and wind stress anomalies presented as composite maps based on extreme years of SWWA annual rainfall in the coupled climate model. Anomalies are shown where they exceed a 90% significance level as estimated by a two-tailed t-test. Anomalous wind stress below the significance level is displayed as grey vectors. Wind anomaly vectors of magnitude less than 0.5×10^{-3} N m^{-2} are not shown.

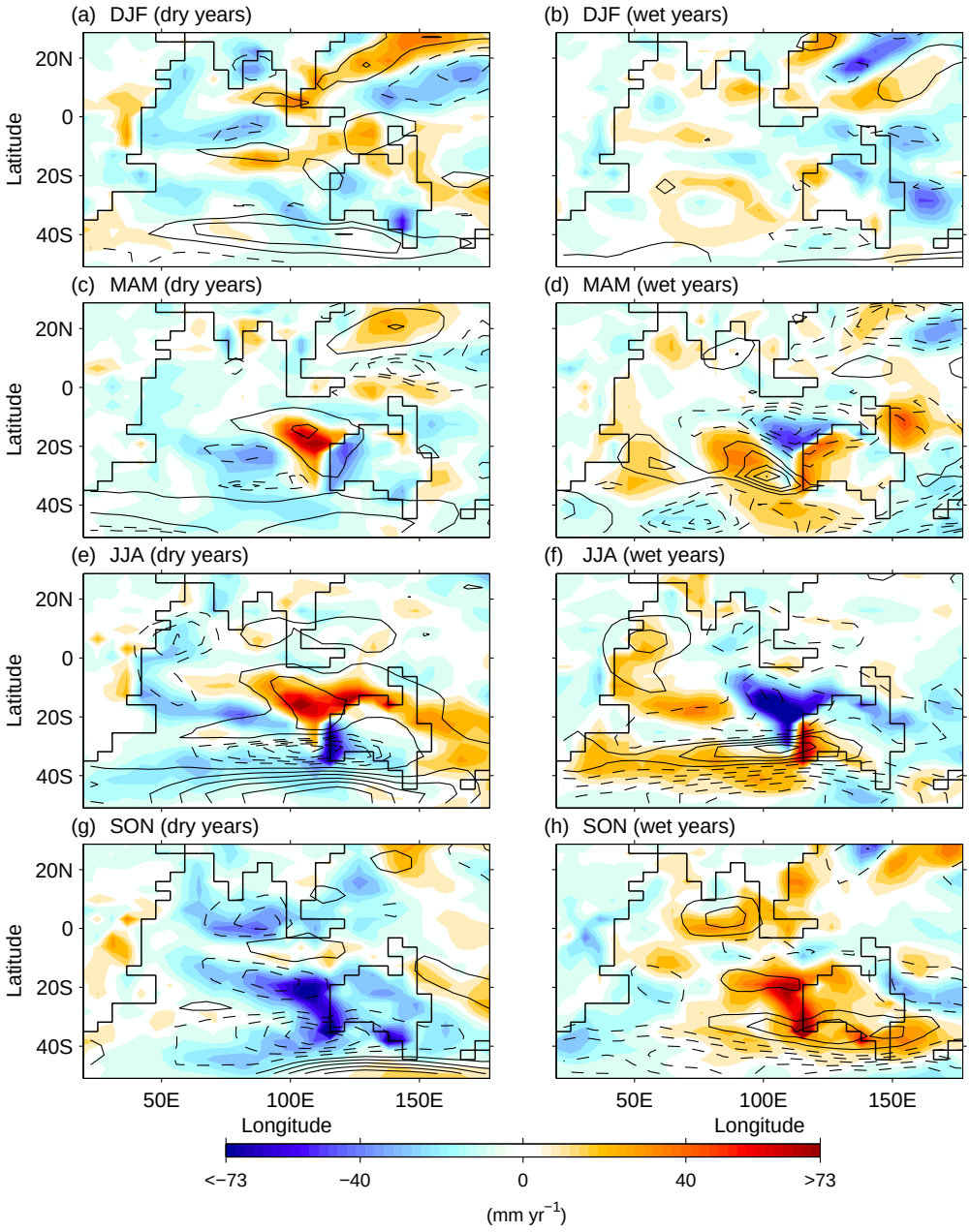

Figure 28: Seasonal evolution of latent heat flux (colour shading) and wind strength (contour) anomalies presented as composite maps based on extreme years of SWWA annual rainfall in the model.

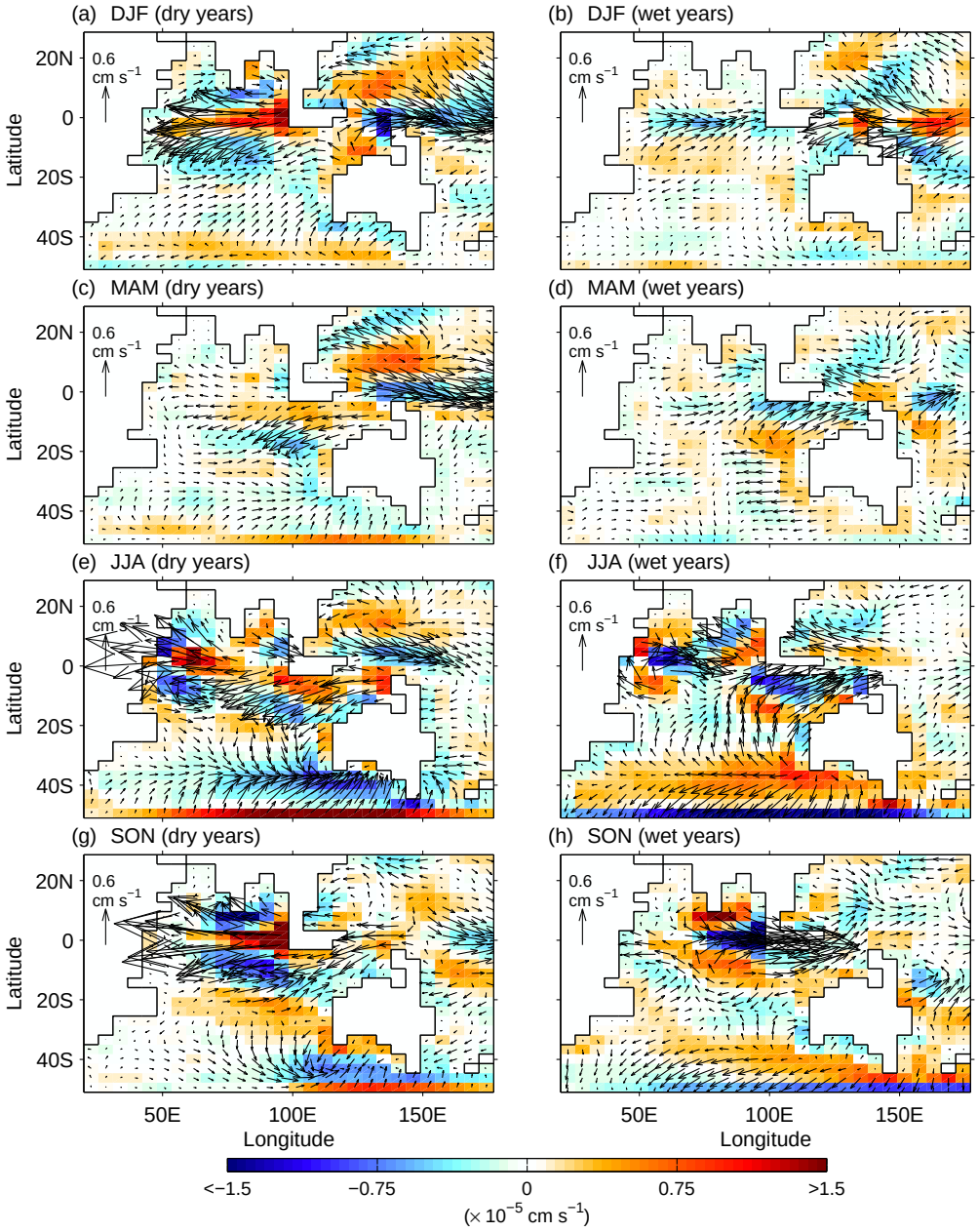

Figure 29: As in Fig. 28 but for ocean surface velocities. Horizontal velocities are presented as vectors. Vertical velocities are presented in colour shading.

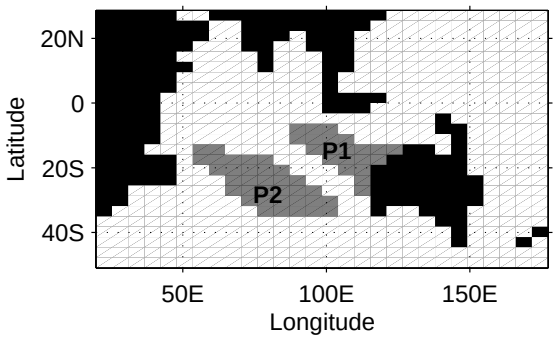

Figure 30: Location of P1 and P2 shown in grey shading, corresponding to the SST dipole shown in the model composite maps in Fig. 24c, d.

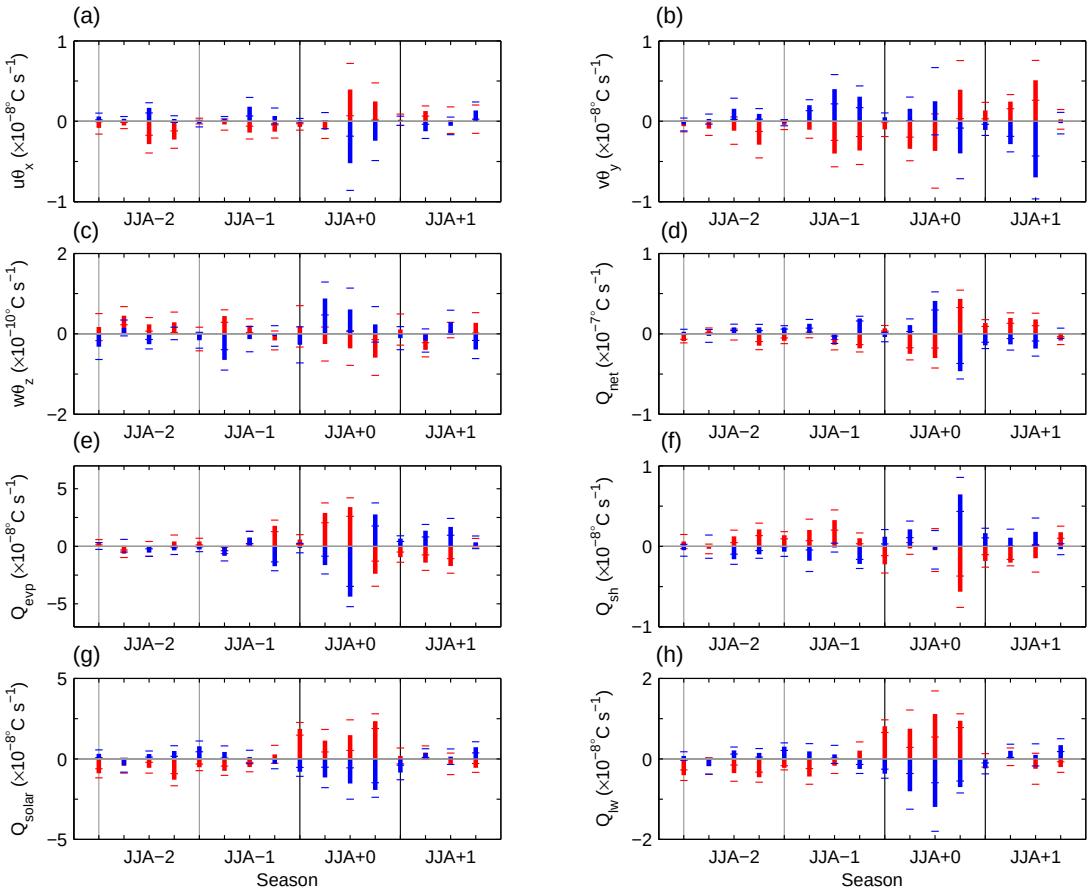

Figure 31: Seasonal evolution of composite anomalies of model atmosphere-oceanic heat fluxes spatially averaged over P1 (see Fig. 30 for the location) from two years prior to one year following the SWWA rainfall extreme years (indicated by the dark vertical lines at year+0). The oceanic heat flux variables are (a) zonal advection ($u\theta_x$), (b) meridional advection ($v\theta_y$), and (c) vertical advection ($w\theta_z$). The atmospheric heat fluxes at the air-sea interface include (d) net downward heat flux (Q_{net}), (e) upward latent heat (Q_{evp}), (f) upward sensible heat (Q_{sh}), (g) downward solar radiation (Q_{solar}), and (h) outgoing long-wave radiation (Q_{lw}). Composite anomalies corresponding to dry and wet years are displayed in red and blue, respectively. The red and blue horizontal lines corresponding to the dry and wet year composites mark the upper and lower cut-off values of the 95% significance level as determined by a two-tailed t-test indicating sampling spread of the composite estimates due to spatial averaging over P1.

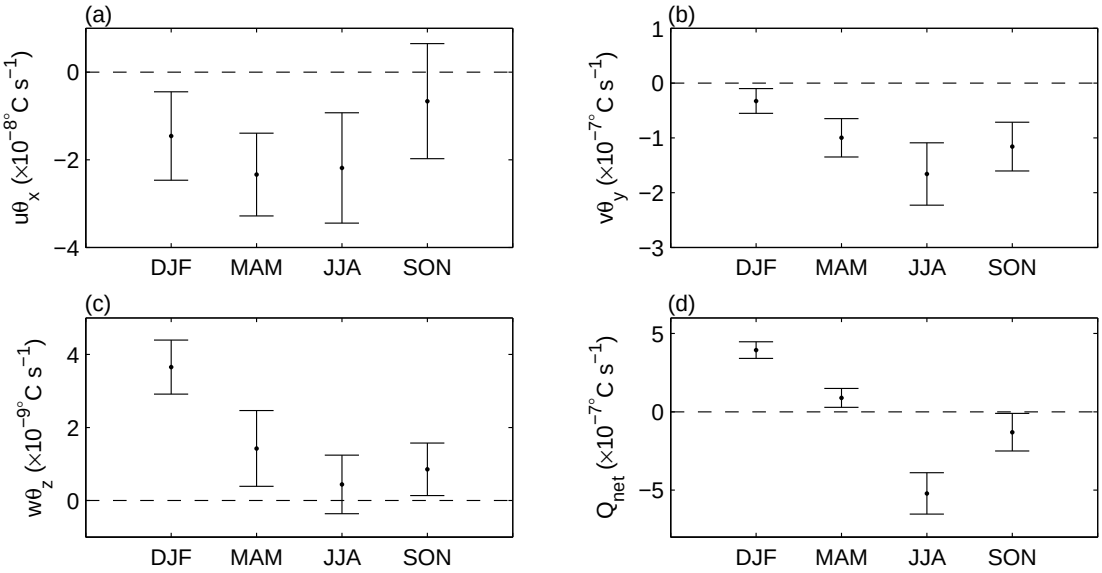

Figure 32: Seasonal mean of (a) zonal advection ($u\theta_x$), (b) meridional advection ($v\theta_y$), (c) vertical advection ($w\theta_z$), and (d) net air-sea heat flux Q_{net} spatially averaged over P1 (see Fig. 30 for location). The sampling spread at 95% significance level is indicated by the upper and lower horizontal lines.

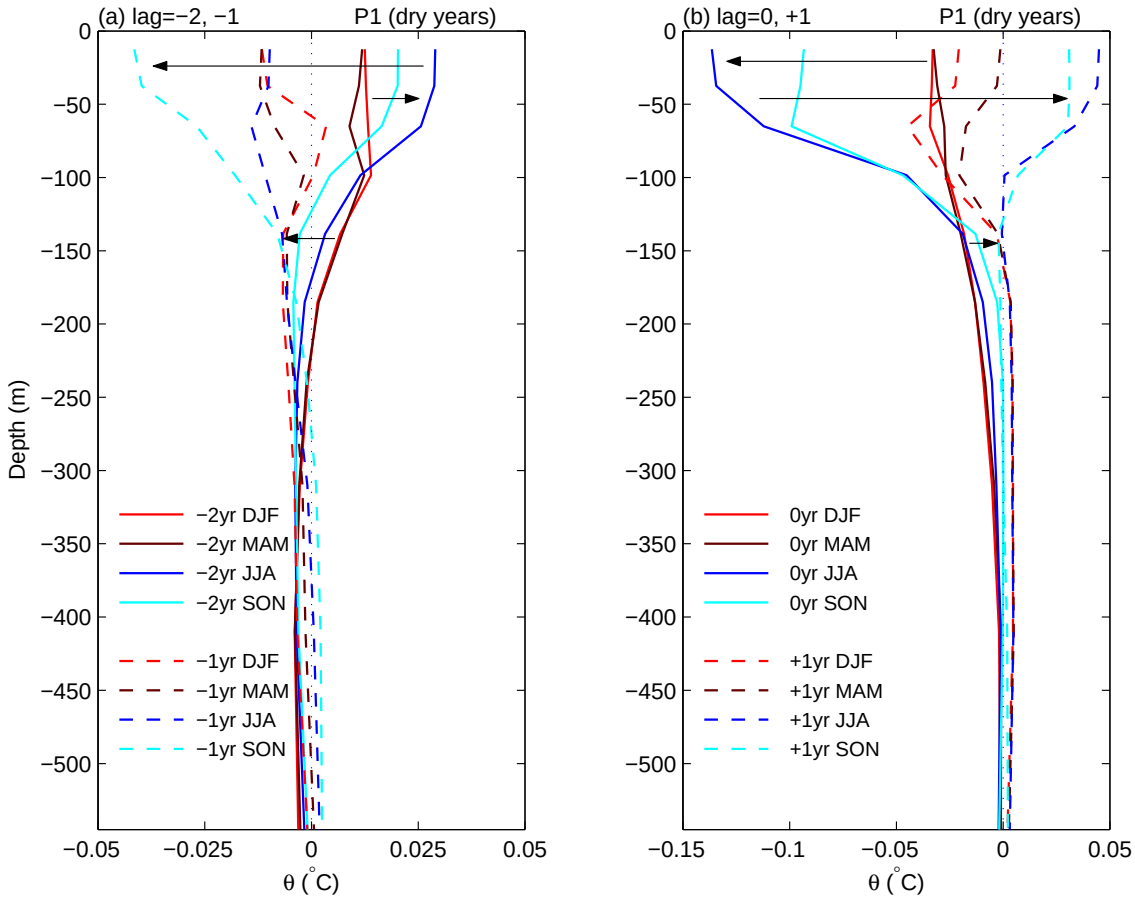

Figure 33: Depth profile of potential temperature (θ) anomalies from the surface to $\approx$ 550-m depth showing seasonal evolution during (a) two years preceeding SWWA dry years (referred to as year-2, year-1 in text). Solid line indicates θ anomalies during year-2, dashed lines indicate anomalies during year-1. (b) Depth profile of θ anomalies during SWWA dry years (year$+0$; solid lines) and one year following the extreme year (year$+1$; dashed lines). The colour indicates the seasons. The arrows illustrate the temporal shift of the anomalies.

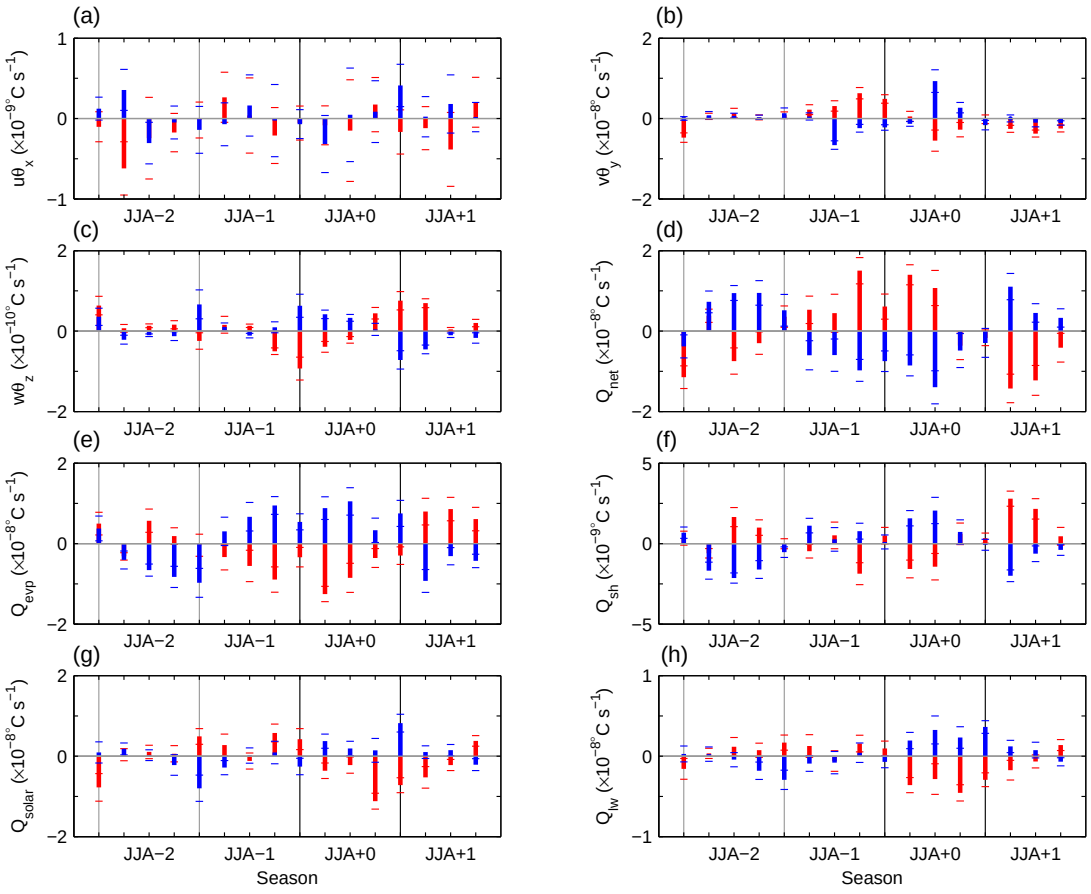

Figure 34: As Fig. 31 but for P2.

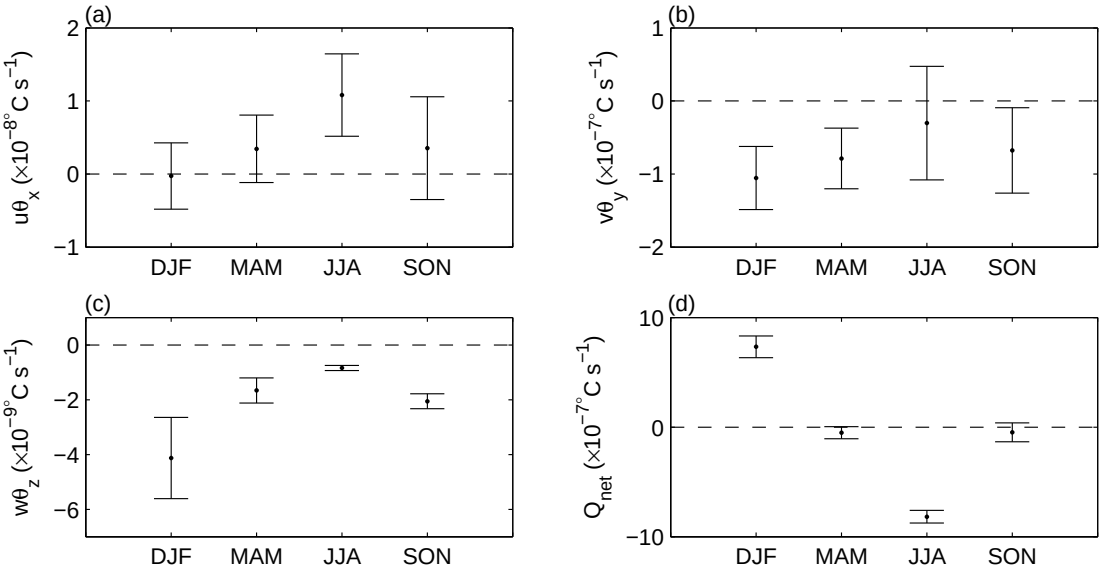

Figure 35: As Fig. 32 but for P2.

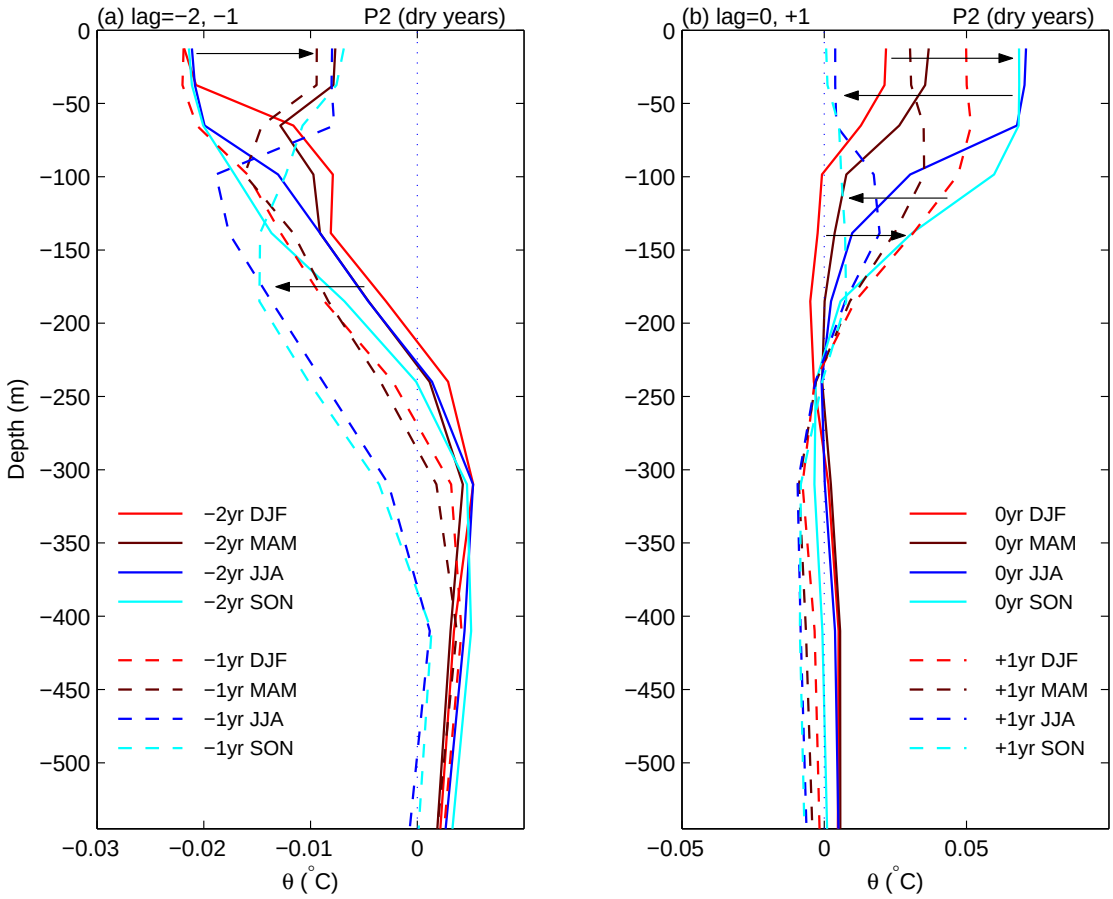

Figure 36: As Fig. 33 but for P2.

Concluding Remarks

The natural variability of the Southern Ocean water masses on interannual to centennial time scales has been studied using the CSIRO coupled climate model. We have presented methods of analysis and documentation of the spatial and temporal variability of the water masses. Dominant modes of temperature and salinity variability within the Southern Ocean were identified and found to be climate signals transmitted from the water mass formation regions. Modes of interannual variability in the Indian Ocean were also investigated. We have demonstrated that regional rainfall variability over southwest Western Australia is linked to the presence of local SST modes that evolve synchronously.

The reason the magnitude of variability in the model is weaker than the observed remains an open question. Possibilities include the fact that the model is of coarse resolution and is flux-corrected. In addition, with the documented signature of anthropogenic climate change in recent observational records, it is possible that apparent variability in the real system is actually forced in part by 20^{th} century increase in atmospheric CO_2. To directly observe modes of variability in the deep ocean we need to obtain longer observational records than are currently available. Until then, a better understanding of natural variability can be achieved by comprehensive analyses of coupled climate models as demonstrated in this study. Moreover, as atmospheric CO_2 concentrations continue to rise, the ocean's natural modes of variability may become obscured by change in the future. Thus, identification and understanding of the natural variability of the climate system may ultimately depend largely on model-based studies such as these. Similar analyses will undoubtedly be carried out in the future as the next generation climate models become available. This thesis has established a methodology for the diagnosis and interpretation of oceanic variability over interannual to multi-centennial time

scales, revealing physical variability mechanisms for the major water masses of the Southern Ocean.

References

Allan, R. J., and M. R. Haylock, 1993: Circulation features associated with the winter rainfall decrease in Southwestern Australia. *J. Climate*, **6**, 1356-1367.

Ansell, T. J., C. J. C. Reason, I. N. Smith, and K. Keay, 2000: Evidence for decadal variability in southern Australian rainfall and relationships with regional pressure and sea surface temperature. *Int. J. Climatology*, **20**, 1113-1129.

Arbic, B. K., and W. B. Owens, 2001: Climatic Warming of Atlantic Intermediate Waters. *J. Climate*, **14**, 4091-4108.

Ashok, K. Z. Guan, and T. Yamagata, 2001: Impact of the Indian Ocean dipole on the relationship between Indian monsoon rainfall and ENSO. *Geophys. Res. Lett.*, **28**, 4499-4502.

Ashok, K., Z. Guan, and T. Yamagata, 2003: Influence of the Indian Ocean dipole on the Australian winter rainfall. *Geophys. Res. Lett.*, **30**, doi:10.1029/2003GL017926.

Banks, H. T., R. A Wood, J. M. Gregory, T. C. Johns, and G. S. Jones, 2000: Are observed decadal changes in intermediate water masses a signature of anthropogenic climate change? *Geophys. Res. Lett.*, **27**, 2961-2964.

Baquero-Bernal, A., M. Latif, and S. Legutke, 2002: On dipolelike variability of sea surface temperature in the tropical Indian Ocean. *J. Climate*, **15**, 1358-1367.

Barnett, T. P., 1983: Interaction of the monsoon and Pacific trade wind system at interannual time scales. Part I: The equatorial zone. *Mon. Wea. Rev.*, **111**, 756-773.

Behera, S. K., P. S. Salvekar, and T. Yamagata, 2000: Simulation of interannual SST variability in the tropical Indian Ocean. *J. Climate*, **13**, 3487-3499.

Behera, S. K., and T. Yamagata, 2001: Subtropical SST dipole events in the southern Indian Ocean. *Geophys. Res. Lett.*, **28**, 327-330.

Behera, S. K., J. Luo, S. Masson, T. Yamagata, P. Delecluse, S. Gualdi, and A. Navarra, 2003: Implact of the Indian Ocean Dipole on the East African short rains: A CGCM study. *Exchanges*, **27**, 1-4.

Bennett, S. L, 1986: The relationship between vertical, diapycnal, and isopycnal velocity and mixing in the ocean general circulation. *J. Phys. Oceanogr.*, **16**, 167-174.

Bianchi, A. A., C. F. Giulivi, and A. R. Piola, 1993: Mixing in the Brazil-Malvinas Confluence. *Deep-Sea Res. I*, **40**, 1345-1358.

Bindoff, N. L., and J. A. Church, 1992: Warming of the water column in the southwest Pacific. *Nature*, **357**, 59-62.

Bindoff, N. L., and T. J. McDougall, 1994: Diagnosing climate change and ocean ventilation using hydrographic data. *J. Phys. Oceanogr.*, **24**, 1137-1152.

Bindoff, N. L., and T. J., McDougall, 2000: Decadal changes along an Indian Ocean section at 32°S and their interpretation. *J. Phys. Oceanogr.*, **30**, 1207-1222.

Black, E., 2003: The impact of Indian and Pacific Ocean processes on the East African short rains. *Exchanges*, **27**, 1-4.

Bonekamp, H., A. Sterl, and G. J. Komen, 1999: Interannual variability in the Southern Ocean from an ocean model forced by European Centre for Medium-Range Weather Forecasts reanalysis fluxes. *J. Geophys. Res.*, **104**, 13317-13331.

Bryan, K., 1969: A numerical method for the study of the circulation of the World Ocean. *J. Comput. Phys.*, **3**, 347-376.

Bryden, H. L., E. L. McDonagh, and B. A. King, 2003: Changes in ocean water mass properties: Oscillations or trends? *Science*, **300**, 2086-2088.

Cai, W., P. G. Baines, and H. B. Gordon, 1999: Southern mid- to high- latitude variability, a zonal wavenumber-3 pattern, and the Antarctic Circumpolar Wave in the CSIRO coupled model. *J. Climate*, **12**, 3087-3104.

Cai, W., and I. G. Watterson, 2002: Modes of interannual variability of the Southern Hemisphere circulation simulated by the CSIRO climate model. *J. Climate*, **15**, 1159-1174.

Callahan, J. E., 1972: The structure and circulation of Deep Water in the Antarctic. *Deep-Sea Res.*, **19**, 563-575.

Chambers, D. P., B. D. Tapley, R. H. Stewart, 1999: Anomalous warming in the Indian Ocean coincident with El Niño. *J. Geophysical Research*, **104**, 3035-3047.

Charles, C. D., and R. G. Fairbanks, 1992: Evidence from Southern Ocean sediments for the effect of North Atlantic deep-water flux on climate. *Nature*, **355**, 416-419.

Coles, V. J., M. S. McCartney, D. B. Olson, and W. M. Smethie Jr., 1996: Changes in the Antarctic Bottom Water properties in the western South Atlantic in the late 1980s. *J. Geophys. Res.*, **101**, 8957−8970.

Covey, C., K. M. AchutaRao, S. J. Lambert, and K. E. Taylor, 2000: Intercomparison of present and future climates simulated by coupled ocean-atmosphere GCMs. PCMDI Rep 66, PCDMI, Lawrence Livermore National Laboratory, Livermore 94550, USA.

Cox, M. D., 1984: A primitive equation, three-dimensional model of the ocean. GFDL Ocean Group Tech. Rep. No. 1. GFDL. Princeton University, Princeton, NJ, 141 p.

Davis, R. E., 2005: Intermediate-depth circulation of the Indian and South Pacific Oceans measured by autonomous floats. *J. Phys. Oceanogr.*, **35**, 683-707.

Deacon, G. E. R., 1933: A general account of the hydrology of the South Atlantic Ocean. *Discovery Rep.*, **7**, 171-238.

Dickson, R. R., and J. Brown, 1994: The production of North Atlantic Deep Water: Sources, rates, and pathways. *J. Geophys. Res.*, **99**, 12319-12341.

Doney, S. C., and M. W. Hecht, 2002: Antarctic Bottom Water formation and deep-water chlorofluorocarbon distributions in a global ocean climate model. *J. Phys. Oceanogr.*, **32**, 1642-1666.

Döös, K., and A. Coward, 1997: The Southern Ocean as the major upwelling zone of North Atlantic Deep Water. *International WOCE Newsletter*, **27**, 3-4.

Drosdowsky, W., 1993: Potential predictability of winter rainfall over southern and eastern Australia using Indian Ocean sea-surface temperature anomalies. *Australian Meteorology Magazine*, **42**, 1−6.

Drosdowsky, W., and L. E. Chambers, 2001: Near-global sea surface temperature anomalies as predictors of Australian seasonal rainfall. *J. Climate.*, **14**, 1677-1687.

Duffy, P. B., and K. Caldeira, 1997: Sensitivity of simulated salinity in a three-dimensional ocean model to upper ocean transport of salt from sea-ice formation. *Geophys. Res. Lett.*, **24**, 1323-1326.

Duffy, P. B., M. Eby, and A. J. Weaver, 1999: Effects of sinking of salt rejected during formation of sea ice on results of an ocean-atmosphere-sea ice climate model. *Geophys. Res. Lett.*, **26**, 1739-1742.

Duffy, P. B., M. Eby, and A. J. Weaver, 2001: Climate model simulations of effects of increased atmospheric CO_2 and loss of sea ice on ocean salinity and tracer uptake. *J. Climate*, **14**, 520-532.

Dutay, J.-C, and co-authors, 2002: Evaluation of ocean model ventilation with CFC-11: comparison of 13 global ocean models. *Ocean Modelling*, **4**, 89-120.

Emery, W. J., and R. E. Thomson, 1998: Data Analysis Methods in Physical Oceanography. Pergamon. 634 p.

England, M. H., 1992: On the formation of Antarctic Intermediate and Bottom Water in ocean general circulation models. *J. Phys. Oceanogr.*, **22**, 918-926.

England, M. H., 1993: Representing the global-scale water masses in ocean general circulation models. *J. Phys. Oceanogr.*, **22**, 1523-1552.

England, M. H., J. S. Godfrey, A. C. Hirst, and M. Tomczak, 1993: The mechanism for Antarctic Intermediate Water Renewal in a World Ocean Model. *J. Phys. Oceanogr.*, **23**, 1553-1560.

England, M. H., 1995: Using chlorofluorocarbons to assess ocean climate models. *Geophys. Res. Lett.*, **22**, 3051-3054.

England, M. H., and A. C. Hirst, 1997: Chlorofluorocarbon uptake in a World Ocean model 2. Sensitivity to surface thermohaline forcing and subsurface mixing parameterizations. *J. Geophys. Res.*, **102**, 15,709-15,731.

England, M. H., and G. Holloway, 1998: Simulations of CFC content and water mass age in the deep North Atlantic. *J. Geophys. Res.*, **103**, 15,885-15,901.

England, M. H., and S. Rahmstorf, 1999: Sensitivity of ventilation rates and radiocarbon uptake to subgrid-scale mixing in ocean models. *J. Phys. Oceanogr.*, **29**, 2802-2827.

England, M.H., C.C. Ummenhofer, and A. Santoso, 2006: Interannual rainfall extremes over southwest Australia linked to Indian Ocean climate variability. *J. Climate*, **19**, 1948-1969.

Fahrbach, E., M. Hoppema, G. Rohardt, M. Schröder, and A. Wisotzki, 2004: Decadal-scale variations of water mass properties in the deep Weddell Sea. *Ocean Dynamics*, **54**, 77−91.

Flato, G. M., and W. D. Hibler, 1990: On a simple sea-ice dynamics model for climate studies. *Ann. Glaciol.*, **14**, 72-77.

Foldvik, A., T. Gammelsrød, S. Østerhus, E. Fahrbach, G. Rohardt, M. Schröder, K. W. Nicholls, L. Padman, and R. A. Woodgate, 2004: Ice shelf water overflow and bottom water formation in the southern Weddell Sea. *J. Geophys. Res.*, **109**, doi:10.1029/2003JC002008.

Foster, T. D., and E. C. Carmack, 1976: Frontal zone mixing and Antarctic Bottom Water formation in the southern Weddell Sea. *Deep-Sea Research*, **23**, 301-317.

Frank, M., N. Whiteley, S. Kasten, J. R. Hein, and K. O'Nions, 2002: North Atlantic Deep Water export to the Southern Ocean over the past 14 Myr: Evidence from Nd and Pb isotopes in ferromanganese crusts. *Paleoceanography*, **17**, doi:10.1029/2000PA000606.

García, M. A., I. Bladé, A. Cruzado, Z. Velásquez, H. García, J. Puigdefäbregas, and J. Sospedra, 2002: Observed variability of water properties and transports

on the World Ocean Circulation Experiment SR1b section across the Antarctic Circumpolar Current. *J. Geophys. Res.*, **107**, doi:10.1029/2000JC000277.

Garzoli, S. L., and C. Giulivi, 1994: What forces the variability of the southwestern Atlantic boundary currents? *Deep-Sea Res. I*, **41**, 1527-1550.

Gent, P. R., and J. C. McWilliams, 1990: Isopycnal mixing in ocean circulation models. *J. Phys. Oceanogr.*, **20**, 150-155.

Gent, P. R., J. Willebrand, T. J. McDougall, and J. C. McWilliams, 1995: Parameterizing eddy-induced tracer transports in ocean circulation models. *J. Phys. Oceanogr.*, **25**, 463-474.

Georgi, D. T., 1979: Modal properties of Antarctic Intermediate Water in the Southeast Pacific and the South Atlantic. *J. Phys. Oceanogr.*, **9**, 456-468.

Georgi, D. T., 1981: On the relationship between the large-scale property variations and fine structure in the Circumpolar Deep Water. *J. Geophys. Res.*, **86**, 6556-6566.

Goodman, P. J., 1998: The role of North Atlantic Deep Water formation in an OGCM's ventilation and thermohaline circulation. *J. Phys. Oceanogr.*, **28**, 1759-1785.

Goodman, P. J., 2001: Thermohaline adjustment and advection in an OGCM. *J. Phys. Oceanogr.*, **31**, 1477-1497.

Gordon, A. L., 1971: Oceanography of Antarctic waters. In: *Antarctic Oceanography I*, Antarctic Research Series, Vol. 15, edited by J. L. Reid, p. 169-203, AGU, Washington DC.

Gordon, A. L., 1972: Spreading of Antarctic Bottom Waters, II. In: *Studies in Physical Oceanography—a tribute of George Wüst on his 80th birthday*, Vol. II, p. 1-17, Gordon and Breach, New York.

Gordon, A. L., 1989: Brazil-Malvinas Confluence—1984. *Deep-Sea Res.*, **36**, 359-384.

Gordon, A. L., R. F. Weiss, W. M. Smethie, and M. J. Warner, 1992: Thermocline and Intermediate Water communication between the South Atlantic and Indian Oceans. *J. Geophys. Res.*, **97**, 7223-7240.

Gordon, H. B., and S. P. O'Farrell, 1997: Transient climate change in the CSIRO coupled model with dynamic sea ice. *Monthly Weather Review*, **125**, 875-907.

Gordon, A. L., M. Visbeck, and B. Huber, 2001: Export of Weddell Sea Deep and Bottom Water. *J. Geophys. Res.*, **106**, 9005-9017.

Hall, A., and M. Visbeck, 2002: Synchronous variability in the Southern Hemisphere atmosphere, sea ice, and ocean resulting from the Annular Mode. *J. Climate*, **15**, 3043-3057.

Hirst, A. C., and W. Cai, 1994: Sensitivity of a world ocean GCM to changes in subsurface mixing parameterization. *J. Phys. Oceanogr.*, **24**, 1256-1279.

Hirst, A. C., and T. J. McDougall, 1996: Deep-water properties and surface buoyancy flux as simulated by a z-coordinate model including eddy-induced advection. *J. Phys. Oceanogr.*, **26**, 1320-1343.

Hirst, A. C., S. P. O'Farrell, and H. B. Gordon, 2000: Comparison of a coupled ocean-atmosphere model with and without oceanic eddy-induced advection. Part I: ocean spinup and control integrations. *J. Climate*, **13**, 139-163.

Hogg, N. G., and W. Zenk, 1997: Long-period changes in the bottom water flowing through Vema Channel. *J. Geophys. Res.*, **102**, 15639-15646.

Horel, J. D., 1984: Complex principal component analysis: Theory and examples. *J. Climate Appl. Meteor.*, **23**, 1660-1673.

Hunt, G. B., 2001: A description of persistent climate anomalies in a 1000-year climatic model simulation. *Climate Dynamics*, **17**, 717-733.

Hunt, B. B., and T. I. Elliott, 2003: Secular variability of ENSO events in a 1000-year climatic simulation. *Climate Dynamics*, **20**, 689-703.

Indian Ocean Climate Initiative (IOCI), 2002: Climate variability and change in southwest Western Australia. Indian Ocean Climate Initiative Panel, Perth, Western Australia, 34 p.

Jackett, D. R., and T. J. McDougall, 1997: A neutral density variable for the World's Oceans. *J. Phys. Oceanogr.*, **27**, 237-263.

Jacobs, S. S., 2004: Bottom water production and its links with the thermohaline circulation. *Antarctic Science*, **4**, 427-437.

Janowiak, J. E., A. Gruber, C. R. Kondragunta, R. E. Livezey, and G. F. Huffman, 1998: A comparison of the NCEP-NCAR reanalysis precipitation and the GPCP rain gauge-satellite combined dataset with observational error considerations. *J. Climate*, **11**, 2960-2979.

Johnson, G. C., and A. H. Orsi, 1997: Southwest Pacific Ocean Water-Mass Changes between 1968/69 and 1990/91. *J. Climate*, **10**, 306-316.

Kamenkovich, I. V., and E. S. Sarachik, 2004: Mechanisms controlling the sensitivity of the Atlantic thermohaline circulation to the parameterization of eddy transports in ocean GCMs. *J. Phys. Oceanogr.*, **34**, 1628-1647.

Klein, S. A., B. J. Soden, and N.-C. Lau, 1999: Remote sea surface temperature variations during ENSO: Evidence for a tropical atmospheric bridge. *J. Climate*, **12**, 917-932.

Kowalczyk, E. A., J. R. Garratt, and P. B. Krummel, 1994: Implementation of a soil canopy scheme into the CSIRO GCM − Regional aspects of the model response. CSIRO Division of Atmospheric Research, Tech. Paper 32, 59 p. [Available from CSIRO Atmospheric Research, PMB1, Aspendale, Vic. 3195, Australia.]

Lareef, Z., S. Rao, and T. Yamagata, 2003: Modulation of Sri Lanka rainfall by the Indian Ocean Dipole. *Geophys. Res. Lett.*, **10**, 1063-1066.

Large, W. G., G. Danabasoglu, S. C. Doney, and J. C. McWilliams, 1997: Sensitivity to surface forcing and boundary layer mixing in a global ocean model: Annual-mean climatology. *J. Phys. Oceanogr.*, **27**, 2418-2447.

Larqué, L., K. Maamaatuaiahutapu, V. Garçon, 1997: On the intermediate and deep water flows in the South Atlantic Ocean. *J. Geophys. Res.*, textbf102, 12,425-12,440.

Lau, N.-C., and M. J. Nath, 2003: Atmosphere-ocean variations in the Indo-Pacific sector during ENSO episodes. *J. Climate*, **16**, 3-20.

Levitus, S., R. Burgett, and T. P. Boyer, 1994: World Ocean Atlas 1994. Volume 3: Salinity. NOAA ATLAS NESDIS 3, 99 p.

Levitus, S., and T. Boyer, 1994: World Ocean Atlas 1994. Volume 4: Temperature. NOAA ATLAS NESDIS 4, 117 p.

Li, T., B. Wang, C.-P. Chang, and Y. Zhang, 2003: A theory for the Indian Ocean dipole-zonal mode. *J. Atmospheric Sciences*, **60**, 2119-2135.

Locarnini, R. A., T. Whitworth, and W. D. Nowlin Jr., 1993: The importance of the Scotia Sea on the outflow of Weddell Sea Deep Water. *J. Marine Research*, **51**, 135-153.

Lynn, R.J. and J.L. Reid, 1968: Characteristics and circulation of deep and abyssal waters. *Deep Sea Res.*, **15**, 577-598.

Maamaatuaiahutapu, K., V. C. Garçon, C. Provost, 1992: Brazil-Malvinas confluence: water mass composition. *J. Geophys. Res.*, **97**, 9493-9505.

Manabe, S., and R. J. Stouffer, 1996: Low-frequency variability of surface air temperature in a 1000-year integration of a coupled atmosphere−ocean−land surface model. *J. Climate*, **9**, 376-393.

Mann, M. E., and J. M. Lees, 1996: Robust estimation of background noise and signal detection in climatic time series. *Climatic Change*, **33**, 409-445.

Mantyla, A. W., and J. L. Reid, 1983: Abyssal characteristics of the World Ocean Waters. *Deep-Sea Res.*, **30**, 805-833.

Mantyla, A. W., and J. L. Reid, 1995: On the origins of deep and bottom waters of the Indian Ocean. *J. Geophys. Res.*, **100**, 2417-2439.

May, B. D., and D. E. Kelley, 2002: Contrasting the interleaving in two baroclinic ocean fronts. *Dynamics of Atmospheres and Oceans*, **36**, 23-42.

Mo, K. C., 2000: Relationships between low-frequency variability in the Southern Hemisphere and sea surface temperature anomalies. *J. Climate*, **13**, 3599-3610.

McCartney, M. S., 1977: Subantarctic Mode Water. *A Voyage of Discovery*, M. V. Angel, Ed., *Deep-Sea Res.*, **24**(Suppl.), 103-119.

McDougall, T. J., 1984: The relative roles of diapycnal and isopycnal mixing on subsurface water mass conversion. *J. Phys. Oceanogr.*, **14**, 1577-1589.

McNeil, B. I., R. J. Matear, and B. Tilbrook, 2001: Does carbon-13 track anthropogenic CO2 in the Southern Ocean? *Global Biogeochemical Cycles*, **15**, 597-613.

Mémery, L., M. Arhan, X. A. Alvarez-Salgado, M.-J. Messias, H. Mercier, C. G. Castro, A. F. Rios, 2000: The water masses along the western boundary of the south and equatorial Atlantic. *Prog. Oceanogr.*, **47**, 69-98.

Meredith, M. P., R. A. Locarnini, K. A. Van Scoy, A. J. Watson, K. J. Heywood, and B. A. King, 2000: On the sources of Weddell Gyre Antarctic Bottom Water. *J. Geophys. Res.*, **105**, 1093-1104.

Meredith, M. P., A. C. Naveira Garabato, D. P. Stevens, K. J. Heywood, and R. J. Sanders, 2001: Deep and bottom waters in the Eastern Scotia Sea: Rapid changes in properties and circulation. *J. Phys. Oceanogr.*, **31**, 2157-2168.

Mikolajewicz, U., and E. Maier-Reimer, 1990: Internal secular variability in an ocean general circulation model. *Climate Dynamics*, **4**, 145-156.

Mizoguchi, K., S. D. Meyers, S. Basu, and J. J. O'Brien, 1999: Multi- and quasi-decadal variations of sea surface temperature in the North Atlantic. *J. Phys. Oceanogr.*, **29**, 3133-3144.

Molinelli, E. J., 1981: The Antarctic influence on Antarctic Intermediate Water. *J. Marine Research*, **39**, 267-293.

Murtugudde, R., A. J. Busalacchi, 1999: Interannual variability of the dynamics and thermodynamics of the tropical Indian Ocean. *J. Climate*, **12**, 2300-2325.

Naveira Garabato, A. C., K. J. Heywood, and D. P. Stevens, 2002a: Modification and pathways of Southern Ocean deep waters in the Scotia Sea. *Deep-Sea Research I*, **49**, 681-705.

Naveira Garabato, A. C., E. L. McDonagh, D. P. Stevens, K. J. Heywood, and R. J. Sanders, 2002b: On the export of Antarctic Bottom Water from the Weddell Sea. *Deep-Sea Research II*, **49**, 4715-4742.

Nichols, N., 1989: Sea surface temperatures and Australian winter rainfall. *J. Climate*, **2**, 965−973.

Nof, D., 2003: The Southern Ocean's grip on the northward meridional flow. *Prog. Oceanogr.*, **56**, 223−247.

North, G. R., T. L. Bell, R. F. Cahalan, and F. J. Moeng, 1982: Sampling errors in the estimation of Empirical Orthogonal Functions. *Mon. Wea. Rev.*, **110**, 699-706.

O'Farrell, S.P., 1998: Sensitivity study of a dynamical sea ice model: The effect of the external stresses and land boundary conditions on ice thickness distribution. *J. Geophys. Res.*, **103**, 15751-15782.

O'Farrell, S. P., 2002: Use of passive tracers as a diagnostic tool in coupled model simulations - Northern Hemisphere. *J. Phys. Oceanogr.*, **32**, 831-850.

Oke, P. R., and M. H. England, 2004: Oceanic response to changes in the latitude of the Southern Hemisphere subpolar westerly winds. *J. Climate*, **17**, 1040-1054.

Orsi, A. H., G. C. Johnson, and J. L. Bullister, 1999: Circulation, mixing, and production of Antarctic Bottom Water. *Progress in Oceanography*, **43**, 55-109.

Osborn, T. J., 1997: Thermohaline oscillations in the LSG OGCM: Propagating anomalies and sensitiviy to parameterizations. *J. Phys. Oceanogr.*, **27**, 2233-2255.

Percival, D. B., and A. T. Walden, 1993: Spectral Analysis for Physical Applications. Cambride University Press, Cambridge, U.K., 583 p.

Pickard, G. L., and W. J. Emery, 1990: Descriptive Pysical Oceanography. Butterworth Heinemann. 320 p.

Pierce, D. W., T. P. Barnett, and U. Mikolajewicz, 1995: Competing roles of heat and freshwater flux in forcing thermohaline oscillations. *J. Phys. Oceanogr.*, **25**, 2046- 2064.

Piola, A. R., and D. T. Georgi, 1982: Circumpolar properties of Antarctic Intermediate Water and Subantarctic Mode Water. *Deep-Sea Res.*, **29**, 687-711.

Piola, A. R., and A. L. Gordon, 1989: Intermediate water in the southwestern South Atlantic. *Deep-Sea Res.*, **36**, 1-16.

Pitman, A. J., G. T. Narisma, R. A. Pielke Sr., and N. J. Holbrook, 2004: Impact of land cover change on the climate of southwest Western Australia. *J. Geophys. Res.*, **109**, D18109, doi:10.1029/2003JD004347.

Preisendorfer, R. W., 1988: Principal Component Analyses in Meteorology and Oceanography. Elsevier. 425 p.

Prézelin, B. B., E. E. Hofmann, C. Mengelt, J. M. Klinck, 2000: The linkage between Upper Circumpolar Deep Water (UCDW) and phytoplankton assemblages on the west Antarctic Peninsula continental shelf. *J. Mar. Res.*, **58**, 165-202.

Putman, W. M., D. M. Legler, and J. J. O'Brien, 2000: Interannual variability of synthesized FSU and NCEP-NCAR reanalysis pseudostress products over the Pacific Ocean. *J. Climate*, **13**, 3003-3016.

Qu, T., and G. Meyers, 2005: Seasonal characteristics of circulation in the southeastern tropical Indian Ocean. *J. Phys. Oceanogr.*, **35**, 255-267

Raghavan, K., P. V. Puranik, V. R. Mujumdar, P. M. M. Ismail, D. K. Paul, 1978: Interaction between west Arabian Sea and Indian monsoon. *Mon. Wea. Rev.*, **106**, 719-724.

Rahmstorf, S., M. H., England, 1997: Influence of Southern Hemisphere winds on North Atlantic Deep Water flow. *J. Phys. Oceanogr.*, **27**, 2040-2054.

Reason, C. J. C., 1999: Interannual warm and cool events in the subtropical/midlatitude South Indian Ocean region. *Geophys. Res. Lett.*, **26**, 215-218.

Redi, M. H., 1982: Oceanic isopycnal mixing by coordinate rotation. *J. Phys. Oceanogr.*, **12**, 1154-1158.

Reid, J.L. and R. J. Lynn, 1971. On the influence of the Norwegian-Greenland and Weddell seas upon the bottom waters of the Indian and Pacific oceans. *Deep-Sea Res.*, **18**, 1063-1088.

Reid, J. L, W. D. Nowlin, W. C. Patzert, 1977: On the characteristics and circulation of the Southwestern Atlantic Ocean. *J. Phys. Oceanogr.*, **7**, 62-91.

Reid, J. L., 1986: On the total geostrophic circulation of the South Pacific Ocean: flow patterns, tracers and transports. *Prog. Oceanog.*, **16**, 1-61.

Reid, J. L, 1994: On the total geostrophic circulation of the North Atlantic Ocean: Flow patterns, tracers and transports. *Progress in Oceanography*, Vol. 33, Pergamon, 192 p.

Richman, M. B., 1986: Rotation of principal components. *J. Climatology*, **6**, 293-335.

Rintoul, S. R., 1998: On the origin and influence of Adélie Land Bottom Water. In: *Ocean, Ice, and Atmosphere: Interactions at the Antarctic Continental Margin*, Antarctic Research Series, Vol. 75, edited by S. S. Jacobs and R. F. Weiss, p. 151-171, AGU, Washington DC.

Rintoul, S. R., and S. Sokolov, 2001: Baroclinic transport variability of the Antarctic Circumpolar Current south of Australia (WOCE repeat section SR3). *J. Geophys. Res.*, **106**, 2795-2814.

Rintoul, S. R., and M. H. England, 2002: Ekman transport dominates local air-sea fluxes in driving variability of Subantarctic Mode Water. *J. Phys. Oceanogr.*, **32**, 1308-1320.

Robertson, R., M. Visbeck, A. L. Gordon, and E. Fahrbach, 2002: Long-term temperature trends in teh deep waters of the Weddell Sea. *Deep-Sea Res. II*, **49**, 4791-4806.

Robinson, P. J., and A. Henderson-Sellers, 1999: Contemporary Climatology. Pearson Education Limited, Singapore, 317 p.

Ruddick, B., 1983: A practical indicator of the stability of the water column to double-diffusive activity. *Deep-Sea Res.*, **30**, 1105-1107.

Sabine, C. L., and co-authors, 2004: The oceanic sink for anthropogenic CO_2. *Science*, **305**, 367-371.

Saenko, O. A., and A. J. Weaver, 2001: Importance of wind-driven sea ice motion for the formation of Antarctic Intermediate Water in a global climate model. *Geophys. Res. Lett.*, **28**, 4147-4150.

Saenko, O. A., A. J. Weaver, and M. H. England, 2003: A region of enhanced northward Atlantic Intermediate Water transport in a coupled climate model. *J. Phys. Oceanogr.*, **33**, 1528-1535.

Saha, K.R., 1970: Zonal anomaly of sea surface temperature in equatorial Indian ocean and its possible effect upon monsoon circulation. *Tellus*, **22**, 403-405.

Saji, N. H., B. N. Goswami, P. N. Vinayachandran, and T. Yamagata, 1999: A dipole mode in the tropical Indian Ocean. *Nature*, **401**, 360-362.

Saji, N. H., and T. Yamagata, 2003: Indian Ocean Dipole mode events and African rain variability. *Exchanges*, **27**, 1-4.

Santoso, A., and M. H. England, 2004: Antarctic Intermediate Water circulation and variability in a coupled climate model. *J. Phys. Oceanogr.*, **34**, 2160-2179.

Santoso, A., M. H. England, and A. C. Hirst, 2005: Circumpolar Deep Water circulation and variability in a coupled climate model. *J. Phys. Oceanogr.*, in press.

Santoso, A., and M. H. England, 2006: Antarctic Bottom Water circulation and variability in a coupled climate model. *J. Phys. Oceanogr.*, (to be submitted).

Schmid, C., G. Siedler, and W. Zenk, 2000: Dynamics of Intermediate Water Circulation in the Subtropical South Atlantic. *J. Phys. Oceanogr.*, **30**, 3191-3211.

Sciremammano, F., 1979: A suggestion for the presentation of correlations and their significance levels. *J. Phys. Oceanogr.*, **9**, 1273-1276.

Schmitz Jr., W. J., 1995: On the interbasin-scale thermohaline circulation. *Rev. of Geophys.*, **33**, 151-173.

Schneider, N., 2000: A decadal spiciness mode in the tropics. *Geophys. Res. Lett.*, **27**, 257-260.

Schott, A. F., and J. McCreary, 2001: The monsoon circulation of the Indian Ocean.*Prog. Oceanogr.*, **51**, Pergamon, 1-123.

Semtner, A. J., 1976: A model of the thermodynamics growth of sea ice in numerical investigations of climate. *J. Phys. Oceanogr.*, **6**, 379-389.

Sen Gupta, A., and M. H. England, 2004: Evaluation of interior circulation in a high resolution global ocean model, Part I: Deep and Bottom Waters. *J. Phys. Oceanogr.*, **34**, 2592-2614..

Sen Gupta, A., and M. H. England, 2006: Coupled ocean-atmosphere-ice response to variations in the Southern Annular Mode. *J. Climate*, in press.

Shaffer, G., O. Leth, O. Ulloa, J. Bendtsen, G. Daneri, V. Dellarossa, S. Hormazabal, and P.-I., Sehlstedt, 2000: Warming and circulation change in the eastern South Pacific Ocean. *Geophys. Res. Lett.*, **27**, 1247-1250.

Shinoda, T., M. A. Alexander, and H. H. Hendon, 2004: Remote response of the Indian Ocean to interannual SST variations in the tropical Pacific. *J. Climate*, **17**, 362-372.

Shukla, J., and B. M. Misra, 1977: Relationships between sea surface temperature and wind speed over the central Arabian Sea, and monsoon rainfall over India. *Mon. Wea. Rev.*, **105**, 998-1002.

Sievers, H. A., and W. D. Nowlin, Jr., 1984: The stratification and water masses at Drake Passage. *J. Geophys. Res.*, **89**, 10,489-10,514.

Sigman, D. M., and E. A. Boyle, 2000: Glacial/interglacial variations in atmospheric carbon dioxide. *Nature*, **407**, 859-869.

Sijp, W.P., Bates, M.L., and M.H. England, 2006: Can isopycnal mixing control the stability of the thermohaline circulation in ocean climate models? *J. Climate*, in press.

Simmons, H. L., and I. V. Polyakov, 2004: Restoring and flux adjustment in simulating variability of an idealized ocean.
Geophys. Res. Lett., **31**, doi:10.1029/2004GL020197.

Sloyan, B. M., and S. R. Rintoul, 2001a: The Southern Ocean limb of the global deep overturning circulation. *J. Phys. Oceanogr.*, **31**, 143-173.

Sloyan, B. M., and S. R. Rintoul, 2001b: Circulation, renewal, and modification of Antarctic Mode and Intermediate Water. *J. Phys. Oceanogr.*, **31**, 1005-1030.

Smethie Jr., W. M., R. A. Fine, A. Putzka, and E. P. Jones, 2000: Tracing the flow of North Atlantic Deep Water using chlorofluorocarbons. *J. Geophys. Res.*, **105**, 14,297-14,323.

Smith, I. N., P. McIntosh, T. J. Ansell, C. J. C. Reason, and K. McInnes, 2000: Southwest Western Australian winter rainfall and its association with Indian Ocean climate variability. *Int. J. Climatology*, **20**, 1913-1930.

Sokolov, S., and S. R. Rintoul, 2000: Circulation and water masses along WOCE section P11: Papua New Guinea to Tasmania. *J. Mar. Res.*, **58**, 223-268.

Sørensen, J. V. T., J. Ribbe, and G. Shaffer, 2001: Antarctic Intermediate Water mass formation in ocean general circulation models. *J. Phys. Oceanogr.*, **31**, 3295-3311.

Speer, K., E. Guilyardi, and G. Madec, 2000: Southern Ocean transformation in a coupled model with and without eddy mass fluxes. *Tellus*, **52A**, 554-565.

Storch, H. V., and F. W. Zwiers, 1999: Statistical Analysis in Climate Research. Cambridge University Press, 484 p.

Stössel, A., and S.-J. Kim, 1998: An interannual Antarctic sea-ice-ocean mode. *Geophys. Res. Lett.*, **25**, 1007-1010.

Stössel, A., and S.-J. Kim, 1998: The impact of Southern Ocean sea ice in a global ocean model. *J. Phys. Oceanogr.*, **28**, 1999-2018.

Stössel, A., S. J. Kim, 2001: Decadal deep-water variability in the subtropical Atlantic and convection in the Weddell Sea. *J. Geophys. Res.*, **106**, 22425-22440.

Stössel, A., K. Yang, and S.-J. Kim, 2002: On the role of sea ice and convection in a global ocean model. *J. Phys. Oceanogr.*, **32**, 1194-1208.

Stramma, L., and M. England, 1999: On the water masses and mean circulation of the South Atlantic Ocean. *J. Geophys. Res.*, **104**, 20,863-20,883.

Suzuki, R., S. K. Behera, S. Iizuka, and T. Yamagata, 2004: Indian Ocean subtropical dipole simulated using a coupled general circulation model. *J. Geophys. Res.*, **109**, doi:10.1029/2003JC001974.

Sverdrup, H. U., M. W. Johnson, and R. H. Fleming, 1942: The Oceans: Their Physics, Chemistry, and General Biology. Prentice Hall, 1087 p.

Swift, J. H., 1984: The circulation of the Denmark Strait and Iceland-Scotland overflow waters in the North Atlantic. *Deep Sea Res.*, **31**, 1339-1355.

Talley, L. D., and M. S. McCartney, 1982: Distribution and circulation of Labrador Sea Water. *J. Phys. Oceanogr.*, **12**, 1189-1205.

Talley, L. D., 1996: Antarctic Intermediate Water in the South Atlantic. *The South Atlantic: Present and Past Circulation.* G. Wefer, W. H. Berger, G. Siedler, and D. J. Webb, Eds., Springer Verlag, 219-238.

Talley, L. D., 2003: Shallow, intermediate, and deep overturning components of the global heat budget. *J. Phys. Oceanogr.*, **33**, 530-560.

Toggweiler, J. R., and B. Samuels, 1995: Effect of Drake Passage on the global thermohaline circulation. *Deep-Sea Res. I*, **42**, 477-500.

Toggweiler, J. R., and B. Samuels, 1995: Effect of sea ice on the salinity of Antarctic Bottom Water. *J. Phys. Oceanogr.*, **25**, 1980-1997.

Tomczak, M., and J. S. Godfrey, 2003: Regional Oceanography: An Introduction. Delhi, Daya Pub., 390 p.

Treguier, A. M., O. Boebel, B. Barnier, G. Madec, 2003: Agulhas eddy fluxes in a 1/6° Atlantic model. *Deep-Sea Res. II*, **50**, 251-280.

Tsuchiya, M., L. D. Talley, and M. S. McCartney, 1994: Water-mass distributions in the western South Atlantic: A section from South Georgia Island (54S) northward across the equator. *J. Marine Res.*, **52**, 55-81.

Venegas, S. A., L. A. Mysak, and D. N. Straub, 1997: Atmosphere-ocean coupled variability in the South Atlantic. *J. Climate*, **10**, 2904-2920.

Venzke, S., M. Latif, and A. Villwock, 2000: The coupled GCM ECHO-2. Part II: Indian Ocean response to ENSO. *J. Climate*, **13**, 1371-1383.

Vimont, D., D. S. Battisti, and A. C. Hirst, 2002: Pacific interannual and interdecadal Equatorial variability in a 1000-year simulation of the CSIRO coupled general circulation model. *J. Climate*, **15**, 160-178.

Wainer, I., and S. A. Venegas, 2002: Multidecadal variability in the Climate System Model. *J. Climate*, **15**, 1408-1420.

Wallace, J. M., E. M. Rasmusson, T. P. Mitchell, V. E. Kousky, E. S. Sarachik, and H. von Storch, 1998: On the structure and evolution of ENSO-related climate variability in the tropical Pacific: Lessons from TOGA. *J. Geophys. Res.*, **103**, 14241-14259.

Walland, D. J., S. B. Power, and A. C. Hirst, 2000: Decadal climate variability simulated in a coupled general circulation model. *Climate Dynamics*, **16**, 201-211.

Weare, B. C., 1979: A statistical study of the relationships between ocean surface temperatures and the Indian Monsoon. *J. Atmospheric Sciences*, **36**, 2279-2291.

Weaver, A. J., and T. M. C. Hughes, 1992: Stability and variability of the thermohaline circulation and its link to climate. *Trends in Phys. Oceanogr.*, **1**, 15-69.

Webster, P. J., A. M. Moore, J. P. Loschnigg, and R. R. Leben, 1999: Coupled ocean-atmosphere dynamics in the Indian Ocean during 1997-98. *Nature*, **401**, 356-363.

Weijer, W., and H. A. Dijkstra, 2003: Multiple oscillatory modes of the global ocean circulation. *J. Phys. Oceanogr.*, **33**, 2197-2213.

White, W. B., and R. G. Peterson, 1996: An Antarctic circumpolar wave in surface pressure, wind, temperature and sea-ice extent. *Nature*, **380**, 699-702.

Whitworth, T., and W. D. Nowlin, 1987: Water masses and currents of the Southern Ocean at the Greenwich meridian, *J. Geophys. Res.*, **92**, 6462-6476.

Whitworth, T., A. H. Orsi, S.-J. Kim, and W. D. Nowlin Jr., 1989: Water masses and mixing near the Antarctic slope front. In: *Ocean, Ice, and Atmosphere: Interactions at the Antarctic Continental Margin*, Antarctic Research Series, Vol. 75, edited by S. S. Jacobs and R. F. Weiss, p. 1-27, AGU, Washington DC.

Whitworth, T., B. A. Warren, W. D. Nowlin, Jr., S. B. Rutz, R. D. Pillsbury, M. I. Moore, 1999: On the deep western-boundary current in the Southwest Pacific Basin. *Prog. Oceanogr.*, **43**, 1-54.

Wijffels, S. E., J. M. Toole, and R. Davis, 2001: Revisiting the South Pacific subtropical circulation: a synthesis of World Ocean Circulation Experiment observations along 32°S. *J. Geophys. Res.*, **106**, 19 481−19 513.

Wong, A. P. S., N. L. Bindoff, and J. Church, 1999: Large-scale freshening of intermediate waters in the Pacific and Indian Oceans. *Nature*, **400**, 440-443.

Wong, A. P. S., N. L. Bindoff, J. A. Church, 2001: Freshwater and heat changes in the North and South Pacific Oceans between the 1960s and 1985-94. *J. Phys. Oceanogr.*, **14**, 1613-1633.

Wright, W.J., 1997: Tropical-extratropical cloudbands and Australian rainfall: I. Climatology. *Int. J. Climatology*, **17**, 807-829.

Wunsch, C., D. Hu, and B. Grant, 1983: Mass, heat, salt and nutrient fluxes in the South Pacific Ocean. *J. Phys. Oceanogr.*, **13**, 725-753.

Wüst, G., 1935: Schichtung und Zirkulation des Atlantischen Ozeans. Das Bodenwasser und die Stratosphäre. *Wiss. Ergeb. Dt.Atl. Exp. METEOR*, **6**, 1-288.

Yeager, S. G., and W. G. Large, 2004: Late-winter generation of spiciness on subducted isopycnals. *J. Phys. Oceanogr.*, **34**, 1528-1547.

You, Y.-Z., 2000: Implications of the deep circulation and ventilation of the Indian Ocean on the renewal mechanism of North Atlantic Deep Water. *J. Geophys. Res.*, **105**, 23,895-23,926.

Xie, P., and P. A. Arkin, 1996: Analyses of global monthly precipitation using gauge observations, satellite estimates, and numerical model predictions. *J. Climate*, **9**, 840-858.

List of Acronyms

AABW	Antarctic Bottom Water
AAIW	Antarctic Intermediate Water
AASW	Antarctic Surface Water
ACC	Antarctic Circumpolar Current
ACW	Antarctic Circumpolar Wave
APFZ	Antarctic Polar Front Zone
AR	autoregressive
BMCZ	Brazil-Malvinas Confluence Zone
BoM	Australian Bureau of Meteorology
CDW	Circumpolar Deep Water
CEOF	complex empirical orthogonal function
cpy	cycle per year
CSIRO	Commonwealth Scientific and Industrial Research Organisation
DWBC	Deep Western Boundary Current
ENSO	El Niño Southern Oscillation
EOF	empirical orthogonal function
GCM	general circulation model
GFDL	Geophysical Fluid Dynamics Laboratory
GM	Gent and McWilliams parameterisation
IPCC	Intergovernmental Panel on Climate Change
IOD	Indian Ocean Dipole
IOSD	Indian Ocean Subtropical Dipole
ITF	Indonesian throughflow
LCDW	lower Circumpolar Deep Water

LNADW	lower North Atlantic Deep Water
NADW	North Atlantic Deep Water
NCAR	National Center for Atmospheric Research
NCEP	National Center for Environmental Prediction
NEC	North Equatorial Current
NH	Northern Hemisphere
NOAA	National Oceanic and Atmospheric Administration
PSD	power spectral density
psu	practical salinity units
SAM	Southern Annular Mode
SAMW	Subantarctic Mode Water
SEC	South Equatorial Current
SH	Southern Hemisphere
SO	Southern Ocean
SOI	Southern Oscillation Index
SST	sea surface temperature
SSS	sea surface salinity
SLP	sea level pressure
SWWA	southwest Western Australia
UCDW	upper Circumpolar Deep Water
UNADW	upper North Atlantic Deep Water
WDW	Warm Deep Water
WOCE	World Ocean Circulation Experiment
WSBW	Weddell Sea Bottom Water
WSDW	Weddell Sea Deep Water